Nanotechnology platforms for detection and analysis of clinically relevant biological nanoparticles

Pepijn Beekman

Propositions:

1. Reproducible, high-purity immunocapture of submicroscopic objects is only possible under controlled flow conditions. (this thesis)

2. Electrochemistry methods outperform the frequently used optical techniques in tumor-derived extracellular vesicle enumeration in terms of throughput. (this thesis)

3. The reverse transcription polymerase chain reaction provides a shockingly inadequate method of identifying a SARS-CoV-2 infection. (in response to: L. M. Kucirka, S. A. Lauer, O. Laeyendecker, D. Boon and J. Lessler, *Ann. Intern. Med.*, 2020, 173, 262–267.)

4. In-vitro fertilization is a miracle of natural science of the same order of magnitude as SARS-CoV-2 vaccines.

5. Biologists are worse than Americans when it comes to the use of SI units.

6. Lunch is an overappreciated luxury.

Propositions belonging to the thesis entitled

'Nanotechnology platforms for detection and analysis of clinically relevant biological nanoparticles'

Pepijn Beekman

Wageningen, July 2nd 2021

Nanotechnology platforms for detection and analysis of clinically relevant biological nanoparticles

Pepijn Beekman

Thesis committee
Promotor
Prof. Dr H. Zuilhof
Professor of Organic Chemistry
Wageningen University & Research

Co-promotor
Prof. Dr S. Le Gac
Associate Professor, Applied Microfluidics for BioEngineering Research
University of Twente, Enschede

Other members
Prof. Dr Yoon-Kyoung Cho,
Ulsan National Institute of Science & Technology, Republic of Korea
Prof. Dr F.A.M. Leermakers, Wageningen University & Research
Prof. Dr T.G. van Leeuwen, Amsterdam UMC, University of Amsterdam
Prof. Dr Menno Prins, Technische Universiteit Eindhoven

This research was conducted under the auspices of the Graduate School VLAG (Advanced studies in Food Technology, Agrobiotechnology, Nutrition and Health Sciences).

Nanotechnology platforms for detection and analysis of clinically relevant biological nanoparticles

Pepijn Beekman

Thesis
submitted in fulfilment of the requirements for the degree of doctor
at Wageningen University
by the authority of the Rector Magnificus,
Prof. Dr A.P.J. Mol,
in the presence of the
Thesis Committee appointed by the Academic Board
to be defended in public
on Friday 2 July 2021
at 1:30 p.m.

Pepijn Beekman
Nanotechnology platforms for detection and analysis of clinically relevant biological nanoparticles,
239 pages.
PhD thesis, Wageningen University, Wageningen, the Netherlands (2021)
With references, with summary in English

ISBN 978-94-6395-827-1

DOI https://doi.org/10.18174/547562

“Got to be good-lookin’ ‘cause they’re so hard to see”
- Lennon

Contents

GLOSSARY

Å	*Ångström*
ADPA	*aminododecyl phosphonic acid*
AFM	*atomic force microscopy*
ALP	*alkaline phosphatase*
AUT	*aminoundecanethiol*
C-AE	*capture antibody*
CD_n	*[cluster of differentiation]$_n$*
CDPA	*carboxydecyl phosphonic acid*
CK	*cytokeratine*
CM	*chylomicrons*
CT	*computed tomography*
CTC	*circulating tumor cell*
DAPI	*diamidinophenylindole*
DNA	*deoxyribonucleic acid*
EGFR	*epidermal growth factor receptor*
EpCAM	*epithelial cell adhesion molecule*
ELISA	*enzyme-linked immunosorbent assay*
EV	*extracellular vesicle*
FC(M)	*flow cytometry*

FM	*fluorescent microscopy*
FDA	*Food and Drug Administration*
FITC	*fluorescein isothiocyanate*
HDL	*high-density lipoprotein*
HER2	*Human epidermal growth factor receptor 2*
HMDS	*hexamethyl disilazane*
LDL	*low-density lipoprotein*
LOC	*lab-on-a-chip*
LOD	*limit of detection*
ltdEV	*large tumor-derived extracellular vesicle*
MRI	*magnetic resonance imaging*
MS	*mass spectrometry*
nIDE	*nano-interdigitated electrode*
NIPA	*nanoelectrodes for individual particle analysis*
NTA	*nanoparticle tracking analysis*
NWO	*Nederlandse organisatie voor Wetenschappelijk Onderzoek*
pAP	*para-aminophenol*
pAPP	*para-aminophenol phosphate*
PBS	*phosphate buffered saline*
PCR	*polymerase chain reaction*
pdEV	*plasma-derived extracellular vesicle*
PDMS	*poly(dimethylsiloxane)*
PEGDGE	*poly(ethylene glycol) diglycidyl ether*
pEV	*platelet-derived extracellular vesicle*

pQI	*paraquinone imine*
RBC	*red blood cell*
RE	*reference electrode*
R-AE	*reporter antibody*
RNA	*ribonucleic acid*
SAM	*self-assembled monolayer*
SAV-ALP	*alkaline phosphatase-conjugated streptavidin*
SEC	*size exclusion chomatrography*
SEM	*scanning electron microscopy*
SPR	*surface plasmon resonance*
SPRi	*surface plasmon resonance imaging*
stdEV	*small tumor-derived extracellular vesicle*
tdEV	*tumor-derived extracellular vesicle*
TEM	*transmission electron microscopy*
VLDL	*very low-density lipoprotein*
WBC	*white blood cell*
WE	*working electrode*
XPS	*X-ray photoelectron spectroscopy*

1

Introduction

1.1 Liquid biopsy for cancer diagnosis

Cancer is currently by far the leading cause of death in the Netherlands, responsible for 30% of deaths.[1] The most lethal part of the pathogenesis is metastasis.[2] In metastasis, cells dislodge from the primary tumor and traverse the surrounding epithelium, entering nearby blood vessels through the endothelium. Through the blood circulation, the cells migrate to other locations in the body during which time they are called circulating tumor cells (CTCs).[3] If these cells are not cleared, they can extravasate and form metastatic clusters in other organs to form secondary tumors (metastases).[4,5]

1.1.1 Circulating tumor cells

It has been shown that the concentration of CTCs in the blood of metastatic cancer patients correlates with their clinical outcome, *i.e.,* with their probability of survival, for extended periods.[6–9] Moreover, a decrease in CTC concentration in response to a treatment is indicating successful treatment, which is accompanied by an increased probability of survival.[5,7,10] This can be monitored using liquid biopsies. In this procedure, samples of blood or other bodily fluids are analyzed for the presence and concentration of biomarkers like CTCs. This method can be complementary to, or replace imaging techniques like magnetic resonance imaging (MRI) or computed tomography (CT) and traditional tissue biopsies.[11] An advantage that CTC-targeting liquid biopsies have over tissue biopsies is that blood samples can be taken repeatedly to monitor the progression of the disease, recognizing a change in concentration.[12] In comparison with CT and MRI, CTC-targeting liquid biopsies can be considered better prognostic tools because the mentioned imaging techniques lack the spatial resolution to discover the smallest secondary tumors.[13,14] Moreover, a response to treatment does not necessarily result in a direct change in the presence of metastases.[15–17]

1.1.2 CTC abundance

However, the development of liquid biopsies also requires overcoming technological challenges. For CTCs, the inherent obstacle to reliable measurements is the complexity of blood as a medium. A milliliter of blood of metastatic cancer patients contains several billions of red blood cells (RBCs),

millions of white blood cells (WBCs) and only a few CTC (although severely ill patients may have up to 3×10^3 CTC/ml).[18,19] The only instrument for CTC-targeting liquid biopsies that is FDA-approved for clinical purposes is CellSearch.[20] It uses antibody-modified magnetic nanoparticles to enrich CTCs in 7.5 ml of blood based on the expression of the epithelial marker EpCAM (Epithelial Cell Adhesion Molecule). This system allows discarding all RBCs and ∽99.9% of WBCs, yielding a ratio of about 1 CTC per $\backsim10^2$-10^3 total retained cells.[21] The resulting cells are stained with a mixture of fluorescently labeled reagents for specific markers of interest (such as EpCAM, nucleus, cytokeratine, or CD45). An automated fluorescence microscope identifies CTCs as such when the objects match a predefined appearance profile.[22,23] This process with its many sequential processing steps has been optimized to have an estimated detection efficiency in the order of 30% - which is subject to inter-operator variation.[18] When the number of CTCs found in a sample exceeds a threshold value of 3-5 per sample, depending on the type of cancer, the patient gets an "unfavorable" prognosis. The Kaplan-Meier plot in Figure 1.1a shows that for a specific set of patients and a specific type of prostate cancer, an unfavorable prognosis implied having a 50% probability of surviving for 11.6 months after the sample is collected. Conversely, patients in this group with a "favorable" prognosis have a 50% probability of surviving for 29.6 months.

Considering the low abundance of CTCs in blood, impactful decisions are based on very small datasets. A single cell out of only 3-5 can influence the decision between different treatment plans. That means that, statistically, the data obtained with the CellSearch system are not very robust. If, for instance, a patient has 667 CTCs distributed over 5 L of blood, the probability of finding ≥1 CTC in 7.5 ml is only 63%.[19] In that regard, tumor-derived extracellular vesicles (tdEVs) are more promising biomarkers, as explained in the next section.

1.2 tdEVs as liquid biopsy target

1.2.1 Extracellular vesicles

Extracellular vesicles (EVs) are small (30 nm – 1 µm) particles released by cells through various mechanisms.[25–29] Initially these particles were discarded as cellular debris,[30] but with the increasing availability of sub-microscopic analytical tools in recent years, EVs have received increasing attention (see Figure 1.2a). All eukaryotic cells release EVs and they are present in all bodily fluids;[28] *e.g.,* blood likely contains about $\sim 10^{10}$ EVs/ml (± 2 orders of magnitude depending on the study),[31,32] mostly originating from blood cells and platelets.[33] There are variousmembranes. To distinguish EVs from other lipid-containing blood components, a few *generic EV-specific markers* have been identified, *e.g.,* CD9, CD63 and CD81.[36,41] These proteins are found in higher concentrations on EVs than on other biological species. CD9 and CD63 were originally thought of as exosome-specific markers, *i.e.,* specific to a certain type of small EV.[26] However, it has been shown that EV size and amount of these biomarkers do not

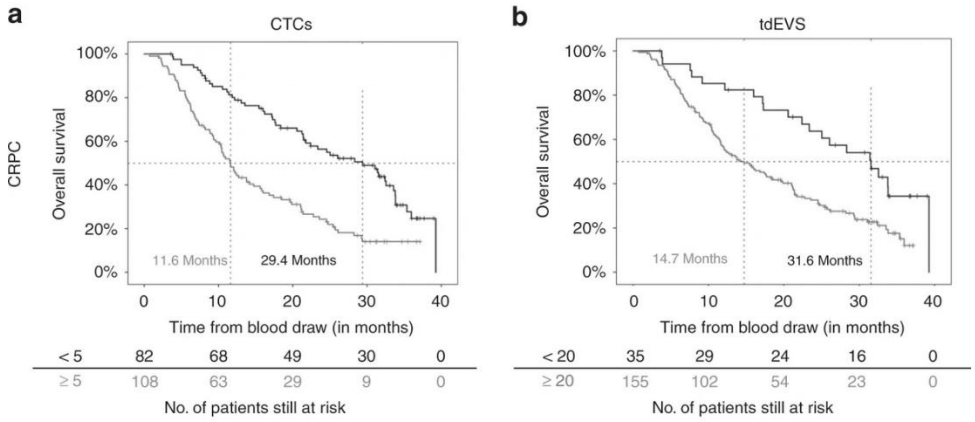

Figure 1.1: *Kaplan-Meier plots showing survival of castration-resistant prostate cancer (CRPC) patients with <5 CTCs per sample (a) or <20 tdEVs (b) versus the survival of patients with ≥5 CTCs per sample or ≥20 tdEVs. Overall, patients with higher concentrations have smaller probability of survival for a given time. Reproduced from Nanou et al.*[24]

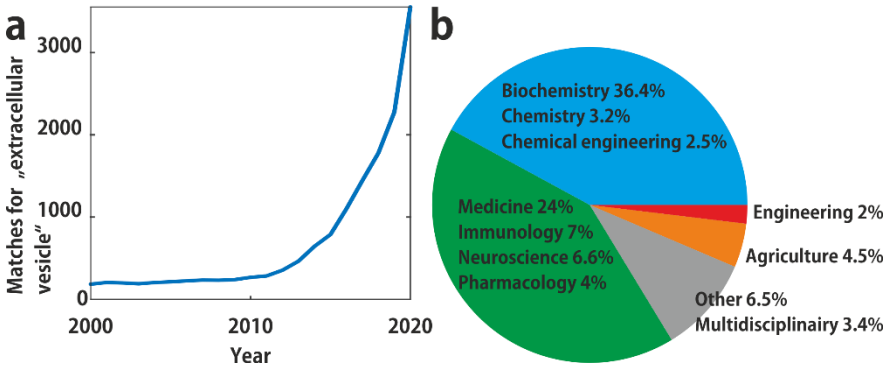

Figure 1.2: *Impression of the extracellular vesicle field as analyzed by scopus.com. a) the number of publications with the term "extracellular vesicle" in the title, abstract or keywords has exponentially increased for the past decade. b) At least 80% of journals reporting about EVs have a biomedical scope.*

necessarily correlate. The mentioned markers are often used in studies where the presence of all EVs, regardless of their origin, is investigated.

1.2.2 Specific EV types

For diagnostic purposes, targeting *specific EVs* is more interesting.[42–44] Liquid biopsies targeting CTCs as well as solid biopsies can stain cells for the presence of cancer-specific membrane proteins, *e.g.,* Human Epidermal growth factor Receptor 2 (HER2), Epidermal growth factor receptor (EGFR), or the epithelial cell adhesion molecule (EpCAM). The CellSearch system uses anti-EpCAM to enrich cells which express this tetraspanin molecule. EpCAM is present on all epithelial tissue, but since epithelial cells are not expected in blood of healthy individuals, it has proven to be a "smoking gun" – indicating that there is an anomaly.[45,46] It has been shown that the concentration of all EpCAM-positive particles (*i.e.,* particles that evidently contain EpCAM) in metastatic cancer patient samples has prognostic value. Figure 1.1b shows data obtained with the CellSearch system using different identification criteria; not showing cells but the smaller EpCAM-positive particles believed to be (large) EVs. A similar prognostic value was found for EpCAM-positive EVs and CTCs. Because these EVs are derived from tumor tissue, they are known as tdEVs to illustrate the distinction from EVs that are also found in healthy individuals. Actual

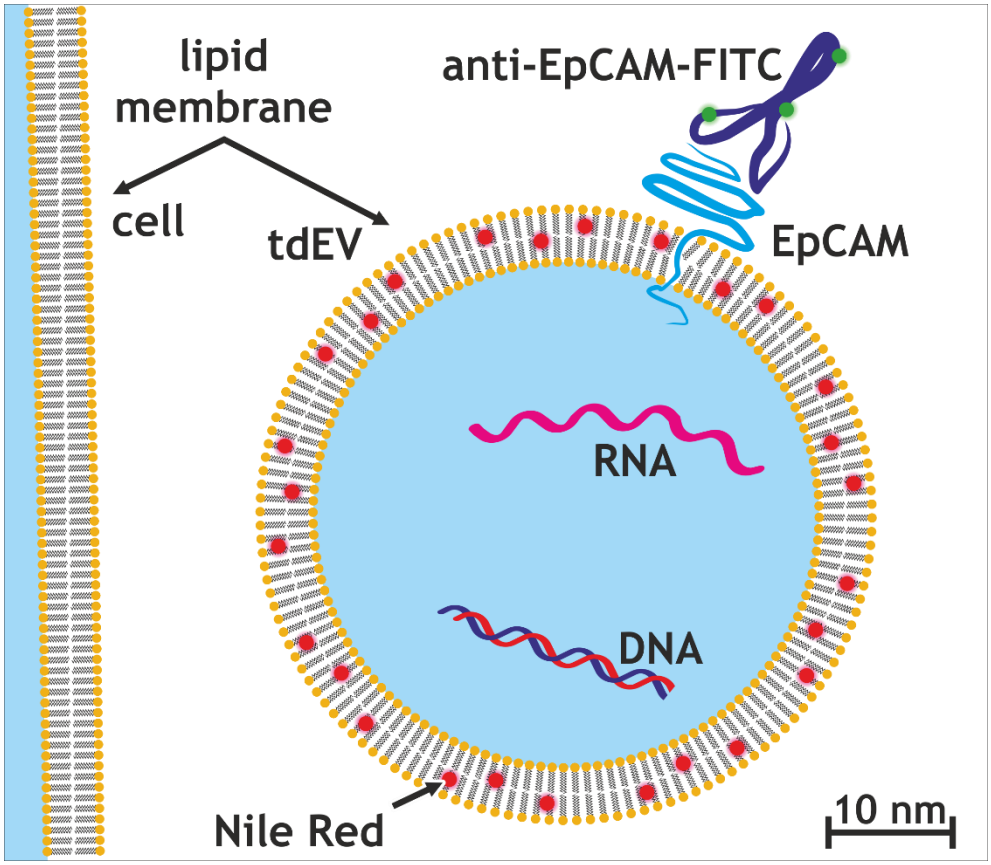

Figure 1.3: *Cartoon of a 50 nm tdEV containing nucleic acid fragments and 1 membrane protein (in reality, EVs contain many). The phospholipid membrane closely resembles that of a cell and can be stained with a non-specific lipophilic dye, e.g. Nile Red. The curvature at this scale of a typical cell is illustrated on the left.*

concentrations of tdEVs in patients are unknown, but are expected to range from 10^2-10^6 tdEVs/ml.[47,48]. Consider a typical patient with 5 L of blood containing 6667 CTCs and 5×10^7 tdEVs, both distributed over the whole volume of blood following a Poisson distribution.[49] In a Poisson distribution, the probability P of finding n events with an expected number of events u is:

$$P(n) = \frac{u^n e^{-u}}{n!} \qquad (1)$$

If a large number of tubes (7.5 ml) of blood from this patient were analyzed by a system that perfectly detects every CTC with no false positives, and many droplets of blood (100 µl) were analyzed by a perfect tdEV detector, the results would be similar to those depicted in Figure 1.4. Here, the difference in reliability of the two measurements is shown; targeting CTCs entails obtaining a smaller dataset that is inherently less accurate. With $u = 10$, (for a high typical number of CTCs in 7.5 ml of this patient's blood) 63% of samples will have a value deviating by >10% from u. However, when u is as high as 1000, (for a typical low average number of tdEVs in 0.1 ml of this patient's blood) the most deviant 52% of samples will have a value deviating by only >2% from u, *i.e.,* the relative error is much less for higher numbers.

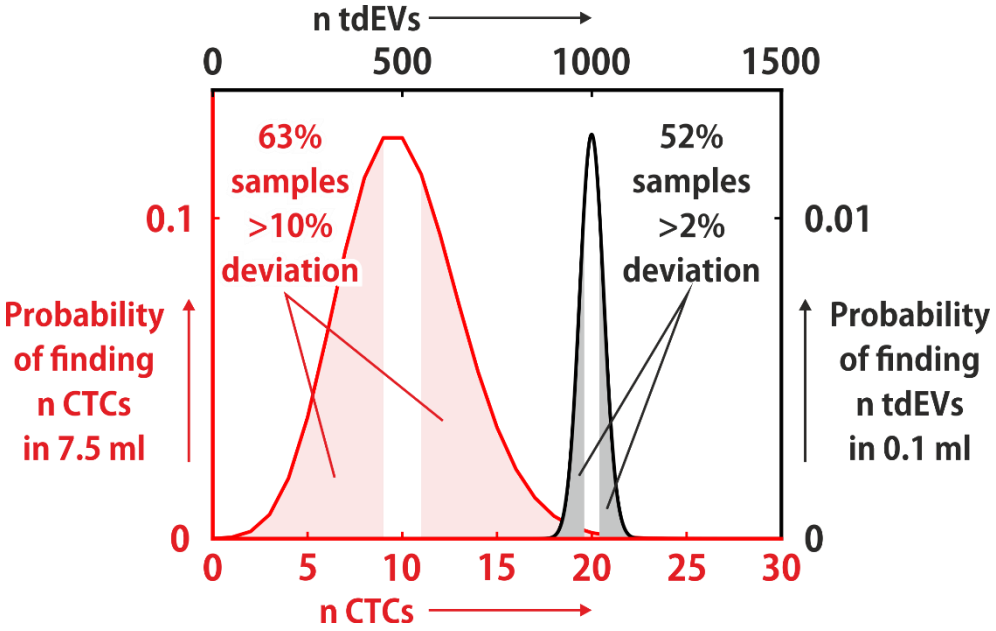

Figure 1.4: *Modeled distribution of CTCs over tubes of blood and tdEVs over droplets of blood. Shaded areas indicate the smallest error that can be expected in at least half of the measurements. Larger sample sizes give more accurate results.*

1.2.3 Detection limit

Since the CellSearch instrument was designed to identify tumor cells (6 – 30 µm), it is with its current optical components unfit to reliably detect all the (much smaller) tdEVs. Hence, it is estimated that the CellSearch system underestimates the tdEV concentration by two orders of magnitude. [47,50]

In general, it is noted by many experts in the field that there is much still unclear about EVs because of challenges involved in the characterization of EVs, as well as in their isolation. This has led to many misunderstandings (like the nomenclature as mentioned before) and the reporting of false and inaccurate data.[39,51–53] This thesis summarizes the findings of one out of 9 PhD projects in the NWO Perspectief project "Cancer-ID", which was collectively aiming at studying EVs to gain a better understanding of their composition, to assess their clinical utility and to develop new tools for their enumeration and characterization. To address the issues introduced in this section, both novel isolation (see next section) and detection (see section 1.4) methods were required.

1.3 Isolating EVs

1.3.1 Conventional generic EV isolation

Isolation of EVs is conventionally performed using ultracentrifugation, separating samples based on the densities of the components. In complex samples, this often leads to co-precipitation of components with similar densities like lipoproteins.[54–57] In a milliliter of blood, there are billions of red blood cells and millions of white blood cells. On a smaller scale, there are in the order of 10^8 platelets and there are lipoproteins of various sizes ranging from chylomicrons (100-1000 nm, 10^{13} ml^{-1}) to high-density lipoproteins (10 nm, 10^{16} ml^{-1}). On a molecular level there are many different proteins, such as albumin and immunoglobulins (few nm in size), and a wide variety of smaller molecules (0.2 - few nm). Since it is challenging with most techniques to discriminate between lipoproteins and EVs, the assumption that ultracentrifugation results in pure EV samples typically leads to overestimation of the EV concentration in a sample. It

is also a challenge to some techniques to perform measurements on EVs specifically and not to contaminate a dataset with measurements erroneously performed on other components of a sample.[58,59]

Another often used purification method is size exclusion chromatography, whereby a sample is passed through a column containing a porous material.[60–62] Components that fit in the pores are retained in the column for more time, while bigger components are more quickly eluted. Therefore, this size difference affects the overall residence time in the column. By separating fractions based on the time they need to exit the column, which effectively distinguishes fractions on the size of their components, larger particles can be separated from smaller ones. If pores of few tens of 10 nm are used, proteins and other molecules that are smaller than EVs can reside in these pores, but EVs will be rejected. This allows for discarding smaller species like proteins, but again it does not help to separate lipoproteins in the same size range, like very-low-density-lipoproteins (VLDL) or chylomicrons.[59]

1.3.2 Specific EV isolation

Specific analysis of EVs requires functionalized surfaces with enhanced affinity towards the specific type of targeted EVs. This presupposes the immobilization of specific recognition elements such as antibodies to the surface. Ideally, the relative affinity is further improved by reducing the ability of other sample components to non-specifically adsorb, by means of embedding the recognition element in an anti-fouling layer to construct a so-called romantic surface. [63–65]

The first step in such surface modification strategy frequently consists of forming a monolayer on a substrate to incorporate functional groups to which antibodies can be immobilized through standard aqueous phase processes. The type of chemicals used for forming the monolayer depends on the nature of the substrate: for noble metals such as gold or platinum, widely used in biosensors,[66–68] thiol-based compounds are commonly employed,[69] whereas metal oxides can be more stably functionalized with phosphonic acid compounds,[70,71] while glass, silicon oxide and poly(dimethyl siloxane) can be treated through a silanization process.[72–75]

Antifouling layers can be composed of various moieties, which are typically

hydrophilic with a degree of intermolecular ordering. This ordering – either in between chains such as in poly(hydroxypropyl methacrylamide) – or between chain-water complexes in polyzwitterionics and poly-ethylene oxides (also called: PEGs) yields a structure that is enthalpically and/or entropically unfavorable for proteins to disrupt. The most ubiquitous antifouling layer is based on PEGs.[74,76,77] Yet superior anti-fouling properties are attributed to zwitterionic polymer brushes. [63–65,78]

This surface-bound polymer layer can contain reactive moieties, to which a recognition element is next covalently attached. These recognition elements include lectins (i.e. sugar-binding proteins),[79,80] peptides,[81,82] aptamers[83,84] or antibodies.[85,86] The most commonly used method for crosslinking these molecules to surface-bound layers is carbodiimide chemistry.[87] It employs a "zero-length linker" to bind a carboxyl group on the surface to a primary amine present on the surface of the antibody, such as those presented by lysine residues, to form a stable amide bond.[88] Other crosslinking approaches use reactive groups like aldehydes[89,90] , epoxide groups[91,92] and recently also click chemistry.[93] Once immobilized, recognition elements can form relatively stable complexes with antigens (uniquely) present on EVs. These, frequenly multivalent, electrostatic and hydrogen-bonding based interactions can withstand shear forces that are strong enough to remove other, non-specifically adsorbed species that do only weakly adhere on the antifouling background. As such, affinity coatings can be used to enrich EVs from samples *in situ*, as demonstrated throughout this thesis, based on the presence of antigens of interest.

1.4 Studying EVs

For the quantification and characterization of EVs, many techniques are available.[94] Techniques detecting generic EVs can be distinguished from those that target specific subsets of EVs, like tdEVs.[39,95] Furthermore, they can be divided into different categories based on whether they target individual particles, or generate a signal as an average response to the presence of an

ensemble of particles being present in the samples. Some of these techniques are explained in more detail in Chapter 2.

1.4.1 Generic individual EV detection

To characterize EVs individually, e.g. to study their morphology and size or estimate their concentration, high-resolution techniques are available, including electron microscopy[50,51] and scanning probe microscopy.[96,97] These instruments allow imaging EVs in high detail. They do not yield any biological information however; it is possible to distinguish EVs from lipoproteins, but among EVs there is no apparent difference between various types using these methods. Moreover, because electron microscopy is performed in vacuum and scanning probe microscopy on a surface, dedicated sample preparation requirements make it difficult to image EVs in their native physiological state (see Chapter 3). Nonetheless, these high-resolution methods can be used as supplemental methods in experiments studying EVs in more detail.

An alternative technique is Nanoparticle Tracking Analysis (NTA) which uses light scattering of diluted samples to determine the hydrodynamic radius of nanoparticles using Brownian motion.[94] NTA does not give any information about the composition or origin of these particles, but provides an estimate of the size distribution and concentration of a colloidal sample. It underestimates the concentration of small particles (<70 nm), and reproducibility is a challenge, but it remains currently the gold standard in the EV field for its purpose.[98]

1.4.2 Specific bulk EV detection

Using *e.g.* the markers mentioned in section 1.2.3, a signal can be obtained from EVs that present certain antigens. The simplest assay in this category is the dot blot,[99,100] where some EV material is deposited on a surface, stained with a fluorescently labeled marker, washed and imaged on a (fluorescence) microscope. Although this method is at best semi-quantitative, it conveniently gives information about presence of antigens in different types of EVs.

More elaborate techniques include the well-established enzyme-linked immunosorbent assay (ELISA) whereby analytes are immobilized on a first antibody and tagged with an enzyme-conjugated second antibody.[101] The enzyme is then used to amplify the signal (colorimetric or fluorescence

detection), greatly increasing the sensitivity of this technique. After establishing a calibration curve and optimizing the process to ensure reproducibility, this method provides quantitative information on analyte concentration.

In chapter 6 of this thesis, a variation on this principle is presented, where the final recorded signal is not optical but electrochemical. The enzyme was in that case used to convert an electrochemically inert molecule into a molecule that can be reversibly oxidized and reduced. This repeated process yielded a further amplification by so-called redox cycling.

1.4.3 Specific individual EV detection

The Abbe diffraction limit dictates that even in optimized optical detection systems, the smallest resolvable feature size is larger than approximately one third of the wavelength of the light it scatters.[102] Considering inherent technical limitations like aberration, large aperture and limited detector sensitivity, with most microscopes available in biomedical labs, resolving submicron particles is challenging.

There is a range of ingenious solutions to modify optical equipment to increase the resolution beyond the diffraction limit mentioned earlier. These so-called super-resolution microscopy systems include confocal laser scanning microscopy, whereby a single point of illumination is scanned across the sample rather than using widefield illumination. Out-of-focus light is then blocked using a pinhole. This way, the resolution limit can be improved by a factor of ~ 2.[103,104] More advanced systems exist that use non-linear photonic effects or by superimposing multiple widefield images, allowing to resolve objects of several tens of nanometers. [102,105,106] However, given the complexity of these techniques, very few studies of EVs have been conducted, if any.

1.4.3.1 Specific optical imaging of all EVs

In principle, in a well-built system, it is possible to detect a single photon with sensors that are commonly available. But even with confocal microscopy (employing such detectors), in practice it is challenging to distinguish faint signals emitted by the sample from the autofluorescent background of the environment.[103] The signal intensity is related to the labeling density. Taking EpCAM as an example, it has been estimated that CTCs express up to 2.5×10^5

EpCAM molecules distributed across their membrane.[107] Assuming that the density is the same for tdEVs (for microvesicles shedding from the cell membrane, this hypothesis does not seem unreasonable) and considering that surface area scales quadratically with radius, a tdEV of 150 nm is expected to appear 10^4 times less bright than a CTC of 15 µm. Under these crude assumptions, that corresponds to $2.5\times10^5/10^4$ = only 25 molecules. Even smaller EVs may not be labeled at all or too dim to detect, resulting again in an underestimation of the EV concentration.

1.4.3.2 Generic optical imaging of specifically captured tdEVs

A brighter signal can be achieved using lipophilic stains. Apolar fluorescent molecules like Nile Red or di-8-annepps can strongly bind to the aliphatic chains in the phospholipid membranes of EVs, yielding a stable embedding therein via exploitation of the hydrophobic effect (as illustrated in Figure 1.3).[108] Considering again a tdEV of 150 nm diameter composed of phospholipid molecules with a headgroup area of 45 $Å^2$, that corresponds to slightly more than 1.5×10^5 molecules. Even if only 1% of the membrane area would be occupied by fluorophores (assuming equal quantum yield of the fluorophores etc.) the resulting signal would be 60 times more intense than that of specifically stained EVs.

Staining using lipophilic dyes is not specific to any EV type; it is selective only to the dipole moment of the environment. In an immunologically perfectly enriched sample, generic labeling can still be useful to get an estimate of the concentration of (specifically) captured EVs. However, in practice, non-specifically adsorbed species including protein aggregates and lipoproteins may be stained, resulting in an overestimation of the background signal.

Conversely, it has been demonstrated that no dye stains all EVs in a sample.[108] Therefore there is always an underestimation of the total EV concentration in a sample. The combination of these two factors, *i.e.* overestimation of background and underestimation of sample signal, greatly complicates reliable quantification of tdEVs.

1.4.3.3 Multimodal analysis

These issues can be overcome by combining multiple techniques, whereby *e.g.* spectroscopic or fluorescence microscopy data are collected using high-resolution optical microscopy, and those same individual particles are measured with electron microscopy, scanning probe microscopy, or both, to make sure that also the smaller particles are detected.[109,110] The biological or chemical data obtained with the optical methods can confirm the origin of the largest EVs and give an indication of the purity of the sample. The morphological data from the other techniques may be used to define characteristics of particles of those species with more certainty. Chapters 3 and 4 describe the development of substrates that are compatible with optical, scanning probe, and electron microscopy techniques, and which feature micron-sized navigation markers to easily retrace individual particles on a relatively large surface area in the sample stages of the different instruments.

1.4.3.4 Electrical detection of specifically captured tdEVs

As mentioned before, detection of (td)EVs is also possible using a change in electrical signal. Phospholipid membranes are effective dielectric materials – as exemplified by the "gigaOhm seal" formed by intact membranes in patch clamp measurements.[111] If a volume of electrolyte is replaced by a non-conductive tdEV, the area of a nearby electrode that is accessible decreases. Assuming for simplicity that the distribution of ions throughout the electrolyte does not change, any direct current flowing through that electrode would decrease, linearly proportional to the decrease in area. On most electrodes this change is infinitesimal, but if the area of the electrode is reduced to approach that of the analyte particles, the effect becomes significant. This is (part of) the Coulter Counter principle, used in methods that are sometimes used as alternative to NTA as described in section 1.4.1.[112,113] This approach gives no biological information as EVs of all origins would appear roughly the same. Chapter 6 describes a platform using this basic principle in conjunction with antibody-antigen interactions to get data about the concentration of tdEVs specifically.

1.5 Lab-on-a-chip

By far, most analysis of EVs has been performed in biomedical labs, see Figure 1.2b. One could perhaps slightly oversimplify to conclude that in biomedical labs, most sample handling (including centrifugation) occurs in plastic tubes, and most analysis is done either with fluorescence microscopes or with molecular characterization like PCR. But using relatively new semiconductor fabrication methods, the isolation and detection of tdEVs can come together in integrated systems.[114–117]

The abundance of tdEVs (up to 10^5 tdEVs/ml blood) makes them uniquely well suited for analysis of small samples, *e.g.* a single drop of blood (∽100 µl, Fig. 1.4). This is convenient since the antibodies used for immunocapture, the basis for most of the work described in this thesis, are typically very expensive and should be used sparingly. Confining the sample handling to small volumes furthermore allows control over the flow and, importantly, allows to wash non-specifically adsorbed contaminants while retaining the analyte for further analysis.

Moreover, as mentioned earlier (and explained in following chapters), scaling down sensing elements to the nano- or microscale makes it possible to detect very small analytes accurately.

A system where sample purification is integrated with a section designed for the characterization or detection of the analyte, embedded in a microfluidic environment that facilitates sample handling, is often popularly called a "lab-on-a-chip".[115] This term efficiently illustrates the premise of the concept: much of the work that normally requires a variety of lab equipment can now be done inside of a single chip the size of a thumbnail. As will become apparent from this thesis, labs are still needed to make these chips and the work still needs to be done by someone at some point. But besides the technological and economic benefits of miniaturizing these systems, there is also a logistic benefit. If no more than a benchtop readout device and a handheld lab-on-a-chip are required for a "sample in, result out" analysis, then the system can be truly described as "point-of-care". This holds the promise to allow the system to be distributed to clinical specialists without requiring any other lab facilities.

1.6 This thesis

In this thesis, the development of platforms for tdEV research is described from two perspectives, both in line with the objectives of the overarching Cancer-ID program mentioned in Section 1.2.

- First, systems designed for the fundamental characterization of tdEVs and tdEV containing samples. Uniquely, these systems give certainty that the object under study is indeed a tdEV, allowing to make rigid statements about the characteristics of these particles. These platforms were designed to get a better fundamental understanding of EVs.
- Second, high-throughput sensors for enumeration of tdEVs. Using some of the information obtained by more detailed studies in the earlier platforms, these lab-on-a-chip systems in principle only determine the concentration of tdEVs. These systems were designed with the application of point-of-care diagnosis in mind.

Chapter 2 gives an overview of the results obtained in the encompassing Cancer-ID program, presenting more detailed alternatives for studying EVs like flow cytometry, transmission electron microscopy and Raman spectroscopy. It also presents some alternative approaches to lab-on-a-chip devices for enumerating tdEVs from other projects within the Cancer ID program.

Chapter 3 further introduces the concept of multi-modal analysis and describes the development of stainless steel substrates, their functionalization for the specific capture of tdEVs and the integration of navigation markers using microfluidic polymer injection. Raman spectroscopy, scanning electron microscopy and atomic force microscopy (AFM) were combined to characterize individual tdEVs.

Chapter 4 describes a more advanced multi-modal analysis platform, using a transparent substrate and micromachined navigation markers, whereby fluorescence microscopy, Raman spectroscopy and AFM were used to identify tdEVs spiked in plasma samples.

Chapter 5 illustrates an application of multi-modal analysis techniques. Using a combination of various methods, it is proven that organosilicon compounds

coordinate with cell membranes and lipid assemblies in general. This has consequences for sample preparation techniques and data interpretation.

Chapter 6 describes the development of a lab-on-a-chip sensor for the specific and highly sensitive bulk quantification of tdEVs in cell culture media using a detection scheme with multiple amplification steps and multiple recognition steps.

Chapter 7 presents the holy grail: a lab-on-a-chip sensor for the specific detection of single EVs and virions directly from patient samples.

Finally, **chapter 8** presents a brief summary and a general discussion of the obtained results, together with a concise perspective on potential future developments.

1.7 References

(1) CBS. *Deaths; Underlying Cause of Death (Shortlist), Sex, Age*; 2018.

(2) Dillekås, H.; Rogers, M. S.; Straume, O. Are 90% of Deaths from Cancer Caused by Metastases? *Cancer Med.* **2019**, *8* (12), 5574–5576. https://doi.org/10.1002/cam4.2474.

(3) Brugger, W.; Bross, K. J.; Glatt, M.; Weber, F.; Mertelsmann, R.; Kanz, L. Mobilization of Tumor Cells and Hematopoietic Progenitor Cells into Peripheral Blood of Patients with Solid Tumors. *Blood* **1994**, *83* (3), 636–640.

(4) Braun, S.; Pantel, K.; Müller, P.; Janni, W.; Hepp, F.; Kentenich, C. R. M.; Gastroph, S.; Wischnik, A.; Dimpfl, T.; Kindermann, G.; et al. Cytokeratin-Positive Cells in the Bone Marrow and Survival of Patients with Stage I, II, or III Breast Cancer. *N. Engl. J. Med.* **2000**, *342* (8), 525–533. https://doi.org/10.1056/NEJM200002243420801.

(5) Racila, E.; Euhus, D.; Weiss, a J.; Rao, C.; McConnell, J.; Terstappen, L. W.; Uhr, J. W. Detection and Characterization of Carcinoma Cells in the Blood. *Proc. Natl. Acad. Sci. U. S. A.* **1998**, *95* (April), 4589–4594. https://doi.org/10.1073/pnas.95.8.4589.

(6) Cristofanilli, M.; Budd, G. T.; Ellis, M. J.; Stopeck, A.; Matera, J.; Miller, M. C.; Reuben, J. M.; Doyle, G. V; Allard, W. J.; Terstappen, L. W. M. M.; et al. Circulating Tumor Cells, Disease Progression, and Survival in Metastatic Breast Cancer. *N. Engl. J. Med.* **2004**, *351* (8), 781–791. https://doi.org/10.1056/NEJMoa040766.

(7) Cohen, S. J.; Punt, C. J. A.; Iannotti, N.; Saidman, B. H.; Sabbath, K. D.; Gabrail, N. Y.; Picus, J.; Morse, M.; Mitchell, E.; Miller, M. C.; et al. Relationship of Circulating Tumor Cells to Tumor Response, Progression-Free Survival, and Overall Survival in Patients with Metastatic Colorectal Cancer. *J. Clin. Oncol.* **2008**, *26* (19), 3213–3221. https://doi.org/10.1200/JCO.2007.15.8923.

(8) Allard, W. J.; Matera, J.; Miller, M. C.; Repollet, M.; Connelly, M. C.; Rao, C.; Tibbe, A. G. J.; Uhr, J. W.; Terstappen, L. W. M. M. Tumor Cells Circulate in the Peripheral Blood of All Major Carcinomas but Not in Healthy Subjects or Patients with Nonmalignant Diseases. *Clin. Cancer Res.* **2004**, *10* (20), 6897–6904. https://doi.org/10.1158/1078-0432.CCR-04-0378.

(9) Cristofanilli, M.; Hayes, D. F.; Budd, G. T.; Ellis, M. J.; Stopeck, A.; Reuben, J. M.; Doyle, G. V; Matera, J.; Allard, W. J.; Miller, M. C.; et al. Circulating Tumor Cells: A Novel Prognostic Factor for Newly Diagnosed Metastatic Breast Cancer. *J. Clin. Oncol.* **2005**, *23* (7), 1420–1430. https://doi.org/10.1200/JCO.2005.08.140.

(10) De Bono, J. S.; Scher, H. I.; Montgomery, R. B.; Parker, C.; Miller, M. C.; Tissing, H.; Doyle, G. V.; Terstappen, L. W. W. M.; Pienta, K. J.; Raghavan, D. Circulating Tumor Cells Predict Survival Benefit from Treatment in Metastatic Castration-Resistant Prostate Cancer. *Clin. Cancer Res.* **2008**, *14* (19), 6302–6309.

https://doi.org/10.1158/1078-0432.CCR-08-0872.

(11) Hamdeni, T.; Fnaiech, F.; Gasmi, S.; Ginoux, J.-M.; Naeck, R.; Bouchouicha, M.; Ben Khedher Zidi, A.; Tshibasu, F. Overview and Definitions on Lung Cancer Diagnosis. In *Middle East Conference on Biomedical Engineering, MECBME*; 2018; Vol. 2018-March, pp 165–170. https://doi.org/10.1109/MECBME.2018.8402427.

(12) Ligthart, S. T.; Coumans, F. A. W.; Bidard, F. C.; Simkens, L. H. J.; Punt, C. J. A.; de Groot, M. R.; Attard, G.; de Bono, J. S.; Pierga, J. Y.; Terstappen, L. W. M. M. Circulating Tumor Cells Count and Morphological Features in Breast, Colorectal and Prostate Cancer. *PLoS One* **2013**, *8* (6). https://doi.org/10.1371/journal.pone.0067148.

(13) Nanou, A.; Coumans, F. A. W.; van Dalum, G.; Zeune, L. L.; Dolling, D.; Onstenk, W.; Crespo, M.; Fontes, M. S.; Rescigno, P.; Fowler, G.; et al. Circulating Tumor Cells, Tumor-Derived Extracellular Vesicles and Plasma Cytokeratins in Castration-Resistant Prostate Cancer Patients. *Oncotarget* **2018**, *9* (27), 19283–19293. https://doi.org/10.18632/oncotarget.25019.

(14) Nowak, A. K. CT, RECIST, and Malignant Pleural Mesothelioma. *Lung Cancer* **2005**, *49* (SUPPL. 1), S37–S40. https://doi.org/10.1016/j.lungcan.2005.03.030.

(15) Rastogi, A.; Baheti, A. D.; Patra, A.; Tirumani, S. H. Tumor Response Criteria in Oncoimaging: RECIST Criteria and beyond—Part 1. *J. Gastrointest. Abdom. Radiol.* **2019**, *02* (02), 098–106. https://doi.org/10.1055/s-0039-1692021.

(16) Weiss, J.; Notohamiprodjo, M.; Bedke, J.; Nikolaou, K.; Kaufmann, S. Imaging Response Assessment of Immunotherapy in Patients with Renal Cell and Urothelial Carcinoma. *Curr. Opin. Urol.* **2018**, *28* (1), 35–41. https://doi.org/10.1097/MOU.0000000000000463.

(17) Sheth, P. J.; del Moral, S.; Wilky, B. A.; Trent, J. C.; Cohen, J.; Rosenberg, A. E.; Temple, H. T.; Subhawong, T. K. Desmoid Fibromatosis: MRI Features of Response to Systemic Therapy. *Skeletal Radiol.* **2016**, *45* (10), 1365–1373. https://doi.org/10.1007/s00256-016-2439-y.

(18) Coumans, F. A. W.; Ligthart, S. T.; Uhr, J. W.; Terstappen, L. W. M. M. Challenges in the Enumeration and Phenotyping of CTC. *Clin. Cancer Res.* **2012**, *18* (20), 5711–5718. https://doi.org/10.1158/1078-0432.CCR-12-1585.

(19) Tibbe, A. G. J.; Miller, M. C.; Terstappen, L. W. M. M. Statistical Considerations for Enumeration of Circulating Tumor Cells. *Cytom. Part A* **2007**, *71* (3), 154–162. https://doi.org/10.1002/cyto.a.20369.

(20) Garber, K. Trial Results Boost Circulating Tumor Cell Field. *Journal of the National Cancer Institute*. Oxford University Press July 21, 2004, pp 1055–1057. https://doi.org/10.1093/jnci/96.14.1055.

(21) Kagan, M.; Trainer, M.; Bendele, T.; Rao, C.; Horton, A.; Tibbe, A.; Greve, J.;

Terstappen, L. W. M. M. CellTracks Cell Analysis System for Rare Cell Detection. *Proc. SPIE - Int. Soc. Opt. Eng.* **2002**, *4625*, 20–28. https://doi.org/10.1117/12.469792.

(22) Tibbe, A. G. J.; De Grooth, B. G.; Greve, J.; Liberti, P. A.; Dolan, G. J.; Terstappen, L. W. M. M. Optical Tracking and Detection of Immunomagnetically Selected and Aligned Cells. *Nat. Biotechnol.* **1999**, *17* (12), 1210–1213. https://doi.org/10.1038/70761.

(23) Wit, S. de; Dalum, G. van; Lenferink, A. T. M.; Tibbe, A. G. J.; Hiltermann, T. J. N.; Groen, H. J. M.; van Rijn, C. J. M.; Terstappen, L. W. M. M. The Detection of EpCAM+ and EpCAM– Circulating Tumor Cells. *Sci. Rep.* **2015**, *5* (1), 12270. https://doi.org/10.1038/srep12270.

(24) Nanou, A.; Miller, M. C.; Zeune, L. L.; de Wit, S.; Punt, C. J. A.; Groen, H. J. M.; Hayes, D. F.; de Bono, J. S.; Terstappen, L. W. M. M. Tumour-Derived Extracellular Vesicles in Blood of Metastatic Cancer Patients Associate with Overall Survival. *Br. J. Cancer* **2020**. https://doi.org/10.1038/s41416-019-0726-9.

(25) Denzer, K.; Kleijmeer, M. J.; Heijnen, H. F.; Stoorvogel, W.; Geuze, H. J.; Advani, R. J.; Yang, B.; Prekeris, R.; Lee, K. C.; Klumperman, J.; et al. Exosome: From Internal Vesicle of the Multivesicular Body to Intercellular Signaling Device. *J. Cell Sci.* **2000**, *113 Pt 19* (19), 3365–3374. https://doi.org/10.1083/jcb.146.4.765.

(26) Simons, M.; Raposo, G. Exosomes - Vesicular Carriers for Intercellular Communication. *Current Opinion in Cell Biology*. August 2009, pp 575–581. https://doi.org/10.1016/j.ceb.2009.03.007.

(27) Segura, E.; Nicco, C.; Lombard, B.; Veron, P.; Raposo, G.; Batteux, F.; Amigorena, S.; Thery, C. ICAM-1 on Exosomes from Mature Dendritic Cells Is Critical for Efficient Naive T Cell Priming. *Blood* **2005**, *106* (1), 216–223. https://doi.org/10.1182/blood-2005-01-0220.Supported.

(28) Yáñez-Mó, M.; Siljander, P. R. M.; Andreu, Z.; Zavec, A. B.; Borràs, F. E.; Buzas, E. I.; Buzas, K.; Casal, E.; Cappello, F.; Carvalho, J.; et al. Biological Properties of Extracellular Vesicles and Their Physiological Functions. *J. Extracell. Vesicles* **2015**, *4* (2015), 1–60. https://doi.org/10.3402/jev.v4.27066.

(29) Trajkovic, K.; Hsu, C.; Chiantia, S.; Rajendran, L.; Wenzel, D.; Wieland, F.; Schwille, P.; Brügger, B.; Simons, M. Ceramide Triggers Budding of Exosome Vesicles into Multivesicular Endosomes. *Science (80-.).* **2008**, *319* (5867), 1244–1247. https://doi.org/10.1126/science.1153124.

(30) Wolf, P. The Nature and Significance of Platelet Products in Human Plasma. *Br. J. Haematol.* **1967**, *13* (3), 269–288. https://doi.org/10.1111/j.1365-2141.1967.tb08741.x.

(31) Shah, M. D.; Bergeron, A. L.; Dong, J. F.; López, J. A. Flow Cytometric Measurement of Microparticles: Pitfalls and Protocol Modifications. *Platelets* **2008**, *19* (5), 365–

372. https://doi.org/10.1080/09537100802054107.

(32) Arraud, N.; Gounou, C.; Turpin, D.; Brisson, A. R. Fluorescence Triggering: A General Strategy for Enumerating and Phenotyping Extracellular Vesicles by Flow Cytometry. *Cytom. Part A* **2016**, *89* (2), 184–195. https://doi.org/10.1002/cyto.a.22669.

(33) Johnsen, K. B.; Gudbergsson, J. M.; Andresen, T. L.; Simonsen, J. B. What Is the Blood Concentration of Extracellular Vesicles? Implications for the Use of Extracellular Vesicles as Blood-Borne Biomarkers of Cancer. *Biochimica et Biophysica Acta - Reviews on Cancer*. Elsevier B.V. January 1, 2019, pp 109–116. https://doi.org/10.1016/j.bbcan.2018.11.006.

(34) Raposo, G.; Stoorvogel, W. Extracellular Vesicles: Exosomes, Microvesicles, and Friends. *J. Cell Biol.* **2013**, *200* (4), 373–383. https://doi.org/10.1083/jcb.201211138.

(35) Colombo, M.; Raposo, G.; Théry, C. Biogenesis, Secretion, and Intercellular Interactions of Exosomes and Other Extracellular Vesicles. *Annu. Rev. Cell Dev. Biol.* **2014**, *30* (1), 255–289. https://doi.org/10.1146/annurev-cellbio-101512-122326.

(36) Mathivanan, S.; Ji, H.; Simpson, R. J. Exosomes: Extracellular Organelles Important in Intercellular Communication. *J. Proteomics* **2010**, *73* (10), 1907–1920. https://doi.org/10.1016/J.JPROT.2010.06.006.

(37) van der Pol, E.; Böing, A. N.; Gool, E. L.; Nieuwland, R. Recent Developments in the Nomenclature, Presence, Isolation, Detection and Clinical Impact of Extracellular Vesicles. *J. Thromb. Haemost.* **2016**, *14* (1), 48–56. https://doi.org/10.1111/jth.13190.

(38) Witwer, K. W.; Théry, C. Extracellular Vesicles or Exosomes? On Primacy, Precision, and Popularity Influencing a Choice of Nomenclature. *Journal of Extracellular Vesicles*. Taylor and Francis Ltd. December 1, 2019. https://doi.org/10.1080/20013078.2019.1648167.

(39) Théry, C.; Witwer, K. W.; Aikawa, E.; Alcaraz, M. J.; Anderson, J. D.; Andriantsitohaina, R.; Antoniou, A.; Arab, T.; Archer, F.; Atkin-Smith, G. K.; et al. Minimal Information for Studies of Extracellular Vesicles 2018 (MISEV2018): A Position Statement of the International Society for Extracellular Vesicles and Update of the MISEV2014 Guidelines. *J. Extracell. Vesicles* **2018**, *7* (1), 1535750. https://doi.org/10.1080/20013078.2018.1535750.

(40) Kalluri, R.; LeBleu, V. S. The Biology, Function, and Biomedical Applications of Exosomes. *Science (80-.).* **2020**, *367* (6478). https://doi.org/10.1126/science.aau6977.

(41) Dignat-George, F.; Boulanger, C. M. The Many Faces of Endothelial Microparticles. *Arterioscler. Thromb. Vasc. Biol.* **2011**, *31* (1), 27–33. https://doi.org/10.1161/ATVBAHA.110.218123.

(42) Xu, R.; Rai, A.; Chen, M.; Suwakulsiri, W.; Greening, D. W.; Simpson, R. J. Extracellular Vesicles in Cancer — Implications for Future Improvements in Cancer Care. *Nat. Rev. Clin. Oncol.* **2018**, *15* (10), 617–638. https://doi.org/10.1038/s41571-018-0036-9.

(43) El Andaloussi, S.; Mäger, I.; Breakefield, X. O.; Wood, M. J. A. Extracellular Vesicles: Biology and Emerging Therapeutic Opportunities. *Nature Reviews Drug Discovery*. May 2013, pp 347–357. https://doi.org/10.1038/nrd3978.

(44) György, B.; Szabó, T. G.; Pásztói, M.; Pál, Z.; Misják, P.; Aradi, B.; László, V.; Pállinger, É.; Pap, E.; Kittel, Á.; et al. Membrane Vesicles, Current State-of-the-Art: Emerging Role of Extracellular Vesicles. *Cellular and Molecular Life Sciences*. August 2011, pp 2667–2688. https://doi.org/10.1007/s00018-011-0689-3.

(45) Alix-Panabières, C.; Schwarzenbach, H.; Pantel, K. Circulating Tumor Cells and Circulating Tumor DNA. *Annu. Rev. Med.* **2012**, *63* (1), 199–215. https://doi.org/10.1146/annurev-med-062310-094219.

(46) Terstappen, L. W. M. M.; Rao, C.; Gross, S.; Kotelnikov, V.; Racilla, E.; Uhr, J.; Weiss, A. Flowcytometry - Principles and Feasibility in Transfusion Medicine. Enumeration of Epithelial Derived Tumor Cells in Peripheral Blood. *Vox Sang.* **1998**, *74* (SUPPL. 2), 269–274.

(47) Coumans, F.; Dalum, G. Van; Terstappen, L. W. M. M. CTC Technologies and Tools. *Cytom. Part A* **2018**, No. 93A, 1197–1201. https://doi.org/10.1002/cyto.a.23684.

(48) Beekman, P.; Enciso-Martinez, A.; Rho, H. S.; Pujari, S. P.; Lenferink, A. T. M.; Zuilhof, H.; Terstappen, L. W. M. M.; Otto, C.; Le Gac, S. Immuno-Capture of Extracellular Vesicles on Stainless Steel Substrates for Individual Multimodal Characterization Using AFM, SEM and Raman Spectroscopy. *Lab Chip* **2019**. https://doi.org/10.1039/C9LC00081J.

(49) Tibbe, A. G. J.; Miller, M. C.; Terstappen, L. W. M. M. Statistical Considerations for Enumeration of Circulating Tumor Cells. *Cytom. Part A* **2007**, *71A* (3), 154–162. https://doi.org/10.1002/cyto.a.20369.

(50) Arraud, N.; Linares, R.; Tan, S.; Gounou, C.; Pasquet, J.-M.; Mornet, S.; Brisson, A. R. Extracellular Vesicles from Blood Plasma: Determination of Their Morphology, Size, Phenotype and Concentration. *J. Thromb. Haemost.* **2014**, *12* (5), 614–627. https://doi.org/10.1111/jth.12554.

(51) Rikkert, L. G.; Nieuwland, R.; Terstappen, L. W. M. M.; Coumans, F. A. W. Quality of Extracellular Vesicle Images by Transmission Electron Microscopy Is Operator and Protocol Dependent. *J. Extracell. Vesicles* **2019**, *8* (1). https://doi.org/10.1080/20013078.2018.1555419.

(52) van der Pol, E.; de Rond, L.; Coumans, F. A. W.; Gool, E. L.; Böing, A. N.; Sturk, A.; Nieuwland, R.; van Leeuwen, T. G. Absolute Sizing and Label-Free Identification of Extracellular Vesicles by Flow Cytometry. *Nanomedicine Nanotechnology, Biol.*

Med. **2018**, *14* (3), 801–810. https://doi.org/10.1016/j.nano.2017.12.012.

(53) Gasecka, A.; Böing, A. N.; Filipiak, K. J.; Nieuwland, R. Platelet Extracellular Vesicles as Biomarkers for Arterial Thrombosis. *Platelets*. Taylor and Francis Ltd April 3, 2017, pp 228–234. https://doi.org/10.1080/09537104.2016.1254174.

(54) Sódar, B. W.; Kittel, Á.; Pálóczi, K.; Vukman, K. V.; Osteikoetxea, X.; Szabó-Taylor, K.; Németh, A.; Sperlágh, B.; Baranyai, T.; Giricz, Z.; et al. Low-Density Lipoprotein Mimics Blood Plasma-Derived Exosomes and Microvesicles during Isolation and Detection. *Sci. Rep.* **2016**, *6* (January), 1–12. https://doi.org/10.1038/srep24316.

(55) Yuana, Y.; Levels, J.; Grootemaat, A.; Sturk, A.; Nieuwland, R. Co-Isolation of Extracellular Vesicles and High-Density Lipoproteins Using Density Gradient Ultracentrifugation. *J. Extracell. Vesicles* **2014**, *3* (1), 23262. https://doi.org/10.3402/jev.v3.23262.

(56) Tauro, B. J.; Greening, D. W.; Mathias, R. A.; Ji, H.; Mathivanan, S.; Scott, A. M.; Simpson, R. J. Comparison of Ultracentrifugation, Density Gradient Separation, and Immunoaffinity Capture Methods for Isolating Human Colon Cancer Cell Line LIM1863-Derived Exosomes. *Methods* **2012**, *56* (2), 293–304. https://doi.org/10.1016/j.ymeth.2012.01.002.

(57) Coumans, F. A. W.; Brisson, A. R.; Buzas, E. I.; Dignat-George, F.; Drees, E. E. E.; El-Andaloussi, S.; Emanueli, C.; Gasecka, A.; Hendrix, A.; Hill, A. F.; et al. Methodological Guidelines to Study Extracellular Vesicles. *Circ. Res.* **2017**, *120* (10), 1632–1648. https://doi.org/10.1161/CIRCRESAHA.117.309417.

(58) Enciso-Martinez, A.; van der Pol, E.; Lenferink, A. T. M.; Terstappen, L. W. M. M.; van Leeuwen, T. G.; Otto, C. Synchronized Rayleigh and Raman Scattering for the Characterization of Single Optically Trapped Extracellular Vesicles. *Nanomedicine Nanotechnology, Biol. Med.* **2020**, *24*. https://doi.org/10.1016/j.nano.2019.102109.

(59) Enciso-Martinez, A.; Van Der Pol, E.; Hau, C. M.; Nieuwland, R.; Van Leeuwen, T. G.; Terstappen, L. W. M. M.; Otto, C. Label-Free Identification and Chemical Characterisation of Single Extracellular Vesicles and Lipoproteins by Synchronous Rayleigh and Raman Scattering. *J. Extracell. Vesicles* **2020**, *9* (1). https://doi.org/10.1080/20013078.2020.1730134.

(60) Böing, A. N.; Pol, E. Van Der; Grootemaat, A. E.; Coumans, F. a.; Sturk, A.; Nieuwland, R. Single-Step Isolation of Extracellular Vesicles from Plasma by Size-Exclusion Chromatography. *Int. Meet. ISEV Rotterdam* **2014**, *3*, 118. https://doi.org/10.3402/jev.v3.23430.

(61) Lobb, R. J.; Becker, M.; Wen, S. W.; Wong, C. S. F.; Wiegmans, A. P.; Leimgruber, A.; Möller, A. Optimized Exosome Isolation Protocol for Cell Culture Supernatant and Human Plasma. *J. Extracell. Vesicles* **2015**, *4* (1), 1–11. https://doi.org/10.3402/jev.v4.27031.

(62) Nordin, J. Z.; Lee, Y.; Vader, P.; Mäger, I.; Johansson, H. J.; Heusermann, W.; Wiklander, O. P. B.; Hällbrink, M.; Seow, Y.; Bultema, J. J.; et al. Ultrafiltration with Size-Exclusion Liquid Chromatography for High Yield Isolation of Extracellular Vesicles Preserving Intact Biophysical and Functional Properties. *Nanomedicine Nanotechnology, Biol. Med.* **2015**, *11* (4), 879–883. https://doi.org/10.1016/j.nano.2015.01.003.

(63) Baggerman, J.; Smulders, M. M. J.; Zuilhof, H. Romantic Surfaces: A Systematic Overview of Stable, Biospecific, and Antifouling Zwitterionic Surfaces. *Langmuir* **2019**, *35* (5), 1072–1084. https://doi.org/10.1021/acs.langmuir.8b03360.

(64) Van Andel, E.; Lange, S. C.; Pujari, S. P.; Tijhaar, E. J.; Smulders, M. M. J.; Savelkoul, H. F. J.; Zuilhof, H. Systematic Comparison of Zwitterionic and Non-Zwitterionic Antifouling Polymer Brushes on a Bead-Based Platform. *Langmuir* **2019**, *35* (5), 1181–1191. https://doi.org/10.1021/acs.langmuir.8b01832.

(65) Roeven, E.; Scheres, L.; Smulders, M. M. J.; Zuilhof, H. Design, Synthesis, and Characterization of Fully Zwitterionic, Functionalized Dendrimers. *ACS Omega* **2019**, *4* (2), 3000–3011. https://doi.org/10.1021/acsomega.8b03521.

(66) Mendes, R. K.; Carvalhal, R. F.; Kubota, L. T. Effects of Different Self-Assembled Monolayers on Enzyme Immobilization Procedures in Peroxidase-Based Biosensor Development. *J. Electroanal. Chem.* **2008**, *612* (2), 164–172. https://doi.org/10.1016/j.jelechem.2007.09.033.

(67) Damos, F. S.; Luz, R. C. S.; Kubota, L. T. Determination of Thickness, Dielectric Constant of Thiol Films, and Kinetics of Adsorption Using Surface Plasmon Resonance. *Langmuir* **2005**, *21* (2), 602–609. https://doi.org/10.1021/la0487038.

(68) Pujari, S. P.; Scheres, L.; Marcelis, A. T. M.; Zuilhof, H. Covalent Surface Modification of Oxide Surfaces. *Angew. Chemie - Int. Ed.* **2014**, *53* (25), 6322–6356. https://doi.org/10.1002/anie.201306709.

(69) Love, J. C.; Estroff, L. A.; Kriebel, J. K.; Nuzzo, R. G.; Whitesides, G. M. *Self-Assembled Monolayers of Thiolates on Metals as a Form of Nanotechnology*; 2005; Vol. 105. https://doi.org/10.1021/cr0300789.

(70) Pujari, S. P.; Scheres, L.; Marcelis, A. T. M.; Zuilhof, H. Covalent Surface Modification of Oxide Surfaces. *Angew. Chemie - Int. Ed.* **2014**, *53* (25), 6322–6356. https://doi.org/10.1002/anie.201306709.

(71) Kosian, M.; Smulders, M. M. J.; Zuilhof, H. Structure and Long-Term Stability of Alkylphosphonic Acid Monolayers on SS316L Stainless Steel. *Langmuir* **2016**, *32* (4), 1047–1057. https://doi.org/10.1021/acs.langmuir.5b04217.

(72) Maoz, R.; Sagiv, J. On the Formation and Structure of Self-Assembling Monolayers. I. A Comparative Atr-Wettability Study of Langmuir-Blodgett and Adsorbed Films on Flat Substrates and Glass Microbeads. *J. Colloid Interface Sci.* **1984**, *100* (2), 465–496. https://doi.org/10.1016/0021-9797(84)90452-1.

(73) Sagiv, J. Organized Monolayers by Adsorption. 1. Formation and Structure of Oleophobic Mixed Monolayers on Solid Surfaces. *J. Am. Chem. Soc.* **1980**, *102* (1), 92–98. https://doi.org/10.1021/ja00521a016.

(74) Sui, G.; Wang, J.; Lee, C. C.; Lu, W.; Lee, S. P.; Leyton, J. V.; Wu, A. M.; Tseng, H. R. Solution-Phase Surface Modification in Intact Poly(Dimethylsiloxane) Microfluidic Channels. *Anal. Chem.* **2006**, *78* (15), 5543–5551. https://doi.org/10.1021/ac060605z.

(75) Sia, S. K.; Whitesides, G. M. Microfluidic Devices Fabricated in Poly(Dimethylsiloxane) for Biological Studies. *Electrophoresis* **2003**, *24* (21), 3563–3576. https://doi.org/10.1002/elps.200305584.

(76) Rosso, M.; Nguyen, A. T.; De Jong, E.; Baggerman, J.; Paulusse, J. M. J.; Giesbers, M.; Fokkink, R. G.; Norde, W.; Schroën, K.; Van Rijn, C. J. M.; et al. Protein-Repellent Silicon Nitride Surfaces: UV-Induced Formation of Oligoethylene Oxide Monolayers. *ACS Appl. Mater. Interfaces* **2011**, *3* (3), 697–704. https://doi.org/10.1021/am100985c.

(77) Amiji, M.; Park, K. Prevention of Protein Adsorption and Platelet Adhesion on Surfaces by PEO/PPO/PEO Triblock Copolymers. *Biomaterials* **1992**, *13* (10), 682–692. https://doi.org/10.1016/0142-9612(92)90128-B.

(78) Holmlin, R. E.; Chen, X.; Chapman, R. G.; Takayama, S.; Whitesides, G. M. Zwitterionic SAMs That Resist Nonspecific Adsorption of Protein from Aqueous Buffer. *Langmuir* **2001**, *17* (9), 2841–2850. https://doi.org/10.1021/la0015258.

(79) Gerlach, J. Q.; Krüger, A.; Gallogly, S.; Hanley, S. A.; Hogan, M. C.; Ward, C. J.; Joshi, L.; Griffin, M. D. Surface Glycosylation Profiles of Urine Extracellular Vesicles. *PLoS One* **2013**, *8* (9). https://doi.org/10.1371/journal.pone.0074801.

(80) Gerlach, J. Q.; Griffin, M. D. Getting to Know the Extracellular Vesicle Glycome. *Mol. Biosyst.* **2016**, *12* (4), 1071–1081. https://doi.org/10.1039/c5mb00835b.

(81) Ghosh, A.; Davey, M.; Chute, I. C.; Griffiths, S. G.; Lewis, S.; Chacko, S.; Barnett, D.; Crapoulet, N.; Fournier, S.; Joy, A.; et al. Rapid Isolation of Extracellular Vesicles from Cell Culture and Biological Fluids Using a Synthetic Peptide with Specific Affinity for Heat Shock Proteins. *PLoS One* **2014**, *9* (10). https://doi.org/10.1371/journal.pone.0110443.

(82) Knol, J. C.; de Reus, I.; Schelfhorst, T.; Beekhof, R.; de Wit, M.; Piersma, S. R.; Pham, T. V.; Smit, E. F.; Verheul, H. M. W.; Jiménez, C. R. Peptide-Mediated "miniprep" Isolation of Extracellular Vesicles Is Suitable for High-Throughput Proteomics. *EuPA Open Proteomics* **2016**, *11*, 11–15. https://doi.org/10.1016/j.euprot.2016.02.001.

(83) Gaillard, M.; Thuaire, A.; Nonglaton, G.; Agache, V.; Roupioz, Y.; Raillon, C. Biosensing Extracellular Vesicles: Contribution of Biomolecules in Affinity-Based Methods for Detection and Isolation. *Analyst*. Royal Society of Chemistry March 21,

2020, pp 1997–2013. https://doi.org/10.1039/c9an01949a.

(84) Liu, C.; Zhao, J.; Tian, F.; Chang, J.; Zhang, W.; Sun, J. λ - DNA- and Aptamer-Mediated Sorting and Analysis of Extracellular Vesicles. **2019**. https://doi.org/10.1021/jacs.9b00007.

(85) Gool, E. L.; Stojanovic, I.; Schasfoort, R. B. M.; Sturk, A.; van Leeuwen, T. G.; Nieuwland, R.; Terstappen, L. W. M. M.; Coumans, F. A. W. Surface Plasmon Resonance Is an Analytically Sensitive Method for Antigen Profiling of Extracellular Vesicles. *Clin. Chem.* **2017**, *63* (10), 1633–1641. https://doi.org/10.1373/clinchem.2016.271049.

(86) Shao, H.; Im, H.; Castro, C. M.; Breakefield, X.; Weissleder, R.; Lee, H. New Technologies for Analysis of Extracellular Vesicles. *Chem. Rev.* **2018**, *118* (4), 1917–1950. https://doi.org/10.1021/acs.chemrev.7b00534.

(87) Hermanson, G. T. *Bioconjugate Techniques*, 2nd ed.; Academic Press, 2013. https://doi.org/10.1016/B978-0-12-382239-0.00004-2.

(88) Williams, A.; T. Ibrahim, I. Carbodiimide Chemistry: Recent Advances. *Chem. Rev.* **2002**, *81* (6), 589–636. https://doi.org/10.1021/cr00046a004.

(89) Avrameas, S.; Ternynck, T. Peroxidase Labelled Antibody and Fab Conjugates with Enhanced Intracellular Penetration. *Immunochemistry* **1971**, *8* (12), 1175–1179. https://doi.org/10.1016/0019-2791(71)90395-8.

(90) Yakovleva, J.; Davidsson, R.; Lobanova, A.; Bengtsson, M.; Eremin, S.; Laurell, T.; Emnéus, J. Microfluidic Enzyme Immunoassay Using Silicon Microchip with Immobilized Antibodies and Chemiluminescence Detection. *Anal. Chem.* **2002**, *74* (13), 2994–3004. https://doi.org/10.1021/ac015645b.

(91) Yang, L.; Li, Y. AFM and Impedance Spectroscopy Characterization of the Immobilization of Antibodies on Indium-Tin Oxide Electrode through Self-Assembled Monolayer of Epoxysilane and Their Capture of Escherichia Coli O157:H7. *Biosens. Bioelectron.* **2005**, *20* (7), 1407–1416. https://doi.org/10.1016/j.bios.2004.06.024.

(92) Ruan, C.; Yang, L.; Li, Y. Immunobiosensor Chips for Detection of Escherichia Coli O157:H7 Using Electrochemical Impedance Spectroscopy. *Anal. Chem.* **2002**, *74* (18), 4814–4820. https://doi.org/10.1021/ac025647b.

(93) Van Andel, E.; De Bus, I.; Tijhaar, E. J.; Smulders, M. M. J.; Savelkoul, H. F. J.; Zuilhof, H. Highly Specific Binding on Antifouling Zwitterionic Polymer-Coated Microbeads as Measured by Flow Cytometry. *ACS Appl. Mater. Interfaces* **2017**, *9* (44), 38211–38221. https://doi.org/10.1021/acsami.7b09725.

(94) Van Der Pol, E.; Hoekstra, A. G.; Sturk, A.; Otto, C.; Van Leeuwen, T. G.; Nieuwland, R. Optical and Non-Optical Methods for Detection and Characterization of Microparticles and Exosomes. *J. Thromb. Haemost.* **2010**, *8* (12), 2596–2607. https://doi.org/10.1111/j.1538-7836.2010.04074.x.

(95) de Rond, L.; van der Pol, E.; Hau, C. M.; Varga, Z.; Sturk, A.; van Leeuwen, T. G.; Nieuwland, R.; Coumans, F. A. W. Comparison of Generic Fluorescent Markers for Detection of Extracellular Vesicles by Flow Cytometry. *Clin. Chem.* **2018**, *64* (4), 680–689. https://doi.org/10.1373/clinchem.2017.278978.

(96) Piontek, M. C.; Lira, R. B.; Roos, W. H. Active Probing of the Mechanical Properties of Biological and Synthetic Vesicles. *Biochim. Biophys. Acta - Gen. Subj.* **2019**. https://doi.org/10.1016/j.bbagen.2019.129486.

(97) Vorselen, D.; van Dommelen, S. M.; Sorkin, R.; Piontek, M. C.; Schiller, J.; Döpp, S. T.; Kooijmans, S. A. A.; van Oirschot, B. A.; Versluijs, B. A.; Bierings, M. B.; et al. The Fluid Membrane Determines Mechanics of Erythrocyte Extracellular Vesicles and Is Softened in Hereditary Spherocytosis. *Nat. Commun.* **2018**, *9* (1). https://doi.org/10.1038/s41467-018-07445-x.

(98) van der Pol, E.; Coumans, F. A. W.; Grootemaat, A. E.; Gardiner, C.; Sargent, I. L.; Harrison, P.; Sturk, A.; van Leeuwen, T. G.; Nieuwland, R. Particle Size Distribution of Exosomes and Microvesicles Determined by Transmission Electron Microscopy, Flow Cytometry, Nanoparticle Tracking Analysis, and Resistive Pulse Sensing. *J. Thromb. Haemost.* **2014**, *12* (7), 1182–1192. https://doi.org/10.1111/jth.12602.

(99) Abali, F.; Broekmaat, J.; Tibbe, A.; Schasfoort, R. B. M.; Zeune, L.; Terstappen, L. W. M. M. A Microwell Array Platform to Print and Measure Biomolecules Produced by Single Cells. *Lab Chip* **2019**, *19* (10), 1850–1859. https://doi.org/10.1039/c9lc00100j.

(100) Ong, P. Y.; Ohtake, T.; Brandt, C.; Strickland, I.; Boguniewicz, M.; Ganz, T.; Gallo, R. L.; Leung, D. Y. M. Endogenous Antimicrobial Peptides and Skin Infections in Atopic Dermatitis. *N. Engl. J. Med.* **2002**, *347* (15), 1151–1160. https://doi.org/10.1056/NEJMoa021481.

(101) Logozzi, M.; De Milito, A.; Lugini, L.; Borghi, M.; Calabrò, L.; Spada, M.; Perdicchio, M.; Marino, M. L.; Federici, C.; Iessi, E.; et al. High Levels of Exosomes Expressing CD63 and Caveolin-1 in Plasma of Melanoma Patients. *PLoS One* **2009**, *4* (4), e5219. https://doi.org/10.1371/journal.pone.0005219.

(102) Sahl, S. J.; Hell, S. W.; Jakobs, S. Fluorescence Nanoscopy in Cell Biology. *Nature Reviews Molecular Cell Biology*. Nature Publishing Group September 6, 2017, pp 685–701. https://doi.org/10.1038/nrm.2017.71.

(103) Cox, G.; Sheppard, C. J. R. Practical Limits of Resolution in Confocal and Non-Linear Microscopy. *Microsc. Res. Tech.* **2004**, *63* (1), 18–22. https://doi.org/10.1002/jemt.10423.

(104) Hansen, H. P.; Engels, H.-M.; Dams, M.; Paes Leme, A. F.; Pauletti, B. A.; Simhadri, V. L.; Dürkop, H.; Reiners, K. S.; Barnert, S.; Engert, A.; et al. Protrusion-Guided Extracellular Vesicles Mediate CD30 Trans-Signalling in the Microenvironment of Hodgkin's Lymphoma. *J. Pathol.* **2014**, *232* (4), 405–414.

https://doi.org/10.1002/path.4306.

(105) Sauer, M.; Heilemann, M. Single-Molecule Localization Microscopy in Eukaryotes. *Chemical Reviews*. American Chemical Society June 14, 2017, pp 7478–7509. https://doi.org/10.1021/acs.chemrev.6b00667.

(106) Vicidomini, G.; Bianchini, P.; Diaspro, A. STED Super-Resolved Microscopy. *Nature Methods*. Nature Publishing Group March 1, 2018, pp 173–182. https://doi.org/10.1038/nmeth.4593.

(107) Rao, C. G.; Chianese, D.; Doyle, G. V; Miller, M. C.; Russell, T.; Sanders Jr., R. A.; Terstappen, L. W. M. M. Expression of Epithelial Cell Adhesion Molecule in Carcinoma Cells Present in Blood and Primary and Metastatic Tumors. *Int. J. Oncol.* **2005**, *27* (1), 49–57.

(108) De Rond, L.; Van Der Pol, E.; Hau, C. M.; Varga, Z.; Sturk, A.; Van Leeuwen, T. G.; Nieuwland, R.; Coumans, F. A. W. Comparison of Generic Fluorescent Markers for Detection of Extracellular Vesicles by Flow Cytometry. *Clin. Chem.* **2018**, *64* (4), 680–689. https://doi.org/10.1373/clinchem.2017.278978.

(109) Cascione, M.; de Matteis, V.; Rinaldi, R.; Leporatti, S. Atomic Force Microscopy Combined with Optical Microscopy for Cells Investigation. *Microsc. Res. Tech.* **2017**, *80* (1), 109–123. https://doi.org/10.1002/jemt.22696.

(110) Sharma, S.; LeClaire, M.; Gimzewski, J. K. Ascent of Atomic Force Microscopy as a Nanoanalytical Tool for Exosomes and Other Extracellular Vesicles. *Nanotechnology* **2018**, *29* (13), 132001. https://doi.org/10.1088/1361-6528/AAAB06.

(111) Reccius, C. H.; Fromherz, P. Giant Lipid Vesicles Impaled with Glass Microelectrodes: GigaOhm Seal by Membrane Spreading. *Langmuir* **2004**, *20* (25), 11175–11182. https://doi.org/10.1021/la048233h.

(112) Coumans, F. A. W.; van der Pol, E.; Böing, A. N.; Hajji, N.; Sturk, G.; van Leeuwen, T. G.; Nieuwland, R. Reproducible Extracellular Vesicle Size and Concentration Determination with Tunable Resistive Pulse Sensing. *J. Extracell. Vesicles* **2014**, *3* (1). https://doi.org/10.3402/jev.v3.25922.

(113) Vogel, R.; Coumans, F. A. W.; Maltesen, R. G.; Böing, A. N.; Bonnington, K. E.; Broekman, M. L.; Broom, M. F.; Buzás, E. I.; Christiansen, G.; Hajji, N.; et al. A Standardized Method to Determine the Concentration of Extracellular Vesicles Using Tunable Resistive Pulse Sensing. *J. Extracell. Vesicles* **2016**, *5* (1). https://doi.org/10.3402/jev.v5.31242.

(114) Im, H.; Shao, H.; Park, Y. Il; Peterson, V. M.; Castro, C. M.; Weissleder, R.; Lee, H. Label-Free Detection and Molecular Profiling of Exosomes with a Nano-Plasmonic Sensor. *Nat. Biotechnol.* **2014**, *32* (5), 490–495. https://doi.org/10.1038/nbt.2886.

(115) Whitesides, G. The Lab Finally Comes to the Chip! *Lab on a Chip*. Royal Society of Chemistry September 7, 2014, pp 3125–3126. https://doi.org/10.1039/c4lc90072c.

(116) Joung, H. A.; Ballard, Z. S.; Wu, J.; Tseng, D. K.; Teshome, H.; Zhang, L.; Horn, E. J.; Arnaboldi, P. M.; Dattwyler, R. J.; Garner, O. B.; et al. Point-of-Care Serodiagnostic Test for Early-Stage Lyme Disease Using a Multiplexed Paper-Based Immunoassay and Machine Learning. *ACS Nano* **2020**, *14* (1), 229–240. https://doi.org/10.1021/acsnano.9b08151.

(117) Schulze Greiving, V. C.; de Boer, H. L.; Bomer, J. G.; van den Berg, A.; Le Gac, S. Integrated Microfluidic Biosensing Platform for Simultaneous Confocal Microscopy and Electrophysiological Measurements on Bilayer Lipid Membranes and Ion Channels. *Electrophoresis* **2018**, *39* (3), 496–503. https://doi.org/10.1002/elps.201700346.

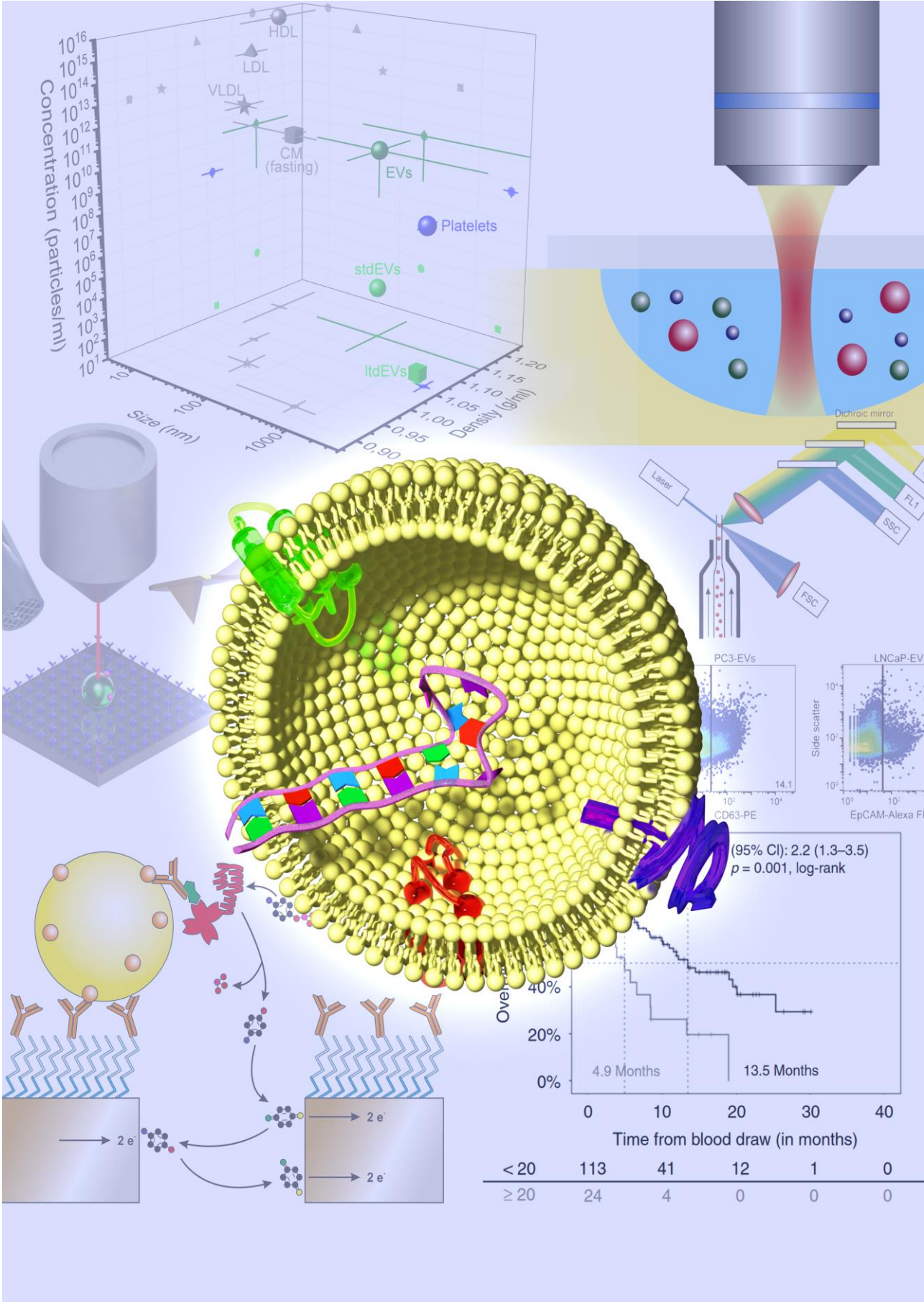

< 20	113	41	12	1	0
≥ 20	24	4	0	0	0

2

The Cancer ID Project

This chapter was originally published as:

L.G. Rikkert, P. Beekman, J. Caro, F.A.W. Coumans, A. Enciso Martinez, G. Jenster, S. Le Gac, W. Lee, T. G. van Leeuwen, G. B. Loozen, A. Nanou, R. Nieuwland, H. L. Offerhaus, C. Otto, D. M. Pegtel, M. C. Piontek, E. van der Pol, L. de Rond, W. H. Roos, R. B. M. Schasfoort, M. H. M. Wauben, H. Zuilhof, L.W.M.M. Terstappen, *Cancer-ID: towards identification of cancer by tumor-derived extracellular vesicles in blood,* Frontiers in Oncology, June 2020.

2.1 Abstract

Extracellular Vesicles (EVs) have great potential as biomarkers since their composition and concentration in biofluids are disease state-dependent and their cargo can contain disease related information. Large tumor-derived EVs (tdEVs, > 1 μm) in blood from cancer patients are associated with poor outcome and changes in their number can be used to monitor therapy effectiveness. Whereas small tumor-derived EVs (<1 μm) are likely to outnumber their larger counterparts, thereby offering better statistical significance, identification and quantification of small tdEVs is more challenging. In the blood of cancer patients, a subpopulation of EVs originate from tumor cells, but these EVs are outnumbered by non-EV particles and EVs from other origin. In the Dutch NWO Perspectief Cancer-ID program, we developed and evaluated detection and characterization techniques to distinguish EVs from non-EV particles and other EVs. Despite low signal amplitudes, we identified characteristics of these small tdEVs that may enable the enumeration of small tdEVs and extract relevant information. The insights obtained from Cancer-ID can help to explore the full potential of tdEVs in the clinic.

2.2 Introduction

Extracellular Vesicles (EVs) are cell-derived particles with a phospholipid membrane. Because the membrane composition and content of EVs reflect the origin and state of the parental cells, EVs have become promising disease biomarkers.[1-4] Participants from eight universities and 21 companies, who collaborate in the Dutch NWO Perspectief program Cancer-ID, aim to develop and evaluate technology to detect tumor-derived EVs (tdEVs) in blood as biomarker for cancer. Throughout the project, two main challenges involved in the detection of EVs in blood became apparent. First, EV detection is hampered because EVs are outnumbered by the presence of non-EV particles in blood, like soluble proteins and lipoprotein particles at the low end of the EV size and

density range, and platelets at the high end of the EV size and density range. [5-7] Moreover, the concentration of larger lipoproteins, such as chylomicrons, depends on food intake, thereby emphasizing the need to discriminate EVs from other such particles. To illustrate this challenge, we determined that 1 mL of human blood of metastatic castration resistant prostate cancer patients contains about 10 large (> 1 µm) tdEVs[8, 9] and we extrapolated this to encompass the small tdEVs to arrive at an estimated 10^4 tdEVs per 1 ml. Furthermore, the blood contains up to 10^{16} lipoproteins, up to 10^9 platelets, and up to 10^{11} other EVs,[5, 6, 10-12] see Figure 2.1. The second challenge is the heterogeneity of EVs in many aspects, including morphology,[13] size,[13-15] membrane composition,[9, 15-19] and refractive index,[20, 21] which complicates EV isolation, detection, and enumeration. In sum, utilization of tdEVs as cancer biomarker requires (i) the discrimination of EVs from non-EV particles, (ii) identification of their cellular origin, and/or (iii) analysis of the EV molecular content. The insight that an EV-based cancer biomarker requires the ability to detect, identify and enumerate tdEVs amongst other particles plasma is an essential Cancer-ID outcome, because it defines the state-of-the-art. Therefore, we will use this definition to evaluate the ten techniques that were developed or improved throughout the project. The project includes techniques that (i) detect single particles attached to a surface, such as atomic force microscopy (AFM), electrochemical (EC) detection, scanning electron microscopy (SEM), and transmission electron microscopy (TEM), (ii) detect an ensemble of EVs attached to a surface, such as surface plasmon resonance imaging (SPRi), (iii) detect single EVs in suspension, such as flow cytometry (FCM), or (iv) can measure either single or multiple EVs attached to a substrate or in a suspension, such as Raman microspectroscopy. The other evaluated technologies are integrated photonics lab-on-chip devices for Raman Spectroscopy, hybrid AFM-SEM-Raman, and immunomagnetic EpCAM (epithelial cell adhesion molecule) enrichment followed by fluorescence microscopic (FM) detection. The evaluated techniques including key characteristics are listed in Table 2.1. This Table also gives an impression of the clinical utility of each technique by giving an estimate of the throughput in terms of tdEVs that can be processed in a given amount of time considering the vast majority of non-tdEV particles in plasma that may or may not contribute to the

signal. To compare all techniques, EVs derived from prostate cancer cell lines and EVs derived from platelet and red blood cell concentrates were distributed among the participants and measured. Based on the aforementioned requirements, we aimed to qualify the ability of a technique to (i) detect or image EVs, (ii) identify tdEVs, which involves differentiation of tdEVs from EVs and non-EV particles, and (iii) relate the measured signal or count to the concentration of tdEVs in plasma.

2.3 Preparation of EV samples

Two prostate cancer cell lines (PC3 and LNCaP) purchased from the American Type Culture Collection (ATCC, Manassas, VA) were used to obtain prostate cancer-derived EVs. The cell lines were cultured at 37 °C and 5% CO_2 in RPMI-1640 with L-glutamine (Lonza, Basel, Switzerland) supplemented with 10% v/v fetal bovine serum (FBS), and 1% v/v penicillin and streptomycin (Lonza). Medium was refreshed every second day. The initial cell density was 10,000 cells/cm^2 as recommended by the ATCC. The cells were washed three times with phosphate buffered saline (PBS; Sigma, Saint Louis, MO) when they reached 80–90% confluence. Next, FBS-free RPMI medium supplemented with 0.1% v/v penicillin and streptomycin was added to the cells. After 48 h of cell culture, the cell supernatant was collected and centrifuged for 30 minutes at 1,000 g. The supernatant was collected and aliquots were snap-frozen in liquid nitrogen and stored at –80 °C.

Red blood cell concentrate (150 mL) obtained from Sanquin (Amsterdam, The Netherlands) was diluted in a 1:1 ratio with filtered PBS (154 mM NaCl, 1.24 mM $Na_2HPO_4{\cdot}2H_2O$, 0.2 mM $NaH_2PO_4{\cdot}2H_2O$, pH 7.4; 0.22 µm filter (Merck Chemicals BV, Darmstadt, Germany)) and centrifuged three times for 20 minutes at 1,560 g. Platelet concentrate (100 mL) obtained from Sanquin was diluted in a 1:1 ratio with filtered PBS. Next, 40 mL acid of citrate dextrose (ACD; 0.85 M trisodiumcitrate, 0.11 M D-glucose, and 0.071 M citric acid) was added and the suspension was centrifuged for 20 minutes at 800 g. Thereafter, the supernatant

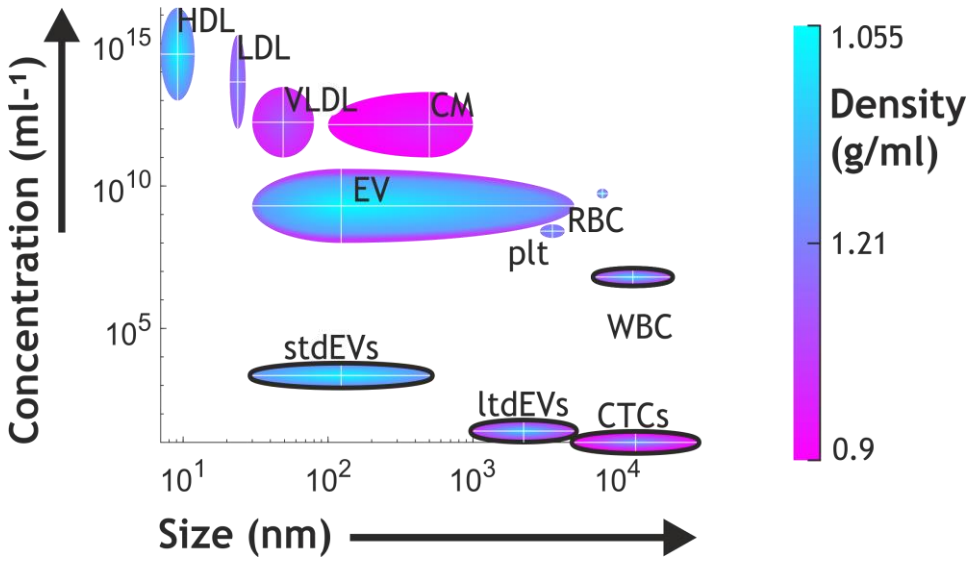

Figure 2.1: *Distributions of size, concentration and density of typical blood components before (A) and after isolation by EpCAM-based immunomagnetic isolation (B), size exclusion chromatography (C) and centrifugation (D). The axes of the spots (white lines) indicate the mode of these distributions. The vertices of the spots indicate the upper and lower limit of the ranges. The size distribution of the particles is given along the horizontal dimension. The vertical dimension illustrates the range of concentrations detected across patient populations (disregarding the size-dependence of concentrations). The range of the density is given by color gradients. Abbreviations: HDL = high density lipoprotein, LDL = low density lipoprotein, VLDL = very low-density lipoprotein, CM = chylomicrons, EV = (all) extracellular vesicles, RBC = red blood cells, plt = platelets, WBC = white blood cells, stdEVs = small tumor-derived extracellular vesicles, ltdEVs = large tumor-derived extracellular vesicles, CTCs = circulating tumor cells. Distributions of density are assumed to be normal, distributions of size in a typical sample and concentration over patient populations are assumed log-normal, except for EVs (extended to include ltdEVs) and CM (non-parametric).* [8, 9, 11]

Table 2.1. Overview of the techniques used in Cancer-ID.

	Method	Ref.	§	Information obtained	DL* (nm)	Thr* (prt/hr)	T* (hr)[a]
Surface							
Single	TEM	[13]	II.1	Morphology, Size	30	9×10^{3}	2×10^{7}
	SEM	[15]	II.2	Topography, Size	50	50	4×10^{2}
	AFM	[15]	II.3	Morphology, Bending modulus	30	3×10^{3}	50
	Raman	[15]	II.5	Chemical composition	80	100	2×10^{3}
	Electro chemistry	[17]	II.6	Concentration, Antigen expression	-	2×10^{7}	0.5
Bulk	SPRi	[22]	II.7	Antigen expression	-	30×10^{7}	3×10^{-2} [b]
Suspension							
Single	NTA	[23]	I	Particle size distribution	30	400	9×10^{8}
	Raman	[16]	II.4	Chemical composition	80	9×10^{4}	6×10^{7}
	FCM	[20]	II.8	Antigen expression, Refractive index	200	6×10^{6}	4×10^{6}
	FM	[9]	II.9	Antigen expression	1000	4×10^{6}	2×10^{11}

DL=Detection limit; Thr= Throughput in total number of (generic) particles per hour; T=Expected time needed to find 1 tdEV (specifically) in a typical plasma sample.

[a] *This column clarifies the need for in-situ enrichment and sensitive detection for diagnostic applications. Non-enriched techniques are expected to process a third of all particles in 1 µl individually or spread out over a flat surface before encountering 1 tdEV. Considering that the total area of all particles (lipoproteins and EVs, see Figure 2.1) distributed over a densely packed monolayer is ~36 cm², the following assumptions were made:*

TEM: 2.2×2.2µm² imaging area, imaged in 1 min, with a capturing efficiency of 21%. SEM: 25 µl sample, 50µm × 7mm capturing area, 10% capturing efficiency, 10% detected fraction (due to sensitivity limitations), 5 min per 10×10µm² image. AFM: 25 µl sample, 50µm × 7mm capturing area, 10% capturing efficiency, 45 min per 25×25µm² image. Raman on surface: 25 µl sample, 50µm × 7mm capturing area, 10% capturing efficiency, 1% detected fraction (due to sensitivity limitations), 17 min per 30×30µm² image. Electrochemistry: Processing any sample takes ~30 minutes regardless of the number of tdEVs. SPRi: Processing time is 2 minutes.[b] *NTA: This technique can process 100 particles in 15 minutes, i.e. 10^{10} measurements have to be performed to find all tdEVs in 1 µl of plasma. Raman in suspension: ~10^{12} measurements of 38 ms; 50% of particles fall below the detection limit. Flow cytometry: The sample must be diluted 10^9 times to ensure 1 detection event corresponds to 1 particle; 3 µl can be processed in 1 minute; 50% of particles fall below the detection limit. Fluorescence microscopy: An area of 100×100 µm² can be imaged in 0.2s with an automated stage; 99% of particles fall below the detection limit.*

[b] *Please note that 200 µl of sample is needed before the 10^4 EVs/µl limit of detection is reached.*

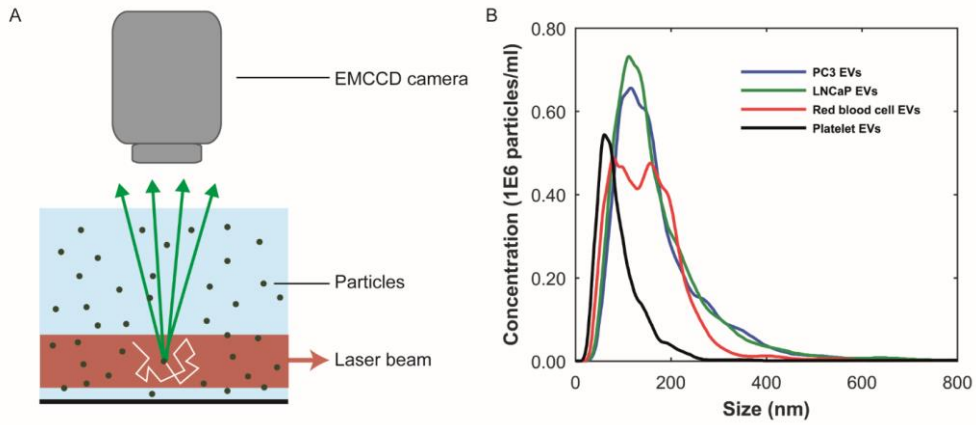

Figure 2.2. Particle size distributions of extracellular vesicle (EV) samples measured using nanoparticle tracking analysis (NTA). *A) Schematic representation of the NTA setup. A laser beam illuminates the particles in suspension. The light scattered by particles undergoing random motion (white arrow) is collected by a microscope objective and detected by an EMCCD camera. The random motion of the particles under Brownian motion can be related to their size. B) NTA analysis results of the PC3 EV (blue), LNCaP EV (green), red blood cell EV (red), and the platelet (black) EV samples, respectively. The bin width is 10 nm. The mean particle size and concentration in the PC3 EV sample are 172 ± 4 nm and 1E8 particles/mL, respectively. The mean particle size and concentration in the LnCaP EV sample are 167 ± 4 nm and 1E8 particles/mL, respectively. The mean particle size and concentration in the red blood cell EV sample are 148 ± 4 nm, and the concentration is 1E8 particles/mL, respectively. The mean particle size and concentration in the platelet EV sample are 89 ± 5 nm and 4E7 particles/mL, respectively. Because the uncertainty in the determined concentration with NTA is unknown, the determined concentration should be interpreted as an order of magnitude estimate 24. Images adapted from 25, 26.*

was centrifuged three times (20 minutes at 1,560 g) to ensure removal of platelets. The supernatant was collected and aliquots of 50 µL were snap-frozen in liquid nitrogen and stored at −80 °C.

The particle size distributions of the EV samples were obtained using nanoparticle tracking analysis (NTA NS500; Nanosight, Amesbury, UK), equipped with an electron multiplying charge-coupled device (EMCCD) camera and a 405 nm diode laser (Figure 2.2A). Silica beads (105 nm; Microspheres-Nanospheres, Cold Spring, NY) were used to focus the microscope objective. Samples were diluted 10 to 2,000 times in filtered PBS to ensure the number of particles in the field of view was below 200 per image. Of each sample, 10 videos of 30 s were captured with the camera shutter set at 33.31 ms and the camera gain set at 400. All samples were analyzed with the instrument software (NTA 2.3.0.15) using a threshold of 10, which was based on the exponential decay constant of the summed intensity histogram of all frames in each movie (MATLAB, v.7.9.0.529; Mathworks, Natrick, MA).

Figure 2.2B shows the measured particle size distributions of the EV samples. We estimate the smallest detectable EV for NTA to be 70-90 nm. [24]

2.4 Analysis of extracellular vesicles

2.4.1 Transmission Electron microscopy

2.4.1.1 Cancer-ID specific method and operating principle

TEM is widely available, it has become the standard technique to confirm the presence of EVs in samples [27]. TEM transmits electrons through sufficiently thin (<100-200 nm for biological materials) samples to make images with possibly sub-nm resolution [28]. Particles from the sample are adhered to a carbon coated formvar grid. Because EVs compete with other negatively charged particles for space on the grid, removal of soluble proteins and/or salts, for example by size exclusion chromatography (SEC)[29] and/or concentration, is required prior to incubation with EV samples. In addition, because TEM is performed in vacuum,

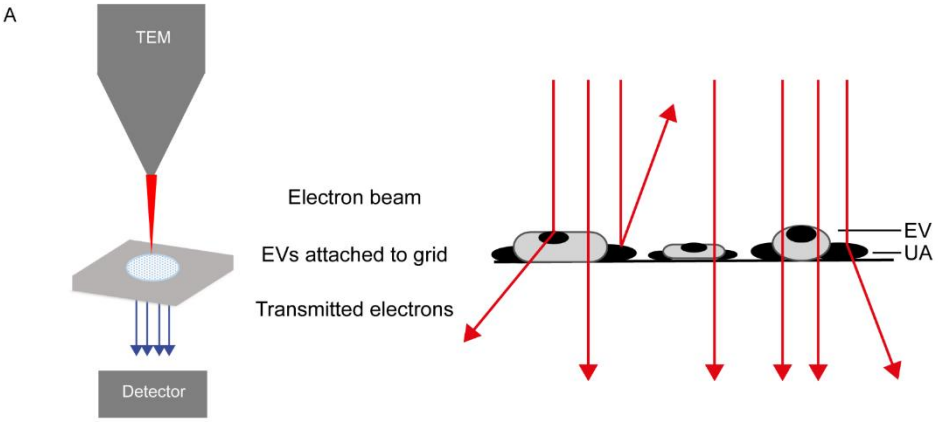
A
TEM
Detector
Electron beam
EVs attached to grid
Transmitted electrons
EV
UA

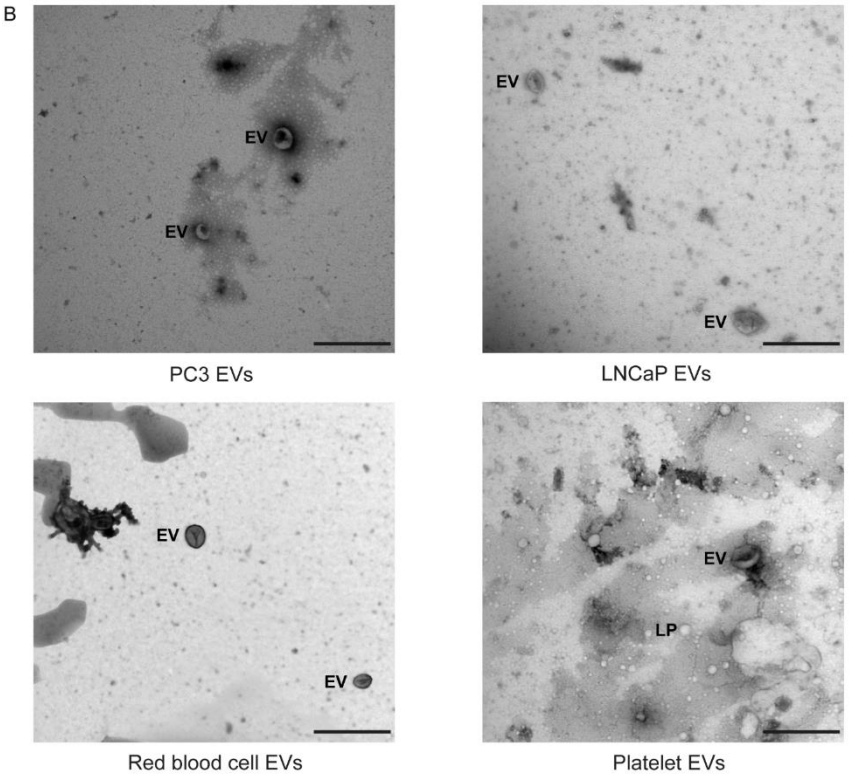
B
EV
EV
PC3 EVs
EV
EV
LNCaP EVs
EV
EV
Red blood cell EVs
EV
LP
Platelet EVs

Figure 2.3. Transmission electron microscopy (TEM) of extracellular vesicle (EV) samples. *A) Schematic representation of TEM imaging for EV samples. The sample on a grid is exposed to an electron beam and images are constructed based on the detected transmitted electrons. The uranyl acetate (UA), scatters electrons efficiently, which results in negative contrast. EVs and lipoproteins (LP) have a low electron density and are seen as bright particles in a dark background [13]. B) TEM images of the EV samples from PC3 and LNCaP, and of red blood cells and platelets after size exclusion chromatography. The scale bar corresponds to 500 nm [25].*

EV samples are fixed with paraformaldehyde. After fixation and adhesion, the grid is placed on a droplet of contrast agent (uranyl acetate). A filter paper is used to remove the excess of contrast agent and the grid is dried at room temperature. [30]

Next, the grid is exposed to an electron beam and images are constructed based on the detected transmitted electrons (Figure 2.3A). The contrast agent scatters electrons efficiently and stains the background more efficiently than the EVs. Consequently, EVs appear as bright particles on top of a dark background.

2.4.1.2 EV definition

Samples were analyzed on an FEI Tecnai 12 (FEI, Eindhoven, the Netherlands). Water, the main cargo of an EV, is evaporated upon TEM. Therefore, EVs often appear as 'cup-shaped'[31-33] or 'saucer/doughnut-shaped' particles[34-36] (Figures 2.3C-F). Because water is not the major component of other particles, other particles maintain their original structure during TEM. For example, lipoproteins appear spherical and protein aggregates have an irregular shape. Therefore, we define EVs as cup-shaped particles larger than 30 nm. [13]

2.4.1.3 Value added by Cancer-ID

We show that TEM images taken by operator selection, the current standard within the EV field, can be used to demonstrate the presence of EVs in a sample. However, the examination of the morphology of EVs by TEM shows an operator bias in their identification,[13] which may lead to "cherry picking" and emphasizes the importance of an automated and objective assessment of EV identification.

Two important steps to improve the comparability and reproducibility of TEM for monitoring the quality of EV samples, are (1) to take images at predefined locations, and (2) provision of both close-up and wide-field images, as adopted by MISEV2018. [37]

2.4.1.4Relevance for cancer diagnostics

Although with appropriate sample preparation TEM can image EVs down to 30 nm, the contrast of TEM images is often insufficient to distinguish EVs from similar sized non-EV particles (Figures 2.3B). Moreover, to identify tdEVs, immuno-gold labeling is necessary. However, the main limitation of TEM for tdEV detection is the low throughput, see Table 1. Because of the low abundance of tdEV among other particles in plasma, many particles need to be analyzed individually before a single tdEV is encountered (see Table 1). Therefore, TEM is not a relevant technique for detection of tdEV in plasma samples.

2.4.2 Scanning Electron microscopy (SEM)

2.4.2.1 Cancer-ID specific method and operating principle

EV samples are fixed in paraformaldehyde, followed by gradual dehydration from 70% to 100% ethanol in water with a 10% concentration increment step every 5-10 minutes. Subsequently, chemical drying of the sample can be achieved using 1:1 hexamethyldisilazane (HMDS) in ethanol for 3-5 minutes, followed by 100% HMDS for 3-5 minutes more. EVs are dehydrated and dried to maintain their morphological and surface features with minimal deformation in the vacuum chamber of the SEM [38, 39]. EV samples are coated with gold to increase the image contrast and avoid surface charging. Furthermore, the sample must be placed on a conductive substrate during imaging. The entire procedure is conducted at room temperature. In SEM imaging, a focused beam of electrons scans the surface of a sample interacting with all atoms in the sample (Figures 2.4A and B). Detection of the secondary electrons, originating from the outer layers of the sample, enables to visualize the topography of a sample. The number of backscattered electrons, originating from the deeper layers of the sample, is associated with the atomic number of the atoms in the sample.

2.4.2.2 EV definition

Since the LNCaP EV sample is derived from cell culture, we don't expect particles like lipoproteins to be present in this sample. Figure 2.4B shows round particles (white arrows) in lower and higher magnification, which we define as EVs.

2.4.2.3 Value added by Cancer-ID

We show that cells and EVs captured on functionalized substrates and in solution can be imaged by SEM.

2.4.2.4 Relevance for cancer diagnostics

SEM can be used to visualize the topography of tdEVs, as small as 50 nm but is unable to discriminate EVs from non-EV particles with a similar morphology. In order to confirm the nature of the particles, immunogold labeling or correlative techniques are required such as AFM, Raman, or fluorescence imaging. Furthermore, similar to TEM, the main limitation of SEM is the low throughput. SEM is a faster technique than TEM, but still a large area needs to be processed before tdEV are encountered (see Table 1). Therefore, SEM is not a relevant technique for detection of tdEV in plasma samples.

2.4.3 Atomic force microscopy (AFM)

2.4.3.1 Cancer-ID specific method and operating principle

EVs are added onto a poly-L-lysine coated coverslip [40-43]. Next, well is filled with filtered PBS (0.2 µm filter; VWR International, Radnor, PA) and placed on the AFM. During AFM imaging, a cantilever with a nm-sized tip probes the sample surface (Figure 2.5A) [44]. Deflection of the cantilever is measured with a laser and photodiode. AFM images are acquired in PeakForce Tapping mode on a Bruker Bioscope catalyst setup using minimal imaging force providing information about the topography of the samples surface. Mechanical properties can be obtained by applying a defined force perpendicular to the surface (indentation), providing force-indentation curves, as presented in Figure 2.5B.

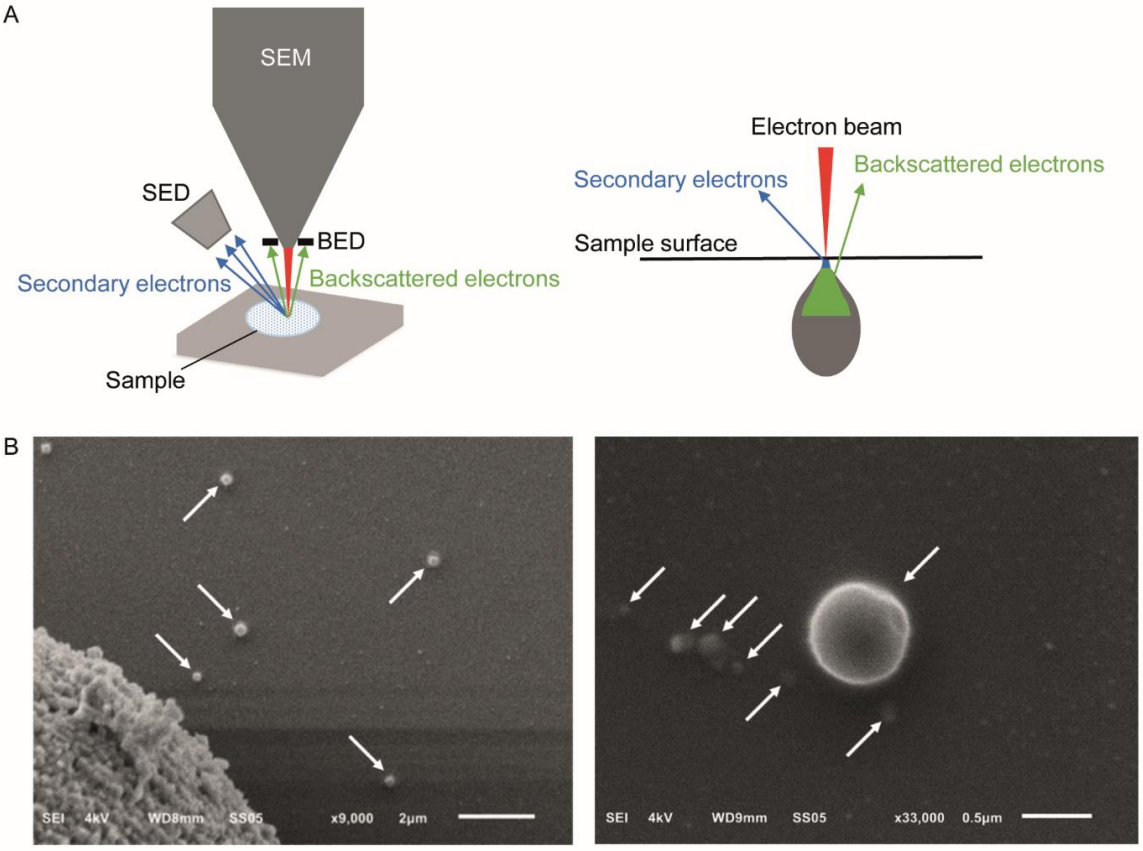

Figure 2.4. Scanning electron microscopy (SEM) of extracellular vesicle (EV) samples. *A) Schematic representation of a SEM setup. SED: secondary electron detector, BED: backscatter electron detector. B) The sample is illuminated by the electron beam. Electrons interact with the sample at different depths, resulting in emitted electrons from the surface (secondary electrons) and from deeper layers (backscattered electrons). C) SEM image of LNCaP EVs indicated by arrows. The large object in the left lower corner is part of a LNCaP cell floating in the cell supernatant and was imaged to show that the contrast of EVs is similar to cells. The scale bar represents 2 µm. D) Higher magnification allows imaging of smaller particles, possibly EVs, with lower contrast. The scale bar represents 500 nm.*

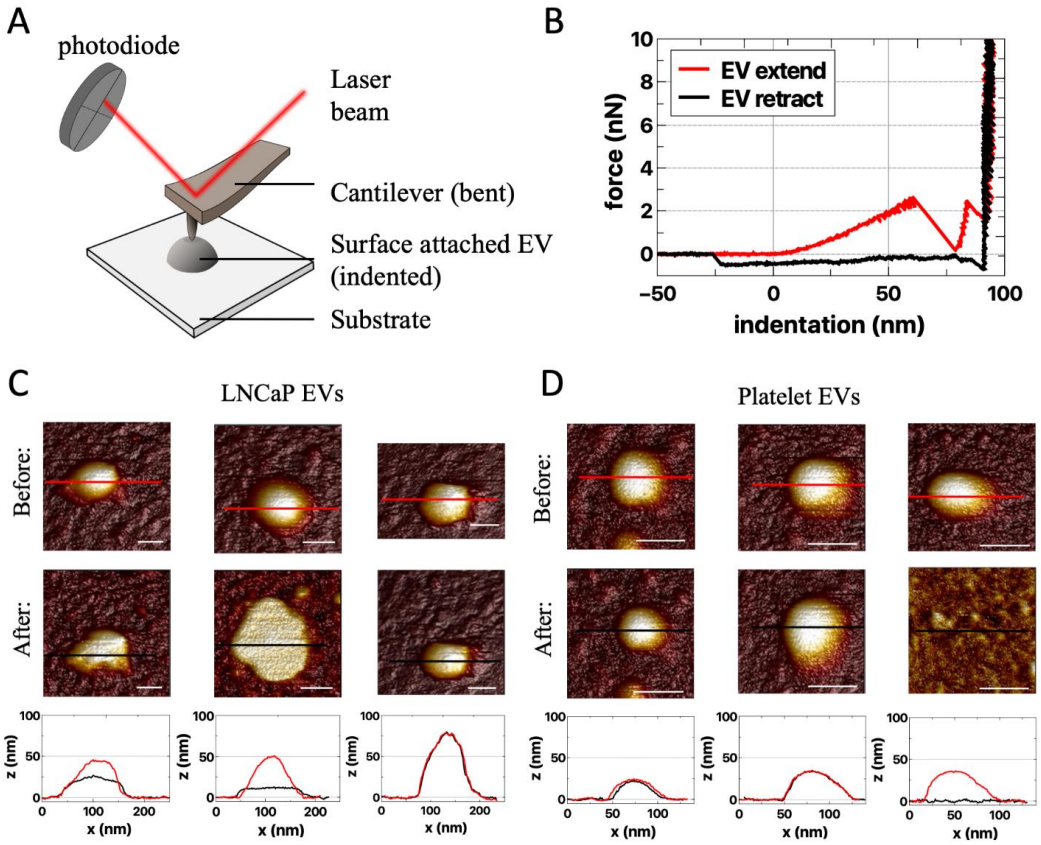

Figure 2.5. Atomic force microscopy (AFM) of extracellular vesicle (EV) samples. *A) Schematic representation of the AFM setup. In AFM, a cantilever interacts with the sample and the reflected laser beam is detected by a photodiode [44]. The experiments are performed in liquid (not depicted). B) Example of force-indentation curves (distance z) of the extend and retract response on an EV [44]. AFM images of responses of LNCaP EVs (C) and platelet EVs (D) to an applied force before (first row) and after indentation (second row). Both the LNCaP and the platelet EVs can change shape upon indentation. The different responses are illustrated by the cross sections (bottom row), taken at the indicated spots in the corresponding AFM images above (red: before indentation; black: after indentation). Scale bars represent 50 nm.*

2.4.3.2 EV definition

With AFM, we characterize an EV as a particle of at least 25 nm in height with a spherical shape. Aggregates typically have a non-spherical shape, and therefore can be excluded. The nanoindentation response is used to identify single EVs [41, 42]. A typical indentation curve is characterized by a (close-to) linear initial increase of force followed by a softening and finally bilayer pinching close to the substrate (Figure 2.5B, red curve).

2.4.3.3 Value added by Cancer-ID

Unique characteristics, like deformability, of tdEVs compared to EVs of other origin still need to be explored. Examples of AFM measurements of LNCaP EVs and platelet EVs are shown in Figure 2.5C and D. Importantly, it should be noted that AFM imaging per se is not distinguishing between EVs and lipoproteins. Therefore, a good purification protocol is necessary (combining gradient-based and size-based isolation methods) in order to assure only EVs are present.

2.4.3.4 Relevance for cancer diagnostics

Because of the nanometer position sensitivity and sub-piconewton force sensitivity, AFM can be used to determine the topography, morphology, and mechanical characteristics of single EVs, and differences between EVs of different origins can be investigated [41, 42]. Since with AFM only one particle can be observed at a time, AFM is not a suitable technique for tdEV identification and enumeration in plasma samples (see Table 1).

2.4.4 Raman microspectroscopy in suspension

2.4.4.1 Cancer-ID specific method and operating principle

EV samples are diluted in PBS to a concentration of approximately 10^9 particles/mL (as measured by NTA) and placed on a well glass slide, covered with a glass cover slip, and sealed with glue. Next, the glass slide is placed under the microscope objective (Figure 2.6A). A Raman optical tweezer (homebuilt system as decribed in Enciso-Martinez et al., 2019) is used to (i) trap single particles

diffusing near the high intensity part of the focus (Figure 2.6A), and (ii) detect both Rayleigh and Raman scattered photons synchronously. The trapping of a single particle is detected by Rayleigh scattering and the corresponding Raman spectrum discloses the chemical composition [16].

2.4.4.2 EV definition

The Raman spectra of sub-micrometer particles in biofluids have distinct spectral features depending on the nature of the particle or the source of EVs.

2.4.4.3 Value added by Cancer-ID

The procedure to trap, release and acquire sequentially the spectrum of single EVs in the focal volume is automated [16]. Furthermore, EVs can be distinguished from lipoproteins and EVs from different sources, like PC3 EVs, LNCaP EVs, and red blood cell EVs. EVs show distinctive peaks at 1004 cm^{-1} and 1607 cm^{-1} (phenylalanine) [25], and a larger protein contribution at 2811-3023 cm^{-1} than lipoproteins (Figures 2.6B and C). The Raman spectrum of red blood cell EVs is different from PC3 EVs and LNCaP EVs around 1200-1385 cm^{-1} and 1510-1631 cm^{-1}. Further classification of EVs and lipoproteins was achieved by multivariate analysis and convolutional neural networks analysis [25, 45].

2.4.4.4 Relevance for cancer diagnostics

Differences in chemical composition are shown between EVs and lipoproteins, and tdEVs compared to red blood cell EVs. However, a limitation of Raman is the throughput. As an example, a typical acquisition time per EV is 1 second [16]. It has become clear that enrichment of tdEVs is needed and a combination with another technique may be required to provide assurance that indeed tdEVs are being investigated. With the current detection principle, the thoughput of this technique is prohibitively low for clinical (non-enriched) samples (see Table 2.1). Nevertheless, spontaneous Raman spectroscopy provides information on the chemical composition of single or multiple EVs in solution or on a surface in a non-invasive and label-free manner [16, 25, 46-50].

2.4.5 Integrated photonics devices for Raman Spectroscopy

2.4.5.1 Cancer-ID specific method and operating principle

Two lab-on-chip devices were developed by Cancer-ID and fabricated in the cleanroom of MESA+ Institute of Technology. From a technological perspective, Cancer-ID exploits the possibility of lab-on-chip devices to localize light in ways that are impossible with traditional optics. For example, compared to optical trapping using a microscope objective (section II.4), we expect that combining

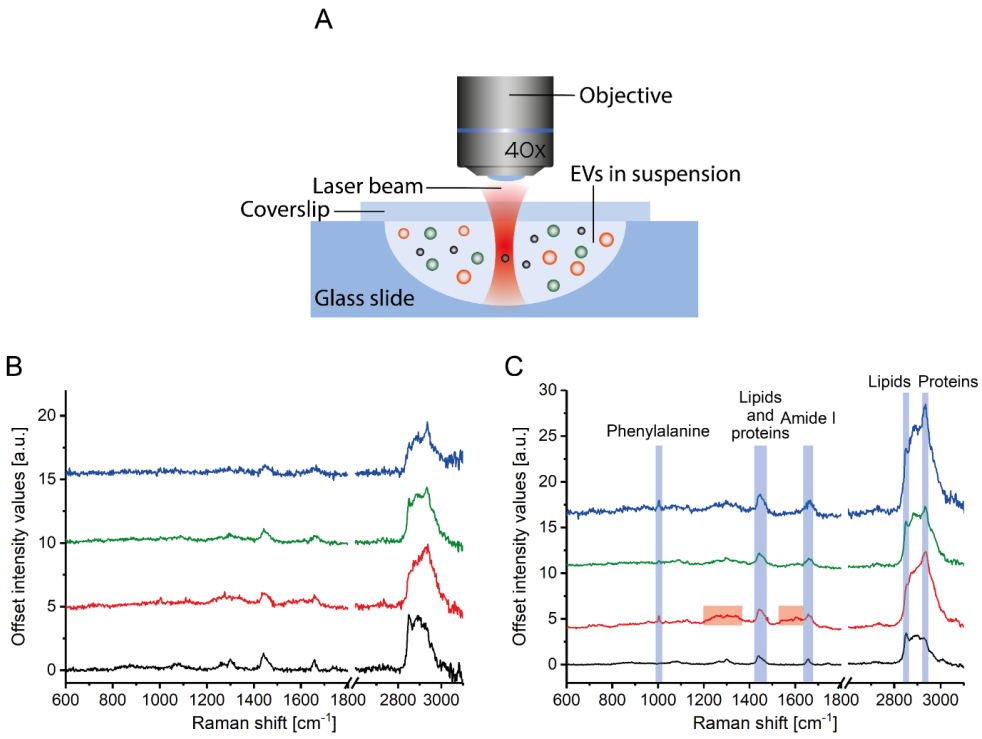

Figure 2.6. Raman spectroscopy of extracellular vesicle (EV) samples. *A) Particles in suspension are loaded in a well glass slide that is mounted under a microscope objective. Incident light illuminates the sample and both Raman and Rayleigh light is backscattered, collected by the lens, and detected by a spectrograph. Raman spectra corresponding to single (B) and multiple (C) PC3 EVs (blue), LNCaP EVs (green), red blood cell EVs (red), and lipoproteins in plasma (black). Figure A is adapted from* [16].

multiple beams will result in higher field gradients and therefore trapping of smaller single EVs. To proof the principle, device type 1 contains multiple waveguides which emit multiple beams of light towards the center of a well as shown in Figure 2.7A. The beams combine coherently to form multiple regions of high light intensity, each serving as an optical trap sufficiently strong to trap single submicrometer particles near the well center. The same concentrated light induces a Raman spectrum from the trapped particle for label-free identification. To increase the throughput, the well may be replaced by a flow cell in future versions.

To increase throughput compared to optical trapping using a microscope objective (section II.4), device type 2 combines an enrichment step with the simultaneous detection of Rayleigh and Raman scattered light from multiple EVs. EVs in suspension bind to antibodies at the surface of a spiral waveguide, which is placed at the bottom of a microfluidic channel as shown in Figure 2.7B [51]. A laser field propagates inside the waveguide and produces an evanescent field that probes the attached EVs simultaneously. The EVs will scatter some of this light with characteristic Raman shifts. A significant portion of this light re-enters the waveguide and can be collected from the entrance through the same objective that launched the excitation light.

2.4.5.2 EV definition

An EV is identified based on the acquired Raman spectrum of the trapped particle. The obtained spectra may be cross-referenced with EV spectra already acquired with standard spontaneous Raman tweezers (section II.4). Furthermore, using device type 2, EVs are bound to the surface of a spiral waveguide by a specific antibody.

2.4.5.3 Value added by Cancer-ID

Both devices are still under development, so the throughput and detection limit remain to be determined. In device type 1, integration of the light beam with a microfluidic channel opens new possibilities of controlled particle delivery to the trap and particle sorting with pressure driven flow which may allow the detection of smaller EVs. In device type 2 specific capture of tdEVs from plasma

is possible by the use of antibodies coated on the surface of a spiral waveguide using the chemistry used in II.6 & II.7.

2.4.5.4 Relevance for cancer diagnostics

Based on the differences in chemical composition tdEVs can be distinguished from non-EV particles like lipoproteins, and EVs from other origin. Furthermore, enrichment can be achieved by the use of antibodies bound to the surface of a waveguide. Raman spectroscopy of EVs provides information on the chemical composition of single or multiple EVs in a non-invasive and label-free manner and may be simplified using integrated photonics devices. The analysis time per particle has not been measured yet, although since every particle needs to be analyzed, the throughput is expected to be prohibitively low.

2.4.6 AFM-SEM-Raman

2.4.6.1 Cancer-ID specific method and operating principle

The surface of stainless-steel substrates is modified with a carboxydecyl phosphonic acid monolayer to covalently link anti-EpCAM antibodies to the substrate (Figure 2.8) [52]. EVs are incubated in poly(dimethylsiloxane) (PDMS) microchannels. The microchannels are washed to remove non-specifically bound material. Next, EVs are incubated with paraformaldehyde in PBS for 15 minutes. The PDMS is removed by immersion in de-ionized water, 70% ethanol in water, and finally 100% ethanol for 5 minutes each step. Dehydration of tdEVs was followed by overnight drying. Alignment markers are embedded on the stainless-steel substrate by injecting patterned microfluidic channels with cyanoacrylate glue. The micro-scale alignment markers facilitate retracing individual EVs in the sample stages of the AFM (MFP-3D, Asylum Research, Wiesbaden, Germany), SEM (JEOL JSM-6610LA Analytical SEM (JEOL, Nieuw-Vennep, The Netherlands) and Raman microspectroscopy (home-built system as described in Beekman et al., 2019). SEM is used here to select regions of interest and confirm that the surface is successfully functionalized based on the attachment of EVs [15].

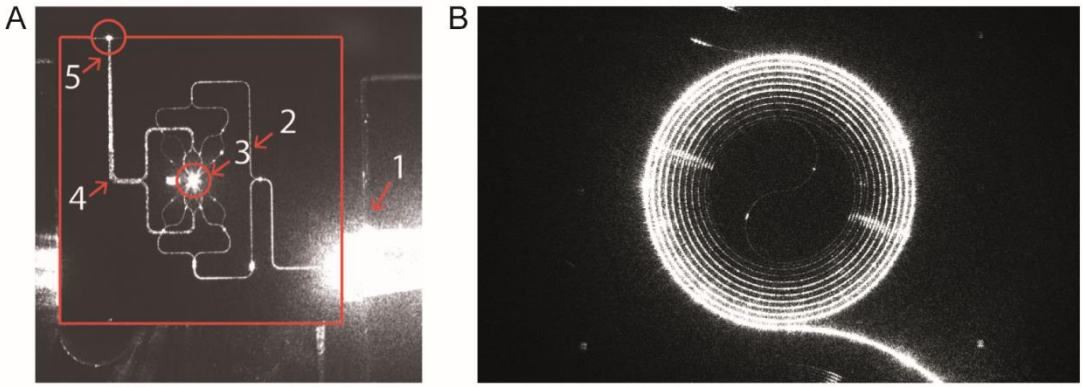

Figure 2.7. Integrated photonics-based lab-on-a-chip Raman spectroscopy. *A) Device type 1: Camera image of a device with 16 waveguides for trapping and 4 waveguides for detection. The device is actuated with light from an input fiber that is embedded in a fiber array unit (FAU) at the lower right-hand side. The various structures light up as a result of light scattering, causing some saturation of the camera. The solid red lines indicate the chip edges. 1: FAU. 2: Excitation-waveguide circuitry. 3: Micro fluidic bath with the central trapping region. 4: Detection-waveguide circuitry. 5: Light from the trap that is coupled out by the detection waveguides. Here, the detection waveguides collect light as a result of direct illumination and scattering. B) Device type 2: Spiral waveguide with the Raman pump light travelling inside the waveguide. The Raman signal is (partially) scattered back into the waveguide and collected at the front entrance. Reproduced with permission from* [51].

2.4.6.2 EV definition

EVs are identified by SEM and a Raman spectrum with lipid-protein peaks (2811-3023 cm^{-1}) characteristic for EVs. The functionalization of the substrate ensures that the EVs are of epithelial cell origin permitting the determination of the mechanical characteristics, like deformability, of the tdEVs by AFM.

2.4.6.3 Value added by Cancer-ID

The use of only one technique is often insufficient to identify and characterize EVs, as discussed in the previous sections [37]. For example, both EVs and

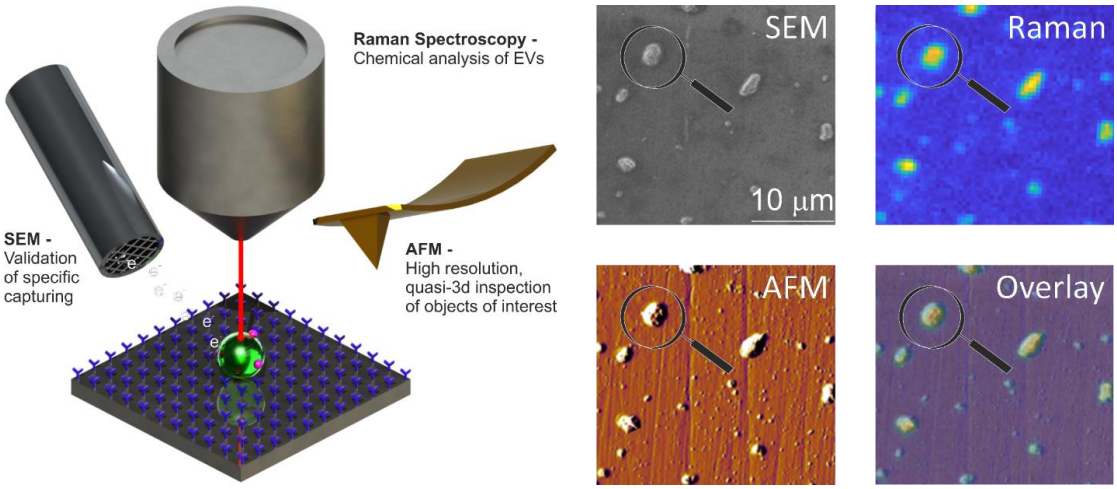

Figure 2.8. Atomic force microscopy (AFM), scanning electron microscopy (SEM), and Raman spectroscopy of extracellular vesicle (EV) sample. *Schematic representation of the system: antibody-functionalized stainless-steel substrate examined with SEM, AFM and Raman for correlated multi-modal analysis of individual EVs. Image adapted from* [15].

lipoproteins appear to be spherical by SEM. By combining SEM with AFM and Raman, we measure characteristics like size, chemical composition, and deformability to add certainty to the identification of tdEVs [15].

2.4.6.4 Relevance for cancer diagnostics

Using a combination of AFM, SEM and Raman and the capture of tdEVs to a functionalized surface helps to distinguish EVs from non-EV particles and adds certainty to the origin of the EV. In principle, this platform does not require distinguishing tdEVs from other species since enrichment is done by the functionalized surface (as assumed in Table 1). Since SEM measurements are faster than AFM or Raman, SEM was used for initial confirmation of tdEV presence on a chip; after enrichment 1000 tdEVs (of >100 nm) can be imaged in 1h. Since AFM detects the more abundant much smaller particles (>30nm) as compared to SEM (>100nm), the fact that AFM is slower in terms of imaged μm^2 per unit time, is offset by a greater number of observed tdEV per imaged μm^2, such that 1000 tdEVs can be imaged in 2h. For Raman, detection of 1000 tdEVs

would require about 100 measurements of 17 min each followed by several days of data processing.

2.4.7 Electrochemistry

2.4.7.1 Cancer-ID specific method and operating principle

Interdigitated nano-electrodes (nIDEs), fabricated in the cleanroom of MESA+ Institute for Nanotechnology, are surface-modified with poly(ethylene glycol) diglycidyl ether to form an amine-reactive anti-fouling layer (Figure 2.9A) [53]. Anti-EpCAM (VU1D9) antibodies are covalently linked to this layer and the remainder of the surface blocked with bovine serum albumin (BSA). EV samples are introduced onto the device to allow binding to the electrodes. After incubation, a biotinylated reporter anti-EpCAM is introduced. The biotin moiety conjugates to streptavidin coupled to alkaline phosphatase (ALP). ALP, only present on EpCAM-positive particles, converts an electrochemically inert molecule (para-aminophenyl phosphate) into a redox-active species (para-aminophenol), to yield a first amplification phase. Next, the para-aminophenol undergoes redox cycling, providing a second amplification phase.

2.4.7.2 EV definition

An increase in the redox current upon binding of particles to the nIDEs defines the presence of EVs. EVs from different species can be distinguished from each other by employing targeted antibodies, yielding a very high selectivity. For example, the signal from platelet EVs did not vary from the background signal, whereas introduction of LNCaP EVs greatly increased the signal (Figure 2.9B). [17]

2.4.7.3 Value added by Cancer-ID

This new and sensitive technique was developed by Cancer-ID in collaboration with researchers from the NanoElectronics group at University of Twente, the Netherlands. Several examples of sensitive integrated systems for (td)EV

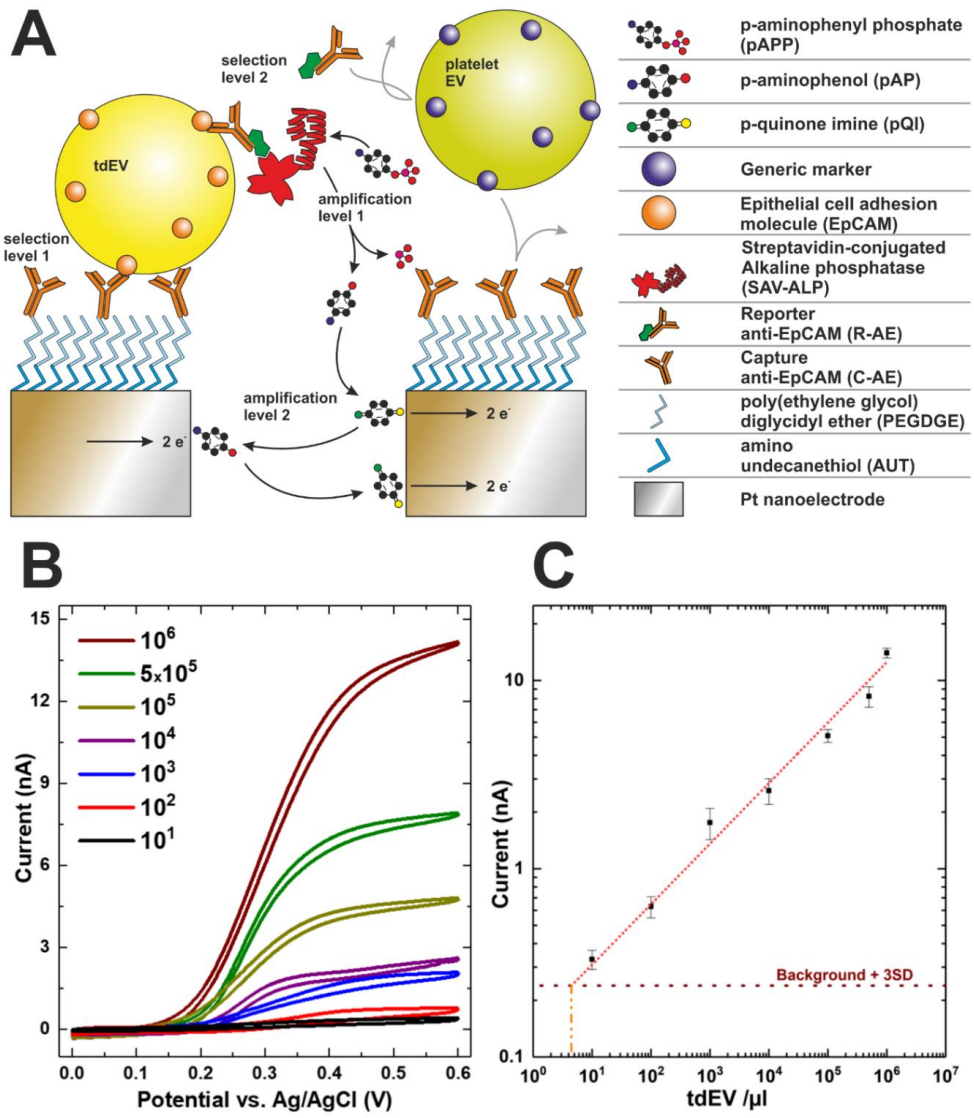

Figure 2.9. Electrochemical detection of extracellular vesicle (EV) samples. *A) Scheme showing selective capture and in-situ labeling of EVs followed by enzymatic amplification of redox species and redox cycling. B) Cyclic Voltammograms recorded for a very wide range of EV concentrations. C) Recorded current at 0.4 V for varying concentrations showing linear response over 6 orders of magnitude. Image adapted from* [17].

2.4.7.4 Value added by Cancer-ID

detection exist [54-56]. A unique feature of the technique discussed here is the ability to detect a low concentration of EVs with a low antigen expression. The linear response covers a broad range of concentrations, which largely overlaps with concentrations of tdEVs in patient blood.

2.4.7.5 Relevance for cancer diagnostics

Using electrochemistry, tdEVs can be discriminated from non-EV particles and EVs from other origin based on the expression of EpCAM. A dilution series of LNCaP EVs in PBS showed a linear response ranging from 5×10^3-10^9 tdEVs/mL (Figure 2.9C) [17], which overlaps with the expected tdEV concentration in plasma [11], showing this technique is promising to identify, count, and characterize tdEVs in the range of clinical samples. Evaluation of the technique with plasma patient samples and association of the read-out with clinical outcome remain to be tested.

The functionalized device is incubated with tdEV-containing sample and subsequently with reporter antibodies and redox mediator. In the experiments performed in the paper these incubations were done over excessively long periods (2.5 h in total) to maximize the efficiency but once optimized, can probably be performed several minutes to 1h. The cyclic voltammetry measurements were performed in 20 minutes, regardless of the concentration of tdEVs (5×10^3 – 10^9 per mL of sample). Using patient plasma rather than cell culture medium may increase the background signal, thereby reducing the sensitivity. Nevertheless, compared to other techniques, electrochemical methods have high promise for clinical utility in terms of throughput.

2.4.8 Surface Plasmon Resonance imaging (SPRi)

2.4.8.1 Cancer-ID specific method and operating principle

The surface of a SPRi sensor is coated with a conductive gold layer and a 3D hydrogel-like layer to reduce non-specific binding of non-EV particles to the surface (Figure 2.10A). Antibodies are printed on 48 spots on the sensor (Figure 2.10B), including isotype controls and a control (PBS) to correct for dissociation

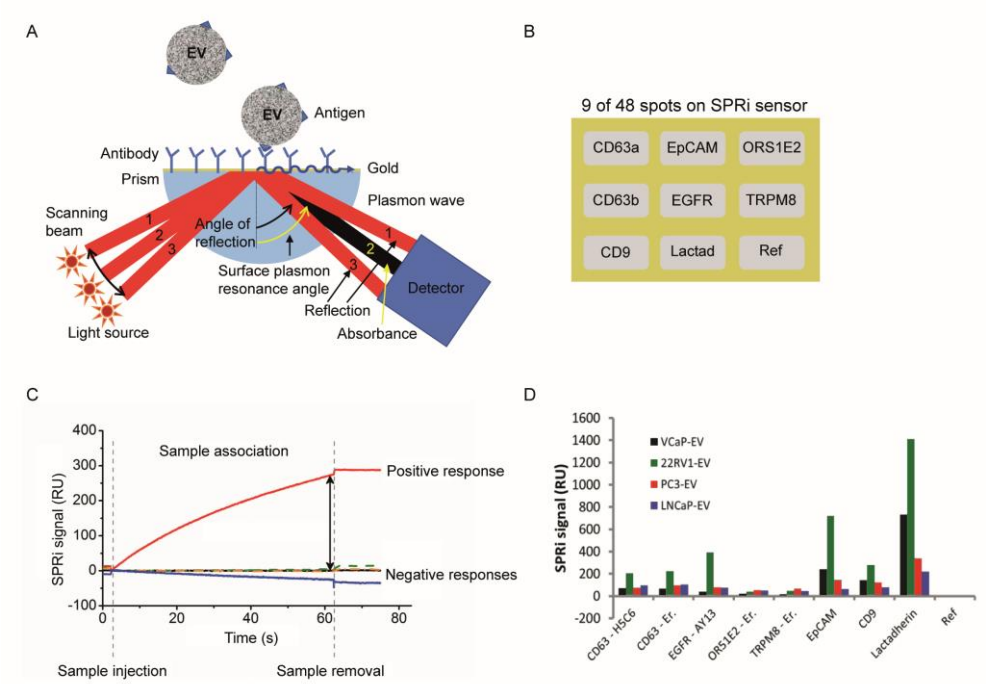

Figure 2.10. Surface plasmon resonance imaging (SPRi) analysis of extracellular vesicles (EVs). *A) Schematic of a SPRi set-up. A SPRi signal is generated when the sensor surface is illuminated at various angles with light and surface plasmons are excited [57]. The resonance angle, specific angle (beam 2) where maximum plasmon excitation and minimal internal reflection occurs [58], depends on the refractive index contrast near the interface in the evanescent field. B) The 48 spots on the SPRi sensor surface can be coated with different antibodies. In this example only 9 antibody coated spots on the SPRi sensor surface are shown. C) An EV sample is exposed to the SPRi sensor and measured for 60 minutes. The attachment of an ensemble of EVs to a specific antibody spot causes a change in the refractive index and generates a SPRi signal over time [18]. D) The SPRi signals after incubation with four prostate cancer-derived EV samples are shown. The two CD63-clones show the same results for all samples. All samples are slightly positive for CD63, EGFR, and CD9. A higher positivity is seen for EpCAM and Lactadherin. The SPRi signals for the 22RV1-EV sample are higher compared to the other samples [18].*

and non-specific binding [18]. Next, the surface is washed and deactivated by incubation with 2-amino ethanol followed by BSA. After an EV sample is exposed to the sensor, EVs bind to the antibody-coated sensor spot, which increases the refractive index near the sensor surface. This increase in refractive index is measured in time using the angle scanning principle of the IBIS MX96 instrument (IBIS Technologies, Enschede, The Netherlands) and corresponds to the number of particles captured on the spot (Figure 2.10C).

2.4.8.2 EV definition

With SPRi, EVs are identified based on their antigen exposure. EVs bind to antibodies printed on the sensor, e.g. anti-CD9, anti-CD63, anti-epidermal growth factor receptor (anti-EGFR), anti-EpCAM, anti-olfactory receptor 51E2 (anti-OR51E2), transient receptor potential cation channel subfamily M member 8 (TRPM8) and lactadherin, see Figure 2.10D. SPRi detects a difference in response on the antibody spots between EV samples derived from different cell lines. Characterization of EVs by SPRi, using the IBIS MX96, revealed the ability to detect cell surface antigens present at relatively low antigen densities compared to cells, as their presence could not be detected by flow cytometry [18].

2.4.8.3 Relevance for cancer diagnostics

SPRi can be used to distinguish tdEVs from non-EV particles and EVs derived from other cells based on the antigen expression. The IBIS MX96 is able to detect antigens present at a low density on EVs compared to cells [18]. Considering throughput, SPRi has superior sample processing rates compared to other techniques reviewed here. However, the required EV concentration to perform these measurements is high (2 x 10^8 EVs/mL), and not within the range of the expected tdEV frequency.

2.4.9 Flow cytometry (FCM)

2.4.9.1 Cancer-ID specific method and operating principle

EV samples are diluted in PBS (21-031-CV; Corning, Corning, NY) to prevent swarm detection [59] and stained with fluorescently-labelled antibodies. Antibody

aggregates are removed by centrifugation prior to use. The "antibody supernatant" is added to the EV sample followed by a two-hour incubation step, which is stopped by diluting the incubated sample with PBS. In a flow cytometer, the sample is hydrodynamically focused with sheath fluid to intersect a laser beam (Figure 2.11A). Scattered light and fluorescence from the particle are collected by a forward scatter detector, a side scatter detector, and multiple fluorescence detectors [60] (Figure 2.11B). The measured scatter and fluorescent signals per particle can be represented and analyzed using scatter plots as shown in Figure 2.11C. In the works referenced here, samples were analyzed on an A60-Micro (Apogee, Hertfordshire, UK).

2.4.9.2 EV definition

EV identification by FCM is commonly based on the expression of one or more antigens, which are detected using fluorescent immunostaining. Recently, we found that the refractive index of particles can be used as an additional parameter to distinguish EVs from lipoproteins [20]. We therefore define an EV as a particle that expresses detectable levels of one or more antigens, and has a refractive index <1.42.

2.4.9.3 Value added by Cancer-ID

Within Cancer-ID, technology to determine the size and refractive index of sub-micrometer particles was partly developed, evaluated and used to find new applications. Based on refractive index, for example, EVs can be differentiated from lipoproteins without antibody labeling [20]. Refractive index determination was used to show that generic EV dyes, which are commonly used to label EVs in FCM measurements, do not label all EVs and do label non-EV particles [19]. The combination of antibody labeling and refractive index determination could be used to increase specificity of EV detection. Furthermore, the side scatter sensitivity of a conventional flow cytometer was improved 30-fold by systematically modifying the hardware and a method was developed to quantify the scatter sensitivity of a flow cytometer.

2.4.9.4 Relevance for cancer diagnostics

FCM measures light scattering and fluorescence from thousands of individual particles per second. Although detection of the smallest single EVs is possible [61], only the most sensitive commercial flow cytometers are able to detect EVs with a diameter < 200 nm [62]. Based on the combination of an antibody and the refractive index, it is possible to discriminate tdEVs from lipoproteins and EVs from other origin. However, plasma samples are typically pre-diluted 10-100 times before measurements to prevent swarm detection (as assumed in Table 1). This dilution means the detection of the few tdEVs that might be present in the plasma sample is impossible.

However, FCM provides information on the concentration, cellular origin and biochemical composition, size and refractive index of single EVs [14, 21, 63].

2.4.10 Immunomagnetic EpCAM enrichment followed by fluorescence microscopic (FM) detection

2.4.10.1 Cancer-ID specific method and operating principle

Blood of individuals is collected in CellSave blood collection tubes (Menarini, Huntingdon Valley, PA). After centrifugation of 7.5 mL of blood for 10 minutes at 800 *g*, the sample is placed in the CellTracks Autoprep (Menarini, Huntingdon Valley, PA). The Autoprep aspirates and discards the plasma whereas the blood cell fraction is incubated with anti-EpCAM (VU1D9) ferrofluid (Figure 2.12A, step 1). The particles (cells and EVs) bound to the ferrofluid are separated from the rest of the blood by the application of magnetic forces (step 2). Following the immunomagnetic isolation, EpCAM-enriched particles are stained with the nuclear dye DAPI and fluorophore-conjugated antibodies recognizing the epithelial specific cytokeratins 8, 18 and 19 (CK-PE) and the leukocyte specific marker CD45 (CD45-APC) (step 3). The stained sample is loaded in a cartridge and placed between two magnets configured in such a way that all stained $EpCAM^+$ enriched particles homogeneously align on the glass slide on the surface of the cartridge (step 4). The cartridge is scanned using the CellTracks Analyzer II (Menarini, Huntingdon Valley, PA), a fluorescence microscope equipped with a

10x 0.45 NA objective (step 4). The images are analyzed using the open-source ACCEPT software to identify circulating tumor cells (CTCs), tdEVs, leukocytes and leukocyte EVs (step 5).

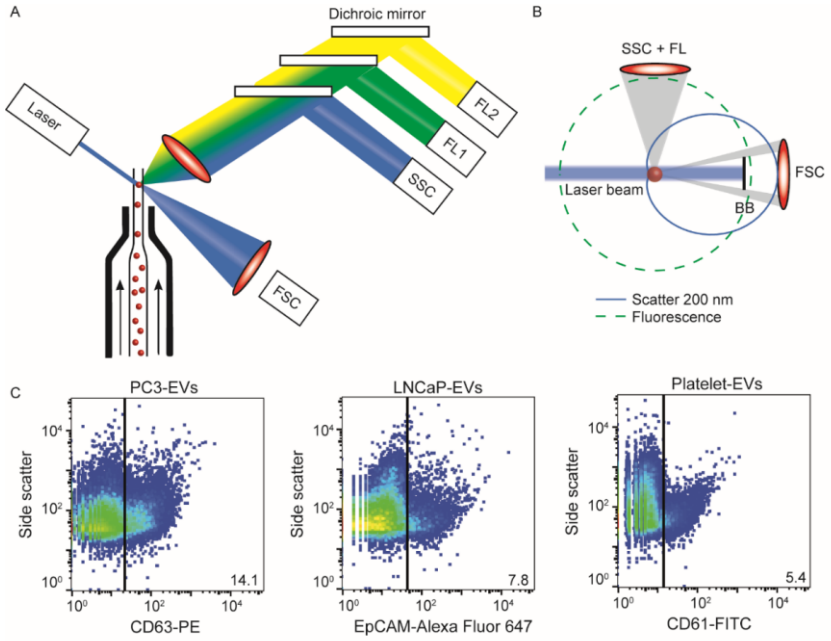

Figure 2.11. Flow cytometry of extracellular vesicle (EV) samples. *A) In flow cytometry, a single particle suspension is hydrodynamically focused with sheath fluid (arrows) to intersect a laser. Light coming from the particle is collected by a forward scatter detector (FSC), a side scatter detector (SSC), and multiple fluorescence detectors (FL1, FL2, etc.). B) Fluorescence (green dashed line) is isotropic and can be used to determine antigen expression and cellular origin. Scatter (blue solid line) has an angular distribution that depends on the size and refractive index of the particle (here 200 nm polystyrene). Knowledge of the flow cytometer collection angles and Mie theory allows derivation of particle size and refractive index from the measured scatter signals [14, 21]. C) Scatter plots of side scatter versus fluorescence for the PC3 EV sample stained with CD63-PE (left), the LNCaP EV sample stained with EpCAM-Alexa Fluor 647 (center), and the platelet EV sample stained with CD61-FITC (right). In PC3 EV sample 14.1% was found to be positive for the EV marker CD63, in the LNCaP EV sample 7.8% was found to be positive for cell surface epithelial marker EpCAM, and in the platelet EV sample 5.4% of the particles was found to be positive for CD61 BB: blocker bar, FL: fluorescence*

2.4.10.2 EV definition

tdEVs are defined as EpCAM+, CK+, DAPI-, CD45- particles. A gate for their automated enumeration from the CellSearch image data sets has previously been reported [9].

2.4.10.3 Value added by Cancer-ID

In the frames of the Cancer-ID program, we re-analyzed digitally stored FM image data sets of retrospective clinical studies acquired after EpCAM-enrichment. Our results suggest that large tdEVs (> 1 µm), co-isolated with CTCs, are negatively associated with the overall survival of metastatic prostate, colorectal, breast and non-small cell lung cancer patients in a similar way as CTCs (Figure 2.12) [8] and could contribute in monitoring the disease and assessing therapeutic efficacy. However, the existing technique was developed for the detection of CTCs and eliminates the detection of smaller tdEVs or tdEVs with low antigen density even if they have been isolated by the anti-EpCAM ferrofluid. To evaluate whereas tdEVs from a model cancer cell line can be isolated using the CellSearch assay, two samples were used as a positive and negative control of the technique. Two blood samples of 7.5 mL, collected in CellSave tubes and

drawn from an anonymous healthy individual, were provided by the TNW-ECTM-donor services (University of Twente, Enschede, The Netherlands). Both samples were processed with the CellSearch system; however, the one sample remained intact without the addition of any EVs (negative control), whereas the other one was spiked with EVs produced from the EpCAM+ LNCaP prostate cancer cell line (positive control). The application of a tdEV gate resulted in 0 events in the negative control and in 3772 events in the positive control (Figures 2.12B and 2.12C). This study was carried out in accordance with the recommendations of Dutch regulations. The protocol was approved by the Medical ethical assessment committee Twente (METC Twente). The subject gave written informed consent in accordance with the Declaration of Helsinki.

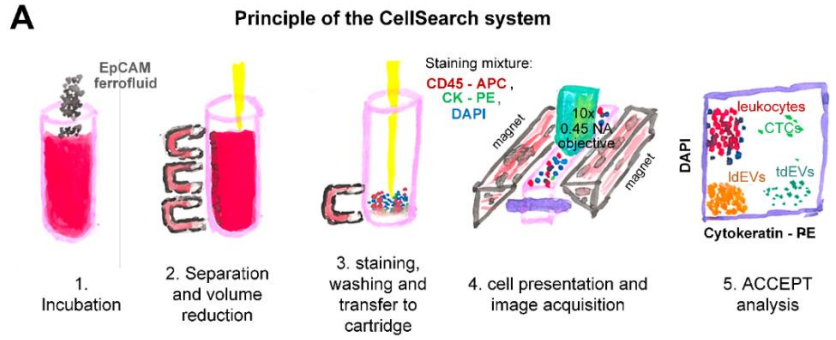

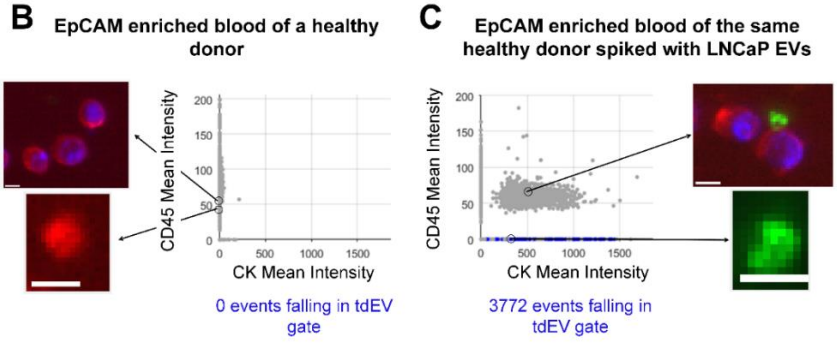

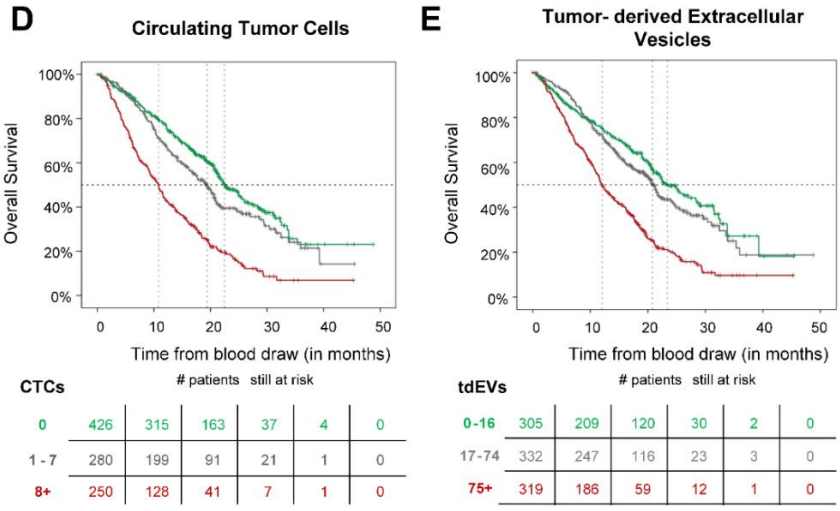

CTCs

	# patients still at risk					
0	426	315	163	37	4	0
1 - 7	280	199	91	21	1	0
8+	250	128	41	7	1	0

tdEVs

	# patients still at risk					
0-16	305	209	120	30	2	0
17-74	332	247	116	23	3	0
75+	319	186	59	12	1	0

Figure 2.12. EpCAM immunomagnetic enrichment and fluorescence microscopic (FM) detection of extracellular vesicle (EV) samples. *A) Principle of the CellSearch system. ACCEPT analysis of two CellSearch cartridges corresponding to EpCAM enriched blood sample of a healthy donor without (B) and with LNCaP EVs spiked (C). CD45 is depicted in red, CK in green and DAPI in blue. The objects falling in the applied tdEV gate are depicted as blue dots in the scatter plots of CD45 Mean Intensity versus CK Mean Intensity. The other particles are shown as grey dots. Thumbnail examples of 4 objects are shown. The CD45+, CK+ particles are attached to the leukocytes, as illustrated. Scale bars indicate 6.4 µm. Panel D and E show Kaplan Meier plots of overall survival of 956 metastatic colorectal, prostate, breast and non-small cell lung cancer patients. Patients were grouped based on their circulating tumor cells (CTC) (Panel D) or tumor-derived EV (tdEV) counts (Panel E) demonstrating the equivalent prognostic power of CTCs and tdEVs 8.*

2.4.10.4 Relevance for cancer diagnostics

The CellSearch system can be used to enrich tdEVs based on their EpCAM expression, as EpCAM is not expected to be present on EVs in blood of healthy individuals [64, 65]. However, tdEVs isolated by the CellSearch system are limited to the relative larger EVs (> 1 µm), as the plasma obtained after centrifugation at 800 *g* is discarded. Considering that the CellSearch is only sensitive to the largest tdEVs and thereby needs to scan a larger area to encounter a representative number of tdEVs (see Table 1), the sensitivity is unfit for clinical purposes.

2.5 Cancer-ID insights

Cancer-ID delivered new techniques and new insights to explore tdEV detection. Taken the complexity of blood into consideration, the necessity of enriching biological samples for tdEVs becomes obvious. EVs secreted from prostate cancer cell lines and EVs derived from red blood cells and platelets, resembling the expected background of EVs in plasma, were used to explore the utility of different techniques. The size distribution of the EV samples was characterized by NTA, the EV size and/or morphology by TEM, SEM and AFM, the biochemical composition by Raman spectroscopy, and their antigen expression profile of EVs

using SPRi, FM and FCM. The techniques were able to detect or image EVs present in EV samples from cultured tumor cells. However, discrimination between EVs and non-EV particles becomes difficult in complex samples like plasma, because non-EV particles outnumber EVs (Figure 2.1). Furthermore, most techniques cannot identify the cellular origin of single EVs and relate the measured signal or count to the concentration of tdEVs in plasma. The results of all individual techniques pointed out that a combination of more than one parameter or technique increases the certainty that tdEVs are being investigated and immune affinity enrichment or detection is needed to cover the large size and density range of EVs.

EV isolation protocols have not been standardized within the EV field [66, 67]. Size-based isolation techniques, such as size exclusion chromatography can purify samples from contaminating lipoproteins and soluble protein of a size below 70 nm [29]. Furthermore, centrifugation is often used to isolate biomarkers from whole blood. In the Cancer-ID program, we developed a model to predict the behavior of particles (cells and EVs) in solution during centrifugation, and showed the co-isolation of for example platelets and large EVs after centrifugation [67]. Furthermore, although the application of rate zonal centrifugation improved the separation of platelets from EVs, the aforementioned isolation techniques result in purification of EVs rather than enrichment of tdEVs.

By the use of affinity-based techniques using antibodies directed to antigens expressed on tumor cells but not on blood cells we demonstrated the enrichment of large (> 1 μm) EpCAM+ tdEVs from blood from metastatic cancer patients [8, 9]. EVs from different origin were eliminated in the enriched sample. Efforts for the immunomagnetic enrichment of smaller (< 1 μm) tdEVs from plasma samples based on EpCAM are ongoing. The frequency of small tdEV shown in Figure 2.1 is based on an extrapolation from the frequency of the large tdEVs and this surely will need to be validated. Moreover, whether the small tdEV have a similar relation with clinical outcome will need to be established. tdEV likely encompass different subclasses for example those responsible for communication with the environment and those involved in the process of apoptosis of cancer cells and as such relation with clinical outcome or its cargo

being informative on the optimal treatment will likely be different between these subclasses. Here only the EpCAM antigen was used to capture tdEVs, the use of different or a mixture of antibodies recognizing different cancer-specific antigens, such as VAR2CSA [68] and HsP70 [69, 70] could increase the capture efficacy and may identify different subclasses of tdEVs. Identification of tdEV among the EpCAM enriched particles was obtained through identification of the presence of intracellular cytokeratins; the use of different components of the tdEV cargo might be important. Exploration of this cargo with label free technologies such as Raman and SPRi identified some alternative avenues that can be explored. The onset of retrieving data from the molecular content of EVs has also been explored in the Cancer-ID program. A challenge is retrieving sufficient RNA to represent the mRNA and long noncoding RNA transcriptome. As a first step, various EV RNA isolation kits were tested, and of the isolation kits tested, the Norgen total RNA isolation protocol resulted in the highest amount of RNA as determined by RT-qPCR of housekeeping and prostate-associated transcripts. Although this Norgen protocol will also extract non-EV RNA from urine, RNA yield and coverage by RNAseq are considered of higher priority than purity for our EV-based biomarker efforts. State-of-the-art integrated systems developed in the Cancer ID Perspectief program come close to reliably detecting tdEVs at clinically relevant concentrations at high throughput. Small tdEVs (< 1 µm) can be isolated using functionalized anti-EpCAM substrates and can be detected electrochemically in a label-free manner [17]. Next, sorting of tdEV populations (as defined by fluorescence, by SPRi, electrochemically, or by Raman spectroscopy) can be used to perform downstream molecular analysis and reveal their genetic content which could play a critical role in identifying the best therapeutic strategy for cancer patients.

2.6 References

1. Conde-Vancells, J.; Rodriguez-Suarez, E.; Embade, N.; Gil, D.; Matthiesen, R.; Valle, M.; Elortza, F.; Lu, S. C.; Mato, J. M.; Falcon-Perez, J. M., Characterization and comprehensive proteome profiling of exosomes secreted by hepatocytes. Journal of Proteome Research 2008, 7 (12), 5157-5166.
2. Verderio, C.; Muzio, L.; Turola, E.; Bergami, A.; Novellino, L.; Ruffini, F.; Riganti, L.; Corradini, I.; Francolini, M.; Garzetti, L.; Maiorino, C.; Servida, F.; Vercelli, A.; Rocca, M.; Dalla Libera, D.; Martinelli, V.; Comi, G.; Martino, G.; Matteoli, M.; Furlan, R., Myeloid microvesicles are a marker and therapeutic target for neuroinflammation. Annals of Neurology 2012, 72 (4), 610-624.
3. Melo, S. A.; Luecke, L. B.; Kahlert, C.; Fernandez, A. F.; Gammon, S. T.; Kaye, J.; LeBleu, V. S.; Mittendorf, E. A.; Weitz, J.; Rahbari, N.; Reissfelder, C.; Pilarsky, C.; Fraga, M. F.; Piwnica-Worms, D.; Kalluri, R., Glypican-1 identifies cancer exosomes and detects early pancreatic cancer. Nature 2015, 523 (7559), 177-82.
4. Meng, Y.; Sun, J.; Wang, X.; Hu, T.; Ma, Y.; Kong, C.; Piao, H.; Yu, T.; Zhang, G., Exosomes: A Promising Avenue for the Diagnosis of Breast Cancer. Technology in cancer research & treatment 2019, 18, 1533033818821421-1533033818821421.
5. Simonsen, J. B., What are we looking at? Extracellular vesicles, lipoproteins, or both? Circ Res 2017, 121 (8), 920-922.
6. Kuchinskiene, Z.; Carlson, L. A., Composition, concentration, and size of low density lipoproteins and of subfractions of very low density lipoproteins from serum of normal men and women. J Lipid Res 1982, 23 (5), 762-9.
7. Corash, L.; Costa, J. L.; Shafer, B.; Donlon, J. A.; Murphy, D., Heterogeneity of human whole blood platelet subpopulations. III. Density-dependent differences in subcellular constituents. Blood 1984, 64 (1), 185-93.
8. Nanou, A.; Miller, M. C.; Zeune, L. L.; de Wit, S.; Punt, C. J. A.; Groen, H. J. M.; Hayes, D. F.; de Bono, J. S.; Terstappen, L., Tumour-derived extracellular vesicles in blood of metastatic cancer patients associate with overall survival. Br J Cancer 2020.
9. Nanou, A.; Coumans, F. A. W.; van Dalum, G.; Zeune, L. L.; Dolling, D.; Onstenk, W.; Crespo, M.; Fontes, M. S.; Rescigno, P.; Fowler, G.; Flohr, P.; Brune, C.; Sleijfer, S.; de Bono, J. S.; Terstappen, L., Circulating tumor cells, tumor-derived extracellular vesicles and plasma cytokeratins in castration-resistant prostate cancer patients. Oncotarget 2018, 9 (27), 19283-19293.
10. Ricklefs, F. L.; Maire, C. L.; Reimer, R.; Duhrsen, L.; Kolbe, K.; Holz, M.; Schneider, E.; Rissiek, A.; Babayan, A.; Hille, C.; Pantel, K.; Krasemann, S.; Glatzel, M.; Heiland, D. H.; Flitsch, J.; Martens, T.; Schmidt, N. O.; Peine, S.; Breakefield, X. O.; Lawler, S.; Chiocca, E. A.; Fehse, B.; Giebel, B.; Gorgens, A.; Westphal, M.; Lamszus, K., Imaging flow cytometry facilitates multiparametric characterization of extracellular vesicles in malignant brain tumours. J Extracell Vesicles 2019, 8 (1), 1588555.
11. Coumans, F.; van Dalum, G.; Terstappen, L., CTC Technologies and Tools. Cytometry A 2018, 93 (12), 1197-1201.
12. Johnsen, K. B.; Gudbergsson, J. M.; Andresen, T. L.; Simonsen, J. B., What is the blood concentration of extracellular vesicles? Implications for the use of extracellular vesicles as blood-borne biomarkers of cancer. Biochim Biophys Acta Rev Cancer 2019, 1871 (1), 109-116.
13. Rikkert, L. G.; Nieuwland, R.; Terstappen, L.; Coumans, F. A. W., Quality of extracellular vesicle images by transmission electron microscopy is operator and protocol dependent. J Extracell Vesicles 2019, 8 (1), 1555419.

14. de Rond, L.; Coumans, F. A. W.; Nieuwland, R.; van Leeuwen, T. G.; van der Pol, E., Deriving extracellular vesicle size from scatter intensities measured by flow cytometry. Curr Protoc Cytom 2018, 86 (1), e43.
15. Beekman, P.; Enciso-Martinez, A.; Rho, H. S.; Pujari, S. P.; Lenferink, A.; Zuilhof, H.; Terstappen, L.; Otto, C.; Le Gac, S., Immuno-capture of extracellular vesicles for individual multi-modal characterization using AFM, SEM and Raman spectroscopy. Lab Chip 2019, 19 (15), 2526-2536.
16. Enciso-Martinez, A.; van der Pol, E.; Lenferink, A. T. M.; Terstappen, L. W. M. M.; Van Leeuwen, T. G.; Otto, C., Synchronized Rayleigh and Raman scattering for the characterization of single optically trapped extracellular vesicles. Nanomedicine: Nanotechnology, Biology and Medicine 2019, 102109.
17. Mathew, D.; Beekman, P.; Lemay, S. G.; Zuilhof, H.; Le Gac, S.; van der Wiel, W. G., Electrochemical detection of tumor-derived extracellular vesicles on nano-interdigitated electrodes. Nano Lett 2019.
18. Gool, E. L.; Stojanovic, I.; Schasfoort, R. B. M.; Sturk, A.; van Leeuwen, T. G.; Nieuwland, R.; Terstappen, L.; Coumans, F. A. W., Surface Plasmon Resonance is an Analytically Sensitive Method for Antigen Profiling of Extracellular Vesicles. Clin Chem 2017, 63 (10), 1633-1641.
19. de Rond, L.; van der Pol, E.; Hau, C. M.; Varga, Z.; Sturk, A.; van Leeuwen, T. G.; Nieuwland, R.; Coumans, F. A. W., Comparison of Generic Fluorescent Markers for Detection of Extracellular Vesicles by Flow Cytometry. Clin Chem 2018, 64 (4), 680-689.
20. de Rond, L.; Libregts, S.; Rikkert, L. G.; Hau, C. M.; van der Pol, E.; Nieuwland, R.; van Leeuwen, T. G.; Coumans, F. A. W., Refractive index to evaluate staining specificity of extracellular vesicles by flow cytometry. J Extracell Vesicles 2019, 8 (1), 1643671.
21. van der Pol, E.; de Rond, L.; Coumans, F. A. W.; Gool, E. L.; Boing, A. N.; Sturk, A.; Nieuwland, R.; van Leeuwen, T. G., Absolute sizing and label-free identification of extracellular vesicles by flow cytometry. Nanomedicine 2018, 14 (3), 801-810.
22. Coumans, F. A. W.; Gool, E. L.; Nieuwland, R., Bulk immunoassays for analysis of extracellular vesicles. Platelets 2017, 28 (3), 242-248.
23. van der Pol, E.; Hoekstra, A. G.; Sturk, A.; Otto, C.; van Leeuwen, T. G.; Nieuwland, R., Optical and non-optical methods for detection and characterization of microparticles and exosomes. Journal of thrombosis and haemostasis : JTH 2010, 8 (12), 2596-607.
24. van der Pol, E.; Coumans, F. A. W.; Grootemaat, A. E.; Gardiner, C.; Sargent, I. L.; Harrison, P.; Sturk, A.; van Leeuwen, T. G.; Nieuwland, R., Particle size distribution of exosomes and microvesicles determined by transmission electron microscopy, flow cytometry, nanoparticle tracking analysis, and resistive pulse sensing. Journal of Thrombosis and Haemostasis 2014, 12 (7), 1182-1192.
25. Lee, W.; Nanou, A.; Rikkert, L.; Coumans, F. A. W.; Otto, C.; Terstappen, L.; Offerhaus, H. L., Label-Free Prostate Cancer Detection by Characterization of Extracellular Vesicles Using Raman Spectroscopy. Anal Chem 2018, 90 (19), 11290-11296.
26. van der Pol, E.; Coumans, F. A.; Sturk, A.; Nieuwland, R.; van Leeuwen, T. G., Refractive index determination of nanoparticles in suspension using nanoparticle tracking analysis. Nano Lett 2014, 14 (11), 6195-201.
27. Lötvall, J.; Hill, A. F.; Hochberg, F.; Buzás, E. I.; Di Vizio, D.; Gardiner, C.; Gho, Y. S.; Kurochkin, I. V.; Mathivanan, S.; Quesenberry, P.; Sahoo, S.; Tahara, H.; Wauben, M. H.; Witwer, K. W.; Théry, C., Minimal experimental requirements for definition of extracellular vesicles and their functions: a position statement from the International Society for Extracellular Vesicles. Journal of Extracellular Vesicles 2014, 3, 10.3402/jev.v3.26913.

28. Pisitkun, T.; Shen, R. F.; Knepper, M. A., Identification and proteomic profiling of exosomes in human urine. Proc Natl Acad Sci U S A 2004, 101 (36), 13368-73.
29. Boing, A. N.; van der Pol, E.; Grootemaat, A. E.; Coumans, F. A.; Sturk, A.; Nieuwland, R., Single-step isolation of extracellular vesicles by size-exclusion chromatography. Journal of Extracellular Vesicles 2014, 3, 10.3402/jev.v3.23430.
30. Keerthikumar, S.; Gangoda, L.; Liem, M.; Fonseka, P.; Atukorala, I.; Ozcitti, C.; Mechler, A.; Adda, C. G.; Ang, C. S.; Mathivanan, S., Proteogenomic analysis reveals exosomes are more oncogenic than ectosomes. Oncotarget 2015, 6 (17), 15375-15396.
31. Hong, C. S.; Muller, L.; Boyiadzis, M.; Whiteside, T. L., Isolation and Characterization of CD34+Blast-Derived Exosomes in Acute Myeloid Leukemia. Plos One 2014, 9 (8), e103310.
32. Atay, S.; Gercel-Taylor, C.; Kesimer, M.; Taylor, D. D., Morphologic and proteomic characterization of exosomes released by cultured extravillous trophoblast cells. Experimental Cell Research 2011, 317 (8), 1192-1202.
33. Sahoo, S.; Klychko, E.; Thorne, T.; Misener, S.; Schultz, K. M.; Millay, M.; Ito, A.; Liu, T.; Kamide, C.; Agrawal, H.; Perlman, H.; Qin, G.; Kishore, R.; Losordo, D. W., Exosomes From Human CD34(+) Stem Cells Mediate Their Proangiogenic Paracrine Activity. Circulation Research 2011, 109 (7), 724-35.
34. Zhang, H.; Xie, Y.; Li, W.; Chibbar, R.; Xiong, S.; Xiang, J., CD4(+) T cell-released exosomes inhibit CD8(+) cytotoxic T-lymphocyte responses and antitumor immunity. Cellular & Molecular Immunology 2011, 8 (1), 23-30.
35. Xie, Y.; Zhang, X.; Zhao, T.; Li, W.; Xiang, J., Natural CD8(+)25(+) regulatory T cell-secreted exosomes capable of suppressing cytotoxic T lymphocyte-mediated immunity against B16 melanoma. Biochem Biophys Res Commun 2013, 438 (1), 152-5.
36. Gangalum, R. K.; Atanasov, I. C.; Zhou, Z. H.; Bhat, S. P., alpha B-Crystallin Is Found in Detergent-resistant Membrane Microdomains and Is Secreted via Exosomes from Human Retinal Pigment Epithelial Cells. Journal of Biological Chemistry 2011, 286 (5), 3261-3269.
37. Thery, C.; Witwer, K. W.; Aikawa, E.; Alcaraz, M. J.; Anderson, J. D.; Andriantsitohaina, R.; Antoniou, A.; Arab, T.; Archer, F.; Atkin-Smith, G. K.; Ayre, D. C.; Bach, J. M.; Bachurski, D.; Baharvand, H.; Balaj, L.; Baldacchino, S.; Bauer, N. N.; Baxter, A. A.; Bebawy, M.; Beckham, C.; Bedina Zavec, A.; Benmoussa, A.; Berardi, A. C.; Bergese, P.; Bielska, E.; Blenkiron, C.; Bobis-Wozowicz, S.; Boilard, E.; Boireau, W.; Bongiovanni, A.; Borras, F. E.; Bosch, S.; Boulanger, C. M.; Breakefield, X.; Breglio, A. M.; Brennan, M. A.; Brigstock, D. R.; Brisson, A.; Broekman, M. L.; Bromberg, J. F.; Bryl-Gorecka, P.; Buch, S.; Buck, A. H.; Burger, D.; Busatto, S.; Buschmann, D.; Bussolati, B.; Buzas, E. I.; Byrd, J. B.; Camussi, G.; Carter, D. R.; Caruso, S.; Chamley, L. W.; Chang, Y. T.; Chen, C.; Chen, S.; Cheng, L.; Chin, A. R.; Clayton, A.; Clerici, S. P.; Cocks, A.; Cocucci, E.; Coffey, R. J.; Cordeiro-da-Silva, A.; Couch, Y.; Coumans, F. A.; Coyle, B.; Crescitelli, R.; Criado, M. F.; D'Souza-Schorey, C.; Das, S.; Datta Chaudhuri, A.; de Candia, P.; De Santana, E. F.; De Wever, O.; Del Portillo, H. A.; Demaret, T.; Deville, S.; Devitt, A.; Dhondt, B.; Di Vizio, D.; Dieterich, L. C.; Dolo, V.; Dominguez Rubio, A. P.; Dominici, M.; Dourado, M. R.; Driedonks, T. A.; Duarte, F. V.; Duncan, H. M.; Eichenberger, R. M.; Ekstrom, K.; El Andaloussi, S.; Elie-Caille, C.; Erdbrugger, U.; Falcon-Perez, J. M.; Fatima, F.; Fish, J. E.; Flores-Bellver, M.; Forsonits, A.; Frelet-Barrand, A.; Fricke, F.; Fuhrmann, G.; Gabrielsson, S.; Gamez-Valero, A.; Gardiner, C.; Gartner, K.; Gaudin, R.; Gho, Y. S.; Giebel, B.; Gilbert, C.; Gimona, M.; Giusti, I.; Goberdhan, D. C.; Gorgens, A.; Gorski, S. M.; Greening, D. W.; Gross, J. C.; Gualerzi, A.; Gupta, G. N.; Gustafson, D.; Handberg, A.; Haraszti, R. A.; Harrison, P.; Hegyesi, H.; Hendrix, A.; Hill, A. F.; Hochberg, F. H.; Hoffmann, K. F.; Holder, B.; Holthofer, H.; Hosseinkhani, B.; Hu, G.; Huang, Y.; Huber, V.; Hunt, S.; Ibrahim, A. G.; Ikezu, T.; Inal, J. M.; Isin, M.; Ivanova, A.; Jackson, H. K.; Jacobsen, S.; Jay, S. M.; Jayachandran, M.;

Jenster, G.; Jiang, L.; Johnson, S. M.; Jones, J. C.; Jong, A.; Jovanovic-Talisman, T.; Jung, S.; Kalluri, R.; Kano, S. I.; Kaur, S.; Kawamura, Y.; Keller, E. T.; Khamari, D.; Khomyakova, E.; Khvorova, A.; Kierulf, P.; Kim, K. P.; Kislinger, T.; Klingeborn, M.; Klinke, D. J., 2nd; Kornek, M.; Kosanovic, M. M.; Kovacs, A. F.; Kramer-Albers, E. M.; Krasemann, S.; Krause, M.; Kurochkin, I. V.; Kusuma, G. D.; Kuypers, S.; Laitinen, S.; Langevin, S. M.; Languino, L. R.; Lannigan, J.; Lasser, C.; Laurent, L. C.; Lavieu, G.; Lazaro-Ibanez, E.; Le Lay, S.; Lee, M. S.; Lee, Y. X. F.; Lemos, D. S.; Lenassi, M.; Leszczynska, A.; Li, I. T.; Liao, K.; Libregts, S. F.; Ligeti, E.; Lim, R.; Lim, S. K.; Line, A.; Linnemannstons, K.; Llorente, A.; Lombard, C. A.; Lorenowicz, M. J.; Lorincz, A. M.; Lotvall, J.; Lovett, J.; Lowry, M. C.; Loyer, X.; Lu, Q.; Lukomska, B.; Lunavat, T. R.; Maas, S. L.; Malhi, H.; Marcilla, A.; Mariani, J.; Mariscal, J.; Martens-Uzunova, E. S.; Martin-Jaular, L.; Martinez, M. C.; Martins, V. R.; Mathieu, M.; Mathivanan, S.; Maugeri, M.; McGinnis, L. K.; McVey, M. J.; Meckes, D. G., Jr.; Meehan, K. L.; Mertens, I.; Minciacchi, V. R.; Moller, A.; Moller Jorgensen, M.; Morales-Kastresana, A.; Morhayim, J.; Mullier, F.; Muraca, M.; Musante, L.; Mussack, V.; Muth, D. C.; Myburgh, K. H.; Najrana, T.; Nawaz, M.; Nazarenko, I.; Nejsum, P.; Neri, C.; Neri, T.; Nieuwland, R.; Nimrichter, L.; Nolan, J. P.; Nolte-'t Hoen, E. N.; Noren Hooten, N.; O'Driscoll, L.; O'Grady, T.; O'Loghlen, A.; Ochiya, T.; Olivier, M.; Ortiz, A.; Ortiz, L. A.; Osteikoetxea, X.; Ostergaard, O.; Ostrowski, M.; Park, J.; Pegtel, D. M.; Peinado, H.; Perut, F.; Pfaffl, M. W.; Phinney, D. G.; Pieters, B. C.; Pink, R. C.; Pisetsky, D. S.; Pogge von Strandmann, E.; Polakovicova, I.; Poon, I. K.; Powell, B. H.; Prada, I.; Pulliam, L.; Quesenberry, P.; Radeghieri, A.; Raffai, R. L.; Raimondo, S.; Rak, J.; Ramirez, M. I.; Raposo, G.; Rayyan, M. S.; Regev-Rudzki, N.; Ricklefs, F. L.; Robbins, P. D.; Roberts, D. D.; Rodrigues, S. C.; Rohde, E.; Rome, S.; Rouschop, K. M.; Rughetti, A.; Russell, A. E.; Saa, P.; Sahoo, S.; Salas-Huenuleo, E.; Sanchez, C.; Saugstad, J. A.; Saul, M. J.; Schiffelers, R. M.; Schneider, R.; Schoyen, T. H.; Scott, A.; Shahaj, E.; Sharma, S.; Shatnyeva, O.; Shekari, F.; Shelke, G. V.; Shetty, A. K.; Shiba, K.; Siljander, P. R.; Silva, A. M.; Skowronek, A.; Snyder, O. L., 2nd; Soares, R. P.; Sodar, B. W.; Soekmadji, C.; Sotillo, J.; Stahl, P. D.; Stoorvogel, W.; Stott, S. L.; Strasser, E. F.; Swift, S.; Tahara, H.; Tewari, M.; Timms, K.; Tiwari, S.; Tixeira, R.; Tkach, M.; Toh, W. S.; Tomasini, R.; Torrecilhas, A. C.; Tosar, J. P.; Toxavidis, V.; Urbanelli, L.; Vader, P.; van Balkom, B. W.; van der Grein, S. G.; Van Deun, J.; van Herwijnen, M. J.; Van Keuren-Jensen, K.; van Niel, G.; van Royen, M. E.; van Wijnen, A. J.; Vasconcelos, M. H.; Vechetti, I. J., Jr.; Veit, T. D.; Vella, L. J.; Velot, E.; Verweij, F. J.; Vestad, B.; Vinas, J. L.; Visnovitz, T.; Vukman, K. V.; Wahlgren, J.; Watson, D. C.; Wauben, M. H.; Weaver, A.; Webber, J. P.; Weber, V.; Wehman, A. M.; Weiss, D. J.; Welsh, J. A.; Wendt, S.; Wheelock, A. M.; Wiener, Z.; Witte, L.; Wolfram, J.; Xagorari, A.; Xander, P.; Xu, J.; Yan, X.; Yanez-Mo, M.; Yin, H.; Yuana, Y.; Zappulli, V.; Zarubova, J.; Zekas, V.; Zhang, J. Y.; Zhao, Z.; Zheng, L.; Zheutlin, A. R.; Zickler, A. M.; Zimmermann, P.; Zivkovic, A. M.; Zocco, D.; Zuba-Surma, E. K., Minimal information for studies of extracellular vesicles 2018 (MISEV2018): a position statement of the International Society for Extracellular Vesicles and update of the MISEV2014 guidelines. J Extracell Vesicles 2018, 7 (1), 1535750.

38. Enciso-Martinez, A.; Timmermans, F. J.; Nanou, A.; Terstappen, L.; Otto, C., SEM-Raman image cytometry of cells. Analyst 2018, 143 (18), 4495-4502.

39. Nanou, A.; Crespo, M.; Flohr, P.; De Bono, J. S.; Terstappen, L., Scanning Electron Microscopy of Circulating Tumor Cells and Tumor-Derived Extracellular Vesicles. Cancers (Basel) 2018, 10 (11).

40. Vorselen, D.; MacKintosh, F. C.; Roos, W. H.; Wuite, G. J., Competition between Bending and Internal Pressure Governs the Mechanics of Fluid Nanovesicles. ACS Nano 2017, 11 (3), 2628-2636.

41. Vorselen, D.; van Dommelen, S. M.; Sorkin, R.; Piontek, M. C.; Schiller, J.; Dopp, S. T.; Kooijmans, S. A. A.; van Oirschot, B. A.; Versluijs, B. A.; Bierings, M. B.; van Wijk, R.; Schiffelers,

R. M.; Wuite, G. J. L.; Roos, W. H., The fluid membrane determines mechanics of erythrocyte extracellular vesicles and is softened in hereditary spherocytosis. Nat Commun 2018, 9 (1), 4960.
42. Sorkin, R.; Huisjes, R.; Boskovic, F.; Vorselen, D.; Pignatelli, S.; Ofir-Birin, Y.; Freitas Leal, J. K.; Schiller, J.; Mullick, D.; Roos, W. H.; Bosman, G.; Regev-Rudzki, N.; Schiffelers, R. M.; Wuite, G. J. L., Nanomechanics of Extracellular Vesicles Reveals Vesiculation Pathways. Small 2018, 14 (39), e1801650.
43. Vorselen, D.; Marchetti, M.; Lopez-Iglesias, C.; Peters, P. J.; Roos, W. H.; Wuite, G. J. L., Multilamellar nanovesicles show distinct mechanical properties depending on their degree of lamellarity. Nanoscale 2018, 10 (11), 5318-5324.
44. Piontek, M. C.; Roos, W. H., Atomic Force Microscopy: An Introduction. Methods Mol Biol 2018, 1665, 243-258.
45. Lee, W.; Offerhaus, H. In Classifying Raman spectra of extracellular vesicles using a convolutional neural network, The 26th International Conference on Raman Spectroscopy 2018, 2018.
46. Krafft, C.; Wilhelm, K.; Eremin, A.; Nestel, S.; von Bubnoff, N.; Schultze-Seemann, W.; Popp, J.; Nazarenko, I., A specific spectral signature of serum and plasma-derived extracellular vesicles for cancer screening. Nanomedicine 2017, 13 (3), 835-841.
47. Carney, R. P.; Hazari, S.; Colquhoun, M.; Tran, D.; Hwang, B.; Mulligan, M. S.; Bryers, J. D.; Girda, E.; Leiserowitz, G. S.; Smith, Z. J.; Lam, K. S., Multispectral Optical Tweezers for Biochemical Fingerprinting of CD9-Positive Exosome Subpopulations. Anal Chem 2017, 89 (10), 5357-5363.
48. Smith, Z. J.; Lee, C.; Rojalin, T.; Carney, R. P.; Hazari, S.; Knudson, A.; Lam, K.; Saari, H.; Ibanez, E. L.; Viitala, T.; Laaksonen, T.; Yliperttula, M.; Wachsmann-Hogiu, S., Single exosome study reveals subpopulations distributed among cell lines with variability related to membrane content. J Extracell Vesicles 2015, 4, 28533.
49. Kruglik, S. G.; Royo, F.; Guigner, J. M.; Palomo, L.; Seksek, O.; Turpin, P. Y.; Tatischeff, I.; Falcon-Perez, J. M., Raman tweezers microspectroscopy of circa 100 nm extracellular vesicles. Nanoscale 2019, 11 (4), 1661-1679.
50. Penders, J.; Pence, I. J.; Horgan, C. C.; Bergholt, M. S.; Wood, C. S.; Najer, A.; Kauscher, U.; Nagelkerke, A.; Stevens, M. M., Single Particle Automated Raman Trapping Analysis. Nat Commun 2018, 9 (1), 4256.
51. Lee, W. Raman Spectroscopy for Extracellular Vesicle Study. Dissertation, University of Twente, Enschede, 2020.
52. Kosian, M.; Smulders, M. M.; Zuilhof, H., Structure and Long-Term Stability of Alkylphosphonic Acid Monolayers on SS316L Stainless Steel. Langmuir 2016, 32 (4), 1047-57.
53. Baggerman, J.; Smulders, M. M. J.; Zuilhof, H., Romantic Surfaces: A Systematic Overview of Stable, Biospecific, and Antifouling Zwitterionic Surfaces. Langmuir 2019, 35 (5), 1072-1084.
54. Zhang, P.; Zhou, X.; He, M.; Shang, Y.; Tetlow, A. L.; Godwin, A. K.; Zeng, Y., Ultrasensitive detection of circulating exosomes with a 3D-nanopatterned microfluidic chip. Nat Biomed Eng 2019, 3 (6), 438-451.
55. Boriachek, K.; Masud, M. K.; Palma, C.; Phan, H. P.; Yamauchi, Y.; Hossain, M. S. A.; Nguyen, N. T.; Salomon, C.; Shiddiky, M. J. A., Avoiding Pre-Isolation Step in Exosome Analysis: Direct Isolation and Sensitive Detection of Exosomes Using Gold-Loaded Nanoporous Ferric Oxide Nanozymes. Anal Chem 2019, 91 (6), 3827-3834.
56. Huang, R.; He, L.; Xia, Y.; Xu, H.; Liu, C.; Xie, H.; Wang, S.; Peng, L.; Liu, Y.; Liu, Y.; He, N.; Li, Z., A Sensitive Aptasensor Based on a Hemin/G-Quadruplex-Assisted Signal Amplification Strategy for Electrochemical Detection of Gastric Cancer Exosomes. Small 2019, 15 (19), e1900735.

57. Kooyman, R. P. H., Physics of surface plasmon resonance. In Handbook for surface plasmon resonance, Schasfoort, R. B. M.; Tudos, A. J., Eds. The Royal Society of Chemistry: Cambridge, UK, 2008; pp 15-34.
58. Ideta, K.; Arakawa, T., Surface plasmon resonance study for the detection of some chemical species. Sensors and Actuators B: Chemical 1993, 13 (1), 384-386.
59. van der Pol, E.; van Gemert, M. J.; Sturk, A.; Nieuwland, R.; van Leeuwen, T. G., Single vs. swarm detection of microparticles and exosomes by flow cytometry. J Thromb Haemost 2012, 10 (5), 919-30.
60. Brown, M.; Wittwer, C., Flow cytometry: Principles and clinical applications in hematology. Clinical Chemistry 2000, 46 (8B), 1221-1229.
61. Zhu, S.; Ma, L.; Wang, S.; Chen, C.; Zhang, W.; Yang, L.; Hang, W.; Nolan, J. P.; Wu, L.; Yan, X., Light-scattering detection below the level of single fluorescent molecules for high-resolution characterization of functional nanoparticles. ACS Nano 2014, 8 (10), 10998-1006.
62. van der Pol, E.; Sturk, A.; van Leeuwen, T.; Nieuwland, R.; Coumans, F.; group, I. S. V. W.; Mobarrez, F.; Arkesteijn, G.; Wauben, M.; Siljander, P. M., Standardization of extracellular vesicle measurements by flow cytometry through vesicle diameter approximation. Journal of Thrombosis and Haemostasis 2018, 16 (6), 1236-1245.
63. Coumans, F. A. W.; Brisson, A. R.; Buzas, E. I.; Dignat-George, F.; Drees, E. E. E.; El-Andaloussi, S.; Emanueli, C.; Gasecka, A.; Hendrix, A.; Hill, A. F.; Lacroix, R.; Lee, Y.; van Leeuwen, T. G.; Mackman, N.; Mager, I.; Nolan, J. P.; van der Pol, E.; Pegtel, D. M.; Sahoo, S.; Siljander, P. R. M.; Sturk, G.; de Wever, O.; Nieuwland, R., Methodological Guidelines to Study Extracellular Vesicles. Circulation Research 2017, 120 (10), 1632-1648.
64. Allard, W. J.; Matera, J.; Miller, M. C.; Repollet, M.; Connelly, M. C.; Rao, C.; Tibbe, A. G.; Uhr, J. W.; Terstappen, L. W., Tumor cells circulate in the peripheral blood of all major carcinomas but not in healthy subjects or patients with nonmalignant diseases. Clin Cancer Res 2004, 10 (20), 6897-904.
65. Zhu, L.; Wang, K.; Cui, J.; Liu, H.; Bu, X.; Ma, H.; Wang, W.; Gong, H.; Lausted, C.; Hood, L.; Yang, G.; Hu, Z., Label-free quantitative detection of tumor-derived exosomes through surface plasmon resonance imaging. Anal Chem 2014, 86 (17), 8857-64.
66. van der Pol, E.; Coumans, F.; Varga, Z.; Krumrey, M.; Nieuwland, R., Innovation in detection of microparticles and exosomes. J Thromb Haemost 2013, 11 Suppl 1, 36-45.
67. Rikkert, L. G.; van der Pol, E.; van Leeuwen, T. G.; Nieuwland, R.; Coumans, F. A. W., Centrifugation affects the purity of liquid biopsy-based tumor biomarkers. Cytometry A 2018, 93 (12), 1207-1212.
68. Agerbæk, M. Ø.; Bang-Christensen, S. R.; Yang, M.-H.; Clausen, T. M.; Pereira, M. A.; Sharma, S.; Ditlev, S. B.; Nielsen, M. A.; Choudhary, S.; Gustavsson, T.; Sorensen, P. H.; Meyer, T.; Propper, D.; Shamash, J.; Theander, T. G.; Aicher, A.; Daugaard, M.; Heeschen, C.; Salanti, A., The VAR2CSA malaria protein efficiently retrieves circulating tumor cells in an EpCAM-independent manner. Nature Communications 2018, 9 (1), 3279.
69. Sherman, M. Y.; Gabai, V. L., Hsp70 in cancer: back to the future. Oncogene 2015, 34 (32), 4153-61.
70. Boudesco, C.; Cause, S.; Jego, G.; Garrido, C., Hsp70: A Cancer Target Inside and Outside the Cell. Methods Mol Biol 2018, 1709, 371-396.

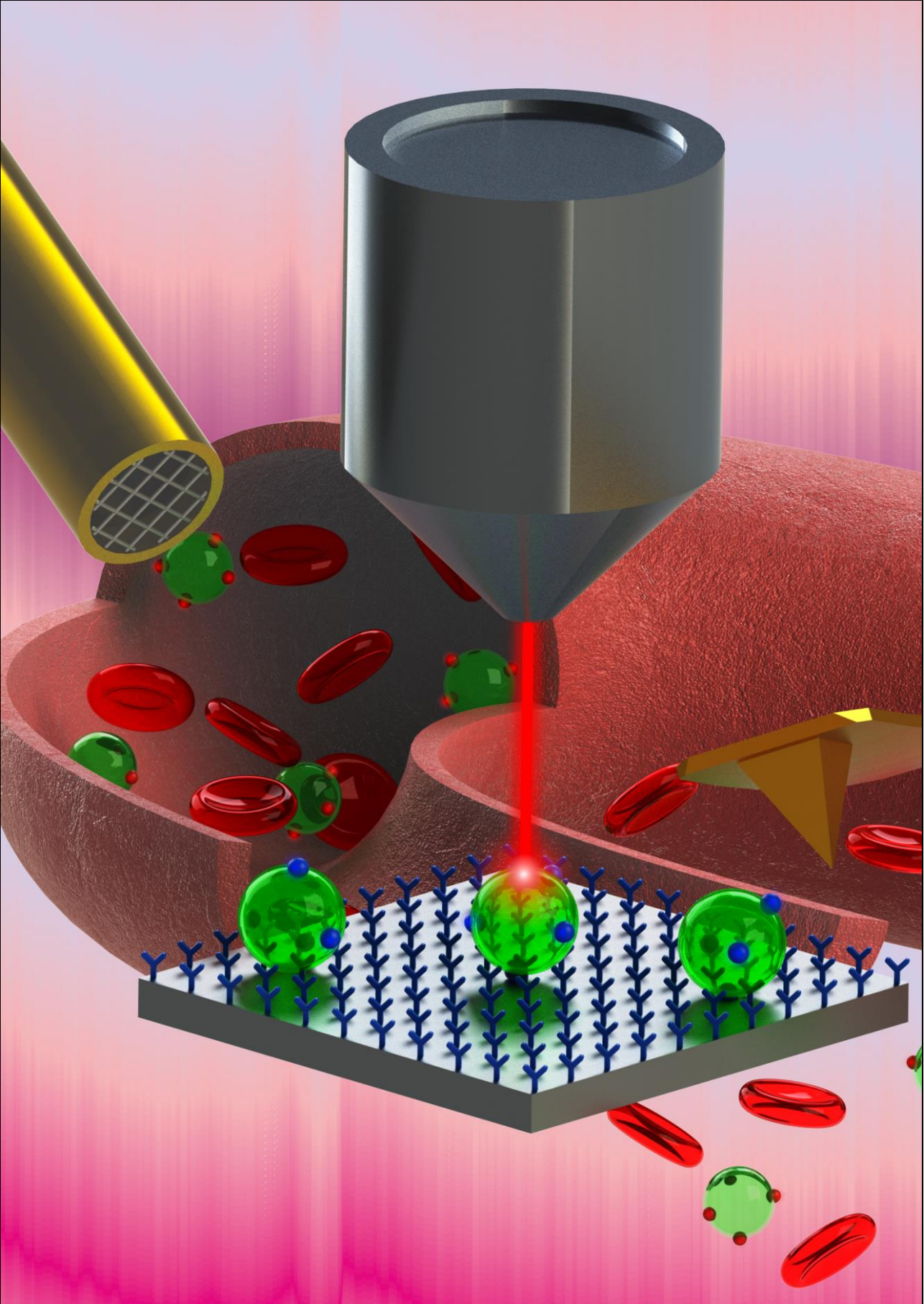

3

Immuno-capture of extracellular vesicles on stainless steel substrates for individual multi-modal characterization using AFM, SEM and Raman spectroscopy

This chapter was originally published as:

Pepijn Beekman, Agustin Enciso-Martinez, Hoon Suk Rho, Sidharam Pundlik Pujari, Aufried Lenferink, Han Zuilhof, Leon W.M.M. Terstappen, Cees Otto, Séverine Le Gac, *Immuno-capture of extracellular vesicles on stainless steel substrates for individual multi-modal characterization using AFM, SEM and Raman spectroscopy,* Lab on a Chip, 2019,**19**, 2526-2536.

3.1 Abstract

Tumor-derived extracellular vesicles (tdEVs) are promising blood biomarkers for cancer disease management. However, blood is a highly complex fluid that contains multiple objects in the same size range as tdEVs (30 nm – 1 µm), which confuses an unimpeded observation of tdEVs. Here, we report a multi-modal analysis platform for the specific capture of tdEVs on antibody-functionalized stainless steel substrates, followed by their analysis using SEM, Raman spectroscopy and AFM, at the single EV level in terms of size and size distribution, and chemical fingerprint. After covalent attachment of anti-EpCAM (Epithelial Cell Adhesion Molecule) antibodies on stainless steel substrates, EV samples derived from a prostate cancer cell line (LnCAP) were flushed into a microfluidic device, assembled with this stainless steel substrate for capture. To track the captured objects between the different analytical instruments and subsequent correlative analysis, navigation markers were fabricated onto the substrate from a cyanoacrylate glue. Specific capture of tdEVs on the antibody-functionalized surface was demonstrated using SEM, AFM and Raman imaging, with excellent correlation between the data acquired by the individual techniques. The particle distribution was visualized with SEM. Furthermore, a characteristic lipid-protein band at 2850-2950 cm^{-1} was observed with Raman spectroscopy, and with AFM the size distribution and surface density of the captured EVs was assessed. Finally, correlation of SEM and Raman images enabled to discriminate tdEVs from cyanoacrylate glue particles, highlighting the capability of this multi-modal analysis platform for distinguishing tdEVs from contamination. The trans-instrumental compatibility of the stainless steel substrate and the possibility to spatially correlate the images of the different modalities with the help of the navigation markers opens new avenues to a wide spectrum of combinations of different analytical and imaging techniques for the study of more complex EV samples.

3.2 Introduction

Liquid biopsies have been proposed as an alternative to conventional approaches (*e.g.*, magnetic resonance imaging or solid biopsies) for the disease management of cancer patients. In this non-invasive approach, a blood sample (7.5 ml) is analyzed for the presence and amount of circulating tumor cells (CTCs), tumor-derived EVs (tdEVs), cell free DNA (cf-DNA), miRNA and/or tumor-associated proteins or peptides.[1,2] CTCs are well suited to characterize a tumor and to evaluate the heterogeneity for subsequent selection of the optimal treatment.[3] The concentration of CTCs is however extremely low ($\backsim$1 CTC mL^{-1}), especially when compared with that of blood cells ($\backsim$10^{9} mL^{-1}).[4] In contrast, tdEVs are much more abundant with concentrations up to 10^{10} tdEVs mL^{-1}.[5] Importantly, the presence and amount of tdEVs in blood has been proven to strongly correlate with the survival of patients with metastatic prostate cancer.[6] EVs are membrane-bound biological carriers of biomolecules, which are shed by all cell types. They are found in all body fluids,[7] and exhibit a size ranging from 30 nm to 1 µm.[8,9] EVs are of great interest because of their implication in intercellular communication and pathogenesis;[7,10,11] they show great promises not only for disease diagnosis but also for drug delivery.[4,11–13] Altogether, EV analysis offers a promising approach for non-invasive cancer patient management as a result of the wealth of biological information they carry, some of which being potential biomarkers.[14].

However, blood is a highly complex fluid[15] that contains lipoproteins, cell debris and protein aggregates, as well as EVs of non-cancerous origin, which are all in the same size and density range as tdEVs, and the same applies for less complex samples originating from cell culture media. In all these cases, tdEVs need to be selectively isolated and/or distinguished from EVs of non-cancerous origin and other small objects.[16,17] Several methods have been proposed for EV isolation, among which ultracentrifugation and size-exclusion chromatography are the most popular.[8,16,18–20] However, these isolation approaches yield highly heterogeneous samples containing tdEVs, other EVs, cell debris and molecular aggregates. Therefore, alternative approaches have been introduced that rely

on the immuno-capture of targeted EVs, using either generic membrane markers (*e.g.,* CD9, CD63 and CD81) to retrieve all exosomes/EVs from a sample,[21,22] or specific membrane markers (*e.g.*, EpCAM,[6] EGFR,[12] HER2[23]) to selectively isolate tdEVs. Microfluidic technology has proven to be instrumental for the immunocapture of EVs by controlling the surface dynamics (*e.g.*, controlling flow rate when washing non-specifically bound species), and drastically reducing the distances over which EVs have to migrate before coming in contact with the functionalized surface. In addition, microfluidics facilitates controlled and sequential handling of (very small) samples.[8,24]

A second main challenge is the high heterogeneity found in any purified EV sample, in terms of size and from a molecular perspective. Therefore, EVs must be thoroughly characterized for their possible and reliable recognition in heterogeneous samples. For that purpose, it is important to study individual EVs and not populations to avoid that ensemble averaging obscures differences. EVs have been analyzed using a great variety of techniques[25–28] such as flow cytometry,[29–31] confocal and non-confocal (fluorescence) microscopy,[22,32] scanning electron microscopy (SEM),[33] atomic force microscopy (AFM),[34] Raman spectroscopy,[35] surface plasmon resonance (SPR),[36,37] mass spectrometry (MS)[38] and µNMR.[39] However, not all techniques allow the collection of information at the single EV level. Furthermore, to get comprehensive information on heterogeneous samples, different techniques yielding complementary information must be combined. In that context, Raman Spectroscopy, SEM and AFM are of great interest. Raman spectroscopy provides chemical information on a sample of interest in a label-free manner.[40,41] SEM enables characterization of the size and morphology of intact EVs.[42,43] Correlating this size and morphology information with Raman fingerprints confirms the cellular origin of individual EVs, and, in previous work, we have demonstrated that using this combination[23] cancer cells could be distinguished from non-cancer cells.[44,45] Finally, AFM yields more detailed information on the size and morphology of EVs, and possibly, on their mechanical properties.[30,46]

In this chapter, we report the specific isolation of tdEVs obtained from prostate cancer cell lines on functionalized stainless-steel substrates followed by their *in*

situ multi-modal characterization with SEM, Raman and AFM imaging (Figure 3.1). Stainless steel substrates were selected for their suitability for all considered modalities: this material gives little background in Raman (See Appendix A.1);[44,45] it is conductive; and mirror-polished stainless steel substrates have a low surface roughness level of *ca.* 7 nm, which is well-suited for the analysis of EVs by AFM. Here, and as depicted in Figure 3.2, stainless steel substrates were first functionalized with a monolayer of carboxydecyl phosphonic acid (CDPA),[47–49] onto which antibodies targeting tdEVs were covalently anchored through carbodiimide-based bioconjugation chemistry.[50] The resulting monolayers were characterized with X-ray photoelectron spectroscopy (XPS) and infrared reflection-absorption spectroscopy (IRRAS), to optimize their formation with respect to the initial CDPA concentration. Next, EVs derived from human prostate cancer cell lines (LNCaP) were injected in a microfluidic channel assembled onto the functionalized stainless steel substrate, for their capture, which was confirmed using individual imaging techniques. For their multi-modal analysis, and to easily track individual EVs in the different

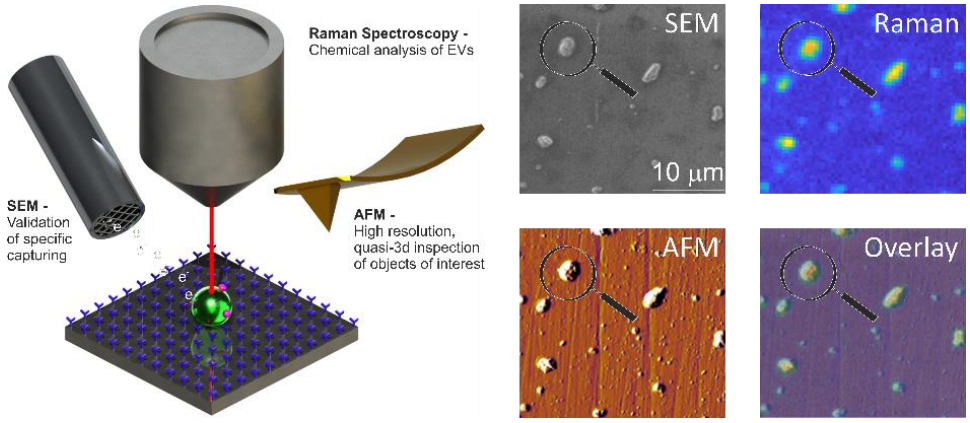

Figure 3.1. Multi-modal analysis of tdEVs on antibody-functionalized stainless steel substrates. *After their selective capture on a stainless-steel surface functionalized with antibodies of interest (here Anti-EpCAM antibodies targeting tdEVs), EVs are successively imaged using Raman spectroscopy, SEM and AFM, and information collected from these different imaging modalities correlated to get a comprehensive picture on the captured objects.*

instruments, navigation markers were fabricated on the functionalized substrates next to a region of interest (ROI). Finally, the captured EVs were successively analyzed by Raman imaging, SEM, and AFM, and data acquired by the different techniques correlated. The trans-instrumental compatibility of the stainless steel substrate and the tracking possibility offered by the navigation markers opens gives the opportunity to apply a wide spectrum of combinations of different analytical and imaging techniques.

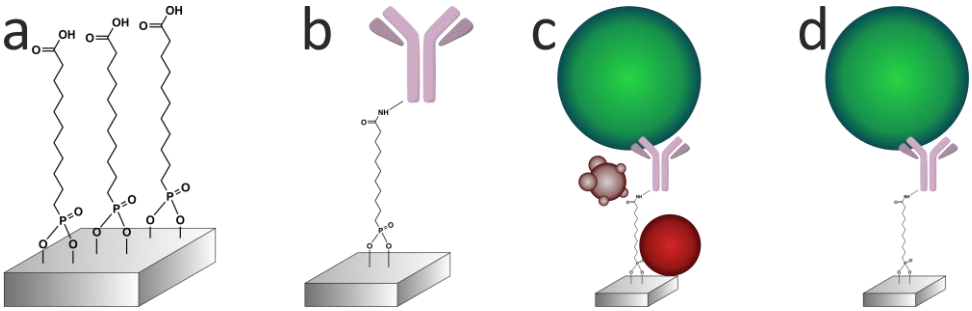

Figure 3.2. Different steps of surface modification and capture of the tdEVs on stainless steel substrates. *a) An oxygen plasma-treated stainless steel substrates is functionalized with a carboxydecyl phosphonic acid (CDPA) monolayer. b) Anti-EpCAM antibodies are conjugated to the CDPA monolayer using NHS/carbodiimide chemistry. c) tdEVs (in green here) are specifically immuno-captured on the antibody-functionalized surface. d) The substrate is washed to remove non-specifically bound materials (in red and purple here), before retained EVs are fixed and dehydrated.*

3.3 Experimental

3.3.1 Materials

1-Ethyl-3-(3-dimethylaminopropyl)carbodiimide (EDC), N-hydroxysuccinimide (NHS), acetone (VLSI grade), paraformaldehyde (PFA), phosphate-buffered saline (PBS), and 2-(N-morpholino)ethanesulfonic acid were purchased from Merck (Zwijndrecht, The Netherlands). Ethanol (VLSI grade) and dichloromethane were purchased from VWR (Amsterdam, The Netherlands).

Carboxydecyl phosphonic acid (CDPA) was purchased from Sikémia (Montpellier, France). Sylgard 184 poly(dimethylsiloxane) (PDMS) was purchased from Farnell (Utrecht, The Netherlands). SS316L Stainless steel foils (0.9 mm thickness, one side mirror polished) were purchased from Goodfellow Inc. (Bad Nauheim, Germany). Anti-EpCAM antibodies were produced at the University of Twente, The Netherlands (Medical Cell BioPhysics Laboratory) from VU1D9 hybridoma cells.

3.3.2 PDMS handling devices

Three different PDMS devices (a 6-mm diameter reservoir, a xurography channel and a navigation marker device) were used for different steps of the sample preparation, as depicted in Figure 3.3. For all devices, PDMS was prepared and cured according to the same procedure. PDMS precursor and cross linker (10:1 weight ratio) were first thoroughly mixed, and subsequently degassed by centrifugation at 1000x g for 1 min. The resulting mixture was poured on different molds for the different devices, and degassed again in a desiccator for 15 min. Curing was performed at 80°C overnight.

3.3.2.1 PDMS Reservoir

A large 6-mm diameter PDMS reservoir was used for the antibody immobilization onto CDPA-functionalized stainless steel substrates. To this end, a 5-mm height PDMS layer was prepared in a petri dish. This PDMS layer was cut in 1 x 1 cm^2 pieces, in which a hole was punched with a Harris Uni-Core 6-mm biopsy punch (VWR International B.V., Amsterdam, The Netherlands).

3.3.2.2 Xurography channel

To capture EVs and their subsequent washing and fixation, a xurography microchannel was used. The mold for this device was produced using a desktop plotter (Silhouette Cameo 2, Silhouette, Wateringen), as follows. First, a 6 mm x 3 mm feature was cut out of a foil laminated with a 200-µm thick adhesive layer, and subsequently placed at the bottom of a clean petri dish. The foil was removed to only leave the adhesive layer. After PDMS curing in this mold, inlets

and outlets were punched using a 1-mm diameter Harris Uni-Core biopsy punch. The resulting device was placed on top of a stainless steel substrate after removal of the previously used PDMS reservoir.

3.3.2.3 Navigation marker device

For the multi-modal analysis, and after dehydration of the captured EVs (see section "Vesicle capture and dehydration"), navigation markers were fabricated on the stainless steel substrates for easy tracking of the captured EVs, using a microfluidic device comprising 3 microchannels: two microchannels featuring navigation markers (Figure 3) and flanking one sample channel. All channels were 30 µm height x 50 µm width x 1 mm length. The distance between the navigation markers and the sample region (80 µm, center-to-center) was chosen to be compatible with the characteristic dimension of the field of view of the bright-field optical objectives in all instruments used in this work (*i.e.*, ∽200 µm for the Raman system, 500 µm for the AFM instrument and freely variable in the SEM, see Appendix A.2). The design of this microfluidic device was drawn in CleWin (WieWeb, Hengelo, The Netherlands), and the mold fabricated in the Nanolab cleanroom of the MESA+ Institute for Nanotechnology. Briefly, a <100> Si wafer was spin-coated with AZ-40XT resist (Microchemicals, Ulm, Germany) at 3000 RPM for 1 min to yield a 30-µm thick layer. The photoresist was exposed, baked and developed according to the manufacturer's specifications. After PDMS casting on the finished mold, fluidic accesses were punched using a 1-mm diameter Harris Uni-Core biopsy punch. The PDMS device was placed on top of a functionalized stainless steel substrate after EV capture and dehydration. No specific care was required for alignment of the device, since the width of the sample region is much smaller than that of the xurography channel. Cyanoacrylate superglue (Tesa SE, Norderstedt, Germany) was injected in the side channels and cured for 30 min to create the navigation markers. After PDMS delamination, the designed micro-features were transferred to the stainless steel surface with high fidelity (Figure 3.3, *bottom left*).

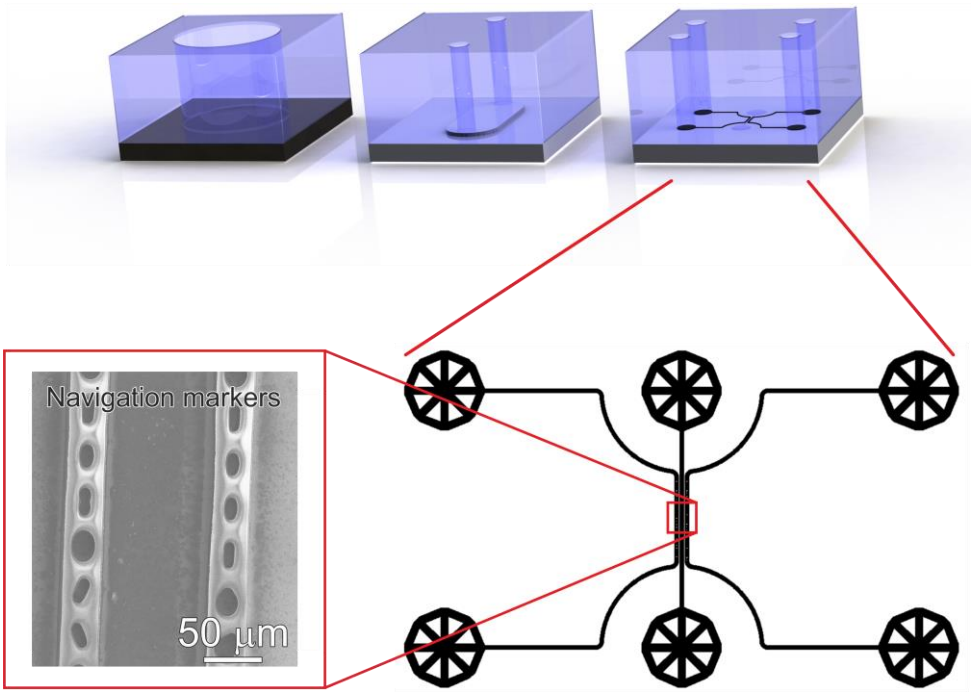

Figure 3.3. Various PDMS devices used in this work. *Top, and from left to right: 6-mm diameter reservoir used for the immobilization of antibodies under static conditions on a CDPA monolayer; xurography microchannel (6 x 3 x 0.2 mm3) used for the capture of EVs and subsequent washing under mild flow conditions (400 µl.min-1); microfluidic device used for the fabrication of navigation markers next to a 50 µm x 1 mm sample region, subsequently considered for analysis using SEM, Raman and AFM. Bottom, right: Design of the microfluidic device used to fabricate the navigation markers, consisting of three microfluidic channels, two microchannels comprising pillars with various geometries, flanking one sample microchannel, all channels being 30 µm height x 50 µm width x 1 mm length, and (Left) actual SEM image showing the navigation markers fabricated from cyanoacrylate glue injected in the side-channels and used to retrace the captured objects in the different imaging instruments.*

3.3.3 CDPA monolayer formation and characterization on stainless steel substrates

3.3.3.1 CDPA monolayer formation

Stainless steel substrates were laser-cut into 1 cm x 1 cm substrates and cleaned in an ultrasonic bath in ethanol, acetone and dichloromethane (7 min for each solvent), followed by an oxygen plasma treatment for 3 min in a Diener Pico (Diener electronic, Bielefeld, Germany) at 250 W. Immediately after plasma treatment, the substrates were transferred to a solution of CDPA in ethanol for overnight incubation at 60°C to form a CDPA monolayer (Figure 3.2a). Three CDPA concentrations were initially tested (0.1, 1 and 10 mM) to identify the optimal concentration. The resulting CDPA monolayer was subsequently cured in a vacuum oven at 130°C for 1 h and finally washed in an ultrasonic bath in ethanol, acetone and dichloromethane (7 min for each solvent).

3.3.3.2 Infrared Reflection/Absorption Spectroscopy (IRRAS)

IRRAS measurements were performed on a Bruker Tensor 27 using a Harrick Auto Seagull™ (Bruker Nederland B.V.). 2000 scans per measurement were recorded under an angle of incidence of 83° using a liquid nitrogen-cooled MCT (mercury-cadmium-telluride) detector. Measurements were taken in triplicates after 35 min of purging with argon to remove moisture and carbon dioxide. Data were averaged and normalized with respect to a reference (O_2 plasma-cleaned stainless steel) to yield relative absorption values.

3.3.3.3 X-ray Photoelectron Spectroscopy (XPS)

XPS measurements were conducted on a JPS-9200 (JEOL, Japan) under ultra-high vacuum conditions with analyser pass energy of 10 eV using monochromatic Al Kα X-ray radiation at 12 kV and 20 mA at an angle of incidence of 80°. Wide scans (0-800 eV) were recorded as well as narrow scans in the 280-300 eV region to more closely inspect the carbon binding energies.

3.3.4 Antibody conjugation onto the CDPA monolayer

VU1D9 (anti-EpCAM) antibodies were conjugated onto the CDPA monolayer using EDC/NHS chemistry (EDC = 1-ethyl-3-(3-

dimethylaminopropyl)carbodiimide, NHS = N-hydroxysuccinimide) at room temperature (Figure 3.2b). In the PDMS reservoir, a solution of 40 mM NHS, 130 mM EDC and 50 mM 2-(N-morpholino)ethanesulfonic acid in Milli-Q (pH 5) was pipetted and left to react with the CDPA monolayer for 30 min. The substrate was subsequently rinsed with 50 µl of a 5 mM acetic acid solution in Milli-Q to stop the reaction, followed by 100 µl PBS. Next, the antibody solution at 20 µg/mL in PBS was pipetted in the reservoir and incubated with the surface for 1 h, followed by extensive washing with PBS to remove unreacted chemicals. Finally, unreacted NHS ester groups were blocked by a 0.1 M ethanolamine solution in Milli-Q for 30 min. The reservoirs were filled with PBS buffer until their use within 24 h.

3.3.5 Vesicle capture and dehydration

EVs were isolated from culture medium (see Appendix A.3 for the isolation protocol) of the human prostate cancer cell line LNCaP, which is known to express epithelial cell adhesion molecules (EpCAM). To avoid any EV contamination from the serum added to the culture medium, the LNCaP cells were cultured in serum-free medium for 48 h before their isolation. Nanoparticle tracking analysis (NTA)[51] of those isolated EVs revealed a concentration of 1.06 x 10^9 EVs ml^{-1} (See Appendix A.4). 25 µl of this EV-containing suspension was introduced into the xurography channel (channel volume: 3.6 µl) using a capillary pipette tip acting as an inlet reservoir, and left under static incubation for 1 h at room temperature. Channels were subsequently washed with 200 µl of PBS at a flow-rate of 400 µl min^{-1} using a syringe-pump connected to the outlet reservoir and operated in withdrawal mode (Fig. 2d). Captured EVs were next fixed in the channel with a 1% PFA solution in PBS. After fixation of the EVs, the PDMS device was removed, the sample rinsed in Milli-Q, dehydrated by immersion in a solution of 70% ethanol in Milli-Q (5 min) followed by immersion in pure ethanol (5 min), and finally dried overnight under ambient conditions. Various negative control experiments were conducted in this study, as summarized in Table Appendix A.5: (i) no activation of the CDPA layer with EDC/NHS; (ii) no immobilization of anti-EpCAM antibodies; and (iii) no incubation with any EV sample.

3.3.6 Multi-modal analysis of the captured EVs on anti-EpCAM-conjugated stainless steel substrates

3.3.6.1 SEM measurements

SEM imaging was performed using a JEOL JSM-6610LA Analytical SEM (JEOL, Nieuw-Vennep, The Netherlands). The SEM was operated in high-vacuum mode, and images were recorded with secondary electron (SE) detection with a low acceleration voltage of 2 kV to avoid sample charging in the absence of conductive coatings.

3.3.6.2 Raman measurements

Hyperspectral Raman micro-spectroscopy was performed by 2D point scanning of a laser beam (λ = 647.09 nm) from a Coherent Innova 70C laser. The Raman scattered light was dispersed in a spectrometer and collected with a CCD sensor (Andor Newton DU-970-BV). The wavenumber interval per pixel is $\backsim$2.3 cm^{-1} on average over the length of the sensor. The laser power was measured underneath the objective (40x, NA: 0.95) and adjusted to 10 mW. The laser focal spot (d$\backsim$0.39 µm, h$\backsim$1.2 µm) was focused on the substrate and a 30 µm x 30 µm ROI was scanned with a step size of 0.47 µm and an illumination time of 250 ms per pixel. Using MATLAB 2017b (Mathworks, Eindhoven, The Netherlands), after wavenumber and intensity calibration, the data were pre-treated by cosmic ray removal and noise reduction by singular value decomposition, maintaining five singular components. Raman spectra were acquired across the entire wavenumber range (0 – 3660 cm^{-1}). Multivariate analysis by means of principal component analysis (PCA) was performed in the high frequency spectral region between 2700 to 3200 cm^{-1}. PCA was used to extract the most relevant information from the data matrix and to represent it as a linear combination of orthogonal principal components (PC or loadings) with coefficients (scores) for the contribution of the variance to the data.[52] For each loading, a single score value was assigned to each measured pixel in the ROI and a Raman image reconstructed based on the scores. A high score value for a certain loading means a high contribution of that loading to the corresponding pixel.

3.3.6.3 AFM measurements

AFM measurements were performed on an Asylum MFP-3D instrument (Asylum Research, Santa Barbara, USA) in AC air topography mode (*i.e.*, tapping mode) with a scan rate of 0.1 Hz and a set point of 400 mV. An Olympus micro cantilever with a nominal spring constant of 2 N m^{-1} was used (resonant frequency ∽70 kHz). The resulting graphs were processed with Gwyddion 2.5.1 SPM analysis software (www.gwyddion.net). A mean plane subtraction and 3rd order polynomial background removal was applied. For object analysis, a 25.0 ± 0.2 nm height threshold was applied to the data and circles were fitted to the remaining islands. A list of radii was exported to MATLAB 2016a (Mathworks, Eindhoven, The Netherlands) for analysis and plotting of a size distribution histogram.

3.4 Results and discussion

3.4.7 Monolayer formation and characterization

To optimize the monolayer formation, different concentrations of carboxydecyl phosphonic acid (CDPA) were tested and the resulting CDPA monolayers analyzed using infrared reflection-absorption spectroscopy (IRRAS) to evaluate the surface coverage, molecular ordering, and the configurations of the carboxyl groups. Spectra recorded for stainless steel substrates functionalized with CDPA (1 mM solution), as well as for CDPA powder, are presented in Figure 3.4a. Bands assigned to the anti-symmetric CH_2 stretch were found around 2914 cm^{-1} for all tested CDPA concentrations (see Appendix A.6). These anti-symmetric CH_2 stretch bands are typically found between 2914 and 2930 cm^{-1}, and their exact values reflect the packing density of the monolayer. Low values, as observed here, suggest densely packed monolayers displaying a short-range inter-chain monolayer ordering.[47,48,53–56] In all samples, the carboxyl band was detected at ~ 1720 cm^{-1}, which is attributed to acyclically dimerized carboxyl groups,[57] *i.e.*, hydrogen-bonding dimerization with nearest neighbors. Higher absorption frequencies for this band (towards 1740 cm^{-1}) indicate non-hydrogen-bonded species, and therefore a less dense monolayer. Lower frequencies (∽1700 cm^{-1})

would suggest cyclic dimerization as a result of multilayer formation. In the 1700-1740 cm^{-1} region, peak broadening was observed in the substrates functionalized with 0.1 and 10 mM solutions (see Appendix A.7), indicating a lesser degree of ordering than for the substrates prepared with a 1 mM solution. The baseline across the relative samples revealed that the signal-to-noise ratio for the substrate prepared with a 1 mM solution was also significantly improved compared to the other samples. Therefore, on the basis of these results, further experiments were conducted using a 1 mM CDPA solution for the 1^{st}-step functionalization of the stainless steel substrates.

After each surface modification step (oxygen plasma treatment, CDPA functionalization, antibody modification), the substrates were also analyzed using XPS (Figure 3.4b). Integration of the peak surface areas provides quantitative information about the proportion of elements found on the substrate. After O_2 plasma (black line, Fig. 4b), relatively little carbon (C 1s signal at $\backsim$285 eV) was found on the stainless steel substrates, and this corresponds to adventitiously adsorbed carbon. A significant oxygen peak (O 1s peak at 532 eV) was detected as a result of the plasma treatment. Finally, various metals were present, such as Fe 2p (710 eV) and Cr 2p (575 eV). After formation of the CDPA monolayer, the signal corresponding to carbon became more intense, and a peak appeared at 134 eV, corresponding to P 2p. Integration of these two peaks reveals a C:P ratio of 11.2 : 1, which is in excellent agreement with the theoretically expected 11 : 1 ratio according to the molecular formula of CDPA (Fig. 4c). Carbon atoms experiencing different electronic environments are characterized by different binding energies, and CDPA molecules comprise carbon atoms in three distinct environments, as depicted in Figure 3.4c. The C atom in the carbonyl group is observed at $\backsim$289 eV; the phosphorous-bound carbon at $\backsim$286.2 eV; and the alkyl chain carbon atoms at 285 eV. Integrating these different C 1s signals yields a ratio of $\backsim$8.8 : 1.1 : 1, which is again in good agreement with the molecular structure of CDPA (9 : 1 : 1).

After formation of the monolayer (red line, Fig. 4b), signals originating from the metal elements decreased by a factor of $\backsim$1.5, indicating successful coverage of the surface by the CDPA monolayer. Using these XPS data, the monolayer

thickness can be derived, together with the tilt angle of the CDPA molecules on the surface. The thickness (t) of the CDPA layer was calculated using $t = -\lambda \times \sin\theta \times \ln\left(\frac{Fe_{CDPA}}{Fe_0}\right)$,[58,59] with λ being the attenuation length estimated for Fe 2p (1.4 nm), ϑ = 80°, and Fe_o and Fe_{CDPA} the signal intensities (counts s^{-1}) for Fe 2p before and after grafting of the CDPA monolayer, respectively. A CDPA monolayer thickness of 1.2 ± 0.1 nm was found. Considering a molecular length of 1.30 nm for CDPA as determined by Chem3D (PerkinElmer Informatics, Inc.), this monolayer thickness corresponds to a tilt angle of 20 ± 10°, which supports the IRRAS data that suggested the formation of a densely packed and ordered monolayer.

Finally, after antibody conjugation (Fig. 4b, blue line), an N 1s signal appeared at 400 eV. The metal signal was further attenuated, which can be accounted for by the formation of a thicker layer on the substrates due to the size of the antibody molecules, which is in the same order of magnitude as the probing depth of the technique, *i.e.*, ∽10 nm.

3.4.8 Capture of LNCaP-derived EVs on antibody-conjugated stainless steel substrates and uncorrelated analysis

The antibody-conjugated surfaces were incubated with an EpCAM-positive tdEV sample prepared from LNCaP culture medium, and subsequently imaged with SEM to demonstrate their ability to immuno-capture tdEVs. As shown in Figure 3.5a, tdEVs were successfully and specifically captured on the antibody-conjugated stainless steel surfaces, onto which quasi-spherical objects in the 100 nm – 1 µm size range were identified. In contrast, in negative controls, for which one step of surface functionalization was omitted or which were not exposed to tdEV sample (see Appendix A.5 and A.7), nothing was captured in the surface (Figure 3.5a). Collectively, this experiment demonstrates the ability of our antibody-functionalized stainless steel substrates to successfully capture tdEVs.

As a next step, the same substrates, after capture of the tdEVs, were analyzed using Raman spectroscopy and AFM imaging. Hyperspectral Raman images were acquired on 30 µm x 30 µm ROIs (64 x 64 pixels), and analyzed using PCA in the

spectral region between 2700 to 3200 cm^{-1} that contains the most intense peaks. EVs were identified as regions with pixels of high intensity values in certain scores. Such pixels were next segmented and used not only as a mask to identify the locations corresponding to EVs in all the images, as depicted in the inset of Figure 3.5b, but also to compute a mean Raman spectrum for EVs, as presented in Figure 3.5b. This spectrum comprises a characteristic lipid-protein band at 2850 – 2950 cm^{-1}, and a clear peak at 2851 cm^{-1} that corresponds to the CH_2 symmetric stretch of lipids.[60]

Finally, AFM images were used for quantitative analysis of the captured EVs. In five considered areas of 50 µm x 50 µm, a total of 5.4 x 10^3 tdEVs were detected, which corresponds to a surface density of 4.3 x 10^5 tdEVs.mm^{-2}. These objects presented a size range of 54 to 3840 nm and an average diameter of 101 ± 111 nm, and Figure 3.5c shows the particle distribution up to 0.7 µm, since most of the particles were found in the 0-0.7 µm range. Noteworthy, the particle size distribution and average size as determined by AFM were overall in good agreement with data obtained using Nanoparticle Tracking Analysis (NTA), with yet a slight shift in the size distribution *i.e.*, 167 ± 91 nm (See Appendix A.4 and Figure 3.5c, *blue line*). The difference observed can be accounted for by the lower detection limit of the latter technique, or by shrinking of the EVs due to dehydration.[51,61]

3.4.9 Multi-modal analysis using SEM, Raman and AFM imaging

Finally, tdEVs captured on functionalized stainless steel substrates were analyzed successively using SEM, Raman and AFM imaging for their multi-modal characterization, and this last series of analysis was performed after fabrication of navigation markers on the stainless steel substrates. To identify interesting ROIs, the samples were first analyzed with SEM at a low resolution. It should be noted that for this first step of SEM imaging, the ROIs were not extensively exposed to the electron beam to avoid electron beam-induced deposition (EBID) of amorphous carbon,[62] which would hinder later analysis by Ramanspectroscopy. Next, the distance between the measured location and the nearest set of markers was noted so as to find back the same region in the different imaging techniques. Following this, the same ROIs on the surface were

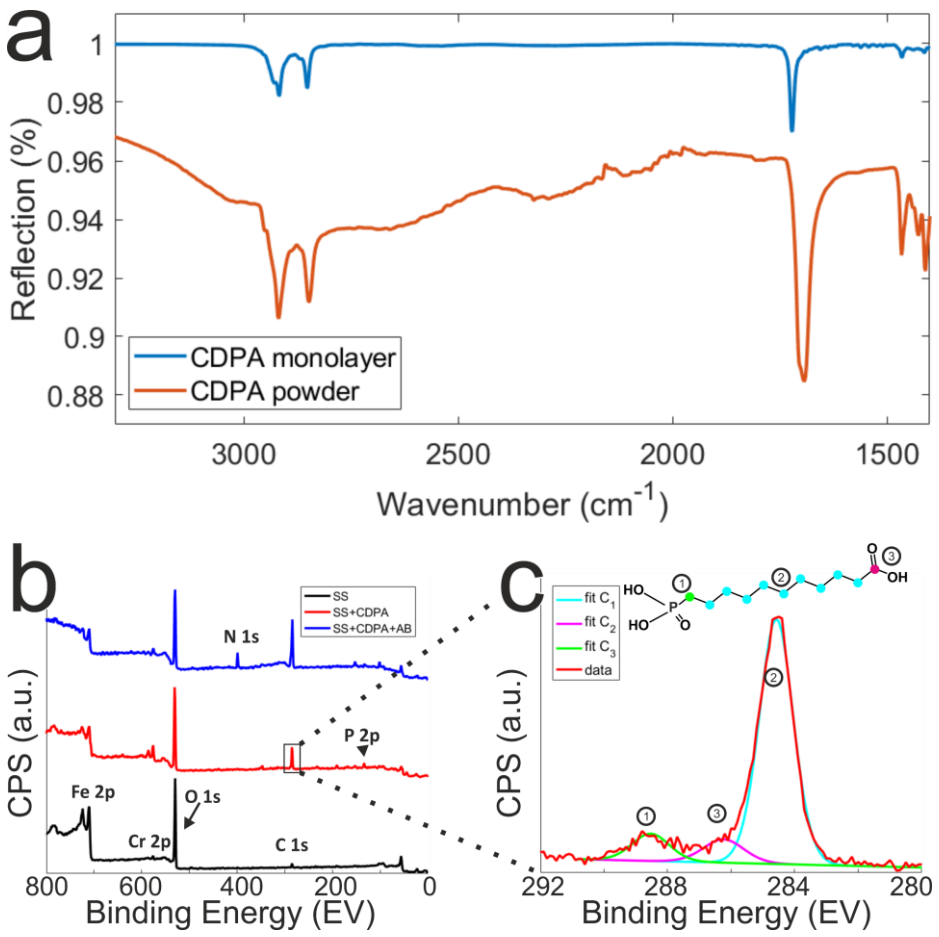

Figure 3.4. Chemical characterization of the stainless steel surfaces after the different surface modification steps. *a) IR reflection-absorption (IRRAS) spectra (which are background corrected) of CDPA monolayers prepared on SS316L stainless steel substrates using a 1 mM CDPA solution (blue trace) and CDPA powder (red trace). b) XPS spectra recorded after the various surface modification steps, as depicted in Figure 3.2. Wide range scans acquired on a O2 plasma-treated stainless steel substrate (SS, black trace), a stainless steel substrate functionalized with a CDPA monolayer (SS+CDPA, red trace); and after antibody conjugation on the CDPA monolayer (SS+CDPA+AB, blue trace). c) C 1s narrow scan showing fitted peaks corresponding to the different carbon species found in a CDPA molecule (inset).*

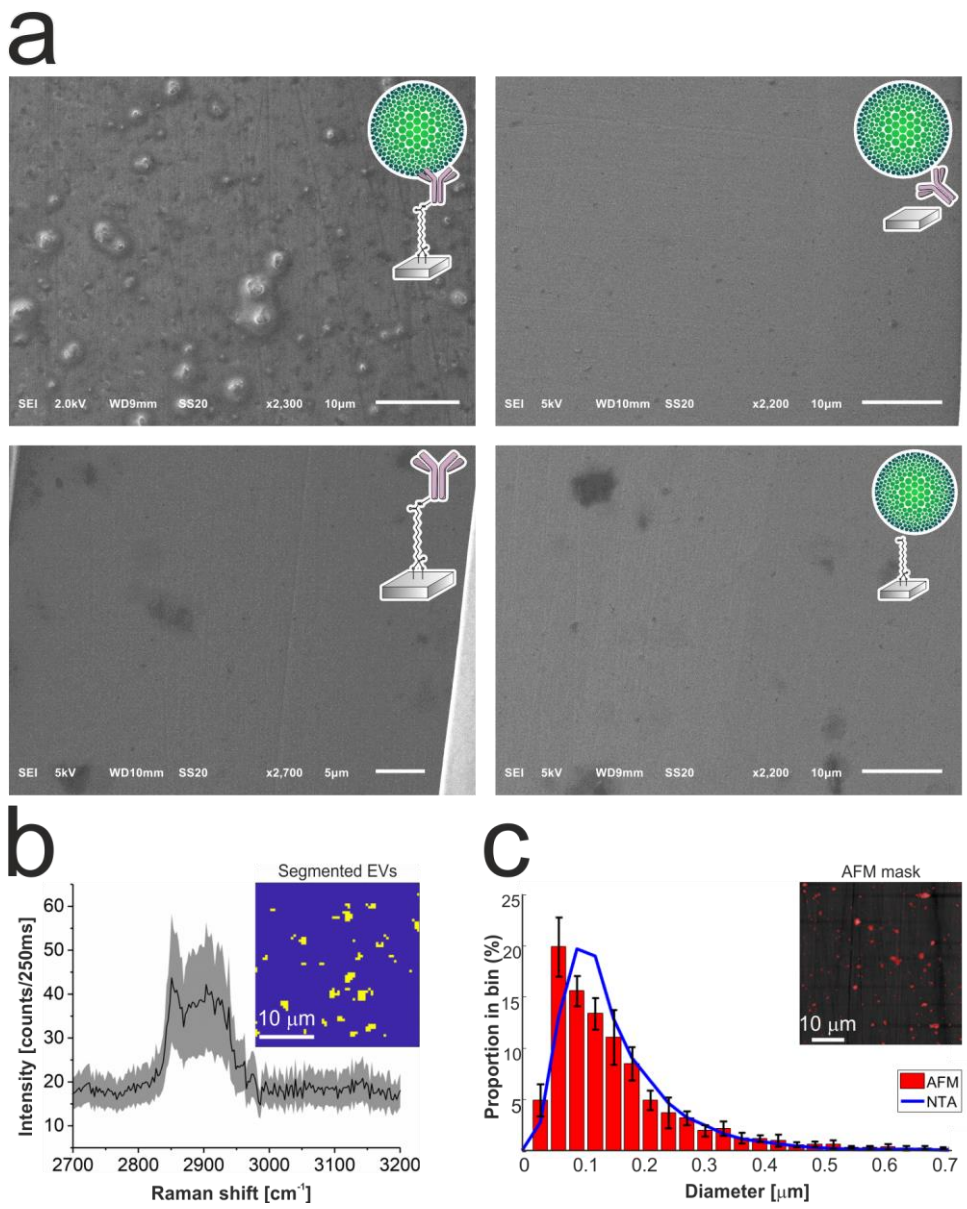
a
SEI 2.0kV WD9mm SS20 x2,300 10µm
SEI 5kV WD10mm SS20 x2,200 10µm
SEI 5kV WD10mm SS20 x2,700 5µm
SEI 5kV WD9mm SS20 x2,200 10µm
b
Segmented EVs
10 µm
Intensity [counts/250ms]
Raman shift [cm-1]
c
AFM mask
10 µm
AFM
NTA
Proportion in bin (%)
Diameter [µm]

Figure 3.5. Analysis of the tdEVs captured on anti-EpCAM functionalized stainless steel substrates. *a) SEM imaging revealing the specific capture of tdEVs (obtained from LNCaP cells) on anti-EpCAM functionalized stainless steel substrates (top left), while no object was captured on negative control samples (top right; without carbodiimide/NHS activation; bottom left; without functionalization with anti-EpCAM antibodies; and bottom right, without exposure to tdEV samples). b) Mean Raman spectrum (black line) and standard deviation (shaded area) of all EVs segmented from the ROI presented in the inset (30 µm x 30 µm and 64 x 64 pixels). The Raman spectrum (Raman shift range 2700-3200 cm-1) shows a lipid-protein band (2850-2950 cm-1) with a characteristic peak at 2851 cm-1, which corresponds to the CH2 symmetric stretch of lipids. In the inset, yellow pixels correspond to EVs and blue to the background. c) Size distribution of the surface-immobilized LNCaP-derived EVs determined by AFM (red histogram), and of the same sample in suspension before its immobilization on the surface as determined by NTA (blue line). Histogram: bin width 30 nm, error bars corresponding to the standard deviation (n=5). Inset: mask used for counting EVs on the AFM image, showing all objects detected with a height greater than 25 nm.*

successively imaged using hyperspectral Raman spectroscopy and SEM to characterize the EV size and morphology. Similarly, and with the help of the navigation markers, the ROIs were traced back and imaged with AFM. A key element in this multi-modal analytical process is the presence of navigation markers: due to their varying pitch, size and shape, each location in the sample region, as defined by the microchannel in the last PDMS device, can be matched to a unique combination of markers to assign spatial reference points to a ROI. This reference enables to retrieve objects of interest after transferring the stainless steel substrates between different instruments. Figure 3.6 presents the images of this multi-modal analysis, for the individual techniques as well as overlaid images. Noteworthy, a very good correlation exists between the images acquired with the individual techniques, with similar patterns observed in all 3 techniques (Figures 3.6 c, f, and i). Surprisingly, SEM imaging (Figure 3.6a) revealed the presence of two types of particles, which could easily be distinguished based on their morphology and size: on one hand, small and elongated objects with an aspect ratio of approximately 1:7, and, on the other hand, compact, solidified crystalline particles with irregular shapes and

well-defined edges, and with a height comparable to their lateral size. The larger particles were identified as cyanoacrylate glue particles, while the smaller particles were captured tdEVs, which was confirmed by Raman imaging (vide infra). Glue particles are presumably created upon release of the last PDMS device used to fabricate the navigation markers. In SEM, tdEVs present a much lower contrast than glue particles due to differences in molecular density. Multivariate analysis of the Raman data by PCA performed in the high frequency region (2700 and 3200 cm^{-1}) as before confirms the presence of distinct populations of objects on the stainless steel substrates, whose Raman profile was distinct enough, as observed from the loading vectors PC3 (for tdEVs) and PC1 (for glue particles), respectively, in Figures 3.6d and 3.6g. Measurements were conducted here on single EVs captured on the surface, and the signal-to-noise ratio was better in the high frequency region, which was therefore solely considered for data analysis. Yet, it allowed distinguishing tdEVs from other particles. As before, a clear Raman peak was found in the PC3 (Fig. 6d) loading at 2851 cm^{-1}, which corresponds to the CH_2 symmetric stretch of lipids, and a lipid-protein band between 2850 and 2950 cm^{-1}, which is characteristic of EVs. These bands were absent in the PC1 loading, and are indeed not expected for cyanoacrylate (glue) particles. In contrast, the PC1 loading (Fig. 6g) presented a CH stretching region with a prominent peak at 2944 cm^{-1} and a CN stretching region with a peak at around 2247 cm^{-1}, which are both characteristic of cyanoacrylate glue.[63] It is worth noticing that the optical contrast of the images of scores is superior to the electron contrast in the SEM images, which clearly highlights the added value of correlative SEM-Raman imaging. The Raman images of the PC3 and PC1 scores in Figures 3.6e and 3.6h reveal the respective distribution of the EVs and glue particles.

As a last analytical modality, AFM was employed to characterize the objects captured on the surface. Although AFM is typically slower than SEM, its resolution is higher, which allows detecting both more and smaller particles compared to the two other techniques. The resolution of particles below ~0.5 µm in SEM is complicated by the low contrast in lieu of gold coating of the sample, whereas if became apparent only from AFM analysis that the majority of particles is in fact smaller than ~120 nm (See Figure 3.5c). Moreover, AFM

provides quasi-3D morphological information, which is of great interest to characterize the height of the captured EVs. Given also the low contrast in SEM due to the low acceleration voltages, the AFM data is altogether more suitable for studying the size distribution of captured EVs (Fig. 3.5c). Figure 3.6b presents an AFM image corresponding to the previously discussed Raman and SEM images, and Figure 3.6c an overlay image of the AFM and SEM data, showing good agreement between the data acquired by both techniques. In future studies, AFM could also be considered to examine the mechanical properties of the captured EVs (*e.g.*, by nanoindentation[64]).

Altogether, data acquired by AFM are fully in line with both Raman and SEM data, and they all demonstrate the specific capture of tdEVs by the covalently bound antibodies on the stainless steel substrates.

3.5 Conclusion

We reported here a platform for the selective capture of tumor derived EVs (tdEVs) followed by their multi-modal analysis using SEM, Raman and AFM imaging to correlate size, morphological and chemical information at the individual EV level. Stainless steel, selected here for its suitability for all three imaging techniques, was first chemically modified with a CDPA monolayer onto which anti-EpCAM antibodies targeting tumor-derived EVs were immobilized. IRRAS and XPS characterization of the CDPA-functionalized surfaces revealed a densely packed and well-ordered monolayer, and XPS confirmed proper immobilization of the antibodies. Furthermore, EVs isolated from LNCaP prostate cancer cell lines were successfully captured on the antibody-conjugated stainless steel substrates, and successively analyzed using Raman spectroscopy, SEM and AFM. The integration of navigation markers on the stainless steel substrates after EV capture was instrumental here to track back individual EVs between the different analytical techniques. However, their fabrication using cyanoacrylate injected in patterned PDMS channels resulted in the creation of

glue particles, which were detected together with the EVs. In future work, therefore, such navigation markers should be machined in the substrate and not onto the substrate to alleviate these contamination issues. Nonetheless, good agreement was found between the three techniques considered here, with excellent overlay of the images acquired by the individual modalities. As a proof of concept, in this paper, tdEVs isolated from cancerous cell lines were captured and analyzed. As a next step, the same platform will be challenged with more complex samples, such as blood samples, after implementation of anti-fouling moieties, *e.g.*, based on polyethylene glycol (PEG). Furthermore, the proposed multi-modal approach can easily be expanded in the future to other optical (*e.g.,* confocal fluorescence microscopy or infrared spectroscopy), electron (*e.g.,* energy-dispersive X-ray spectroscopy) and probe (*e.g.,* force spectroscopy) microscopy techniques as well as other analysis techniques, *e.g.,* surface plasmon resonance (SPR) and mass spectroscopy (MS).

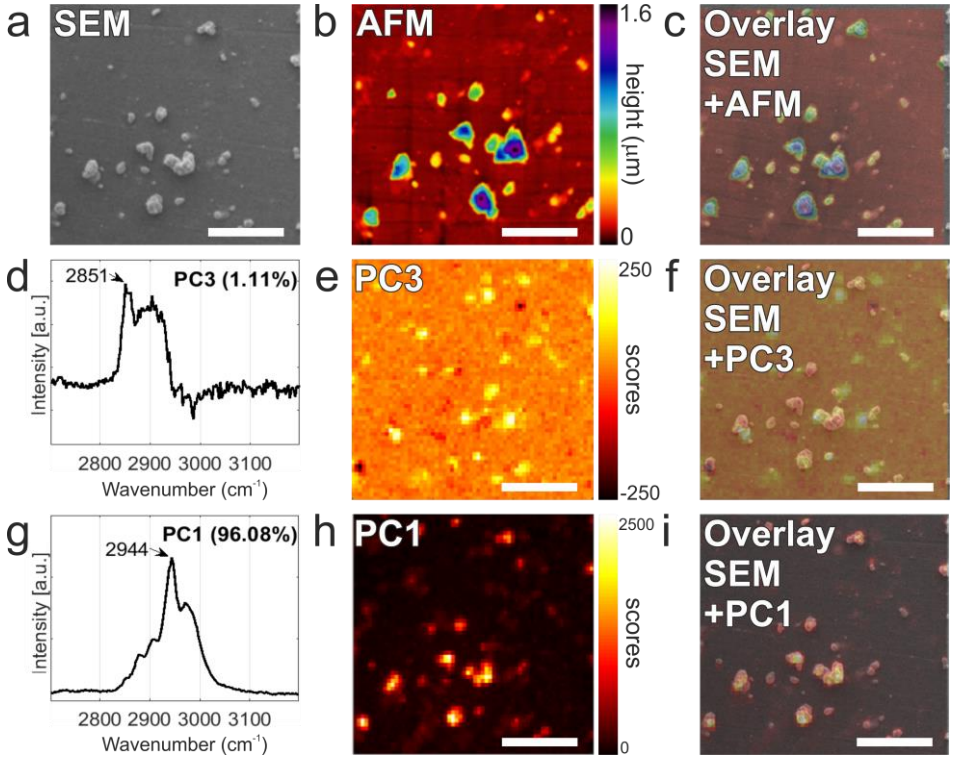

Figure 3.6. Multi-modal analysis of LnCAP-derived EVs on anti-EpCAM functionalized stainless steel substrates. *a) SEM image of a selected ROI (30 µm x 30 µm). b) Corresponding AFM height image of the same ROI. c) AFM – SEM overlaid image. d) Raman spectrum in the 2700-3200 cm-1 region of the PC3 displaying a characteristic lipid-protein band (2850-2950 cm-1) specific to EVs, with a characteristic peat at 2851 cm-1, which corresponds to the CH2 symmetric stretch of lipids. e) Raman image of scores on PC3 (1.11%) showing the position of EVs in the Raman image. f) Overlay image showing excellent correspondence between the PC3 image of scores (h) with the SEM image (a). g) Raman spectrum in the 2700-3200 cm-1 region corresponding to the PC1 displaying a ν(CH) stretching region of the cyanoacrylate glue with a characteristic peak at 2944 cm-1. h) Raman image of scores on PC1 (96.08%) showing the position of the glue particles in the Raman image. i) Overlay image showing excellent correspondence between the PC1 image of scores on PC1 (e) with the SEM image presented in (a).*

3.6 References

(1) Poudineh, M.; Sargent, E. H.; Pantel, K.; Kelley, S. O. Profiling Circulating Tumour Cells and Other Biomarkers of Invasive Cancers. *Nat. Biomed. Eng.* **2018**, *2* (2), 72–84. https://doi.org/10.1038/s41551-018-0190-5.

(2) Vaidyanathan, R.; Soon, R. H.; Zhang, P.; Jiang, K.; Lim, C. T. Cancer Diagnosis: From Tumor to Liquid Biopsy and Beyond. *Lab Chip* **2018**, No. 19, 11–34. https://doi.org/10.1039/C8LC00684A.

(3) Alix-Panabieѐres, C.; Pantel, K. Circulating Tumor Cells: Liquid Biopsy of Cancer. *Clin. Chem.* **2013**, *59* (1), 110–118. https://doi.org/10.1373/clinchem.2012.194258.

(4) Coumans, F. A. W.; Ligthart, S. T.; Uhr, J. W.; Terstappen, L. W. M. M. Challenges in the Enumeration and Phenotyping of CTC. *Clin. Cancer Res.* **2012**, *18* (20), 5711–5718. https://doi.org/10.1158/1078-0432.CCR-12-1585.

(5) Coumans, F.; Dalum, G. Van; Terstappen, L. W. M. M. CTC Technologies and Tools. *Cytom. Part A* **2018**, No. 93A, 1197–1201. https://doi.org/10.1002/cyto.a.23684.

(6) Nanou, A.; Coumans, F. A. W.; van Dalum, G.; Zeune, L. L.; Dolling, D.; Onstenk, W.; Crespo, M.; Fontes, M. S.; Rescigno, P.; Fowler, G.; et al. Circulating Tumor Cells, Tumor-Derived Extracellular Vesicles and Plasma Cytokeratins in Castration-Resistant Prostate Cancer Patients. *Oncotarget* **2018**, *9* (27), 19283–19293. https://doi.org/10.18632/oncotarget.25019.

(7) Yáñez-Mó, M.; Siljander, P. R. M.; Andreu, Z.; Zavec, A. B.; Borràs, F. E.; Buzas, E. I.; Buzas, K.; Casal, E.; Cappello, F.; Carvalho, J.; et al. Biological Properties of Extracellular Vesicles and Their Physiological Functions. *J. Extracell. Vesicles* **2015**, *4* (2015), 1–60. https://doi.org/10.3402/jev.v4.27066.

(8) Sunkara, V.; Woo, H.-K.; Cho, Y.-K. Emerging Techniques in the Isolation and Characterization of Extracellular Vesicles and Their Roles in Cancer Diagnostics and Prognostics. *Analyst* **2016**, *141* (2), 371–381. https://doi.org/10.1039/C5AN01775K.

(9) Liga, A.; Vliegenthart, A. D. B.; Oosthuyzen, W.; Dear, J. W.; Kersaudy-Kerhoas, M. Exosome Isolation: A Microfluidic Road-Map. *Lab Chip* **2015**, *15* (11), 2388–2394. https://doi.org/10.1039/c5lc00240k.

(10) György, B.; Szabó, T. G.; Pásztói, M.; Pál, Z.; Misják, P.; Aradi, B.; László, V.; Pállinger, É.; Pap, E.; Kittel, Á.; et al. Membrane Vesicles, Current State-of-the-Art: Emerging Role of Extracellular Vesicles. *Cell. Mol. Life Sci.* **2011**, *68* (16), 2667–2688. https://doi.org/10.1007/s00018-011-0689-3.

(11) Xu, R.; Greening, D. W.; Zhu, H.; Takahashi, N.; Simpson, R. J. Extracellular Vesicle Isolation and Characterization : Toward Clinical Application. *J Clin Invest* **2016**, *126* (4), 1152–1162. https://doi.org/10.1172/JCI81129.It.

(12) Reátegui, E.; Van Der Vos, K. E.; Lai, C. P.; Zeinali, M.; Atai, N. A.; Aldikacti, B.; Floyd, F. P.; Khankhel, A.; Thapar, V.; Hochberg, F. H.; et al. Engineered Nanointerfaces for Microfluidic Isolation and Molecular Profiling of Tumor-Specific Extracellular Vesicles. *Nat. Commun.* **2018**, *9* (1), 2018. https://doi.org/10.1038/s41467-017-02261-1.

(13) Zhu, Q.; Heon, M.; Zhao, Z.; He, M. Microfluidic Engineering of Exosomes: Editing Cellular Messages for Precision Therapeutics. *Lab Chip* **2018**, *18* (12), 1690–1703. https://doi.org/10.1039/c8lc00246k.

(14) Raposo, G.; Stoorvogel, W. Extracellular Vesicles: Exosomes, Microvesicles, and Friends. *J. Cell Biol.* **2013**, *200* (4), 373–383. https://doi.org/10.1083/jcb.201211138.

(15) Im, H.; Shao, H.; Park, Y. Il; Peterson, V. M.; Castro, C. M.; Weissleder, R.; Lee, H. Label-Free Detection and Molecular Profiling of Exosomes with a Nano-Plasmonic Sensor. *Nat. Biotechnol.* **2014**, *32* (5), 490–495. https://doi.org/10.1038/nbt.2886.

(16) Witwer, K. W.; Buzás, E. I.; Bemis, L. T.; Bora, A.; Lässer, C.; Lötvall, J.; Nolte-'t Hoen, E. N.; Piper, M. G.; Sivaraman, S.; Skog, J.; et al. Standardization of Sample Collection, Isolation and Analysis Methods in Extracellular Vesicle Research. *J. Extracell. Vesicles* **2013**, *2* (1), 2013. https://doi.org/10.3402/jev.v2i0.20360.
(17) Yuana, Y.; Böing, A. N.; Grootemaat, A. E.; van der Pol, E.; Hau, C. M.; Cizmar, P.; Buhr, E.; Sturk, A.; Nieuwland, R. Handling and Storage of Human Body Fluids for Analysis of Extracellular Vesicles. *J. Extracell. Vesicles* **2015**, *4* (1), 2015. https://doi.org/10.3402/jev.v4.29260.
(18) Tauro, B. J.; Greening, D. W.; Mathias, R. A.; Ji, H.; Mathivanan, S.; Scott, A. M.; Simpson, R. J. Comparison of Ultracentrifugation, Density Gradient Separation, and Immunoaffinity Capture Methods for Isolating Human Colon Cancer Cell Line LIM1863-Derived Exosomes. *Methods* **2012**, *56* (2), 293–304. https://doi.org/10.1016/j.ymeth.2012.01.002.
(19) Yoshioka, Y.; Kosaka, N.; Konishi, Y.; Ohta, H.; Okamoto, H.; Sonoda, H.; Nonaka, R.; Yamamoto, H.; Ishii, H.; Mori, M.; et al. Ultra-Sensitive Liquid Biopsy of Circulating Extracellular Vesicles Using ExoScreen. *Nat. Commun.* **2014**, *5*, 3591. https://doi.org/10.1038/ncomms4591.
(20) Willms, E.; Cabañas, C.; Mäger, I.; Wood, M. J. A.; Vader, P. Extracellular Vesicle Heterogeneity: Subpopulations, Isolation Techniques, and Diverse Functions in Cancer Progression. *Front. Immunol.* **2018**, *9* (APR), 2018. https://doi.org/10.3389/fimmu.2018.00738.
(21) Kanwar, S. S.; Dunlay, C. J.; Simeone, D. M.; Nagrath, S. Microfluidic Device (ExoChip) for on-Chip Isolation, Quantification and Characterization of Circulating Exosomes. *Lab Chip* **2014**, *14* (11), 1891–1900. https://doi.org/10.1039/c4lc00136b.
(22) Koliha, N.; Wiencek, Y.; Heider, U.; Jüngst, C.; Kladt, N.; Krauthäuser, S.; Johnston, I. C. D.; Bosio, A.; Schauss, A.; Wild, S. A Novel Multiplex Bead-Based Platform Highlights the Diversity of Extracellular Vesicles. *J. Extracell. Vesicles* **2016**, *5* (1), 2016. https://doi.org/10.3402/jev.v5.29975.
(23) Yadav, S.; Boriachek, K.; Islam, M. N.; Lobb, R.; Möller, A.; Hill, M. M.; Hossain, M. S. Al; Nguyen, N. T.; Shiddiky, M. J. A. An Electrochemical Method for the Detection of Disease-Specific Exosomes. *ChemElectroChem* **2017**, *4* (4), 967–971. https://doi.org/10.1002/celc.201600391.
(24) Guo, S. C.; Tao, S. C.; Dawn, H. Microfluidics-Based on-a-Chip Systems for Isolating and Analysing Extracellular Vesicles. *J. Extracell. Vesicles* **2018**, *7* (1), 1–16. https://doi.org/10.1080/20013078.2018.1508271.
(25) Coumans, F. A. W.; Brisson, A. R.; Buzas, E. I.; Dignat-George, F.; Drees, E. E. E.; El-Andaloussi, S.; Emanueli, C.; Gasecka, A.; Hendrix, A.; Hill, A. F.; et al. Methodological Guidelines to Study Extracellular Vesicles. *Circ. Res.* **2017**, *120* (10), 1632–1648. https://doi.org/10.1161/CIRCRESAHA.117.309417.
(26) Im, H.; Lee, K.; Weissleder, R.; Lee, H.; Castro, C. M. Novel Nanosensing Technologies for Exosome Detection and Profiling. *Lab Chip* **2017**, *17* (17), 2892–2898. https://doi.org/10.1039/c7lc00247e.
(27) Contreras-Naranjo, J. C.; Wu, H. J.; Ugaz, V. M. Microfluidics for Exosome Isolation and Analysis: Enabling Liquid Biopsy for Personalized Medicine. *Lab Chip* **2017**, *17* (21), 3558–3577. https://doi.org/10.1039/c7lc00592j.
(28) Hisey, C. L.; Dorayappan, K. D. P.; Cohn, D. E.; Selvendiran, K.; Hansford, D. J. Microfluidic Affinity Separation Chip for Selective Capture and Release of Label-Free Ovarian Cancer Exosomes. *Lab Chip* **2018**, *18* (20), 3144–3153. https://doi.org/10.1039/c8lc00834e.
(29) Kormelink, T. G.; Arkesteijn, G. J. A.; Nauwelaers, F. A.; van den Engh, G.; Nolte-'t Hoen, E. N. M.; Wauben, M. H. M. Prerequisites for the Analysis and Sorting of Extracellular Vesicle Subpopulations by High-Resolution Flow Cytometry. *Cytom. Part A* **2016**, *89* (2), 135–147. https://doi.org/10.1002/cyto.a.22644.

(30) Yuana, Y.; Oosterkamp, T. H.; Bahatyrova, S.; Ashcroft, B.; Garcia Rodriguez, P.; Bertina, R. M.; Osanto, S. Atomic Force Microscopy: A Novel Approach to the Detection of Nanosized Blood Microparticles. *J. Thromb. Haemost.* **2010**, *8* (2), 315–323. https://doi.org/10.1111/j.1538-7836.2009.03654.x.
(31) van der Pol, E.; Sturk, A.; van Leeuwen, T.; Nieuwland, R.; Coumans, F.; Mobarrez, F.; Arkesteijn, G.; Wauben, M.; Siljander, P. R. M.; Sánchez-López, V.; et al. Standardization of Extracellular Vesicle Measurements by Flow Cytometry through Vesicle Diameter Approximation. *J. Thromb. Haemost.* **2018**, *16* (6), 1236–1245. https://doi.org/10.1111/jth.14009.
(32) Zhang, P.; Crow, J.; Lella, D. J.; Zhou, X.; Samuel, G.; Godwin, A. K.; Zeng, Y. Ultrasensitive Quantification of Tumor MRNAs in Extracellular Vesicles with Integrated Microfluidic Digital Analysis Chip. *Lab Chip* **2018**, *18*, 3790–3801. https://doi.org/10.1039/C8LC01071D.
(33) Zhang, P.; He, M.; Zeng, Y. Ultrasensitive Microfluidic Analysis of Circulating Exosomes Using a Nanostructured Graphene Oxide/Polydopamine Coating. *Lab Chip* **2016**, *16* (16), 3033–3042. https://doi.org/10.1039/c6lc00279j.
(34) Sebaihi, N.; De Boeck, B.; Yuana, Y.; Nieuwland, R.; Pétry, J. Dimensional Characterization of Extracellular Vesicles Using Atomic Force Microscopy. *Meas. Sci. Technol.* **2017**, *28* (3), 8pp. https://doi.org/10.1088/1361-6501/28/3/034006.
(35) Lee, W.; Nanou, A.; Rikkert, L.; Coumans, F. A. W.; Otto, C.; Terstappen, L. W. M. M.; Offerhaus, H. L. Label-Free Prostate Cancer Detection by Characterization of Extracellular Vesicles Using Raman Spectroscopy. *Anal. Chem.* **2018**, *90* (19), 11290–11296. https://doi.org/10.1021/acs.analchem.8b01831.
(36) Shpacovitch, V.; Hergenröder, R. Optical and Surface Plasmonic Approaches to Characterize Extracellular Vesicles. A Review. *Anal. Chim. Acta* **2018**, *1005*, 1–15. https://doi.org/10.1016/j.aca.2017.11.066.
(37) Obeid, S.; Ceroi, A.; Mourey, G.; Saas, P.; Elie-Caille, C.; Boireau, W. Development of a NanoBioAnalytical Platform for "on-Chip" Qualification and Quantification of Platelet-Derived Microparticles. *Biosens. Bioelectron.* **2017**, *93*, 250–259. https://doi.org/10.1016/j.bios.2016.08.100.
(38) Pocsfalvi, G.; Stanly, C.; Vilasi, A.; Fiume, I.; Capasso, G.; Turiák, L.; Buzas, E. I.; Vékey, K. Mass Spectrometry of Extracellular Vesicles. *Mass Spectrom. Rev.* **2015**, *35* (1), 3–21. https://doi.org/10.1002/mas.21457.
(39) Shao, H.; Chung, J.; Balaj, L.; Charest, A.; Bigner, D. D.; Carter, B. S.; Hochberg, F. H.; Breakefield, X. O.; Weissleder, R.; Lee, H. Protein Typing of Circulating Microvesicles Allows Real-Time Monitoring of Glioblastoma Therapy. *Nat. Med.* **2012**, *18* (12), 1835–1840. https://doi.org/10.1038/nm.2994.
(40) Tatischeff, I.; Larquet, E.; Falcón-Pérez, J. M.; Turpin, P.-Y.; Kruglik, S. G. Fast Characterisation of Cell-Derived Extracellular Vesicles by Nanoparticles Tracking Analysis, Cryo-Electron Microscopy, and Raman Tweezers Microspectroscopy. *J. Extracell. Vesicles* **2012**, *1* (1), 19179. https://doi.org/10.3402/jev.v1i0.19179.
(41) Krafft, C.; Wilhelm, K.; Eremin, A.; Nestel, S.; von Bubnoff, N.; Schultze-Seemann, W.; Popp, J.; Nazarenko, I. A Specific Spectral Signature of Serum and Plasma-Derived Extracellular Vesicles for Cancer Screening. *Nanomedicine Nanotechnology, Biol. Med.* **2017**, *13* (3), 835–841. https://doi.org/10.1016/j.nano.2016.11.016.
(42) Eswaran, N.; Agaram Sundaram, V.; Rao, K. A.; Thalaivarisai Balasundaram, S. Simple Isolation and Characterization of Seminal Plasma Extracellular Vesicle and Its Total RNA in an Academic Lab. *3 Biotech* **2018**, *8* (3), 1–6. https://doi.org/10.1007/s13205-018-1157-7.
(43) Kondratov, K. A.; Petrova, T. A.; Yu Mikhailovskii, V.; Ivanova, A. N.; Kostareva, A. A.; Fedorov, A. V. A Study of Extracellular Vesicles Isolated from Blood Plasma Conducted by Low-

Voltage Scanning Electron Microscopy. *Cell tissue biol.* **2017**, *11* (3), 181–190. https://doi.org/10.1134/S1990519X17030051.
(44) Timmermans, F. J.; Otto, C. Contributed Review: Review of Integrated Correlative Light and Electron Microscopy. *Rev. Sci. Instrum.* **2015**, *86* (1), 2015. https://doi.org/10.1063/1.4905434.
(45) Enciso-Martinez, A.; Timmermans, F. J.; Nanou, A.; Terstappen, L. W. M. M.; Otto, C. SEM–Raman Image Cytometry of Cells. *Analyst* **2018**, *143* (18), 4495–4502. https://doi.org/10.1039/C8AN00955D.
(46) Sharma, S.; Rasool, H. I.; Palanisamy, V.; Mathisen, C.; Schmidt, Ḱ. M.; Wong, D. T.; Gimzewski, J. K. Structural-Mechanical Characterization. *ACS Nano* **2010**, *4* (4), 1921–1926.
(47) Kosian, M.; Smulders, M. M. J.; Zuilhof, H. Structure and Long-Term Stability of Alkylphosphonic Acid Monolayers on SS316L Stainless Steel. *Langmuir* **2016**, *32* (4), 1047–1057. https://doi.org/10.1021/acs.langmuir.5b04217.
(48) Raman, A.; Dubey, M.; Gouzman, I.; Gawalt, E. S. Formation of Self-Assembled Monolayers of Alkylphosphonic Acid on the Native Oxide Surface of SS316L. *Langmuir* **2006**, *22* (15), 6469–6472. https://doi.org/10.1021/la060636p.
(49) Tizazu, G.; Adawi, A. M.; Leggett, G. J.; Lidzey, D. G. Photopatterning, Etching, and Derivatization of Self-Assembled Monolayers of Phosphonic Acids on the Native Oxide of Titanium. *Langmuir* **2009**, *25* (18), 10746–10753. https://doi.org/10.1021/la901271c.
(50) Hermanson, G. T. *Bioconjugate Techniques*, 2nd ed.; Academic Press, 2013. https://doi.org/10.1016/B978-0-12-382239-0.00004-2.
(51) van der Pol, E.; Coumans, F. A. W.; Grootemaat, A. E.; Gardiner, C.; Sargent, I. L.; Harrison, P.; Sturk, A.; van Leeuwen, T. G.; Nieuwland, R. Particle Size Distribution of Exosomes and Microvesicles Determined by Transmission Electron Microscopy, Flow Cytometry, Nanoparticle Tracking Analysis, and Resistive Pulse Sensing. *J. Thromb. Haemost.* **2014**, *12* (7), 1182–1192. https://doi.org/10.1111/jth.12602.
(52) Abdi, H.; Williams, L. J. Principal Component Analysis. *Wiley Interdiscip. Rev. Comput. Stat.* **2010**, *2* (4), 433–459. https://doi.org/10.1002/wics.101.
(53) Ter Maat, J.; Regeling, R.; Ingham, C. J.; Weijers, C. A. G. M.; Giesbers, M.; De Vos, W. M.; Zuilhof, H. Organic Modification and Subsequent Biofunctionalization of Porous Anodic Alumina Using Terminal Alkynes. *Langmuir* **2011**, *27* (22), 13606–13617. https://doi.org/10.1021/la203738h.
(54) Porter, M. D.; Bright, T. B.; Allara, D. L.; Chidsey, C. E. Spontaneously Organized Molecular Assemblies. 4. Structural Characterization of n-Alkyl Thiol Monolayers on Gold by Optical Ellipsometry, Infrared Spectroscopy, and Electrochemistry. *J. Am. Chem. Soc.* **1987**, *109* (12), 3559–3568. https://doi.org/10.1021/ja00246a011.
(55) Maoz, R.; Sagiv, J. On the Formation and Structure of Self-Assembling Monolayers. I. A Comparative Atr-Wettability Study of Langmuir-Blodgett and Adsorbed Films on Flat Substrates and Glass Microbeads. *J. Colloid Interface Sci.* **1984**, *100* (2), 465–496. https://doi.org/10.1016/0021-9797(84)90452-1.
(56) Debrassi, A.; Roeven, E.; Thijssen, S.; Scheres, L.; De Vos, W. M.; Wennekes, T.; Zuilhof, H. Versatile (Bio)Functionalization of Bromo-Terminated Phosphonate-Modified Porous Aluminum Oxide. *Langmuir* **2015**, *31* (20), 5633–5644. https://doi.org/10.1021/acs.langmuir.5b00853.
(57) Arnold, R.; Azzam, W.; Terfort, A.; Wöll, C. Preparation, Modification, and Crystallinity of Aliphatic and Aromatic Carboxylic Acid Terminated Self-Assembled Monolayers. *Langmuir* **2002**, *18* (10), 3980–3992. https://doi.org/10.1021/la0117000.
(58) Bain, C. D.; Whitesides, G. M. Attenuation Lengths of Photoelectrons in Hydrocarbon Films. *J. Phys. Chem.* **1989**, *93* (4), 1670–1673. https://doi.org/10.1021/j100341a095.

(59) Laibinis, P. E.; Bain, C. D.; Whitesides, G. M. Attenuation of Photoelectrons in Monolayers of N-Alkanethiols Adsorbed on Copper, Silver, and Gold. *J. Phys. Chem.* **1991**, *95* (18), 7017–7021. https://doi.org/10.1021/j100171a054.
(60) Movasaghi, Z.; Rehman, S.; Rehman, I. U. Raman Spectroscopy of Biological Tissues. *Appl. Spectrosc. Rev.* **2007**, *42* (5), 493–541. https://doi.org/10.1080/05704920701551530.
(61) Van Der Pol, E.; Hoekstra, A. G.; Sturk, A.; Otto, C.; Van Leeuwen, T. G.; Nieuwland, R. Optical and Non-Optical Methods for Detection and Characterization of Microparticles and Exosomes. *J. Thromb. Haemost.* **2010**, *8* (12), 2596–2607. https://doi.org/10.1111/j.1538-7836.2010.04074.x.
(62) Timmermans, F. J.; Chang, L.; van Wolferen, H. A. G. M.; Lenferink, A. T. M.; Otto, C. Observation of Whispering Gallery Modes through Electron Beam-Induced Deposition. *Opt. Lett.* **2017**, *42* (7), 1337–1340. https://doi.org/10.1364/OL.42.001337.
(63) Edwards, H. G. M.; Day, J. S. Fourier Transform Raman Spectroscopic Studies of the Curing of Cyanoacrylate Glue. *J. Raman Spectrosc.* **2004**, *35* (7), 555–560. https://doi.org/10.1002/jrs.1184.
(64) Roos, B. W. H.; Wuite, G. J. L. Nanoindentation Studies Reveal Material Properties of Viruses. *Adv. Mater.* **2009**, 1187–1192. https://doi.org/10.1002/adma.200801709.

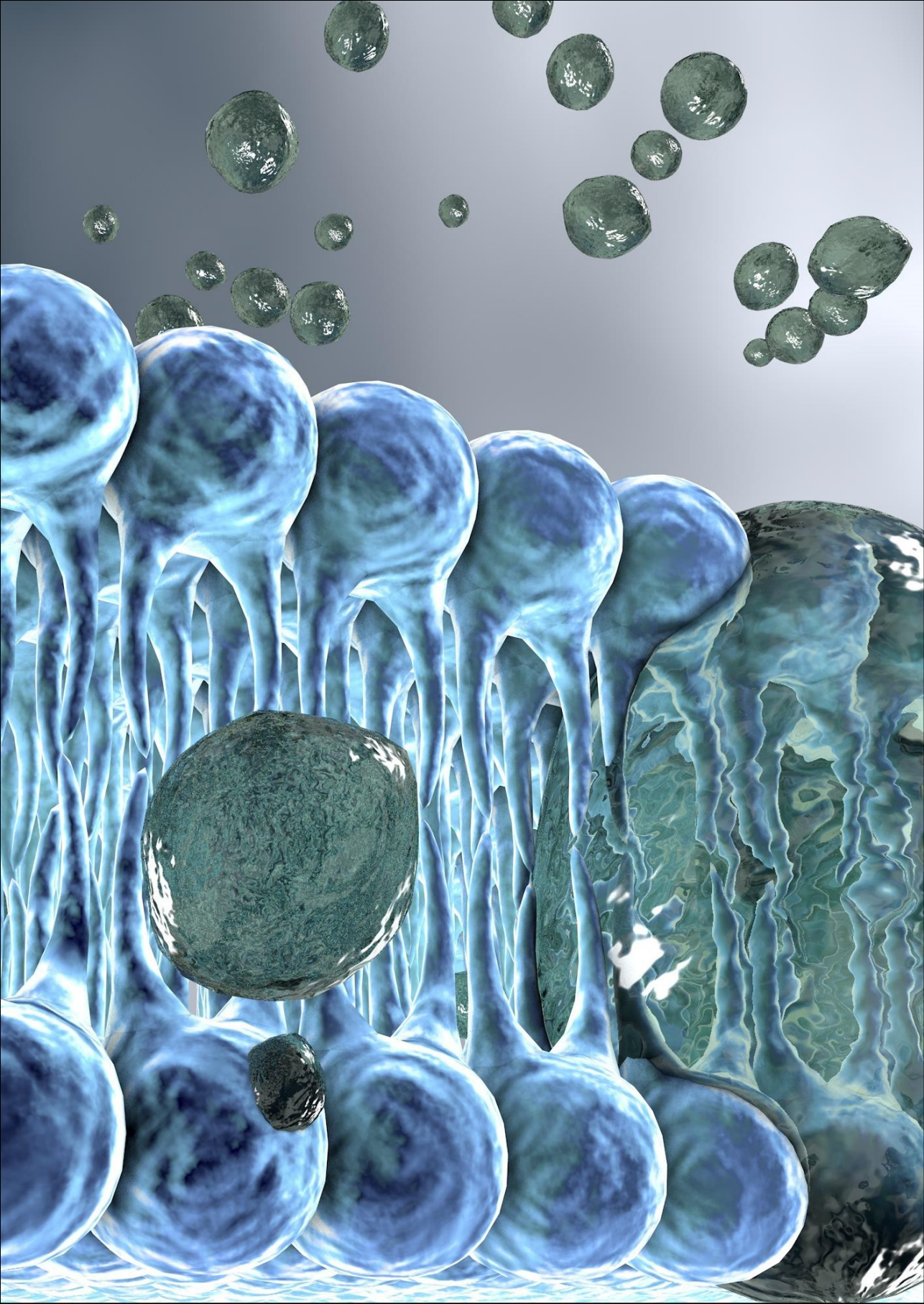

4

Organosilicon uptake by biological membranes

This chapter was originally published as:

Pepijn Beekman, Agustin Enciso-Martinez, Sidharam P. Pujari, Leon W.M.M. Terstappen, Han Zuilhof, Séverine Le Gac, Cees Otto, *Organosilicon uptake by biological membranes,* Nature Communications Biology (in press)

4.1 Abstract

Organosilicon compounds are ubiquitous in everyday use. Application of some of these compounds in food, cosmetics and pharmaceuticals is widespread on the assumption that these materials are not systemically absorbed. Here the interactions of various organosilicon compounds (simeticone, hexamethyldisilazane and polydimethylsiloxane) with cell membranes and models thereof were characterized with a range of analytical techniques, demonstrating that these compounds were retained in or on the cell membrane. The increasing application of organosilicon compounds as replacement of other plastics calls for a better awareness and understanding of these interactions. Moreover, with many developments in biotechnology relying on organosilicon materials, it becomes important to scrutinize the potential effect that silicone leaching may have on biological systems.

4.2 Introduction

Organosilicon compounds, which are silicon-containing hydrocarbons, have a wide range of accepted usage.[1] Examples include silicones like polydimethylsiloxane (PDMS) which is accepted by the European Food Safety Authority (EFSA) as a food additive,[2] and widely used in the field of microfluidics.[3] The silicone-based over-the-counter drug simeticone is used as gastro-intestinal surfactant to treat colic in infants.[4] Interestingly, there is no dosage limitation for this drug since it is claimed not to be absorbed systemically and it has been generally recognized as safe since before the FDA started Over-The-Counter Drug Review in 1972.[5] However, despite the widespread use of silicones in products for use in humans, there is relatively little literature regarding the possible interactions between silicone molecules and lipid membranes and, potentially, other biomolecules vital to living organisms. Moreover, various research disciplines use silicones for a broad range of applications. Leaching of

low-molecular weight components into the samples under study may influence results,[3,6,7] for instance in lab-on-a-chip research and scanning electron microscopy (SEM) studies, which we briefly clarify below:

1) In the lab-on-a-chip field,[8,9] the massive adoption of PDMS for the production of microfluidic and organ-on-a-chip platforms can be attributed to the ease of device fabrication, its optical transparency, its gas-permeability, which is particularly attractive for cell culture experiments, and its elastomeric properties.[10] Finally, PDMS has proven to be biocompatible in the sense that it does not significantly affect cell viability, also for very sensitive cells like embryos, primary cells and *ex vivo* ovarian tissues.[7,11–13] In-vivo short term studies reported no significant changes in survival of rats that were fed diets containing up to 10% PDMS.[14,15] However, to our knowledge, systemic uptake was never comprehensively studied. In contrast, it has been demonstrated that PDMS in the cells' microenvironment do modulate gene expression profiles significantly,[16] especially in comparison with other polymers.[17]
2) In SEM studies, biological samples require pretreatment before they can be placed in a vacuum chamber for imaging. Fixation, dehydration, drying and coating with an electrically conductive layer are typically required. Dehydration and drying seem to be the most critical steps as

they can give rise to artifacts, such as specimen shrinkage and distortion.[18–23] A common method for drying uses hexamethyldisilazane (HMDS).[24,25] The mechanism proposed by which HMDS interacts with biological specimens has been via transfer of trimethylsilyl groups,[26] which can happen with, e.g. sugars and amino acids in biological specimens. In this process proteins crosslink to fix the biological specimen, preventing it from collapsing during drying.[25]

Based on preliminary observations of silicone residue in lipid membranes after incubation in microfluidic channels and HMDS-drying (*vide infra*), we set to investigate whether organosilicons, broadly speaking, interact with biological membranes. To illustrate the generality of the silicone-membrane interactions, three different organosilicon sources were included in this study (See Appendix B.1 for structural information):

1) PDMS (Sylgard 184), whose oligomers leach from incompletely cured microfluidic channels;
2) HMDS used for dehydration in electron microscopy sample preparation; and
3) Infacol, an over-the-counter drug, containing simeticone, an organosilicon compound similar in structure to PDMS, mixed with silica nanoparticles.

Two different specimens were considered: cells (LNCaP and HT-29 cell lines) and supported lipid bilayers (SLBs) prepared from 1,2-dioleoyl-sn-glycero-3-phosphocholine (DOPC), which is abundant in biological membranes.[27] SLBs are widely used as models of cellular membranes;[28] here, they enable to study organosilicon interactions with phospholipid molecules.

Interactions between silicones and biological membranes were studied using four analytical techniques: a) Confocal Raman micro-spectroscopy, to probe the presence of specific chemical bonds down to 400 nm spatial resolution and map the spectra in a hyperspectral image; b) Auger Electron Spectroscopy (AES), to identify atomic species present at the surface of a sample (probing depth of 3 nm), and which allows overlay with electron microscopy images to show the spatial distribution of species; c) X-ray Photoelectron Spectroscopy (XPS) (probing depth of 10 nm), to investigate with high elemental sensitivity whether silicon is present in natively silicon-free samples of SLBs after incubation with silicones; and d) Infrared spectroscopy (IR), to probe chemical bonds and for the presence of organosilicon compounds.

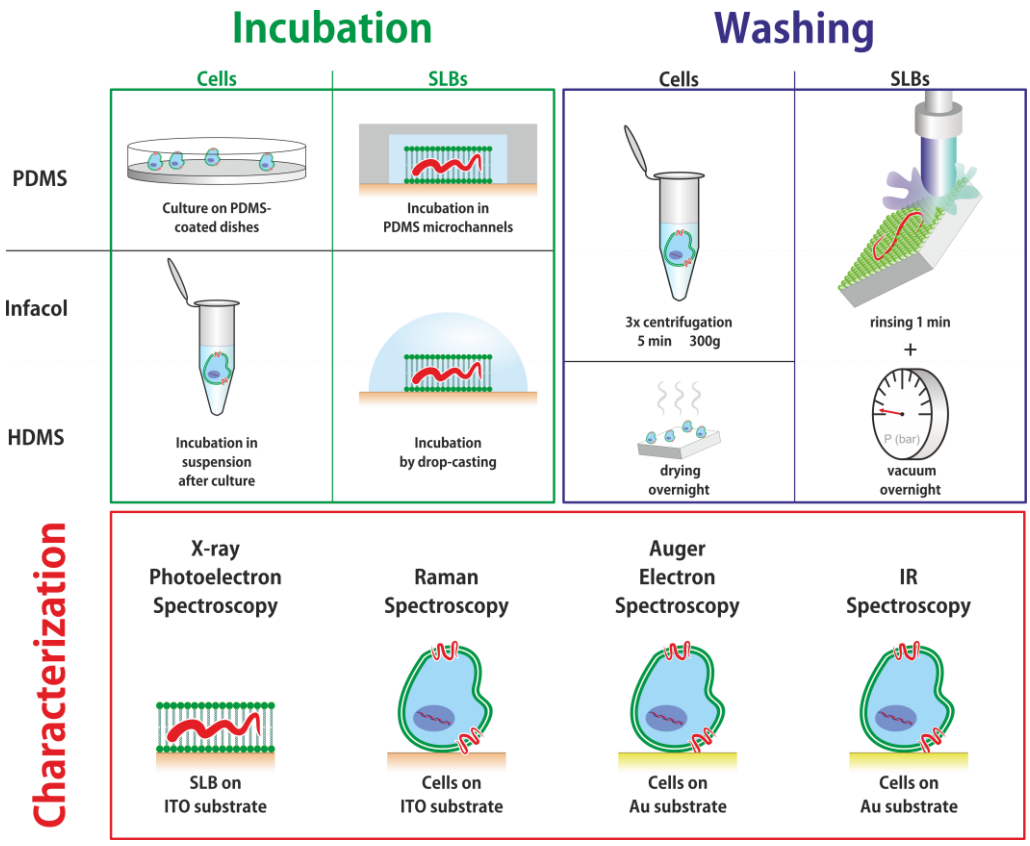

Figure 4.1. Overview of the sample preparation and characterization steps. *Cells and SLBs were first incubated with PDMS, Infacol or HMDS on substrates conforming to the requirements of the intended characterization technique. The organosilicon compounds are presented as "red wavy lines" and their hypothetical interaction with membranes (vide infra) is here suggested. The excess of organosilicon compounds was removed before samples were characterized with various techniques.*

4.3 Materials and methods

A schematic overview of the sample preparation and subsequent characterization steps is presented in Figure 4.1. Each individual step is discussed in more detail in the following sections.

4.3.1 Materials

PDMS was prepared using Sylgard 184 (Dow Corning, Farnell, Utrecht, The Netherlands). Infacol (TEVA) was purchased from a local pharmacy store (Die Grenze (Almelo, The Netherlands). 1,2-dioleoyl-sn-glycero-3-phosphocholine was purchased from Avanti Polar Lipids (AL, USA). All other chemicals were obtained from Sigma Aldrich (Zwijndrecht, The Netherlands), unless otherwise specified. In all experiments, phosphate buffered saline (PBS) was prepared at pH 7.4, and filtered through a 0.2-µm syringe filter before use.

Indium Tin Oxide (ITO) coated fused-silica substrates were used in combination with XPS and Raman spectroscopy. This ITO coating was chosen because of its low Raman background signal. For Auger Electron Spectroscopy and IR, gold-coated substrates were used. ITO and gold coatings were deposited in the cleanroom of the MESA+ Institute for Nanotechnology by sputtering a layer of ~100 nm on fused-silica substrates.[29] Thereafter, substrates were cut by dicing to a size of 1×1 cm^2.

4.3.2 Cell culture

Cells from a prostate cancer cell line (LNCaP) or colon cancer cell line (HT-29), purchased from the American Type Culture Collection (ATCC, Manassas, VA, USA), were cultured in RPMI-1640 medium with L-glutamine (Lonza, Basel, Switzerland) supplemented with 1% penicillin and 1% streptomycin (Westburg, Amersfoort, The Netherlands) in an incubator at 37°C and with 5% CO_2, medium being refreshed every 3 days and cells being reseeded at a density of 10^4

cells/cm^2. For experiments, 8 × 10^6 cells were harvested using a 0.25% Trypsin solution (Thermo Fisher Scientific, Waltham, MA, USA). Subsequently, the cells were fixed in 1% paraformaldehyde (PFA) for 15 min and washed three times in PBS through centrifugation at 300 g for 5 min. Finally, the sample was split in 6 equal fractions, each containing 1.3 ×10^6 cells. While fixation alters the chemical state of proteins and other molecules, it was implemented in all experiments for consistency, since it is required for some experiments. It was made sure that the fixative did not contain any organosilicon species not to introduce additional biases in our study.

4.3.3 Supported lipid bilayers

Supported lipid bilayers (SLBs) were formed by fusing small unilamellar vesicles on the ITO-coated surface. A DOPC solution in chloroform was dried under vacuum, to yield a lipid film on the walls of a glass vial. This lipid film was re-hydrated in PBS to reach a DOPC concentration of 10 mg/ml and ultrasonicated for 15 min to form small unilamellar vesicles (SUVs). ITO substrates were cleaned ultrasonically in dichloromethane, acetone and ethanol for 3 min each, followed by 30 min of O_2-plasma treatment in a Diener Pico (Diener electronic, Bielefeld, Germany) at 250 W. The cleaned surfaces were incubated with a diluted SUV suspension (1 mg/mL in PBS) at room temperature overnight. After incubation, the substrates were thoroughly rinsed with PBS. Before their characterization with XPS, all SLB samples were dried under vacuum overnight.

4.3.4 Sample preparation – organosilicon

Sticky PDMS microchannels were fabricated using xurography, as previously reported by us.[30] Briefly, Sylgard 184 precursor was thoroughly mixed with the curing agent in a 10:1 weight ratio and degassed by centrifugation at 1000 g for 1 min. A mold was prepared by cutting a 0.2-mm thick adhesive film to yield 3×6 mm^2 patterns that were laminated in the bottom of a clean petri dish. The PDMS prepolymer/curing agent mixture was poured over the mold and degassed again under vacuum, before being cured at 80°C for 30 min yielding a sticky solid. Inlet and outlet holes were punched with a Harris Uni-Core 1-mm biopsy punch (VWR

International B.V., Amsterdam, The Netherlands). For control experiments, PDMS microchannels were prepared using the same protocol, but more thoroughly cured at 80°C overnight. Before bonding, the latter PDMS microchannel devices were ultrasonicated in ethanol for 15 min before plasma activation. Solutions were exchanged in these microchannels by pipetting manually in the inlets.

Infacol consists of a 40 mg/ml solution of simeticone in water with various additives, e.g., dispersing and flavoring agents. Simeticone consists primarily of polydimethylsiloxane with molecular weight ranging between 14 and 21 kDa, mixed with silicon dioxide nanoparticles (4-7%).[31] Before use, Infacol was diluted to 1 mg/ml in PBS. Solid particles of few microns in diameter that remained in the solution,were removed by filtering the solution (0.2-µm syringe filter) before experimentation with cells.

Hexamethyldisilazane (HMDS) was used as is, from a recently purchased bottle, extracted through a septum under perfusion with nitrogen by a syringe. Prior to HMDS-drying, cells were dehydrated with ethanol. Since Raman bands from ethanol were not observed neither in the HMDS-dried cells, nor in the control cells, it was concluded that ethanol was successfully fully evaporated from the cells.

4.3.5 PDMS interactions with cells and SLBs

For Auger Electron Spectroscopy (AES), cells were alternatively grown on a 1-mm thick PDMS layer prepared in a Petri dish and cured for 30 min at 80°C. HT-29 cells were seeded at a density of 10^4 cells/cm^2 and left to proliferate for 48 h in RPMI medium supplemented with 1% penicillin and 1% streptomycin at 37°C in a 5% CO_2 atmosphere. Cell adhesion to the PDMS layer after 48 h was comparable to that in standard culture flasks. After trypsinization, cells were fixed for 15 min in 1% paraformaldehyde and washed 3 times with Milli-Q water by centrifugation (300 g, 5 min).

Experiments with SLBs were conducted in sticky microchannels placed on the top of cleaned ITO substrates. A DOPC SUV suspension was injected in the microchannel, and left overnight for incubation at room temperature to yield a

SLB on the ITO-coated substrate. As for the cells, channels were rinsed with PBS and after delamination of the PDMS microchannels, the substrates were rinsed thoroughly with deionized water before analysis with XPS.

4.3.6 HMDS interactions with cells and SLBs

Fixed LnCaP cells in suspension (MilliQ) were dehydrated in increasing concentrations of ethanol (70-100%), followed by HMDS-drying,[32] and deposited on flat substrates overnight.[32] As a negative control, the HMDS-drying step was omitted and cells in 100% ethanol were dried on the substrates overnight. ITO-coated and gold-coated fused-silica substrates were used for Raman and AES spectroscopy, respectively. SLBs prepared on gold-coated fused-silica substrates were fully immersed in 1 ml of HMDS and dried under vacuum overnight.

4.3.7 Simeticone interactions with cells and SLBs

Fixed HT-29 cells were immersed in diluted Infacol solution and left overnight. Before characterization, cells were washed twice in PBS. For AES analysis, cells were deposited on gold-coated silica substrates. SLBs were immersed in 1 ml undiluted Infacol and dried under vacuum overnight after thorough rinsing.

4.3.8 Raman spectroscopy

An in-house Raman spectrometer was employed, that has been described in detail elsewhere.[30] Briefly, 2D point scanning of a laser beam (λ = 647.09 nm) from a Coherent Innova 70C laser was performed. The Raman scattered light was dispersed in a spectrometer and collected with a CCD camera (Andor Newton DU-970-BV, Belfast, United Kingdom). The laser power was measured underneath the objective (40×, NA: 0.95; Olympus Nederland B.V., Leiderdorp, The Netherlands,) and adjusted to 35 mW. The laser focal spot was focused 5 µm above the substrate to ensure it was close to the center of the cells. A 20 µm × 20 µm area was scanned with a step size of 0.31 µm and an illumination time of 100 ms per pixel. Hyperspectral images are created by integrating the Raman band between 450 and 550 cm^{-1}, which contains the band at 490 cm^{-1}, which is

present in all cells dried with HMDS. The area value of each pixel is converted to a color in a heat map scale.

4.3.9 XPS measurements

Using XPS, the atomic composition of the SLBs was characterized after incubation with organosilicon compounds (HMDS, PDMS and Infacol) and compared to control SLBs (no incubation) and bare ITO. Using XPS, with a probing depth of ~10 nm, a signal was detected from the entire SLB and the outer surface of the substrate. As such, this technique gave a comprehensive overview of the elemental composition of a lipid bilayer. Measurements were performed using a JEOL 9200 (JEOL Ltd., Tokyo, Japan) with a monochromatic Al Kα X-ray source operated at 12 kV, with a beam current of 20 mA. The analyzer pass energy was set to 10 eV. Wide scans (0 – 800 eV) were recorded for inspection of all present elements. Narrow scans in the range of 90 – 105 eV were acquired to provide more detailed information about silicon presence. Spectra were fitted by Casa XPS software (www.casaxps.com) for quantification.

4.3.10 Auger Electron Spectroscopy

AES was performed using a JEOL JAMP-9500F field emission scanning Auger microprobe (JEOL Ltd., Tokyo, Japan). Briefly, this instrument probes chemical bonds by irradiating a surface locally with a focused electron beam and measuring the energetic spectrum of electrons emitted through the Auger effect. These secondary electrons with relatively low energy primarily originate from a 2-3 nm layer at the surface. Scanning this beam with a small irradiation spot size allows the acquisition of hyperspectral images with a sub-micron spatial resolution. In conjunction, the instrument can be operated in scanning electron microscopy (SEM) mode, for comparing the morphological appearance of the sample.

Cells incubated with HMDS and Infacol and cells cultured on PDMS dishes were compared to non-incubated cells as negative controls. Areas with around 20 to 200 cells were divided into fields of 256x256 pixels which were scanned in the narrow bands for gold (Au_{MNN}, 2015 eV), silicon (Si_{LMM} 92 eV), carbon (C_{KLL} 263 eV)

and nitrogen (N_{KLL} 375 eV) with a dwell time of 100 ms per pixel. Narrow band signals were integrated and background subtracted in Spectra Inspection Software (JEOL). The resulting bitmaps were converted to binary images and diluted in ImageJ. Across every row of Figure 4.2c, the images were treated with the same threshold settings.

4.3.11 IR spectroscopy

The samples inspected with AES were next analyzed using IR spectroscopy on an Attenuated Total Reflection (ATR) with Alpha-P spectrometer from Bruker (Billerica, MA, USA). All spectra were obtained by averaging 32 scans. The resolution was set at 4 cm^{-1}. All spectra were recorded at room temperature and ambient atmosphere. These samples were also measured by using reflection FTIR spectra using a 50-µm diameter aperture in a Bruker Hyperion 1000 spectrometer equipped with a 15× objective coupled to a Bruker Tensor 27 FTIR spectrometer. A liquid nitrogen cooled MCT wideband detector is used to detect a spectral range from 4000–600 cm^{-1}. A background spectrum was collected from plasma-cleaned gold surfaces. In addition to these samples, a gold substrate was homogeneously coated with a thin layer of liquid PDMS to compare the magnitude of the signal from silicone compounds found in cells to those found in pure polymer. Sylgard 184 base and curing agent were mixed in a 10:1 weight ratio and a droplet of this mixture was placed on a cleaned gold surface and spread uniformly using a clean glass microscope slide, resulting in a thin (several µm), coating. This sample was stored at room temperature and measured after 12 h.

4.3.12 Results and discussion

Figure 4.2a presents the mean Raman spectrum of cells dried in absence (Figure 4.2a (1, green line), negative control) and presence (Figure 4.2a (2, pink line)) of HMDS. HMDS-dried cells give rise to four main peaks at 490, 710, 2906 and 2964 cm^{-1} that are not detected in the negative control samples. This shows that HMDS does not fully evaporate despite its residence at 24-mbar vapor pressure inside the SEM at room temperature. Further confirmation of the presence of

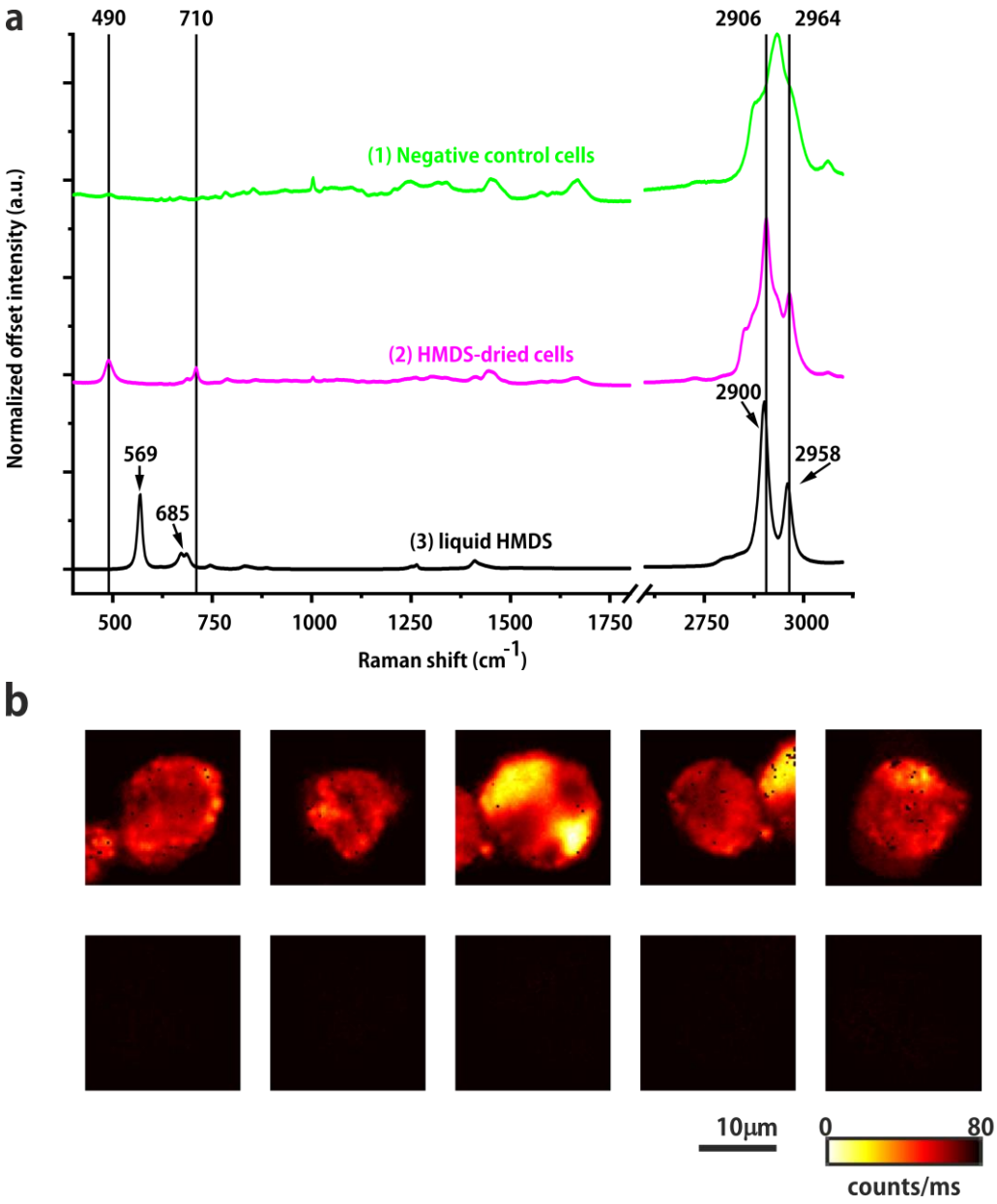
a
490
710
2906
2964
(1) Negative control cells
(2) HMDS-dried cells
2900
569
2958
685
(3) liquid HMDS
Normalized offset intensity (a.u.)
500
750
1000
1250
1500
1750
2750
3000
Raman shift (cm-1)
b
10μm
0
80
counts/ms

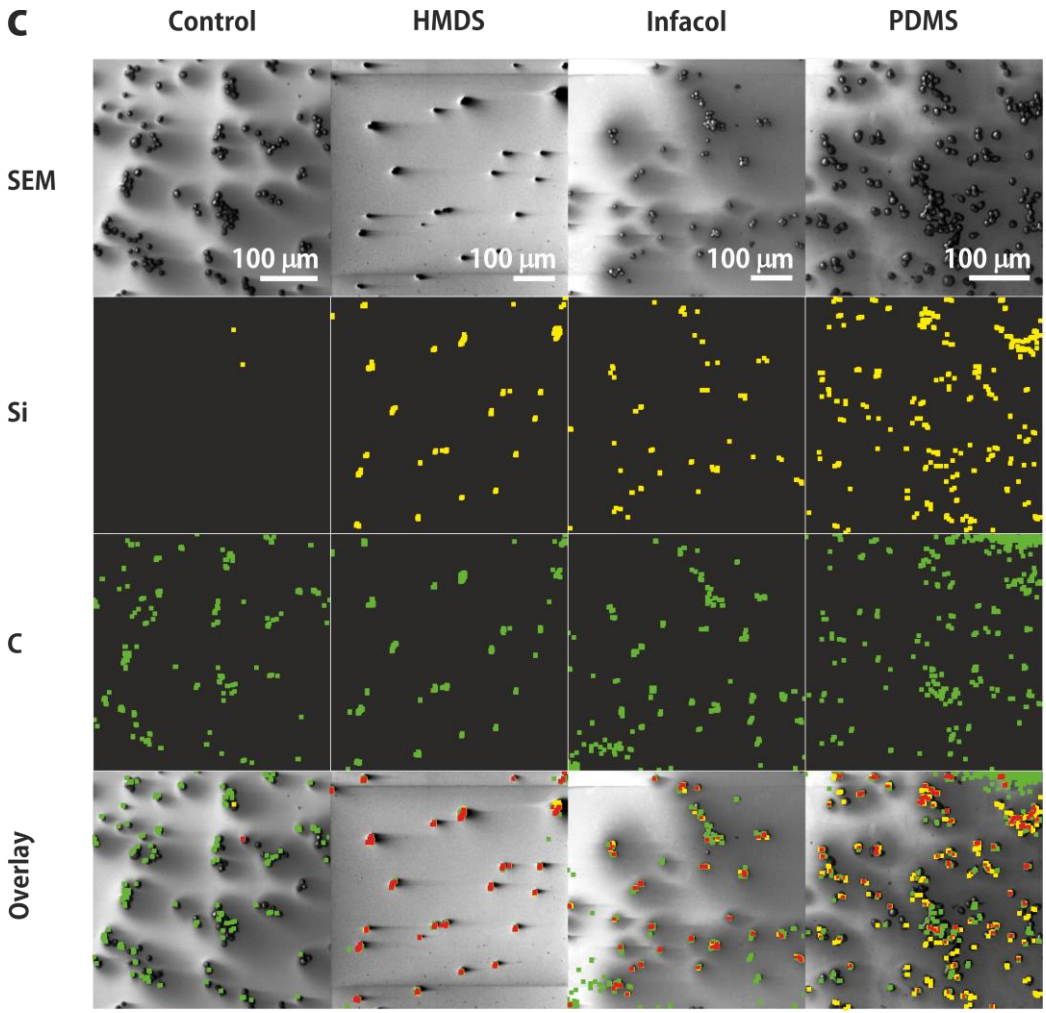

Figure 4.2: Imaging spectroscopic analysis of individual cells. a) Normalized mean Raman spectra of: (1) 5 negative control cells (green), (2) 5 HMDS-dried cells (magenta), (3) neat (liquid) HMDS (black). b) Raman images of HMDS-dried cells (top row) and negative control cells (bottom row) obtained by integration of the band between 450 and 550 cm-1, the region in which the peak assigned to Si-C bonds is located. Raman images were acquired with 35 mW laser excitation power, 100 ms illumination time and 0.31-µm scanning step size. c) AES/SEM inspection of the silicon (yellow) and carbon (green) content of cells incubated with silicones compared to non-incubated samples (negative controls). In the same locations, overlapping with cells as shown by SEM, both silicon and carbon are found (overlapping dilated pixels corresponding to both Si and C are indicated in red). The original AES spectra revealing also the presence of N 1s in all cells are provided in Appendix B.2.

HMDS in cells is presented in Figure Appendix B.4. The spectrum in Figure 4.2a (3, black line) from liquid HMDS shows bands at 569, 685, 2900 and 2958 cm^{-1}, which have shifted to 490, 710, 2906 and 2964 cm^{-1}, respectively for HMDS in cells. The band positions of HMDS are therefore assigned to an interaction product of HMDS with cellular components, potentially membranes, proteins and sugars, and the formation of silyl ethers. Figure 4.2b presents Raman images of cells dried with (top row) and without (negative control, bottom row) HMDS, obtained by integration of the band between 450 and 550 cm^{-1}, confirming the absence of HMDS-related bands in the negative control cells.

Since AES has a probing depth of only 3 nm, it only detects elements located either ***in*** or ***on*** the cell membrane. Therefore, AES was next used to get more insights into the exact localization of the Si species. As depicted on Figure 4.2c, in all incubated samples a Si_{LMM} signal was detected, which was almost entirely absent in the negative control samples, while in all samples including the negative controls, as expected, the presence of carbon atoms was revealed.

Using XPS, whose probing depth reaches ∽10 nm, brings information across the entire SLB thickness, as well as on the supporting substrate. XPS wide scans (see Figure 4.3a) revealed, as expected, the presence of a C 1s signal at 285 eV after formation of a SLB (red), as well as a marked decrease in the signal coming from the ITO (Indium-Tin-Oxide) substrate (e.g., the peak attributed to In 3d at 444 eV). The respective atomic fractions of In 3d, C 1s and Si species per sample indicate that the C 1s signal strongly increased after incubation of the SLBs with any of the organosilicon compounds. This increased carbon signal was accompanied by the emergence of Si 2s and Si 2p peaks at ~153 eV and ~102 eV, respectively, and the concomitant additional decrease of the In 3d signal (Figure 4.3b). Noteworthy, a faint Si 2p signal (shifted to ~102.5 eV), having typically an intensity seven times lower than the three categories above, was consistently observed in the non-incubated SLB samples. The same SLB samples, that were used for AES measurements, were analyzed by IR spectroscopy. Full IR spectra are provided in Appendix B.3. Close inspection of the 1180-1300 cm^{-1} region unveils an absorption band for pure PDMS at 1257 cm^{-1}, corresponding to the symmetric stretch of the Si-C bond.[33] In the same region, broad bands were found in cell samples incubated with organosilicon compounds, but they were

typically red-shifted to ~1230 cm^{-1}.[27] Interestingly, this band was absent in all control samples, suggesting that this absorption band could be associated with the presence of organosilicon species in the cell samples. This shift can be the result of a change in environment of the polymer species, e.g., by confinement within the cell membrane[34] and concomitant change in dipolar interactions.

Previously, it was demonstrated elsewhere[35] that small hydrophobic molecules such as drugs and hormones can absorb into the PDMS matrix. Similarly, PDMS can release unpolymerized precursor molecules in solutions, as notably reported by Regehr et al. .[6,36] The results presented here suggest that a-polar organosilicon compounds *in general* can embed within various biological *membranes*, driven by physicochemical interactions and not by active uptake.

Raman spectroscopy identified the presence of HMDS in cells dried in its presence. The shift of HMDS-related Raman peaks from liquid, neat HMDS to HMDS-dried in cells suggests that HMDS reacts with molecules in cells and/or their membranes. Raman spectroscopic imaging of single cells (Figure 4.2b) reveals that organosilicon compounds are also present intracellularly, at lipid-rich areas, e.g., in the membrane of organelles.

AES results collectively suggest that the presence of Si originates from the incubation of the cells with silicones. Furthermore, these results indicate that these Si-containing compounds are located in the outer 3 nm of the cells, i.e., in or on the plasma membrane of the cells, which does not exclude their presence elsewhere in the cells.

Similar interactions were found in SLBs acting here as simplified models for cell membranes, suggesting that the incorporation of silicones into membranes is a passive process, i.e., not driven by membrane proteins or other endocytic processes. The fact that, using XPS, traces of silicon were observed in DOPC SLBs, potentially as a result of contamination from ambient organosilicon compounds (e.g., silanes), further illustrates the energetic favorability of a-polar organosilicon compounds to interact with the phospholipid aliphatic chains.

The previous results strongly suggest that organosilicon compounds are retained in biological systems and more precisely, associate with lipids in biological membranes. Although the precise interaction is not clear, it is unlikely that a chemical reaction occurred between, on one hand, PDMS and

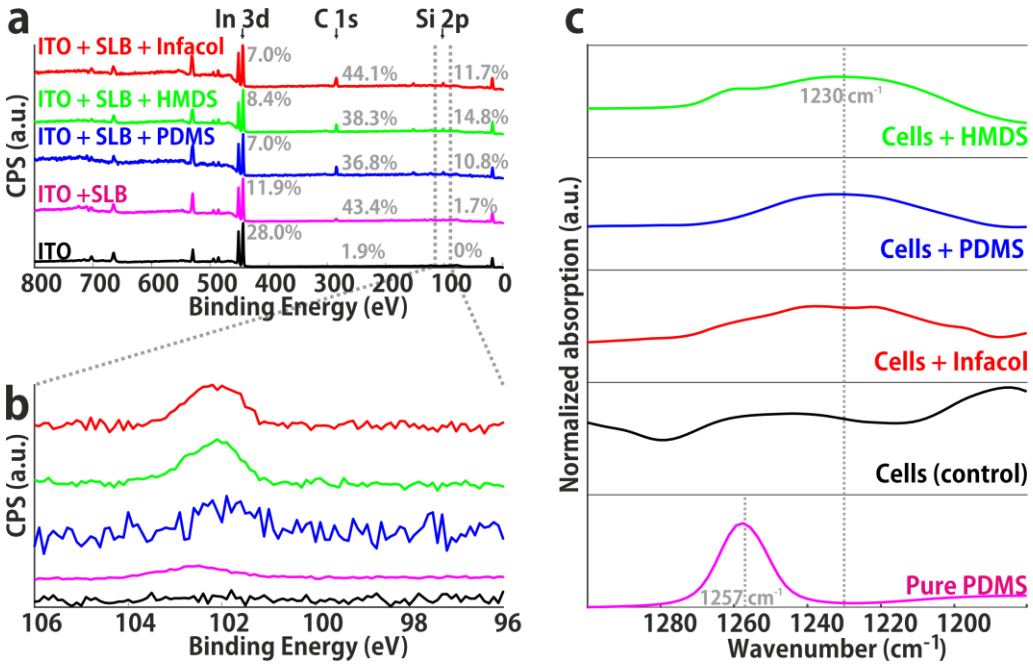

Figure 4.3. Spectroscopic analysis by XPS and IR of biological membranes in the form of SLBs and biological cells. *(a) XPS wide scan showing all atomic species present; carbon content (285 eV) increases after SLB formation and again after silicone introduction. The relative contribution of In 3d (444eV) decreases after incubation steps. (b) XPS narrow scan in the Si 2p region, showing increase after silicone introduction. The presence of a trace amount of Si 2p in DOPC supported lipid bilayers (magenta) indicates a minor impurity of the chemicals. (c) Si-C region in IR spectra obtained from pure PDMS (pink) and cells incubated with various organosilicon compounds (green, HMDS; blue, PDMS; red, Infacol; black, negative control). Incubated cells show a shift in a peak (~1250 cm-1 → ~1230 cm-1) compared to negative control cells.*

(components of) Infacol and, on the other hand, biological specimens, or that any electrostatic interactions took place, since none of the silicones discussed here are charged. The exact location of the silicones – adsorbed on the outside of the membranes or embedded in the membrane – is at present not clear, as both areas would be observed with AES. Embedding in the membrane is most probable, assuming hydrophobic interactions between the trimethyl silyl moieties and the lipid tail environment.

(components of) Infacol and, on the other hand, biological specimens, or that any electrostatic interactions took place, since none of the silicones discussed here are charged. The exact location of the silicones – adsorbed on the outside of the membranes or embedded in the membrane – is at present not clear, as both areas would be observed with AES. Embedding in the membrane is most probable, assuming hydrophobic interactions between the trimethyl silyl moieties and the lipid tail environment.

PDMS and (components of) Infacol were not observed inside the cells, but HMDS, having a much lower molecular weight, was able to transfer into the intracellular compartment. Some understanding can be derived from a thermodynamic argument, which is that the polymer molecules in the vicinity of lipids have lower interfacial energy than those surrounded by water. From this reasoning, it follows that the larger the molecule, the more stable the coordination, which may explain that PDMS oligomers (1.5 – 6 kDa) and Infacol (14 – 21 kDa) were not observed inside cells, but HMDS (MW = 161 Da) was able to transfer into the intracellular compartment. To minimize the contact with water, the polymers (with a length of several tens of nanometers) would need to be completely internalized within the phospholipid bilayer (with a thickness of around 5 nanometers), thereby stretching out to fit in this quasi-2D landscape (Figure 4.4, right panel). This reduction in solvation energy[37] is balanced by an entropic cost, as it is entropically more favorable for polymers to assume a coiled or globular conformation[38,39] (Figure 4.4, middle panel) and since trimethyl silyl groups are large compared to linear alkyl chains. Alternatively, the polymer molecules may also span the membrane in multiple regions, much like a transmembrane protein (Figure 4.4, middle panel). This compromise would give the organosilicon molecules more fluidity, while overall still resulting in an energetically favorable coordination. To study the actual conformation (which may also depend non-linearly on concentration)[40], computation modeling is required, or the use of advanced optical tools, such as FRAP (Fluorescence recovery after photobleaching), which should reveal changes in the overall lipid bilayer properties. Although the precise conformation of organosilicon compounds in biological membranes is thus not clear, the results presented here demonstrate that interactions occur passively and for multiple types of compounds and membranes.

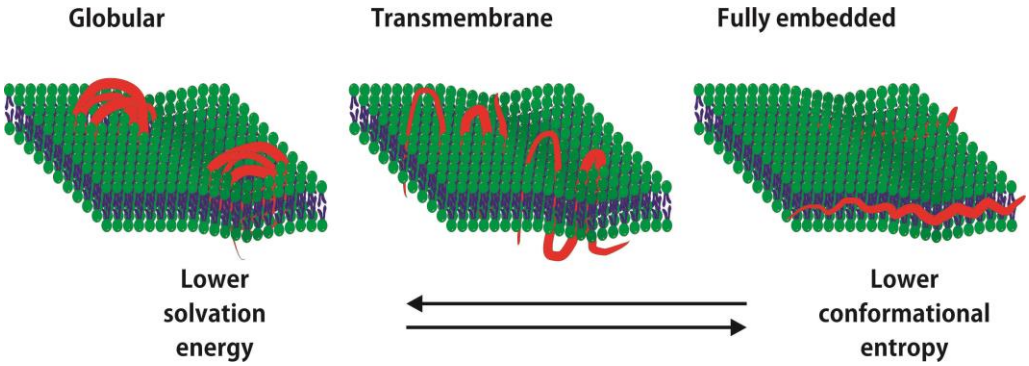

Figure 4.4. Models proposed with different possible conformations for silicone oligomers and polymers in lipid membranes. *Embedding of the polymer within the membrane decreases the solvation energy but is balanced by the entropic cost of uncoiling the oligomer molecule.*

In conclusion, the results presented here reveal the incorporation of organosilicon compounds in cellular membranes. From this, it can be inferred that the impact of organosilicon compounds on sample preparation, experimental outcome and perhaps even human health should not be ignored. As an example, in studies involving chemical analysis of HMDS-fixed cells[41], it should be noted that the HMDS interferes with the signal. The FDA has cleared several organosilicon compounds for applications in food, cosmetics and pharmaceuticals on the assumption that these materials are not systemically absorbed.[1,42–44] Knowing that interactions with biological membranes are relatively stable, the notion that silicones are not systemically absorbed needs to be reconsidered.

4.4 References

1. Linti, G. Organosilicon Chemistry V. From Molecules to Materials. By Norbert Auner and Johann Weis. *Angew. Chemie Int. Ed.* **43**, 2744 (2004).
2. Joint FAO/WHO Expert Committee on Food Additives (JECFA). WHO Technical Report Series 966 EVALUATION OF CERTAIN FOOD ADDITIVES AND CONTAMINANTS. *World Heal. Organ.* 27–32 (2011). doi:10.1016/S0140-6736(02)11326-2
3. Berthier, E., Young, E. W. K. & Beebe, D. Engineers are from PDMS-land, biologists are from polystyrenia. *Lab Chip* **12**, 1224–1237 (2012).
4. Metcalf, T. J., Irons, T. G., Sher, L. D. & Young, P. C. Simethicone in the Treatment of Infant Colic: A Randomized, Placebo-Controlled, Multicenter Trial. *Pediatrics* **94**, 29 LP – 34 (1994).
5. PART 332-ANTIFLATULENT PRODUCTS FOR OVER-THE-COUNTER HUMAN USE. *Fed. Regist.* **39**, 19877 (1974).
6. Regehr, K. J. *et al.* Biological implications of polydimethylsiloxane-based microfluidic cell culture. *Lab Chip* **9**, 2132–2139 (2009).
7. de Almeida Monteiro Melo Ferraz, M., Nagashima, J. B., Venzac, B., Le Gac, S. & Songsasen, N. 3D printed mold leachates in PDMS microfluidic devices. *Sci. Rep.* **10**, 1–9 (2020).
8. Duffy, D. C., McDonald, J. C., Schueller, O. J. A. & Whitesides, G. M. Rapid prototyping of microfluidic systems in poly(dimethylsiloxane). *Anal. Chem.* **70**, 4974–4984 (1998).
9. Delamarche, E., Schmid, H., Michel, B. & Biebuyck, H. Stability of molded polydimethylsiloxane microstructures. *Adv. Mater.* **9**, 741–746 (1997).
10. Unger, M. A., Chou, H. P., Thorsen, T., Scherer, A. & Quake, S. R. Monolithic microfabricated valves and pumps by multilayer soft lithography. *Science (80-.).* **288**, 113–116 (2000).
11. Esteves, T. C. *et al.* A microfluidic system supports single mouse embryo culture leading to full-term development. *RSC Adv.* **3**, 26451–26458 (2013).
12. Kieslinger, D. C. *et al.* In vitro development of donated frozen-thawed human embryos in a prototype static microfluidic device: A randomized controlled trial. *Fertil. Steril.* **103**, 680-686.e2 (2015).
13. De Almeida Monteiro Melo Ferraz, M. *et al.* Potential Health and Environmental Risks of Three-Dimensional Engineered Polymers. *Environ. Sci. Technol. Lett.* **5**, 80–85 (2018).
14. Ryan, J. W. Prevention of anal leakage of polyorganosiloxane fluids used as fat substitutes in foods. 1–4 (1988).
15. H.M. Lee, J. Baines, R. Walker, P. M. K. *Safety evaluation of certain food additives*. (2009).
16. Futrega, K. *et al.* Polydimethylsiloxane (PDMS) modulates CD38 expression, absorbs retinoic acid and may perturb retinoid signalling. *Lab Chip* **16**, 1473–1483 (2016).
17. Łopacińska, J. M., Emnéus, J. & Dufva, M. Poly(Dimethylsiloxane) (PDMS) Affects Gene Expression in PC12 Cells Differentiating into Neuronal-Like Cells. *PLoS One* **8**, 1–11 (2013).
18. Gusnard, D. & Kirschner, R. H. Cell and organelle shrinkage during preparation for scanning electron microscopy: effects of fixation, dehydration and critical point drying. *J. Microsc.* **110**, 51–57 (1977).
19. Lytton, D. G., Yuen, E. & Rickard, K. A. Scanning electron and light microscope correlation of individual human bone marrow cells before and after culture in nutrient agar. *J. Microsc.* **115**, 35–49 (1979).
20. Boyde, A. & Maconnachie, E. *Histochemistry Treatment with Lithium Salts Reduces Ethanol Dehydration Shrinkage of Glutaraldehyde Fixed Tissue*. *Histochemistry* **66**, (1980).

21. Katsen-Globa, A., Puetz, N., Gepp, M. M., Neubauer, J. C. & Zimmermann, H. Study of SEM preparation artefacts with correlative microscopy: Cell shrinkage of adherent cells by HMDS-drying. *Scanning* **38**, 625–633 (2016).
22. Boyde, A. & Maconnachie, E. Morphological correlations with dimensional change during SEM specimen preparation. *Scan. Electron Microsc.* **4**, 27–34 (1981).
23. Brunk, U., Collins, V. P. & Arro, E. The fixation, dehydration, drying and coating of cultured cells for SEM. *J. Microsc.* **123**, 121–131 (1981).
24. Braet, F., De Zanger, R. & Wisse, E. Drying cells for SEM, AFM and TEM by hexamethyldisilazane: A study on hepatic endothelial cells. *J. Microsc.* **186**, 84–87 (1997).
25. Nation, J. L. A new method using hexamethyldisilazane for preparation of soft insect tissues for scanning electron microscopy. *Biotech. Histochem.* **58**, 347–351 (1983).
26. Nicholson, J. D. Derivative formation in the quantitative gas-chromatographic analysis of pharmaceuticals. Part II: A review. *Analyst* **103**, 193–222 (1978).
27. Essaid, D. *et al.* Artificial plasma membrane models based on lipidomic profiling. *Biochim. Biophys. Acta - Biomembr.* **1858**, 2725–2736 (2016).
28. Sackmann, A. E., Science, S., Series, N., Jan, N. & Sackmann, E. Supported Membranes : Scientific and Practical Applications. *Science (80-.).* **271**, 43–48 (2019).
29. Milbrat, A. *et al.* Integration of Molybdenum-Doped, Hydrogen-Annealed BiVO 4 with Silicon Microwires for Photoelectrochemical Applications. *ACS Sustain. Chem. Eng.* **7**, 5034–5044 (2019).
30. Beekman, P. *et al.* Immuno-capture of extracellular vesicles for individual multi-modal characterization using AFM, SEM and Raman spectroscopy. *Lab Chip* **19**, 2526–2536 (2019).
31. Desai, G. *et al.* Oral Pharmaceutical Compositions of Simethicone. 28 (2008).
32. Enciso-Martinez, A., Timmermans, F. J., Nanou, A., Terstappen, L. W. M. M. & Otto, C. SEM–Raman image cytometry of cells. *Analyst* **143**, 4495–4502 (2018).
33. Tsao, M. W. *et al.* Formation and characterization of self-assembled films of thiol-derivatized poly(dimethylsiloxane) on gold. *Macromolecules* **30**, 5913–5919 (1997).
34. Soga, I. & Granick, S. *Backbone orientation of adsorbed polydimethylsiloxane*. *Studies in Surface Science and Catalysis* **132**, (Elsevier Masson SAS, 2001).
35. Halldorsson, S., Lucumi, E., Gómez-Sjöberg, R. & Fleming, R. M. T. Advantages and challenges of microfluidic cell culture in polydimethylsiloxane devices. *Biosens. Bioelectron.* **63**, 218–231 (2015).
36. Carter, S.-S. D. *et al.* PDMS leaching and its implications for on-chip studies focusing on bone regeneration applications. *Organs-on-a-Chip* **2**, 100004 (2020).
37. Leermakers, F. A. M., Scheutjens, J. M. H. M. & Lyklema, J. On the statistical thermodynamics of membrane formation. *Biophys. Chem.* **18**, 353–360 (1983).
38. Kuhl, T. *et al.* Direct measurement of polyethylene glycol induced depletion attraction between lipid bilayers. *Langmuir* **12**, 3003–3014 (1996).
39. Polson, J. M. & Moore, N. E. Simulation study of the coil-globule transition of a polymer in solvent. *J. Chem. Phys.* **122**, (2005).
40. Zhang, H.-Y. & Hill, R. J. Lipopolymer gradient diffusion in supported bilayer membranes. *J. R. Soc. Interface* **8**, 312–321 (2011).
41. Enciso-Martinez, A., Timmermans, F. J., Nanou, A., Terstappen, L. W. M. M. & Otto, C. SEM–Raman image cytometry of cells. *Analyst* **143**, 4495–4502 (2018).
42. Code of Federal Regulations. *Title 21, Volume 3, section 173.340*. (2018).
43. Code of Federal Regulations. *Title 21, Volume 5, section 347.10*. (2018).
44. Code of Federal Regulations. *Title 21, Volume 8, section 878.3530*. (2018).

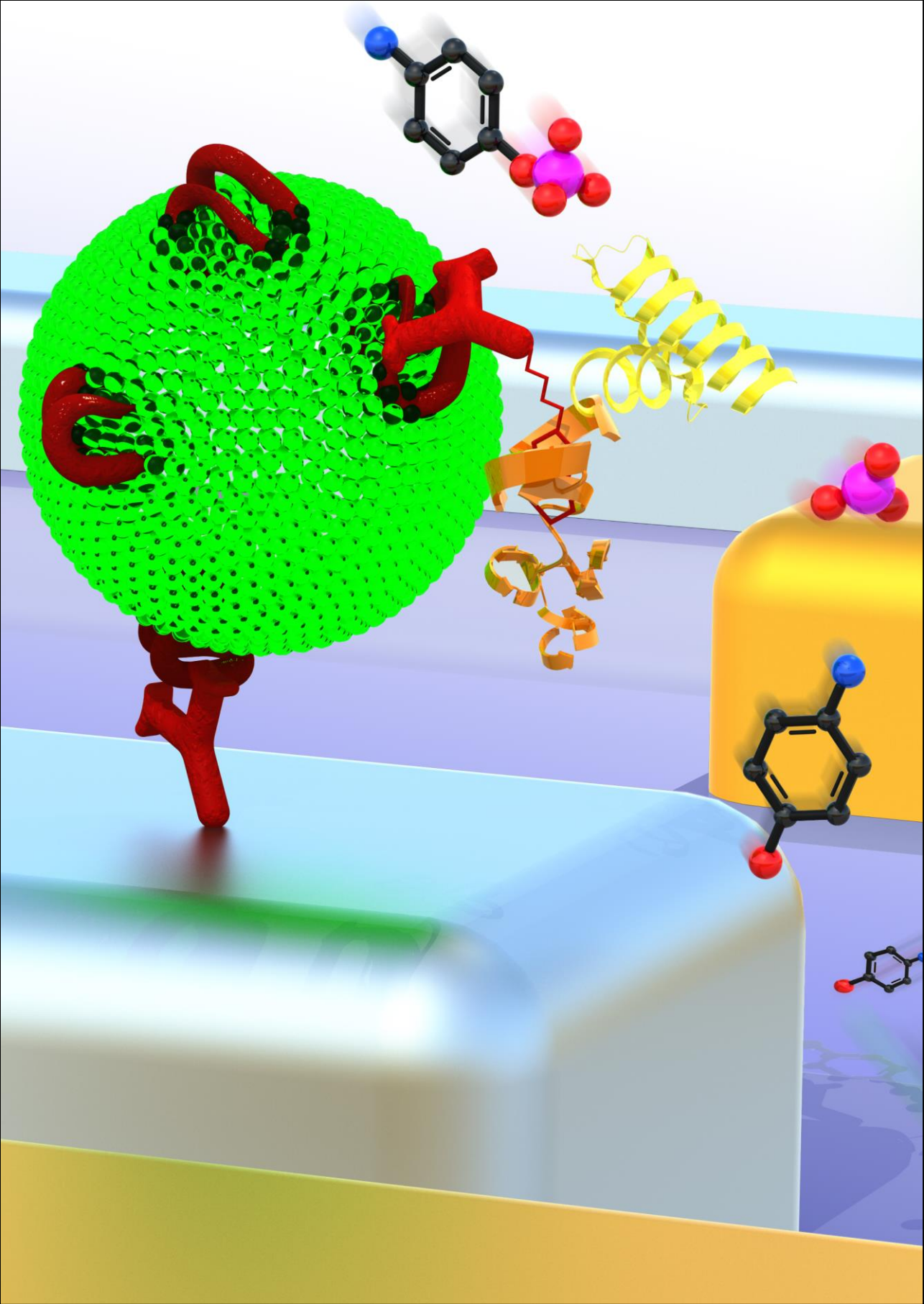

5

Electrochemical detection of tumor-derived extracellular vesicles on nano-interdigitated electrodes

This chapter was originally published as:

Dilu G. Mathew, Pepijn Beekman, Serge G. Lemay, Han Zuilhof, Séverine Le Gac, Wilfred G. van der Wiel, Electrochemical detection of tumor-derived extracellular vesicles on nano-interdigitated electrodes, Nano Letters. 2020, 20, 2, 820–828

5.1 Abstract

Tumor-derived extracellular vesicles (tdEVs) are attracting much attention due to their essential function in intercellular communication and their potential as cancer biomarkers. Although tdEVs are significantly more abundant in blood than other cancer biomarkers, their concentration compared to other blood components remains relatively low. Moreover, the presence of particles in blood with a similar size as that of tdEVs makes their selective and sensitive detection further challenging. Therefore, highly sensitive and specific biosensors are required for tdEV unambiguous detection in complex biological environments especially for decentralized point-of-care analysis. Here, we report an electrochemical sensing scheme for tdEV detection, with two-level selectivity provided by a sandwich immunoassay and two-level amplification through the combination of an enzymatic assay and redox cycling on nano-interdigitated electrodes to respectively enhance the specificity and sensitivity of the assay. Analysis of prostate cancer cell line tdEV samples at various concentrations revealed an estimated limit of detection for our assay as low as 5 tdEVs/µl, as well as an excellent linear sensor response spreading over six orders of magnitude (10 – 10^6 tdEVs/µl), which importantly covers the clinically relevant range for tdEV detection in blood. This novel nanosensor and associated sensing scheme opens new opportunities to detect tdEVs at clinically relevant concentrations from a single blood finger prick.

5.2 Introduction

Liquid biopsies are highly promising for metastatic cancer disease management.[1] In this non-invasive approach, a sample of blood (typically a few ml, *e.g.* from a finger prick) is screened for the presence of tumor biomarkers, such as circulating tumor DNA (ctDNA), miRNAs, tumor-derived extracellular vesicles (tdEVs), or circulating tumor cells (CTCs).[2] It has been established that,

compared to imaging techniques (magnetic resonance imaging (MRI) in conjunction with computed tomography (CT)), CTC quantification in liquid biopsies has a better prognostic value,[1, 3] while being significantly less demanding from a clinical point-of-view: the procedure is much more patient-friendly, cheaper and does not require any administration of toxic contrast agents. Furthermore, blood analysis can be repeated at higher frequency (*e.g.*, a few times per month *vs.* a few times per year for MRI), while allowing close monitoring of a patient's response to therapy. However, the main challenge to be overcome in this approach is the extremely low relative concentration of CTCs. Moreover, for every CTC (typically <10 CTCs per ml of blood), there are millions of white blood cells and billions of red blood cells. In contrast to CTCs, tdEVs, which are constantly released by tumor cells in blood, occur at a much higher concentration (10 – 10^6 EVs per µl of blood).[4] Extracellular vesicles (EVs) are nanometer-sized (30 nm - 1 µm) particles, enclosed by a phospholipid bilayer membrane and containing a great variety of biological molecular information on their cells and/or tissues of origin.[5-7] EVs are shed by all cell types and found in all bodily fluids, where they play an important role in (inter)cellular communication.[8-9] All EVs share the same generic EV-membrane protein repertoire, *e.g.*, CD9, CD63, and CD81 being present on the vast majority of blood cell-derived EVs.[10-11] Next to this, tdEVs exhibit membrane proteins that are specific of their cellular origin, *e.g.*, cancer biomarkers HER2, EGFR, and epithelial cell adhesion molecule (EpCAM).[1, 10, 12] Notably, EpCAM has been widely used for the isolation and detection of both CTCs and tdEVs,[1] which are found in blood from the early stages of cancer to metastasis. The concentration of both CTCs and tdEVs increases with the progression of the tumor.[13-16] The wide spread of tdEV concentrations naturally occurring in blood, makes them promising alternative cancer biomarkers. The variation between patients with low and high tdEV abundance is relatively much higher than for CTCs (a factor of 10^6 for EVs *vs.* a factor of maximally $\backsim 10^3$ for CTCs), and therefore statistically more unlikely to yield false negative results.

However, before tdEVs can be considered in clinical routines and liquid biopsy analysis, reliable, unambiguous, highly sensitive and specific methods must be developed for their isolation, detection and quantification in complex matrices such as blood. Species in the EV size range are difficult to characterize using

existing analytical techniques suitable to single molecules or cells, which are, respectively, smaller and larger than EVs. Furthermore, blood comprises various other entities in the same size range as EVs and often present with much higher concentrations, such as protein aggregates, lipoproteins, cell debris and, most notably, non-cancerous EVs, from which tdEVs need to be unequivocally distinguished.[17] EVs are often studied using flow cytometry and/or fluorescence microscopy.[18-24] Although these techniques provide unique molecular information on tdEVs, they often lack the sensitivity and/or resolution required to detect both the rarest and/or smallest tdEVs. These techniques also require substantial sample volumes. In contrast, single EVs can be detected using atomic force microscopy (AFM),[25] nanoparticle tracking analysis (NTA),[26] resistive pulse sensing,[26] Raman spectroscopy[27-28] or a combination of some of these techniques, whose throughput and level of technicality is however too low for practical medical/clinical use.

Altogether there is a clear need to be able to detect tdEVs at concentrations as low as 1-100 per µl and across an extended clinically relevant concentration range.[4] However, only few endeavors have led to the development of sensors sensitive enough to detect such low concentrations. Recently, Zhang *et al.*[29] reported immunocapturing of tdEVs on antibody-modified herringbone in microfluidic channels followed by their detection using fluorescence microscopy, after amplification of the signal using an enzymatic reaction. Although they reported a limit of detection (LOD) of 10 EVs/µl, the signal was barely distinguishable from the background, and their approach worked over a linear detection range from 10 – 10^3 EVs/µl. Using amperometric detection of enzymatic activity after magnetic immuno-enrichment with nanocubes, Boriachek *et al.*[30] analyzed EVs from placental cells using placenta alkaline phosphatase as marker. Their reported LOD was as low as 1 tdEV/µl; However, again the linear range of their assay only covered a 1 – 10^4 EVs/µl concentration range. Huang *et al.*[31] developed an electrochemical detection platform using aptamers as detection probes and a combination of hemin/G-quadruplex DNAzyme-peroxidase reaction and complex rolling circle amplification to achieve signal amplification. Although they achieved a detection limit of ~1 tdEV/µl, they as well had a narrow linear range of detection of 1 to 10^3 EVs/µl, making it less versatile for clinical applications.

Here, we report an ultrasensitive tdEV detection assay at clinically relevant concentrations using a double amplification mechanism combining redox cycling and an enzymatic reaction, as well as a sandwich immunoassay ensuring a two-level selectivity. The assay is implemented in a lab-on-a-chip (LOC) format allowing the analysis of small sample amounts, in the (low) microliter range.

Uniquely, the linear dynamic range achieved with our assay spanning 6 orders of magnitude largely overlaps with the range of tdEV concentrations naturally occurring in cancer patient blood. Using tdEVs obtained from cell culture medium, we experimentally demonstrated a LOD of 10 tdEVs/µl well above the background signal in our assay and extrapolated a theoretical LOD as low as a 5 tdEVs/µl from the established calibration curve. Compared to previously reported methods, our antifouling coating in combination with our two-fold selective scheme awards excellent specificity for tdEV detection compared to EVs of other origins, as demonstrated here using platelet-derived EVs (giving 60 times less signal at a 10^2-fold higher concentration).

5.3 SANDWICH IMMUNOASSAY ON NANOSCALE INTERDIGITATED ELECTRODES

The detection principle of our assay is illustrated in Figure 5.1. To achieve an amplification level that is powerful enough to detect tdEVs at physiologically relevant concentrations, we use a two-level amplification strategy: (i) a first enzymatic amplification using alkaline phosphatase (ALP), releasing electrochemically active species, followed by (ii) electrical signal amplification via electrochemical redox cycling on nanoscale interdigitated electrodes (nIDEs). Given the complexity of the targeted biological sample, exquisite selectivity is required to get a signal that solely arises from the presence of tumor-derived species, *i.e.*, with a low background signal. Here, a sandwich immunoassay with tumor-specific antibodies is implemented providing a two-level selectivity. The assay comprises a capture anti-EpCAM (C-AE) antibody that captures tdEVs and

a reporter antibody (anti-EpCAM, R-AE) conjugated to ALP through biotin-streptavidin interactions. Here, the same antibody clone is employed for the two steps of the immune-affinity assay, VU1D9, which is an anti-EpCAM clone proven to be stable and to have high affinity for EpCAM ($K_d \sim 2.7\times10^{-10}$ M).[32] Tethering of C-AE on the electrodes involves three steps. Firstly, amine-terminated thiol (amino-undecane thiol, AUT) is self-assembled on the Pt electrodes. Secondly, an amine-reactive bifunctional poly(ethylene glycol) diglycidyl ether (PEGDGE) is reacted with the AUT layer to form a second anti-fouling layer. Subsequently, the C-AE antibody is covalently linked under mild conditions at a slightly basic pH (8.3) and high ionic strength (2 M sodium phosphate).[33] This C-AE enables the specific capture of tdEVs derived from EpCAM-expressing human prostate adenocarcinoma cell lines (LNCaP), and provides as such the first level of selectivity. After their capture, the tdEVs interact with biotinylated reporter anti-EpCAM antibodies (R-AE), to provide the second level selectivity, since non-cancerous EVs (*e.g.*, blood cell-derived) would not be recognized by neither the C-AEs nor the R-AEs. The use of the same antibody clones for both immuno-affinity steps can lead to the partial dissociation of the antibody/antigen complex formed between the C-AE and EVs to form a new antibody/antigen complex with R-AE, releasing thereby the EVs from the surface. Using a distinct pair of antibodies as C-AE and R-AE (e.g., VU1D9 and HO-3) would be more favorable in this context. However, considering it may be entropically unfavorable for R-AE to approach the C-AE/antigen complex and because each EV should be captured through multiple antigen/antibody interactions, it seems very unlikely that EVs are released during the second immune-affinity step. The biotin moiety of R-AE next interacts with streptavidin-conjugated alkaline phosphatase (SAV-ALP). ALP is well known for its ability to cleave substrates containing phosphate groups. Here, the substrate (para-aminophenyl phosphate, pAPP) is chosen since its uncleaved form is electrochemically inert, while its cleaved form, para-aminophenol (pAP), is electrochemically active. This enzymatic reaction provides the first amplification mechanism. During electrochemical measurements, one of the working electrodes of the nIDE is kept at the reduction potential (a potential well below the formal potential) of pAP, while the second working electrode is swept from a potential below to a potential above its formal potential. At the anode, pAP is oxidized into para-quinone imine (pQI), which

diffuses towards the cathode. At the cathode, pQI is reduced back into pAP. The electrochemical reaction can be denoted as: pAP ⇆ pQI + $2e^-$. Since the gaps between the electrodes of the nIDEs are small (120 nm), the pAP and PQI molecules continuously and efficiently shuttle between the two working electrodes via diffusion, producing a steady-state current, which directly scales with the tdEV concentration. This redox cycling provides the second level of amplification.

The nIDEs comprised two sets of interdigitated nanoelectrode arrays (100 nm width, 30 µm length, 120 nm spacing and 70 nm height) defined by electron-beam lithography and platinum evaporation. The narrow spacing between the electrodes tremendously enhanced the redox cycling performance, while still allowing the capture of the smallest (most abundant) EVs in the void between the electrodes.[34] EVs larger than 120 nm can be captured on the top surface of the electrodes and can simply contribute to the signal following the same mechanism.

The sensing area of the nIDEs was embedded in a polydimethylsiloxane (PDMS) microfluidic channel (0.2 × 3 × 6 mm^3) to facilitate the exchange of reagents by simple micropipetting directly through the channel inlet during surface modification and electrochemical measurements (see AppendixC.1).[35] A pipette tip was installed in the outlet of the microfluidic device as a collection reservoir facilitating the back-and-forth injection of sample using pipetting and handling of volumes larger than the microchannel itself. After the introduction of every new component, a washing step was implemented by injecting 100 µl phosphate buffered saline (PBS).

5.4 tdEV detection on nIDEs

tdEVs were prepared following the protocols described in chapter 2. In brief, tdEVs were isolated from LNCaP cells cultured in serum-free medium. The tdEV samples were first characterized using Nanoparticle Tracking Analysis (NTA) to estimate the tdEV concentration. The surface functionalization of the electrodes

and tdEV capture steps were both evaluated using AFM. AFM images acquired on a functionalized unpatterned (plain) Pt surface are presented in Appendix C.2. EV capture was next validated on patterned (nIDE) devices using AFM. A sample of LNCaP-derived tdEVs (25 µl, concentration of 10^6 EVs/µl, as determined by NTA), was incubated on the C-AE-functionalized electrode surface. As depicted in Figure 5.2, which presents AFM images before and after the capture of tdEVs on C-AE functionalized electrodes, circular objects were found on the electrodes, with an estimated diameter of 30-150 nm. These objects correspond to relatively small EVs,[26] which are the least susceptible to shear forces when flushing the microchannel to remove unbound species, since the Stokes drag force linearly

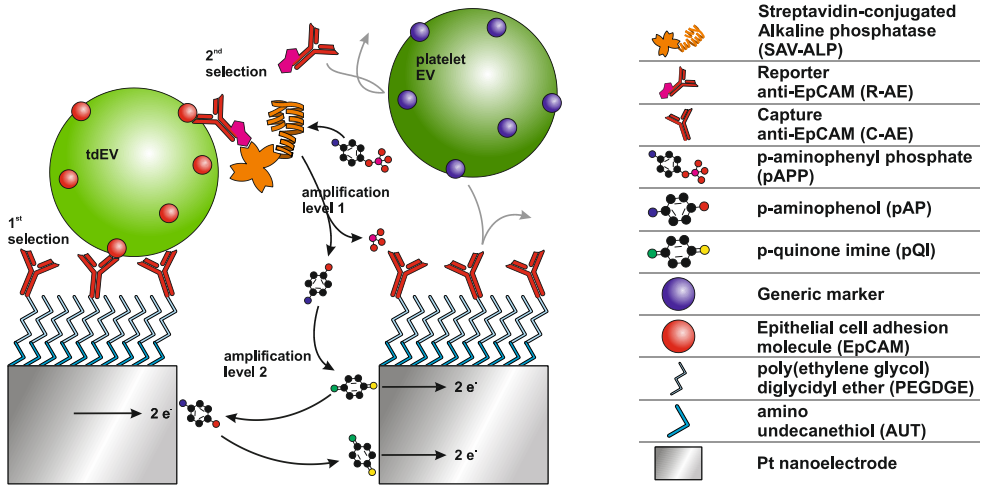

Figure 5.1: *Schematic illustration of tdEV sensing using a sandwich immunoassay and redox cycling on nIDEs resulting in a two-level selectivity and a two-level amplification. tdEVs are captured using C-AE tethered to electrodes (first level of selectivity). The binding of R-AE to the tdEVs completes the antibody-antigen-antibody sandwich (second-level selectivity), after which the enzyme ALP is introduced using a biotin-SAV interaction. ALP provides an enzymatic amplification of pAPP to pAP by substrate cleavage (first-level amplification), which is followed by an electrochemical signal amplification via the oxidation of pAP to pQI and subsequent redox cycling thereof between the nIDE electrodes (second-level amplification).*

scales with the object size (while neglecting viscous deformation or size-dependence of the affinity). The system was not intentionally designed to exclude larger tdEVs, since no short-circuiting

effects are expected based on the dielectric properties of EVs. It may be that tdEVs are captured in the space between the electrodes, which is not modified with the anti-fouling layer and the antibodies. These objects could be captured through antigen/antibody interactions by antibodies present on the side walls of the electrodes. Alternatively, some tdEVs could be non-specifically bound on the surface. The presence of the latter EVs does not influence the outcome of the measurements, which directly depend on the interactions with the second antibody (second level of selectivity). After validation of the surface chemistry on plane substrates (see Appendix C.2), the same functionalization protocol was applied on nIDEs before electrochemical measurements. 100 µl of a tdEV solution in PBS was injected into the microfluidic channel, and this solution was flushed back and forth many times during the incubation for 90 min. Different concentrations in EVs (initially 10^6 EVs per µl) were tested to study the concentration-dependent response of our nanosensor and associated sensing assay. Following this, the microchannel was flushed with a PBS solution to remove unspecifically adsorbed particles on the electrodes. Consequently, the IDEs were incubated with the biotinylated R-AE, (10 µl, 25 mg/ml in PBS, 30 min incubation) and washed with PBS. Subsequently, SAV-ALP was introduced (10 µl, 10 U solution in PBS, 30 min incubation) to interact with the biotin on the R-AE. Next, the IDEs were washed with PBS and incubated with a pAPP solution (100 µl, 10 mM in PBS, 45 min incubation), before electrochemical measurements were started. It should be noted that while the performance of ALP is optimal under alkaline conditions, a physiological pH is preferred for handling EVs. Consequently, the ALP incubation step was performed in PBS (pH 7.4) at room temperature, without active temperature control. Negative control measurements were performed using platelet-derived EVs (pdEV) at 10^7 pdEVs/µl, which are not EpCAM positive, and do not interact as such with anti-EpCAM antibodies (both C-AE and R-AE). Finally, to evaluate the amplification and thereby gain in sensitivity provided by the nanoscale electrodes, their performance was compared to that of microscale IDEs (µIDEs), which were 3 µm

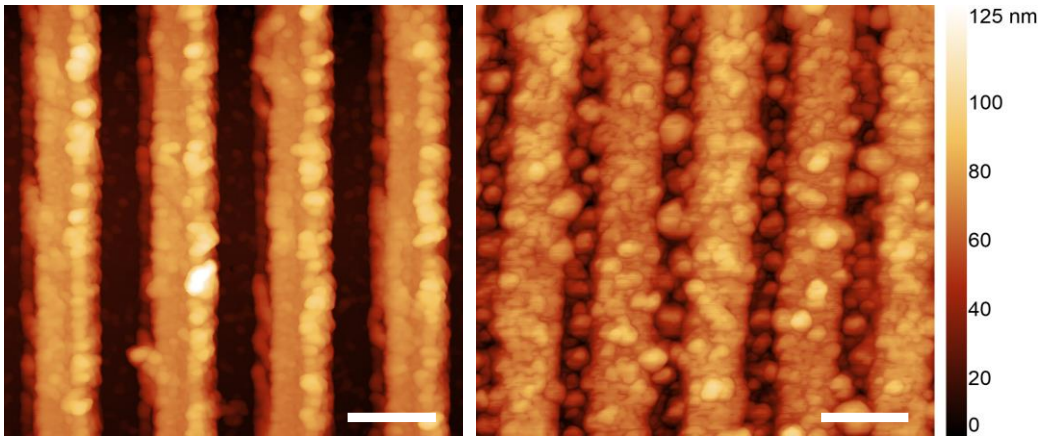

Figure 5.2: Atomic force microscope height images. *(left) bare electrodes before chemical modification. (right) after modification and capture of EpCAM-positive tdEVs derived from LnCAP cell lines on nIDEs. The captured objects are 30 - 150 nm in diameter, which is in good agreement with small EV dimensions. (scale bar: 300 nm).*

wide, 70 nm high and spaced by 3 µm. The height and total sensing area of sets of electrodes were kept the same for both devices to facilitate the performance comparison. The schematic representation of the measurement setup is provided in Figure 5.3(a); it includes two sets of independent working electrodes (WE-1 and WE-2) and an external Ag/AgCl reference electrode (RE). A fixed potential (-0.1 V) was applied to WE-2 with respect to RE. Since the RE current is very low, the stability of RE was not compromised, even when there was no additional counter electrode (CE). Hence, the CE terminal of the potentiostat was connected to RE. The voltammetric responses (scan rate of 50 mV/s) of the nIDEs were first recorded after different steps of functionalization, *i.e.*, (1) after C-AE functionalization, (2) after tdEV capture, (3) after R-AE immobilization, and (4) after conjugation of the biotinylated R-AE to SAV-ALP and subsequent washing, as well as in the presence of pdEVs instead of tdEVs (negative control). Figure 5.3 (b) presents typical cyclic voltammograms obtained after the different surface functionalization steps, yet before the introduction of ALP on the surface. In all three cases considered here, no significant change in the recorded current was observed when pAPP was added in the solution, and a maximum current of 262 pA was recorded at 0.6 V *vs.* Ag/AgCl after addition of the R-AE.

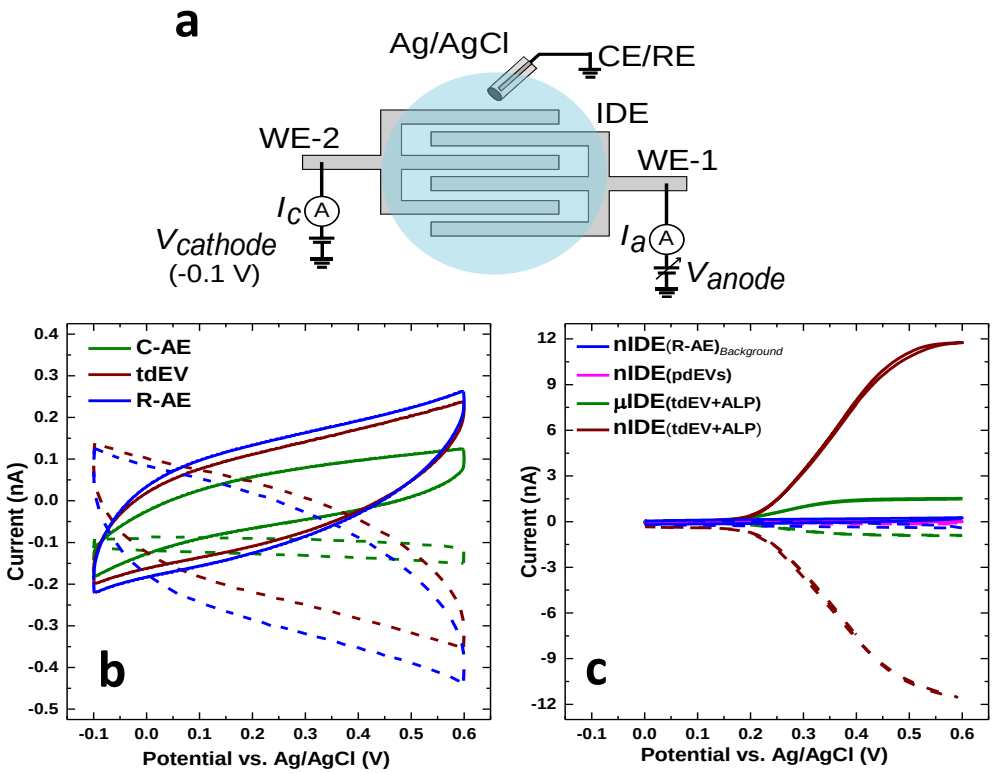

Figure 5.3: Cyclic voltammograms of tdEVs on nIDEs. *Evaluation of the device specificity. (a) Schematic representation of the electrochemical measurement setup. Cyclic voltammograms (CVs) recorded (b) after various steps of functionalization of the nIDEs - after C-AE surface modification (green), after tdEV capture (brown) and after formation of a sandwich with R-AE (blue), and (c) in the presence of tdEVs on nIDEs (brown) and on µIDEs (green), or in presence of pdEVs on nIDEs (magenta). The background signal (blue) corresponds to a device after the antibody sandwich formation. The currents Ianode (solid lines) and Icathode (dashed lines) were measured at the anode and the cathode set of electrodes of the nIDEs/µIDEs, respectively. CVs were acquired for a 1 mM pAPP solution in PBS (pH 7.4) between -0.1 V and + 0.6 V vs. Ag/AgCl at a scan rate of 50 mV/s.*

Since pAPP is electrochemically inactive, no redox activity is expected, as observed here. Noteworthy, the recorded voltammograms are similar to the I/V characteristics of an RC series circuit, with capacitive charging and discharging upon voltage sweeping, and a hysteresis. Furthermore, a change in the maximal amplitude at 0.6 V *vs*. Ag/AgCl was observed after each surface functionalization step. In particular, a considerable capacitive change was found after the immobilization of the tdEVs, which can be noticed with the change in the maximal current value (at 0.6 V *vs*. Ag/AgCl) from 125.1 ± 6.5 pA to 245.1 ± 28.3 pA after the immobilization. Although the capacitive change after the formation of the sandwich assay with R-AE is discernible, it is relatively low compared to the preceding surface functionalization step with tdEVs (from 245.1 ± 28.3 pA to 267.6 ± 15 pA). This behavior might be indicative of capacitive charging through the vesicles. On the sample with negative controls (with pdEVs), as discussed below, this capacitance change was however not observed, corroborating this argument. The contrast between the signals recorded for our positive and negative control samples also indicates that the anti-fouling layer plays an essential role in our device, and has performed as expected.

In a following step, we compared the response of nIDEs and µIDEs, using similar conditions as before (10 µl, 10^6 tdEVs/µl, 1 mM pAPP in PBS (pH 7.4), scan rate of 50 mV/s), after introduction of the SAV-ALP. Figure 5.3 (c) presents characteristic sigmoidal curves of diffusion-limited redox cycling currents on closely spaced working electrodes. The limiting current of nIDEs increases with decreasing the gap size between the electrodes. Therefore, although the total sensing surface area of the nIDEs and µIDEs was the same, the 3-µm gap between the µIDEs resulted in a significantly lower limiting current (1.53 ± 0.01 nA) compared to the nIDEs, which were separated by 120 nm (11.76 ± 0.04 nA). Furthermore, the collector efficiency (ratio of cathode-to-anode limiting currents) of µIDEs was found to be only 62.3% compared to 99.8% for the nIDEs. This significant difference indicates that the redox mediator molecules cycle fewer times between the anode and the cathode for the µIDEs before diffusing into the bulk solution. Altogether, the nanoscale electrodes provided an ~8 times larger amplification of the signal than their microscale counterparts.

Next, we investigated the specificity of our device for the capture and analysis

of tdEVs (Figure 5.3c). tdEVs and pdEV samples were analyzed under the same conditions as before. We compared the response of (1) tdEV+R-AE (blue curve), but before the incubation with SAV-ALP on nIDEs, (2) pdEV on nIDEs (magenta curve), (3) tdEV on nIDEs (brown curve), and (4) tdEV on µIDEs (green curve), after introduction of all required reagents for the assay. The capacitive current (267.6 ± 15 pA) recorded for the tdEV + R-AE sample (10^6 particles/µl) was higher than for the pdEV sample (170.1 ± 13.2 pA) at 0.6 V for ~10^8 particles/µl. Moreover, comparing the limiting currents, a ~ 60 times amplification in signal was observed compared to control sample with pdEV for nIDE devices (magenta curve). Again, these results collectively suggest that tdEVs are specifically captured on the electrode surface, while pdEVs are not, illustrating the specificity of the nanosensor. As a next step, the sensitivity and dynamic range of the assay were evaluated, through serial dilution of the initial tdEV sample on three different devices (n = 3). For each device and for each concentration, CV

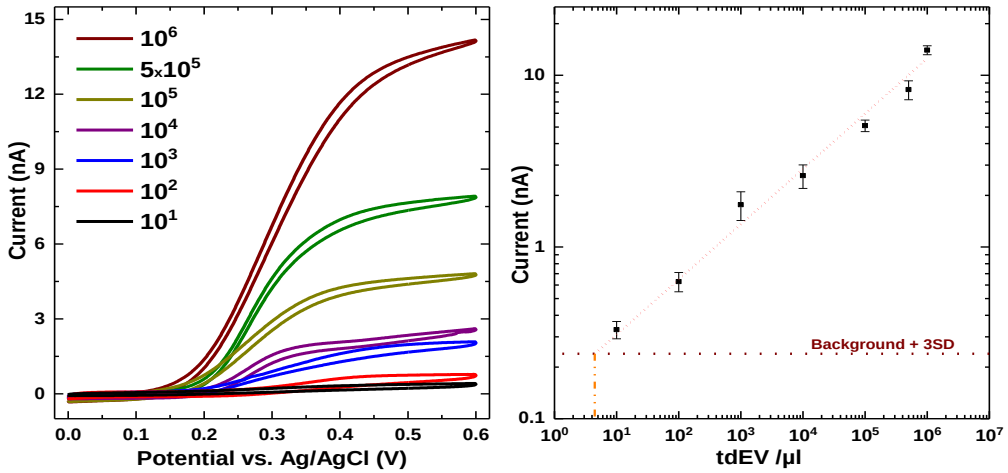

Figure 5.4: Sensitivity and dynamic range of the assay for the detection of tdEVs. *(left) Anodic cyclic voltammograms recorded at the anode for tdEV samples with concentrations ranging from 10 to 106 tdEVs per µL. (right) Associated calibration curve (based on the limiting currents recorded at 0.6 V vs. Ag/AgCl) revealing a dynamic range spanning at least six orders of magnitude (number of devices, n = 3). The horizontal dotted line depicts the background level plus three times the standard deviation (SD) of the redox current; from this horizontal line and the calibration curve, a theoretical LOD as low as 5 tdEVs/µl is found. (Conditions: 1 mM pAPP solution in PBS (pH 7.4); scan rate of 50 mV/s.)*

measurements were performed as before, with 1 mM pAPP in PBS buffer at pH 7.4 with a scan rate of 50 mV/s. This recording was repeated three times with a 5 min interval to demonstrate the stability of the measurements. The CVs recorded after varying the tdEV concentration between 10 and 10^6 EVs per µl are presented in Figure 5.4a, showing a significant influence of the tdEV concentration. From these data recorded using three independent devices, a calibration curve was established (Figure 5.4b) using the limiting current at 0.6 V revealing an excellent linear dynamic range spanning over at least six orders of magnitude and successful measurements at least down to 10 tdEVs/µl, with a readout distinctively above the background signal. By extrapolating the slope of this calibration curve, the current LOD for our assay was evaluated to be *ca.* 5 tdEVs/µl.

5.5 CONCLUSIONS

We report a novel electrochemical biosensor and associated measurement principle for the highly selective, highly sensitive and robust quantification of tumor-derived extracellular vesicles. For this, we used a two-level amplification of the signal and a two-level specificity. High assay sensitivity was attained through enzymatic amplification combined with redox cycling between nanoscale interdigitated electrodes. In addition, the high specificity was achieved from the presence of two independent selection steps in the sandwich assay. Using the herein reported device and sensing protocol, we have reached a very high sensitivity that is clinically relevant for the detection of tdEVs, with a *measured* LOD as low as 10 tdEVs per µl, while extrapolation of the calibration curve suggests a *projected* LOD of 5 tdEVs/µl. While having an LOD in the same order of magnitude as the currently most sensitive reported systems, importantly, the detection range largely covers the concentration of tdEVs (10 – 10^6 tdEVs/µl) found in metastatic cancer patients. Further optimization of the nanosensor and assay performance is ongoing via changes in and stabilization of

experimental conditions like pH, incubation time and operating temperature. Furthermore, the herein used PEG-based anti-fouling layer may not be sufficient when working with samples in more complex media. In that case, the anti-fouling layer can be adjusted, through the incorporation, for instance, of zwitterionic polymer brushes.[36] Importantly, this technology can be applied to a wide range of (rare) biomarkers by simply incorporating a different recognition element (*e.g.,* a different antibody). Furthermore, this amperometric sensing method has the potential to be developed as a portable point-of-care sensing device, which can also be useful in population-wide disease screening.

5.6 MATERIALS AND METHODS

5.6.1 MATERIALS

Dichloromethane and ethanol (VLSI grade) were purchased from VWR (Amsterdam, The Netherlands). Acetone (VLSI grade), Harris Uni-Core 1 mm I.D. biopsy punches, sodium phosphate, 11-amino-1-undecanethiol hydrochloride (AUT), (Poly(ethylene glycol) diglycidyl ether (PEGDGE), PBS tablets, bovine serum albumin (BSA) and 4-aminophenyl phosphate monosodium salt hydrate (pAPP) were obtained from Merck (Zwijndrecht, The Netherlands). Capturing anti-EpCAM (C-AE), biotinylated reporter anti-EpCAM (R-AE), and extracellular vesicles were received as a kind gift from Immunicon corp. (Huntingdon Valley, United States). Streptavidin-conjugated alkaline phosphatase (SAV-ALP) was purchased from Thermo Fisher (Eindhoven, The Netherlands). Sylgard 184 was obtained from Farnell (Utrecht, The Netherlands). Buffers were filtered through a 0.2 µm syringe filter before use (Whatman, Little Chalfont, United Kingdom).

5.6.2 DEVICE FABRICATION

nIDEs and µIDEs were fabricated using a combination of optical and electron-beam lithography (EBL) and metal evaporation and lift-off process. First, a 300

nm SiO_2 layer was thermally grown on a 10-cm Si (100) wafer at 1000 °C. A first optical lithography step was carried out followed by evaporation of metals (Ti, adhesion layer, and Pt) and lift-off for defining the markers for EBL. Subsequently, nIDEs were patterned using EBL. CHF_3-based plasma etching was next performed to recess the adhesive metal layer into the substrate in the following step. After the etching, metal deposition (Ti, 5 nm and Pt, 70 nm) and lift-off was done to form the IDEs. Successively, the nIDEs were connected to contact pads via contact leads using a second optical lithography step followed by another metal evaporation (Ti, 5 nm and Pt, 100 nm) and lift-off. A 300-nm layer of parylene-C was evaporated as a first passivation layer. A third optical lithography step was done and using the patterned photoresist as a mask, SiO_2 (30 nm) was evaporated on top of the parylene-C layer. This oxide layer covered the entire device except the contact pads and a rectangular window of 30×70 μm^2 over the nIDEs. The two passivation layers (parylene and SiO_2) prevented current leakage through the contact leads. The fabricated chips were then diced to 25×20 mm^2 chips (Disco DAD321 dicing machine). Bare Pt substrates to validate and characterize the surface functionalization were prepared by sputtering a 10-nm layer of Ta as an adhesive layer followed by a 100 nm layer of Pt on Mempax glass wafers.

5.6.3 SURFACE MODIFICATION

The platinum nIDEs were first cleaned by rinsing sequentially in dichloromethane, acetone and ethanol (bare Pt substrates were ultrasonicated in the same solvents for 7 min each). Platinum surfaces were finally cleaned in O_2 plasma (Diener Pico, Diener Electronics, Ebhausen, Germany) for 30 s. After placing the PDMS device on the chip (see Appendix C.1), the microchannel was filled with a 1 mM AUT solution in ethanol to form a self-assembled thiol monolayer (SAM) under static incubation at room temperature overnight. Next, the channels were washed with 1 ml of ethanol, blown dry with N_2, filled with neat poly(ethylene glycol) diglycidyl ether (PEGDGE) and left overnight at 40 °C. Afterwards, the channels were again rinsed with 1 ml ethanol and blown dry with N_2. This yields an anti-biofouling layer, which was subsequently functionalized with antibodies. Specifically, a capturing anti-EpCAM (C-AE) solution was diluted

in sodium phosphate buffer (pH 8.3) to a final concentration of 25 mg/ml and injected in the microchannel for overnight incubation. In this step, epoxide groups in the PEGDGE molecules react primarily with amines on the lysine residues on the antibody molecules. Prior to the EV capture, unreacted epoxide groups were blocked with a filtered 1% BSA solution in PBS for 1 h at room temperature, and the device was rinsed with 1 ml PBS.

5.6.4 CHARACTERIZATION OF THE SURFACE FUNCTIONALIZATION

The antibody functionalization was validated on plain Pt-coated silica substrates before being applied on devices with IDEs (see Appendix C.2 and C.3). AFM analysis in air of the dried substrates confirmed the successful and selective capture of tdEVs on the C-AE functionalized Pt surface. Circular objects of 10 nm ± 1 nm height and 0.1 - 1 µm in width were found in all studied regions of 10 × 10 μm^2, corresponding to EVs which have collapsed while drying. In contrast, for negative control samples [(1) no addition of PEGDGE, (2) no antibody conjugation, (3) no incubation with EVs, or (4) incubation with EpCAM-negative EVs derived from the PC3 cell line], no EV was found (see Appendix C.2). In future experiments, these conditions were used to functionalize the IDEs.

5.7 REFERENCES

1. Nanou, A.; Coumans, F. A.; van Dalum, G.; Zeune, L. L.; Dolling, D.; Onstenk, W.; Crespo, M.; Fontes, M. S.; Rescigno, P.; Fowler, G., Circulating tumor cells, tumor-derived extracellular vesicles and plasma cytokeratins in castration-resistant prostate cancer patients. *Oncotarget* **2018,** *9* (27), 19283.
2. Alix-Panabières, C.; Pantel, K., Circulating tumor cells: liquid biopsy of cancer. *Clinical chemistry* **2013,** *59* (1), 110-118.
3. Budd, G. T.; Cristofanilli, M.; Ellis, M. J.; Stopeck, A.; Borden, E.; Miller, M. C.; Matera, J.; Repollet, M.; Doyle, G. V.; Terstappen, L. W., Circulating tumor cells versus imaging—predicting overall survival in metastatic breast cancer. *Clinical Cancer Research* **2006,** *12* (21), 6403-6409.
4. Coumans, F.; Dalum, G.; Terstappen, L. W. M. M., CTC Technologies and Tools. *Cytometry Part A* **2018,** *93* (12), 1197-1201.
5. Vaidyanathan, R.; Soon, R. H.; Zhang, P.; Jiang, K.; Lim, C. T., Cancer diagnosis: from tumor to liquid biopsy and beyond. *Lab on a Chip* **2019,** *19* (1), 11-34.

6. Poudineh, M.; Sargent, E. H.; Pantel, K.; Kelley, S. O., Profiling circulating tumour cells and other biomarkers of invasive cancers. *Nature Biomedical Engineering* **2018,** *2* (2), 72.
7. Yáñez-Mó, M.; Siljander, P. R.-M.; Andreu, Z.; Bedina Zavec, A.; Borràs, F. E.; Buzas, E. I.; Buzas, K.; Casal, E.; Cappello, F.; Carvalho, J., Biological properties of extracellular vesicles and their physiological functions. *Journal of extracellular vesicles* **2015,** *4* (1), 27066.
8. van Niel, G.; D'Angelo, G.; Raposo, G., Shedding light on the cell biology of extracellular vesicles. *Nature reviews Molecular cell biology* **2018,** *19* (4), 213.
9. Mathieu, M.; Martin-Jaular, L.; Lavieu, G.; Théry, C., Specificities of secretion and uptake of exosomes and other extracellular vesicles for cell-to-cell communication. *Nature cell biology* **2019,** *21* (1), 9.
10. Reátegui, E.; Vos, K. E.; Lai, C. P.; Zeinali, M.; Atai, N. A.; Aldikacti, B.; Floyd, F. P.; Khankhel, A.; Thapar, V.; Hochberg, F. H., Engineered nanointerfaces for microfluidic isolation and molecular profiling of tumor-specific extracellular vesicles. *Nature communications* **2018,** *9* (1), 175.
11. Koliha, N.; Wiencek, Y.; Heider, U.; Jüngst, C.; Kladt, N.; Krauthäuser, S.; Johnston, I. C.; Bosio, A.; Schauss, A.; Wild, S., A novel multiplex bead-based platform highlights the diversity of extracellular vesicles. *Journal of extracellular vesicles* **2016,** *5* (1), 29975.
12. Yadav, S.; Boriachek, K.; Islam, M. N.; Lobb, R.; Möller, A.; Hill, M. M.; Hossain, M. S. A.; Nguyen, N. T.; Shiddiky, M. J., An Electrochemical Method for the Detection of Disease-Specific Exosomes. *ChemElectroChem* **2017,** *4* (4), 967-971.
13. Julich, H.; Willms, A.; Lukacs-Kornek, V.; Kornek, M., Extracellular vesicle profiling and their use as potential disease specific biomarker. *Frontiers in immunology* **2014,** *5*, 413.
14. Lobb, R. J.; Lima, L. G.; Möller, A. In *Exosomes: key mediators of metastasis and pre-metastatic niche formation*, Seminars in cell & developmental biology, Elsevier: 2017; pp 3-10.
15. Galindo-Hernandez, O.; Villegas-Comonfort, S.; Candanedo, F.; González-Vázquez, M.-C.; Chavez-Ocaña, S.; Jimenez-Villanueva, X.; Sierra-Martinez, M.; Salazar, E. P., Elevated concentration of microvesicles isolated from peripheral blood in breast cancer patients. *Archives of medical research* **2013,** *44* (3), 208-214.
16. Coumans, F.; Doggen, C. J. M.; Attard, G.; De Bono, J.; Terstappen, L. W. M. M., All circulating EpCAM+ CK+ CD45− objects predict overall survival in castration-resistant prostate cancer. *Annals of oncology* **2010,** *21* (9), 1851-1857.
17. Hattori, Y.; Shimada, T.; Yasui, T.; Kaji, N.; Baba, Y., Micro-and Nanopillar Chips for Continuous Separation of Extracellular Vesicles. *Analytical chemistry* **2019**.
18. Shpacovitch, V.; Hergenroeder, R., Optical and surface plasmonic approaches to characterize extracellular vesicles. A review. *Analytica chimica acta* **2018,** *1005*, 1-15.
19. van der Pol, E.; Sturk, A.; van Leeuwen, T.; Nieuwland, R.; Coumans, F.; group, I. S. V. W.; Mobarrez, F.; Arkesteijn, G.; Wauben, M.; Siljander, P. M., Standardization of extracellular vesicle measurements by flow cytometry through vesicle diameter approximation. *Journal of Thrombosis and Haemostasis* **2018,** *16* (6), 1236-1245.
20. Nolan, J. P.; Duggan, E., Analysis of individual extracellular vesicles by flow cytometry. In *Flow Cytometry Protocols*, Springer: 2018; pp 79-92.
21. Contreras-Naranjo, J. C.; Wu, H.-J.; Ugaz, V. M., Microfluidics for exosome isolation and analysis: enabling liquid biopsy for personalized medicine. *Lab on a Chip* **2017,** *17* (21), 3558-3577.
22. Hisey, C. L.; Dorayappan, K. D. P.; Cohn, D. E.; Selvendiran, K.; Hansford, D. J., Microfluidic affinity separation chip for selective capture and release of label-free ovarian cancer exosomes. *Lab on a Chip* **2018,** *18* (20), 3144-3153.
23. Im, H.; Lee, K.; Weissleder, R.; Lee, H.; Castro, C. M., Novel nanosensing technologies for exosome detection and profiling. *Lab on a Chip* **2017,** *17* (17), 2892-2898.

24. Yukawa, H.; Suzuki, K.; Aoki, K.; Arimoto, T.; Yasui, T.; Kaji, N.; Ishikawa, T.; Ochiya, T.; Baba, Y., Imaging of angiogenesis of human umbilical vein endothelial cells by uptake of exosomes secreted from hepatocellular carcinoma cells. *Scientific reports* **2018,** *8* (1), 6765.
25. Yuana, Y.; Oosterkamp, T.; Bahatyrova, S.; Ashcroft, B.; Garcia Rodriguez, P.; Bertina, R.; Osanto, S., Atomic force microscopy: a novel approach to the detection of nanosized blood microparticles. *Journal of thrombosis and haemostasis* **2010,** *8* (2), 315-323.
26. Van Der Pol, E.; Hoekstra, A.; Sturk, A.; Otto, C.; Van Leeuwen, T.; Nieuwland, R., Optical and non-optical methods for detection and characterization of microparticles and exosomes. *Journal of Thrombosis and Haemostasis* **2010,** *8* (12), 2596-2607.
27. Lee, W.; Nanou, A.; Rikkert, L.; Coumans, F. A.; Otto, C.; Terstappen, L. W.; Offerhaus, H. L., Label-Free Prostate Cancer Detection by Characterization of Extracellular Vesicles Using Raman Spectroscopy. *Analytical chemistry* **2018,** *90* (19), 11290-11296.
28. Beekman, P. E.-M., A; Rho, H.S.; Pujari, S.P.; Lenferink, A.T.M; Zuilhof, J.T.; Terstappen, L.W.M.M; Otto, C.; Le Gac, S., Immuno-capture of extracellular vesicles for individual multi-modal characterization using AFM, SEM and Raman spectroscopy. *Lab on a Chip* **2019**.
29. Zhang, P.; Zhou, X.; He, M.; Shang, Y.; Tetlow, A. L.; Godwin, A. K.; Zeng, Y., Ultrasensitive detection of circulating exosomes with a 3D-nanopatterned microfluidic chip. *Nature Biomedical Engineering* **2019**, 1.
30. Boriachek, K.; Masud, M. K.; Palma, C.; Phan, H.-P.; Yamauchi, Y.; Hossain, M. S. A.; Nguyen, N.-T.; Salomon, C.; Shiddiky, M. J., Avoiding Pre-Isolation Step in Exosome Analysis: Direct Isolation and Sensitive Detection of Exosomes Using Gold-Loaded Nanoporous Ferric Oxide Nanozymes. *Analytical chemistry* **2019**.
31. Huang, R.; He, L.; Xia, Y.; Xu, H.; Liu, C.; Xie, H.; Wang, S.; Peng, L.; Liu, Y.; Liu, Y., A Sensitive Aptasensor Based on a Hemin/G-Quadruplex-Assisted Signal Amplification Strategy for Electrochemical Detection of Gastric Cancer Exosomes. *Small* **2019,** *15* (19), 1900735.
32. Schasfoort, R. B.; Andree, K. C.; van der Velde, N.; van der Kooi, A.; Stojanović, I.; Terstappen, L. W., Interpolation method for accurate affinity ranking of arrayed ligand–analyte interactions. *Analytical biochemistry* **2016,** *500*, 21-23.
33. Hermanson, G. T., *Bioconjugate Techniques*. 2nd ed.; Elsevier Inc.: 2008.
34. Obeid, S.; Sung, P.-S.; Le Roy, B.; Chou, M.-L.; Hsieh, S.-L.; Elie-Caille, C.; Burnouf, T.; Boireau, W., NanoBioAnalytical characterization of extracellular vesicles in 75-nm nanofiltered human plasma for transfusion: A tool to improve transfusion safety. *Nanomedicine: Nanotechnology, Biology and Medicine* **2019,** *20*, 101977.
35. Rho, H. S. Y., Y.; Veltkamp, H.; Gardeniers, H., Direct Delivery of Reagents from a Pipette Tip to a PDMS Microfluidic Device. In *Chips and Tips*, RSC blogs: 2015.
36. Baggerman, J.; Smulders, M. M.; Zuilhof, H., Romantic Surfaces: A Systematic Overview of Stable, Biospecific, and Antifouling Zwitterionic Surfaces. *Langmuir* **2019,** *35* (5), 1072-1084.

6

Chemically modified nanoelectrodes for individual particle analysis

A manuscript based on this chapter entitled "Chemically modified nanoelectrodes for individual particle analysis" by P. Beekman, D.G. Mathew, S. P. Pujari, S. le Gac, H. Zuilhof, W.G. van der Wiel, and S.J. G. Lemay is currently in preparation.

6.1 Abstract

Biosensor technology is developing at a rapid pace, arguably more than ever because of the pandemic. Established technologies perform an important task in present-day diagnostic procedures, but their shortcomings in terms of sensitivity and specificity are clear. Moreover, solutions to these shortcomings are emerging from high-tech-enabled developments. In this chapter, the first steps in the development of a potentially disruptive biosensing technology platform are described. It relies on a relatively simple electrochemical sensing principle which is extremely sensitive thanks to the nanoscale dimensions of the electrodes. This enables the detection of analytes at the single-particle level. The required selectivity is awarded by surface functionalization including biological recognition elements and anti-fouling properties. Thus, a versatile platform is being developed which can be applied to cancer (e.g. tdEV detection) as well as other submicroscopic analytes including viruses and bacteria. Preliminary experiments aimed at EpCAM+ EVs and SARS-CoV-2 detection are presented in this chapter, followed by an outlook regarding the implementation of this technology in various clinical fields.

6.2 Introduction

6.2.1 Analyte concentration

As explained in Chapter 2, tumor-derived extracellular vesicles (tdEVs) are present in metastatic cancer patient blood plasma at concentrations that in some cases are below the limit of detection (LOD) of state-of-the-art sensing systems like the one presented in the previous chapter. To be able to diagnose or monitor all eligible cancer patients, a detection system should have an LOD below 1 tdEV/µl.[1–3]

Apart from the scope of extracellular vesicles, also virus detection systems suffer from a lack of sensitivity. As reported by Kucirka *et al.*, even the current gold

standard in SARS-CoV-2 detection, reverse transcriptase polymerase chain reaction (RT-PCR), has a false negative rate of minimally 20%.[4] In subjects that have been infected less than 8 days prior to the test, the false negative rate is even higher, with in fact up to 100% for subjects that were infected in the prior 2 days.[5–7] In the samples taken from these patients, the "viral load" can be lower than the LOD of RT-PCR, which is typically 10^3 – 10^5 copies/ml.[8–11] In addition to this, the use of RT-PCR is so laborious and slow that it altogether typically takes more than 24 hours to process a sample.[5]

Reliable testing procedures, if widely available, could have arguably prevented or at least helped to curtail the COVID-19 pandemic.[12,13] In reality, the inaccuracy and inefficiency of currently available diagnostic tools thus gravely contribute to the observed lack of control over disease management.

There is a clear need for biosensor technology capable of detecting various analytes at low (sub-attomolar) concentrations. As will be shown in this chapter, combining nanotechnology-based sensing with efficient mass transport opens new avenues to detecting various biomarkers with the ultimate sensitivity of *1 unit per sample*.

This biosensor is based on a principle we have labelled *Nanoelectrodes for Individual Particle Analysis* (*NIPA*). It detects individual particles based on perturbances of an electrochemical signal resulting in peaks of characteristic duration (see Section 6.3.1.). With electrochemical sensing, amplitudes of these peaks are dependent on the size of the particles, but also on the kinetics of the electrochemical reactions which depend on mass transport, pH, temperature and ionic strength, etc. Whereas conventional biosensing applications require calibration and have strict limitations to control for variations in these environmental parameters, *NIPA* simply relies on the number of characteristic peaks rather than their amplitude. Quantitative information comes from counting the discrete peaks and measuring their duration. This robust analysis approach is a new interpretation of the term "digital sensing".

6.2.2 Specificity

One of the biggest challenges in biosensing is to differentiate the signal of non-specifically adsorbed species from that of the targeted analyte. With proper surface chemistry, the affinity between the analyte and the functionalized surface can be enhanced to become much greater than the affinity between the surface and any other component of the sample.[14–17] This can be accomplished by improving the orientation and the coverage of the recognition elements to maximize their performance.[18–20] Complementary to this, anti-fouling layers can be engineered to minimize the binding of non-target components.[16,21–23] However, with the number of non-target components vastly outnumbering the analyte in any real-life sample, contributions of non-specific binding to the dynamics of the sample processing and the signal from the label remain significant.[3] To overcome this, with *NIPA*, a further distinction between specific and non-specific interaction can be made in signal processing because individual interactions between analyte and recognition molecules (*e.g.,* antibodies) are identified by their duration. Under flow conditions, when regarding submicroscopic particles in disposable chips with proper anti-fouling coatings, specific interaction will last for a longer time than a non-specific one.

.

6.2.3 Point-of-care

Before a sensing technology can realistically be adopted by users, it should considerably outperform the alternative(s) that these users have become accustomed to. However, beyond that, switching to a new technology should require as little investment as possible – of money, but most of all time. Even for use by skilled clinical laboratory analysts, a device ideally does not require extensive knowledge on electrochemistry and hydrodynamics. It should rather be a robust system that is designed to eliminate as many modes of failure as possible. Robustness also comes from eliminating sample preparation steps relying on the stability and performance of the reagents as much as possible. Such a simple and robust system can be realized by integrating sample handling and signal analysis. This goes hand in hand with miniaturization, yielding portable systems that are safe and easy to use by non-experts in any environment.[24]

6.2.4 Scope of this chapter

NIPA was invented with extracellular vesicle (EV) detection for cancer-related healthcare applications in mind (see Chapter 7), but during the first lockdown starting March 2020 it became apparent that the need for a sensitive virus detection system was more urgent. Since virus particles and EVs display very similar particle properties, *i.e.,* both are submicron nanoparticles presenting characteristic proteins on their surface, the adaptation of *NIPA* for virus detection simply and only entails changing the antibody on the electrodes. This chapter describes the concept of the *NIPA* technology and its development whereby both EVs and viruses are targeted to demonstrate the proof of concept. EVs were used as biological model particles (rather than *e.g.,* SARS-CoV-2 viruses) considering safety regulations. Throughout this chapter, the experiments were performed with both virus and EV detection in mind and the applications could be considered interchangeably.

6.3 Theory

6.3.1 *NIPA*

Before going into more detail, the basic *NIPA* sensing principle is explained in this paragraph. It is based on *single-particle impact electrochemistry (SPIE),* whereby a redox current is monitored through time (chronoamperometry).[25–28] Here, the presence of a particle near the electrodes obstructs mass transport of a solubilized redox mediator, resulting in a deviation from the baseline redox current. The baseline current scales with the area of the electrode. Similarly, the *current drop* scales with the reduction of accessible electrode area. Hence, the smaller the electrode, the larger the relative current drop for a particle with a given size. Microelectrodes are often used to detect bulk concentrations of analytes from the collective effect of the adsorption of many analyte molecules.[29] By using nanoscale electrodes, single nanoparticles can be detected.[30,31]

So far, there are to our knowledge no reports on *specific detection* of analytes using *SPIE*. *NIPA* is an extension of this existing principle in the sense that it uses the same chronoamperometric signal, but it does not focus on the amplitude but on *the duration* of the current drop to give information on the specificity of interactions between the analytes and the recognition elements, which are immobilized on a generically antifouling electrode surface. This enables to distinguish between non-specific and specific interactions based on the difference in their dissociation rates. The sensors consist of recessed circular nanoelectrodes (diameter 100 - 500nm) embedded in an insulating substrate (a silicon chip with a passivation layer). The design is shown in Appendix D. Each electrode is individually addressable, so the number of sensing electrodes on the chip is limited by the number of recording channels that are available in the readout device (typically 18). A cross-section of two sensing electrodes is shown in Figure 6.1. The nanoelectrodes are coated with a layer with antifouling properties and with recognition elements. The chip is embedded in a microchannel through which the sample is introduced at a steady flow rate. The sample contains analytes and an added redox mediator, which gets reduced at the nanoelectrodes (*i.e.,* the working electrodes) as soon as a reducing potential is applied relative to a distant reference electrode (not shown in Figure 6.1). The current is recorded as a function of time in separate read-out channels for both electrodes. At $t=t_0$ in Figure 6.1, before any particle has approached the surface, a stable baseline current is recorded. If at $t=t_1$ two particles adsorb on two nanoelectrodes, one analyte (*e.g.,* a pathogen or other submicroscopic biomarker like an EV) and a random other similar particle, the mass transport of the redox mediator is obstructed for both electrodes, resulting in a similar current drop observed in both read-out channels. The analyte carries antigens on its outer surface that interact with the recognition elements on the electrodes. The adsorption of the other particle is mainly governed by weaker, non-specific forces. The flowing medium imposes a shear stress on both particles, tending to break the interaction and transport them downstream. Only in the case of the analyte, where the antibody-antigen interactions are strong enough to balance these forces,[32] the particle is retained for some characteristic period, whereas the non-specifically bound particle is

rapidly washed away. Narrow peaks indicating weak interactions are ignored in the sample processing.

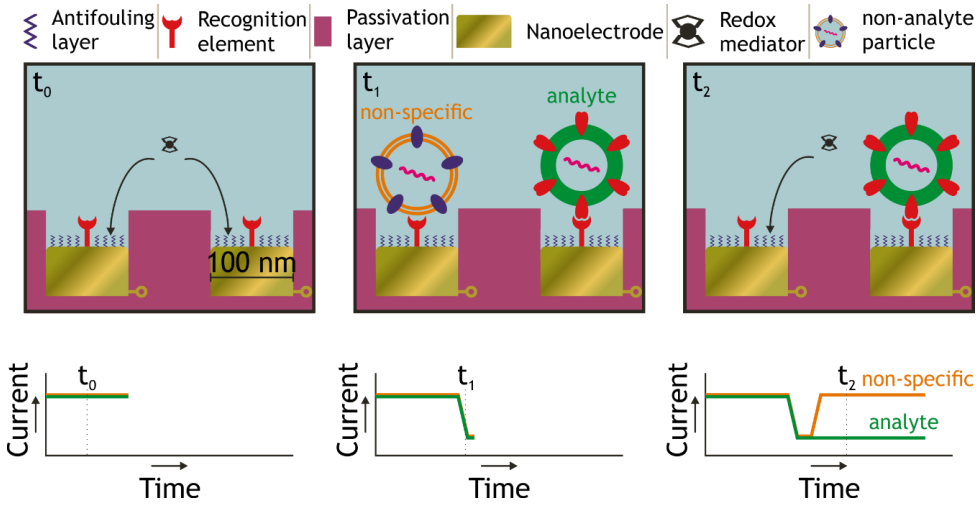

Figure 6.1: NIPA sensing mechanism. Analyte particles (e.g., EVs, viruses or bacteria) are individually and specifically enumerated by counting only the longest current drop events.

6.3.2 Electrochemistry

When a sufficiently high potential difference is applied between multiple electrodes, redox mediators can be oxidized at the anode or reduced at the cathode. Ferrocene (Fc) or a more water-soluble analogue like ferrocene dimethanol is often chosen as redox mediator for its stability and compatibility with various solvents. These molecules are natively neutrally charged, but when oxidized by an anode, they are converted to ferrocenium anions (Fc^+), whereby an electron gets transferred from the mediator to the anode. The neutral charge entails that the supply of Fc is completely governed by diffusion and convection. In addition to these drivers of mass transfer, the Fc^+ anions are also electrophoretically expelled from the anode. This gives a concentration gradient and thereby an additional component to the electric field gradient (especially in static conditions).

The baseline current at optimal formal potential I can here be approximated by:[33,34]

$$I = 4FDCa, \qquad (1)$$

where F is Faraday's constant ($\backsim$9.6×10^5 C/mol), D and C are, respectively, the diffusion constant ($\backsim$7^{-10} m^2/s) and concentration (*e.g.,* 1 mM) of ferrocene dimethanol and a is the radius of the electrode. That is, for submicron electrodes, the current per electrode is in the order of 1 – 10 pA.

When a particle obstructs the migration of Fe to the electrodes, the electrodes are partially shadowed, resulting in an apparent decrease in (active) electrode size Δa, such that the current drop ΔI can be described by

$$\Delta I = 4FDC\Delta a. \qquad (2)$$

Δa scales with the size of the particle until the limit is reached that the current is completely blocked. That is, the current drop dependence on the particle size is most prominent for particles smaller than the electrode.

6.3.3 Electrophoresis

Biological samples can be perceived as colloidal electrolyte solutions, in the sense that they are aqueous distributions of many different species of (sub)microscopic particles as well as ions. If the colloidal species had neutral electric charge or were oppositely charged, they would likely aggregate. Hence, most biological supramolecular assemblies have a negative zeta potential ζ, (typically between -10 and -60 mV). An externally applied electric field can exert a force on this charged particle. Migration due to this force is called electrophoresis. This (partial) charge is screened by charged species in the electrolyte solution. These oppositely charged particles are attracted in the opposite direction. The viscous drag as a result of this is called electroosmosis. The net force on the particle gives it a drift velocity v given by:

$$\mathrm{v} = \mu\mathrm{E} \qquad (3)$$

Here, the mobility μ is can be derived from the Helmholtz-Smoluchowski equation yielding

$$\mu = \frac{\epsilon\zeta}{\eta}. \qquad (4)$$

With ϵ the permittivity (*e.g.* 7.08 x 10^{-10} F/m) and η the viscosity of the fluid (*e.g.* 1 mPa/s).

When a constant potential is applied, electrolytes in the solution are attracted to the electrode until the field is completely screened and there is total net neutrality. The electric field that attracts the particles is a result of the concentration gradient of Fc^+ species that are produced by the Faradaic reaction, being pushed and carried away from the electrode. Considering the nanoscale electrode with small radius a as a hemispherical electrode (valid at a distance $r \gg a$ away from it), the resulting field at r under static conditions can be estimated by:[35]

$$E(r) = \frac{RT}{Fr}\left(1 + \frac{2D_{ox}c_I r}{D_{red}c_{red}a}\right)^{-1}. \qquad (5)$$

Here, R is the universal gas constant ($\backsim$8.31), T temperature (*e.g.* 293 K), F Faraday's constant, D_{ox} and D_{red} the diffusion constants of the oxidized and reduced forms of Fc, and C_I and C_{red} the bulk concentrations of supporting electrolyte and Fc, respectively. Considering particles with $\zeta = 30\ \mathrm{mV}$ and working electrodes with radius a = 250 nm, with D_{ox} and D_{red} having similar values, as well as C_I and C_{red} (both $\backsim$1 mM after dilution), plugging Eq. (4) and (5) into Eq. (3) gives a net drift velocity of $\backsim$60 µm/s close to the electrode ($r = 1\ \mu\mathrm{m}$), which decays non-linearly with r. This is schematically presented in Figure 6.2.

This describes the purely electrodynamic components of the mass transport (*i.e.*, assuming v_{flow} = 0 in Figure 6.2). It can be optimized by tuning the pH and ionic strength, adjusting the zeta potential as well as the Debye layer screening. As will be explained in the next section, a major contribution to the mass transport kinetics also comes from microfluidics.

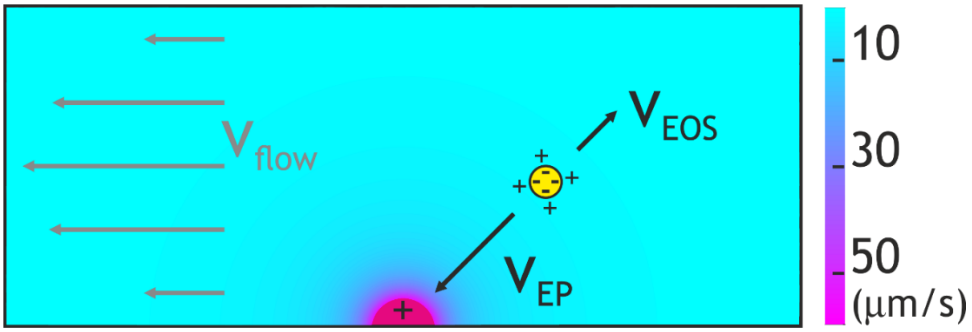

Figure 6.2. Longitudinal cross-section of a typical microchannel *with a small working electrode (a = 250 nm) showing the drift velocity of particles in an electric field produced by a concentration gradient of oxidized redox species. In a typical configuration, the reference electrode would be out-of-plane in close proximity to the working electrode. The color scale gives the net drift velocity in μ/s (ill-defined close to the electrode). Scale: particle is 1 μm.*

6.3.4 Microfluidics

The sample is ideally introduced through a microchannel. Not only does this allow conserving reagents because only minute volumes are required (typically limited by what can accurately be pipetted, so typically high nanoliter range), it also gives more efficient mass transport and allows removing and exchanging reagents more accurately and quickly. Moreover, the collision rate between analyte and the sensor array is further aided by confining the sample to the vicinity of the sensing array, so as to bring about a more frequent contact between the analyte and the sensor.

In addition, as Eq. (3) suggests, the drift velocity increases with electric field strength, which decays with distance from the electrodes. This entails that the attraction is strongest close to the surface, *i.e.,* that capturing can be maximized by making the microchannels as small as possible. However, reducing the size of the microchannel cross-sections comes at the cost of reduced throughput (assuming constant pressure). Mass flow rate Q (in m^3/s) through a channel is given by the driving pressure difference P divided by its hydraulic resistance R_H:

$$Q = \frac{P}{R_H}, \qquad (6)$$

where R_H, in the case of a channel with length L and a cross-section perpendicular to the direction of the flow with width w and height h (i.e., $w > h$) is given by:[36]

$$R_H = \left(\frac{h^3 w}{12\eta L}\left(1 - 0.63 * \frac{h}{w}\right)\right)^{-1}. \qquad (7)$$

For a single rectangular channel with dimensions $(L \times w \times h) = 1.5\ mm \times 25\ \mu m \times 10\ \mu m$, through which water is actuated with a vacuum pump applying 750 mbar negative pressure on the outlet, this would result in a flow rate in the order of 7.5 µl/min, *i.e.,* it would take about 15 min to process 100 µl sample.

Reducing the dimensions even further is most likely counterproductive. At a given mass flow rate, local flow velocity (m/s) scales inversely with cross-sectional area. When the velocity of the analyte is too high, there is insufficient time for antigen-antibody complexes to form. At the other extreme, when the flow velocity is too low (*e.g.,* in large microchannels or in open systems), the shear from the fluid may not be enough to remove non-specifically bound species. In the proposed microchannel, the average flow velocity is 0.5 m/s. It would take about 20 ms for an analyte to traverse the 10 µm long region where the field is the strongest.

The flow velocity strongly deviates from the average along the channel cross-section. As modeled by the Hagen-Poiseuille equation, the velocity develops in a parabolic profile with a maximum in the middle of the channel (see Figure 6.2).[36] Assuming a very strong interaction between the surface and the fluid (*i.e.,* the surface has a very high interfacial energy), the flow velocity may be assumed to be 0 at the boundary of the channel. If, through electrophoresis, particles would be attracted to occupy streamlines close to the surface, they would get more time to interact. To enhance this effect at higher flow rates, many such electrodes could be placed along the long axis of the microchannel.

6.4 Materials and Methods

6.4.1 Materials

All chemicals were obtained from Merck (Zwijndrecht, The Netherlands) unless otherwise noted. All aqueous media were filtered through a 0.2 μm syringe filter directly before use. Ferrocene dimethanol (2 mM final concentration in MilliQ water) was added to all buffers used in chronoamperometry experiments.

6.4.2 Fabrication

6.4.2.1 Chips

NIPA chips were fabricated in the cleanroom of the MESA+ Institute for Nanotechnology using the chemicals available in their standard stock. A summary of the process flow is presented in Figure 6.3. The photolithography mask is shown in Appendix D.

6.4.3 Chemical functionalization of the working electrodes

The chemical functionalization was performed as described in Chapter 5, aiming to functionalize the Pt selectively and not the surrounding alumina. Briefly, *NIPA* chips were ultrasonicated sequentially in dichloromethane (VWR, Amsterdam, The Netherlands), acetone and ethanol VLSI grade (VWR, Amsterdam, The Netherlands) for 1 min and blown dry with N_2. Subsequently the chips were treated with oxygen plasma (Diener Pico, Diener Electronic, Ebhausen, Germany) for 15 min. PDMS microchannels were cast from a 3D printed mold patterning a straight rectangular microchannel 0.2 × 1 × 7 mm^3 in dimensions using Sylgard 184 (Farnell, Utrecht, The Netherlands) prepared following the manufacturer's instructions. The PDMS chips were manually aligned over the *NIPA* electrodes and uncured PDMS was applied along the perimeter of the chip to enhance the bonding stability. The assembly was cured at 80 ◦C for 15 min. Immediately afterward, aliquoted 1-amino-undecanethiol (1 mM ethanolic solution) was injected into the microchannel through a pipette tip and

manipulated back and forth 5 times to remove any residual platinum oxides resulting from the plasma treatment and to form an amine-terminated thiol self-assembled monolayer (SAM).

	*1) A Si(100) wafer was thermally oxidized forming a 300-nm SiO_2 layer. Olin 917 resist was spin-coated at 4000 rpm, and exposed using an EVG-620 mask aligner to pattern microscale contact leads.*
	*2) A 5-nm Ti adhesive layer was deposited by electron-beam metal evaporation (DCA Metal-600) followed by 50 nm Pt.*
	*3) Residual resist and unwanted Pt were removed in acetone in a metal lift-off process. A 20-nm Al_2O_3 passivation layer was deposited with a Picosun Atomic Layer Deposition system.*
	*4) PMMA was spincoated at 4000 rpm (250 nm) and exposed using electron beam lithography (RAITH EBPG5150), patterning the reference electrode (right) and nanoelectrodes at the end of the contact leads (left) with varying diameters (0.1-4 µm).*
	*5) The Al2O3 was etched in Ar plasma using an Oxford i300 system, opening up the electrodes. Residual PMMA was removed in acetone and subsequent oxygen plasma.*

Figure 6.3: Nanofabrication process flow showing thin film deposition and patterning

After incubation overnight in an ethanol vapor-saturated environment, the channels were rinsed by pipetting 1 ml of ethanol VLSI and blown dry with N_2. Poly(ethylene) glycol diglycidyl ether (PEGDGE) was then injected (neat) into the microchannels and left overnight at 50 ◦C to react with the amine groups, forming an amine-reactive PEG oligomer layer on the surface. To complete the functionalization, anti-EpCAM antibodies (VU1D9 1 mg/ml) diluted 50x in 2 M sodium phosphate buffer at pH 9 were left to incubate for 4 h. Remaining reactive sites were blocked by bovine serum albumin (BSA, 1% (w/w) in phosphate buffered saline (PBS)) for 1 h. Finally, channels were rinsed with MilliQ and used immediately.

6.4.3.1 Chemical contrast

Adsorption of species to the alumina passivation layer would not contribute to the electrochemical signal to result in a false positive answer/readout, but it is undesirable since it could deplete the sample of analytes. Lacking a chemical anchor and being net uncharged molecules, the PEGDGE and antibodies (pI ∽7) do not interact with the alumina (pI ∽9). Conversely, BSA has a conveniently low pI (∽4.7) such that at physiological pH it bears charge opposite to that of alumina. So besides functioning as a chemical blocking agent to the PEGDGE, BSA also performs as a fouling reducing agent on the substrate.

To confirm the "chemical contrast" between Pt and alumina, *i.e.,* the ratio of deposited thiols and polymer between Pt and alumina, the same functionalization procedure as described here was applied to 1 × 1 cm^2 chips that were half coated with Pt using tape as a shadow mask in e-beam evaporation, the other half being coated by alumina.

These samples were examined using XPS (JEOL 9200, JEOL, Velp, The Netherlands) (using the same settings as described in Chapter 5) examine the ratio in sulphur coverage after SAM formation and carbon and carboxy group presence after reacting with PEGDGE. To investigate the antibody activity after functionalization and the ratio in

antibody coverage between the two substrates, PDMS microchannels were placed on the chips, crossing regions of both Pt and alumina substrate. Anti-SARS-CoV-2 (BioConnect, Huissen, The Netherlands) was used as an antibody (also diluted to 20 µg/ml in sodium phosphate buffer) in this experiment, to test whether its immobilization is as efficient as the anti-EpCAM used in Chapter 5. After functionalization as described above in Section 6.4.3, the channels were washed with PBS and incubated with fluorescein isothiocyanate-labeled anti-immunoglobulin G to stain surface-immobilized antibodies. On a Nikon TI-E inverted fluorescence microscope, the fluorescence intensity was recorded of Pt and alumina samples both with and without antibody functionalization.

6.4.4 Operation

6.4.4.1 Sensitivity - chronoamperometry with correlated microscopy.

For recording of currents in the order of pA with a noise level in the order of fA, currents must be amplified, and signals should be properly shielded. A FEMTO DDPCA amplifier (FEMTO, Berlin, Germany) was installed in a Faraday cage. *NIPA* chips were contacted with contact probes installed on micromanipulators. A voltage of 400 mV was applied between the nanoelectrodes (working electrodes, anode) and the reference electrode, and the current was monitored for prolonged time (min to hours).

Initial experiments were performed without PDMS channels in open reservoirs (under static conditions) to allow for optical monitoring of the experiments. Recorded binding events could thus be related to video recordings of microparticles adsorbing on the surface. To this end, a suspension of carboxylate-coated 1 µm polystyrene beads (MicroMod, Germany) dispersed in MilliQ water at 10^7 beads/ml was simply drop-cast over the chip before recording the current under ambient conditions. Ferrocene (aq) was added to reach a final concentration of 2 mM. Besides polystyrene beads, also dextran-modified 130 nm iron oxide particles (10^8/ml) (MicroMod, Germany) and gold nanoparticles (10^7/ml, 80 nm) were individually detected (data not shown in this chapter, similar to Figure 6.7) to demonstrate versatile (non-specific) single-nanoparticle detection.

6.4.4.2 Specificity - Extracellular vesicles

To demonstrate detection and identification of specific binding, flow conditions are required to remove non-specifically bound species and to study the dynamics of the interaction as described in Section 2. Placing a pump inside the Faraday cage made it challenging to record currents with acceptable noise levels. In the experiments described in this chapter, the flow was driven by hydrostatic pressure: a pipette tip with sample was left upright in the PDMS microchannel inlet, imposing a pressure difference of <1 mbar, enough to drive a constant flow for prolonged time. Extracellular vesicles were obtained from LNCaP (EpCAM+) cell culture supernatant by centrifuging at 1000 x *g* for 12 min,

giving 10^{10} particles/ml in the size range 100 – 500 nm as determined by Nanoparticle Tracking Analysis (see previous chapters). The supernatant was aliquoted and frozen at -80 ◦C. Before experiments, EVs were fixed by adding paraformaldehyde (PFA). The buffer was then exchanged using ultrafiltration spin filters with a molecular weight cut-off of 100 kDa, centrifuging 3x at 1000g for 11 min to substitute the buffer for MilliQ water with 2% saliva obtained from a consenting donor to mimic a realistic clinical sample; for a coronatest, saliva would be the preferred medium rather than nasal swabs if considering patient comfort. Recall that EVs are used as a model for virus particles..As before, Fc dimethanol (aq) was added to reach a final concentration of 2 mM. Chronoamperometric experiments were then conducted, as described before but now under flow conditions. Three negative control experiments were conducted in which specific interaction was not expected:

- The same sample was used, but instead of anti-EpCAM, anti-SARS-CoV-2 (RBD) was used in the same buffer at the same dilution.
- The same sample was used, but the chips were not functionalized (PEGDGE was blocked by BSA without introduction of anti-EpCAM).
- The chips were prepared the same way, but instead of EVs, latex beads were used (as before in sensitivity experiments)

6.5 Results

6.5.1 Functionalization

6.5.1.1 XPS

1×1 cm^2 chips were prepared with Pt coating on one side and AL_2O_3 coating on the other side to investigate the selectivity of deposition among these materials. First, AL_2O_3 was deposited by atomic layer deposition on the whole chip and then Pt was evaporated over it on one half of the chip, shadowmasking the other half with Kapton foil. Figures 6.4 and 6.5 show XPS wide scans of Pt and AL_2O_3 regions, respectively, on the same chip after 1-amino-undecanethiol SAM formation. On Pt, 2.33% S 2p3/2 was found, *vs.* 0.16% on the AL_2O_3 part.

6.5.1.2Anti-IgG-FITC

After completing the functionalization routine, the surface coverage was inspected by staining the immobilized antibodies with fluorescently labeled anti-IgG. In three Pt/Al_2O_3 chips, the functionalization was completed with anti-SARS-CoV-2 (RBD). In three other negative control chips, the antibody was omitted and the surface was blocked with BSA. Results obtained after exposing and image processing under similar conditions are shown in Fig. 6.6. ImageJ was used to analyze images taken from 3 locations in the channels. Integrating the grey values and subtracting the background gave a ratio of 10.4 in signal between the top left and top right panel, more or less corresponding to the ratio in S 2p3/2 observed on Pt and Al_2O_3 substrates in XPS.

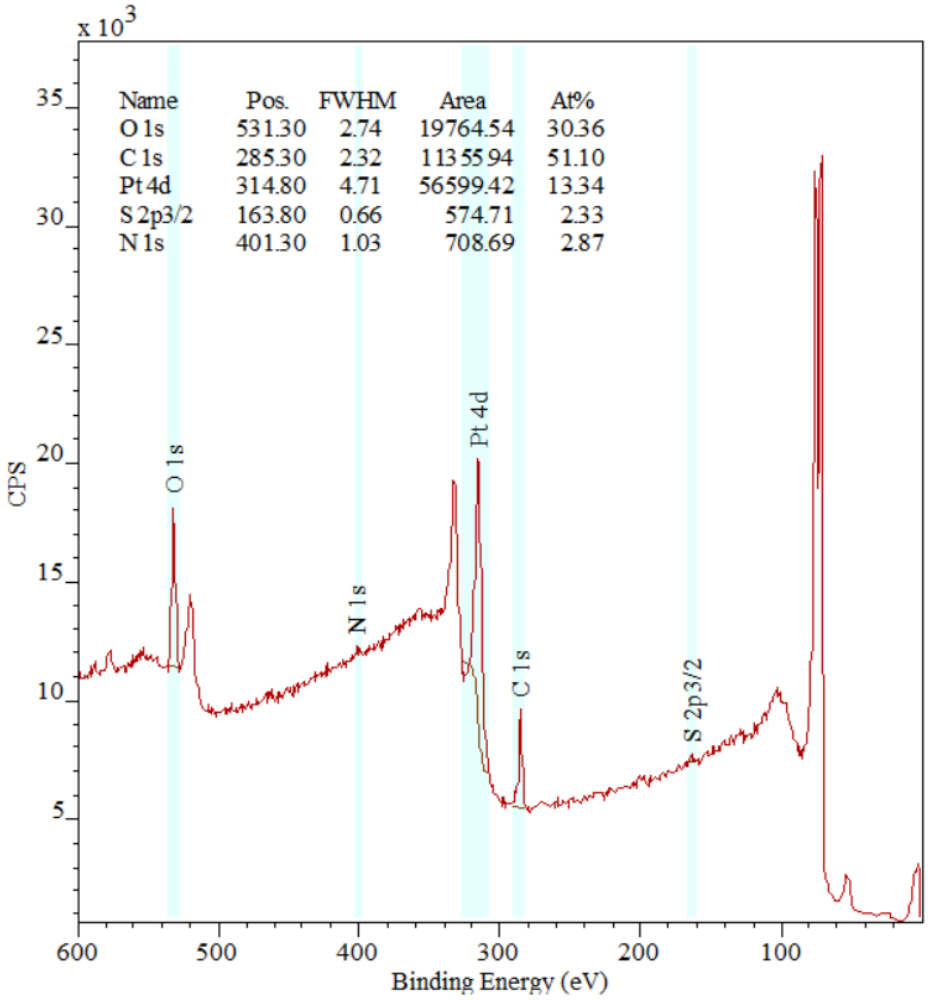

Figure 6.4: XPS wide scan of Pt with a 1-amino-undecanethiol SAM. Sulphur accounts for ~2% of the atomic species in the probed volume.

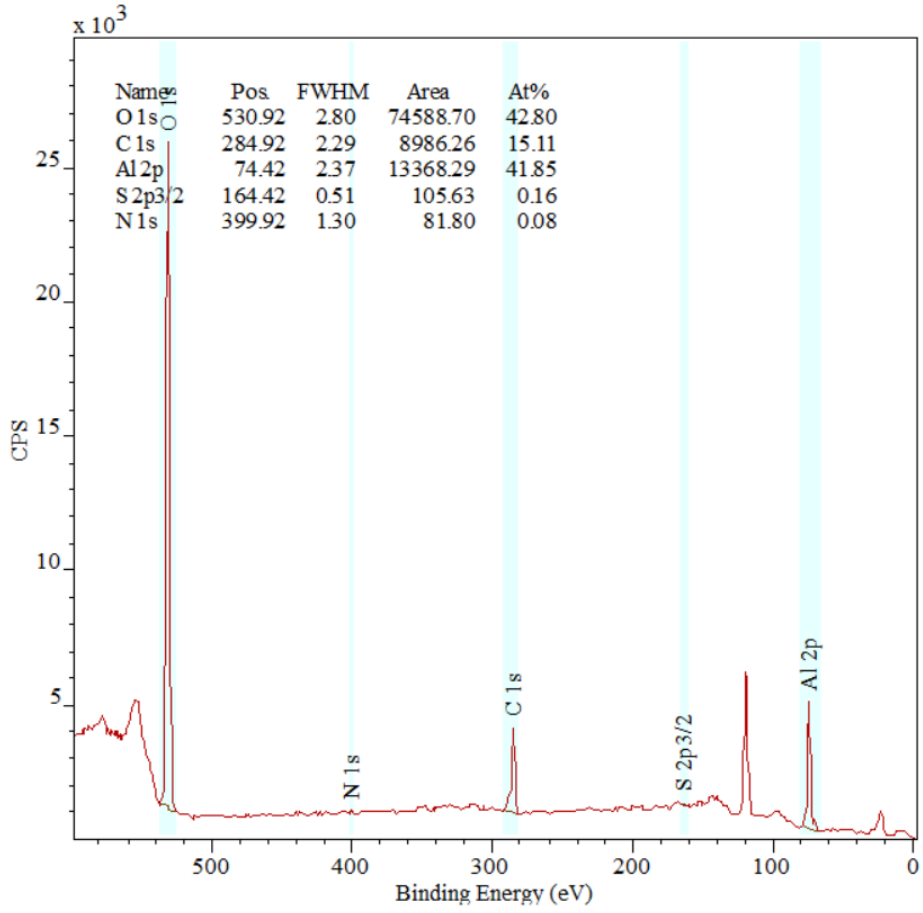

Figure 6.5: XPS wide scan of Al_2O_3 with an 1-amino-undecanethiol SAM. *Sulphur accounts for ~0.2% of the atomic species in the probed volume.*

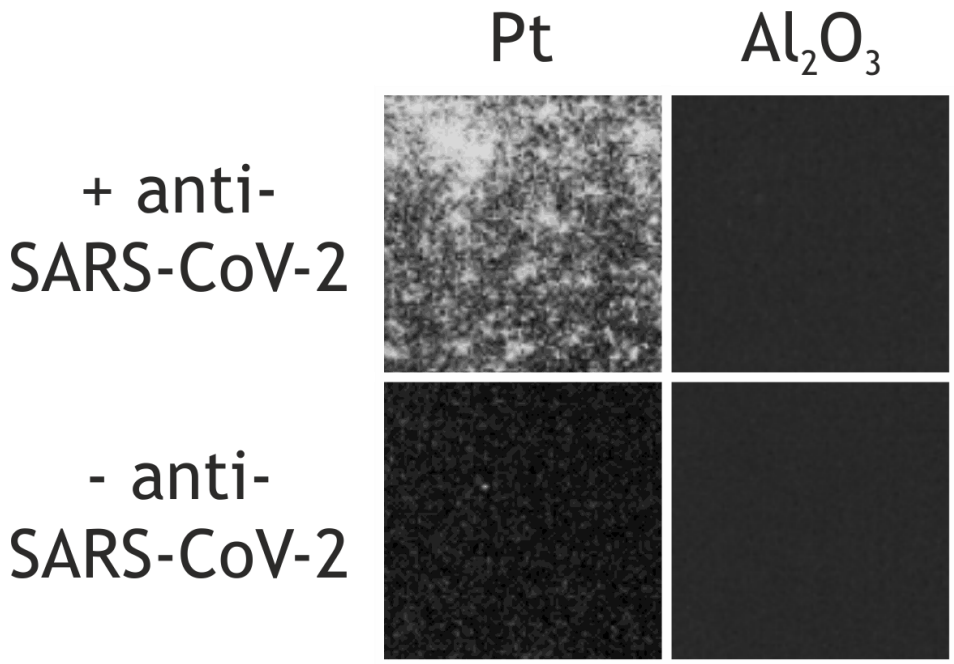

Figure 6.6: *Fluorescence intensity of antibody-coated bare Pt vs. negative controls (antibodies on Pt and bare Pt and Al2O3).*

6.5.2 Sensitivity: single-nanoparticle detection

Chronoamperometric curves recorded in drop-cast latex bead suspensions are shown in Figures 6.7 and 6.8. Figure 6.7 presents multiple sequential adsorption events of 1-µm beads (in MilliQ with 2 mM Fc dimethanol) on a 4µm *NIPA* electrode, each with a discrete current drop, until the *NIPA* electrode was almost completely covered by nanoparticles. As can be seen, the step sizes vary, which is related to the polydispersity of the particles, in line with the polydispersity index as reported by the manufacturer is 0.2. Figure 6.8 shows a single 1-µm bead being electrophoretically attracted before adsorbing on a 500-nm *NIPA* electrode, correlating with a concomitant current drop.

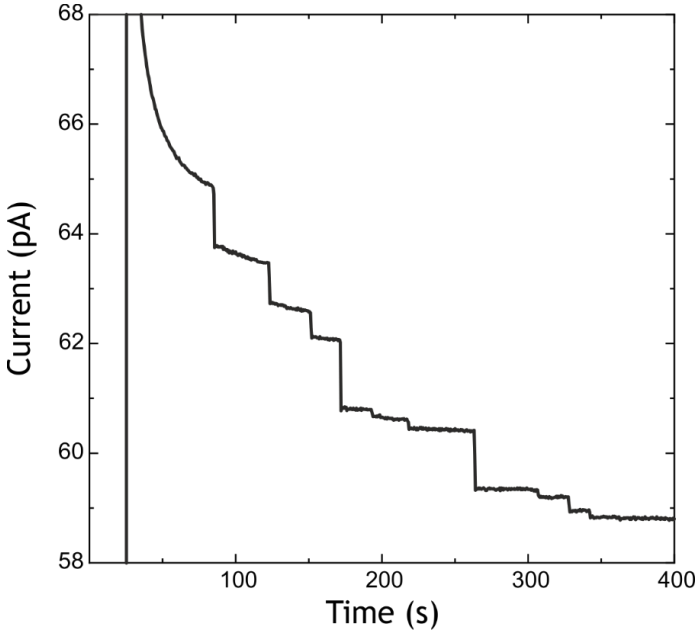

Figure 6.7: *Time trace of current recorded during latex bead absorption showing clear discrete adsorption events.*

6.5.3 Specificity: single extracellular vesicle detection

Figure 6.9a shows a chronoamperometric curve of (EpCAM-presenting) LNCaP extracellular vesicles diluted to 10^6 EVs/ml in MilliQ water with 2% saliva on 500-nm anti-EpCAM functionalized *NIPA* electrodes under mild flow conditions (<2 mbar hydrostatic pressure). Only in these samples were binding events observed that were longer than 1 s. Negative control experiments show shorter interactions (note the scaled *x*-axis). Non-specific interaction of an LNCaP EV with anti-SARS-CoV-2 was recorded as presented in Figure 6.9b; the duration of the event is ∽250 ms. A similar short interaction was recorded for a latex bead (Figure 6.9c). The amplitude of the peak is larger because the radius of the latex bead is much larger (500 nm) than that of an EV (on average ∽150 nm). In absence of any functionalization (Figure 6.9d), the non-specific interaction of EVs is shorter and with smaller amplitude, possibly due to the anti-fouling properties of the BSA coating.

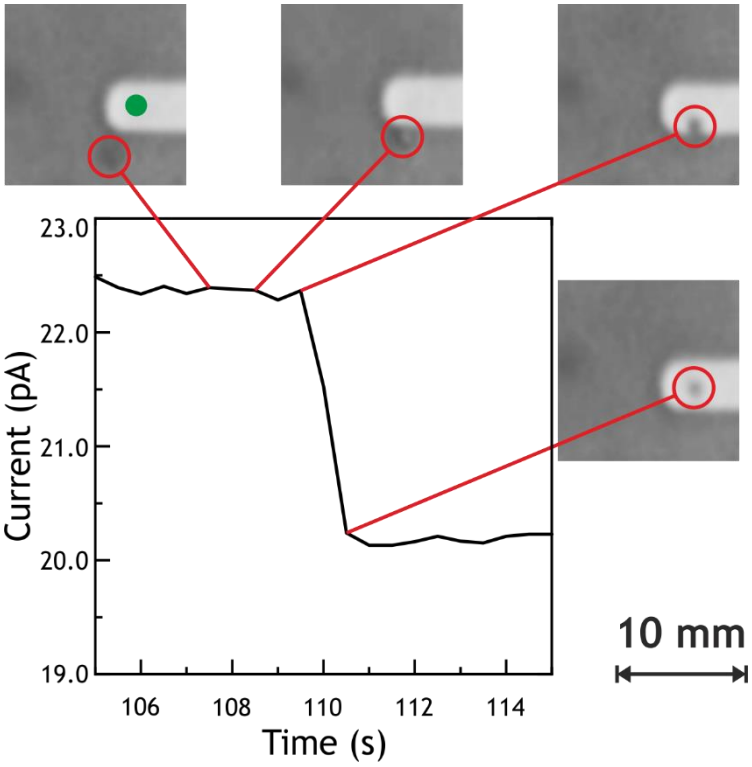

Figure 6.8: Single adsorption event of a latex bead (diameter 1 μm) captured on video. *The location of the bead in the screenshots is correlated with the corresponding timepoints on the curve. The location of the NIPA electrode is not clear from the figures, but is indicated by the green circle in the top left inset.*

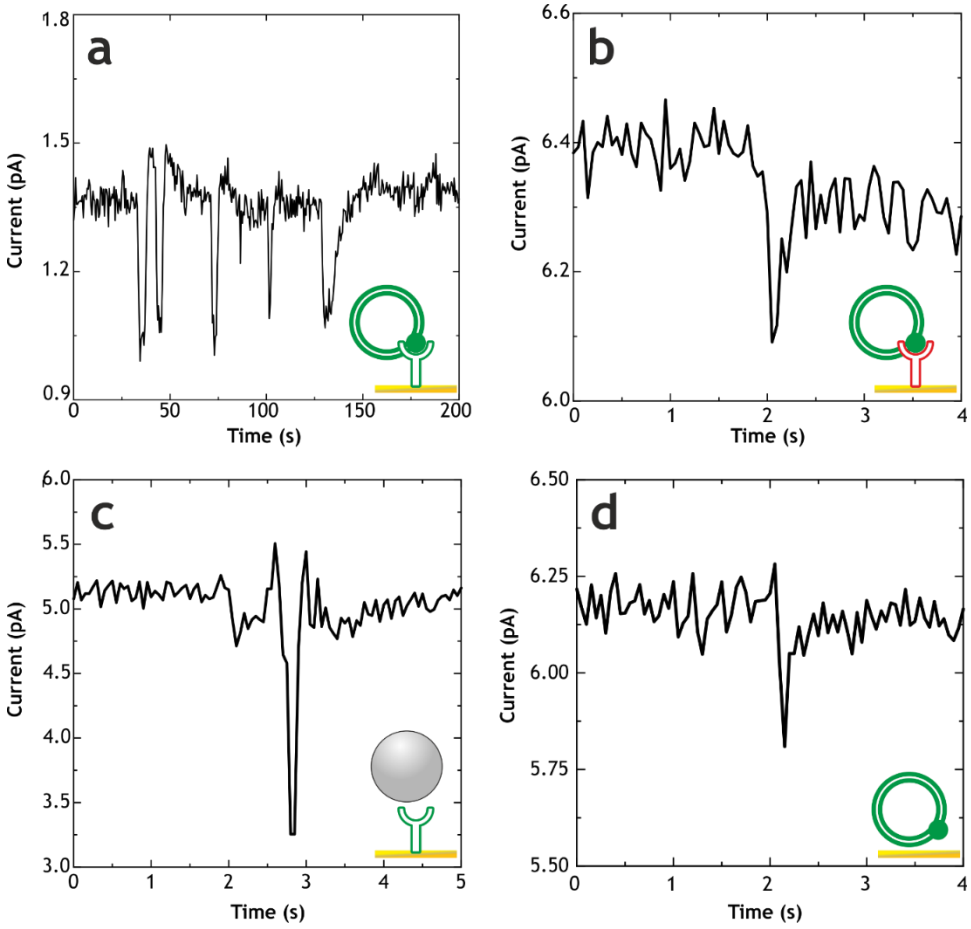

Figure 6.9: NIPA traces showing specific (a) and non-specific (b,c,d,) interaction. *a) Specific interaction of (EpCAM+) tdEVs with anti-EpCAM functionalized electrodes. b) Non-specific interaction of tdEVs on anti-SARS-CoV-2. c) Non-specific interaction of latex beads on anti-EpCAM). d) Non-specific interaction of tdEVs on non-functionalized (BSA-coated) electrodes.*

6.6 Discussion and conclusion

6.6.1 Sensitivity

In the above sections, the concept was presented for a biosensor with ultimate, one-particle sensitivity, and the physical principles of the technology were explained. Using various analytes in various media, it has been demonstrated that indeed, the system can detect nanoparticles at the highest possible resolution by counting micrometer-sized particles one by one. Full integration of the sensors with a functional, high-performance sample handling system is still in progress. Therefore, it is difficult to predict the eventual throughput and sensitivity of the system or to promise that it can detect every single analyte in a sample. Theoretically single-particle detection is not impossible thanks to the process of electrophoresis. However, electrophoresis work best in dilute samples with lower ionic strength, and such dilution does of course limit the chances for single-particle detection. It thus remains to be investigated under which conditions this is possible: *e.g.,* lower flow rates reduce the probability of particles far from the sensor escaping the pull of the electric field. Ultimately, there is a trade-off between desired sample processing time (related to *e.g.,* flow rate) and desired limit of detection. If there is no acceptable balance in the current configuration, then this might be improved by parallelization.

6.6.2 Specificity

Before the specificity of the system can convincingly be demonstrated, the sensor needs to be better integrated with a reliable hydrodynamic actuation system. This will allow for the distinction between specific and non-specific interactions based on stability of the binding under the imposed flow conditions. Remarkably stable extracellular vesicle binding events in the order of seconds were observed when anti-EpCAM was bound to the surface. Such events were not observed in control experiments with vesicles where no antibody was present. Here, events were visible, but showed up as narrow sub-second spikes. However, it is too early to confidently claim that that cannot have to do with

sample preparation. Moreover, these results may only be compared when performed under comparable flow conditions.

Even when the system is fully optimized, even with perfect sensitivity, it can only perform as well as the combination of generic antifouling and the antibody that is immobilized on the electrodes. In addition, such information is only as interesting as the biomarker that is targeted, as can be seen for the case of corona and cancer.

Corona is – detection-wise – a relatively simple case compared to cancer, since presence of a single SARS-CoV-2 virion in a test sample is theoretically enough to identify the donor as being at risk for themselves or others. On the other hand, the choice of antibody needs to be carefully considered, and it is uncertain how the performance will be affected by genetic mutations. It also remains to be seen how the system responds to samples from healed patients with residual neutralized virus.

Such simplicity does, also with this sensor, certainly not apply to cancer. The validity of the epithelial cell adhesion molecule (EpCAM) as a target has been extensively debated. It is known that it does not allow detecting all circulating tumor cells because, these undergo a so-called "epithelial-mesenchymal transition" as the disease progresses, with a concomitant reduction in EpCAM expression. By extension, the same can be assumed for tumor-derived extracellular vesicles. Moreover, EpCAM is not intrinsically tumor related: it is present on all epithelial tissues and only suspicious when found in the blood stream. As an epiphenomenal result of venipuncture, EpCAM+ debris from benign tissue may enter into any sample, and as such, a non-zero background in healthy sample donors may be expected regardless of the performance of the system. It is then crucial to set up the clinical validation in such a way that this is accounted for, and to carefully consider how to interpret the results.

6.6.3 Reliability

The largest unknown in the *NIPA* system is the set of optimal operation parameters. It is difficult to predict (even from a wealth of *ensemble* kinetic data from SPR) what the timescale of *individual* antibody-antigen complex formation and also dissociation is under flow conditions as imposed by the microchannel geometry, and what the inter-sample variation of these parameters could be. In the worst case, the residence times of abundant large sticky non-target components overlap with those of small transient analyte particles. At the other extreme, if analyte particles are very stably bound to the surface such that it is difficult to remove them, the sensor surface (with 18 sensing electrodes in the current design) may be quickly saturated with analytes, preventing other particles from being detected.

For many purposes, detection of the presence of a biomarker in a sample is not enough, but there is also a demand for quantitative data. For instance, in cancer patient monitoring it is important to record changes over the course of time in the concentration of tdEVs. Although the system in its current form does give kinetic data – the time required to saturate the sensor array with analyte is indicative of the analyte concentration – it is not designed for enumeration with this fluidic operation. In addition, it would require significant validation so as to provide stable signals with minimal drift and maximum reproducibility over a period of months. Sample-wise, depending on how stable the analytes are bonded to the surface it may be required to incorporate surface regeneration steps to be able to continuously present a pristine sensor array to the sample (similar to SPR). Such fluidic operation (injecting other buffers) would require a more complex system, which is feasible for a next iteration of the devices, but beyond the scope of this chapter.

6.6.4 Outlook

For commercial purposes, after optimization at the lab scale, it is crucial to develop quality management systems to guarantee the reproducibility and to maintain a high degree of reliability in production. To eventually get CE certification (allowing the product to be sold in the EU), it should not only perform very well to live up to ambitious clinical claims, but compared to the current status, the fabrication yield should increase from 90% to very close to 100%.

For this reason, simplicity is crucial in the design of any component of the system. The sensor chip consists of only three thin films and is fabricated using only two lithographic exposure steps. Importantly, the surface functionalization can be performed reproducibly and completely in-situ after assembling the sensing and the microfluidic chips and occurs mostly in ambient conditions (except only for the PEGDGE grafting which takes place at 50 ◦C). By eliminating as many modes of failure as possible, the aim is to design a platform that is as robust and versatile as it can be.

Ultimately, *NIPA* is the basis for a platform that could be used to detect any biomarker for any purpose. Currently it works theoretically for supramolecular aggregates from >50 nm (∽the lower limit of the lithography techniques available at MESA+) up to bacteria of a few µm, which (including the undiscovered potential of extracellular vesicles as a biomarker) awards opportunities to explore virtually any disease.

6.7 References

(1) Rikkert, L. G.; Beekman, P.; Caro, J.; Coumans, F. A. W.; Enciso-Martinez, A.; Jenster, G.; Le Gac, S.; Lee, W.; van Leeuwen, T. G.; Loozen, G. B.; et al. Cancer-ID: Toward Identification of Cancer by Tumor-Derived Extracellular Vesicles in Blood. *Front. Oncol.* **2020**, *10*, 608. https://doi.org/10.3389/fonc.2020.00608.

(2) Mathew, D.; Beekman, P.; Lemay, S.; Zuilhof, H.; Le Gac, S.; van der Wiel, W. Electrochemical Detection of Tumor-Derived Extracellular Vesicles on Nanointerdigitated Electrodes. *Nano Lett. 0* (0), null-null. https://doi.org/10.1021/acs.nanolett.9b02741.

(3) Coumans, F. A. W.; Ligthart, S. T.; Uhr, J. W.; Terstappen, L. W. M. M. Challenges in the Enumeration and Phenotyping of CTC. *Clin. Cancer Res.* **2012**, *18* (20), 5711–5718. https://doi.org/10.1158/1078-0432.CCR-12-1585.

(4) Kucirka, L. M.; Lauer, S. A.; Laeyendecker, O.; Boon, D.; Lessler, J. Variation in False-Negative Rate of Reverse Transcriptase Polymerase Chain Reaction-Based SARS-CoV-2 Tests by Time Since Exposure. *Annals of internal medicine*. NLM (Medline) August 18, 2020, pp 262–267. https://doi.org/10.7326/M20-1495.

(5) Dinnes, J.; Deeks, J. J.; Adriano, A.; Berhane, S.; Davenport, C.; Dittrich, S.; Emperador, D.; Takwoingi, Y.; Cunningham, J.; Beese, S.; et al. Rapid, Point-of-Care Antigen and Molecular-Based Tests for Diagnosis of SARS-CoV-2 Infection. *Cochrane Database Syst. Rev.* **2020**, *2020* (8). https://doi.org/10.1002/14651858.CD013705.

(6) Cheng, H. Y.; Jian, S. W.; Liu, D. P.; Ng, T. C.; Huang, W. T.; Lin, H. H. Contact Tracing Assessment of COVID-19 Transmission Dynamics in Taiwan and Risk at Different Exposure Periods before and after Symptom Onset. *JAMA Intern. Med.* **2020**, *180* (9), 1156–1163. https://doi.org/10.1001/jamainternmed.2020.2020.

(7) He, X.; Lau, E. H. Y.; Wu, P.; Deng, X.; Wang, J.; Hao, X.; Lau, Y. C.; Wong, J. Y.; Guan, Y.; Tan, X.; et al. Temporal Dynamics in Viral Shedding and Transmissibility of COVID-19. *Nat. Med.* **2020**, *26* (5), 672–675. https://doi.org/10.1038/s41591-020-0869-5.

(8) Vogels, C. B. F.; Brito, A. F.; Wyllie, A. L.; Fauver, J. R.; Ott, I. M.; Kalinich, C. C.; Petrone, M. E.; Landry, M.-L.; Foxman, E. F.; Grubaugh, N. D. Analytical Sensitivity and Efficiency Comparisons of SARS-COV-2 QRT-PCR Assays. *medRxiv* **2020**, 2020.03.30.20048108. https://doi.org/10.1101/2020.03.30.20048108.

(9) To, K. K.-W.; Tsang, O. T.-Y.; Leung, W.-S.; Tam, A. R.; Wu, T.-C.; Lung, D. C.; Yip, C. C.-Y.; Cai, J.-P.; Chan, J. M.-C.; Chik, T. S.-H.; et al. Temporal Profiles of Viral Load in Posterior Oropharyngeal Saliva Samples and Serum Antibody Responses during Infection by SARS-CoV-2: An Observational Cohort Study. *Lancet Infect. Dis.* **2020**, *3099* (20), 1–10. https://doi.org/10.1016/s1473-3099(20)30196-1.

(10) Zou, L.; Ruan, F.; Huang, M.; Liang, L.; Huang, H.; Hong, Z.; Yu, J.; Kang, M.; Song, Y.; Xia, J.; et al. SARS-CoV-2 Viral Load in Upper Respiratory Specimens of Infected Patients. *New England Journal of Medicine*. Massachussetts Medical Society March 19, 2020, pp 1177–1179. https://doi.org/10.1056/NEJMc2001737.

(11) Pfefferle, S.; Reucher, S.; Nörz, D.; Lütgehetmann, M. Evaluation of a Quantitative RT-PCR Assay for the Detection of the Emerging Coronavirus SARS-CoV-2 Using a High Throughput System. *Eurosurveillance* **2020**, *25* (9), 2000152. https://doi.org/10.2807/1560-7917.ES.2020.25.9.2000152.

(12) Matheeussen, V.; Loens, K.; Lammens, C.; Vilken, T.; Koopmans, M.; Goossens, H.; Ieven, M. Preparedness of European Diagnostic Microbiology Labs for Detection of SARS-CoV-

2, March 2020. *J. Clin. Virol.* **2020**, *128*, 104432. https://doi.org/10.1016/j.jcv.2020.104432.
(13) Bielicki, J. A.; Duval, X.; Gobat, N.; Goossens, H.; Koopmans, M.; Tacconelli, E.; van der Werf, S. Monitoring Approaches for Health-Care Workers during the COVID-19 Pandemic. *The Lancet Infectious Diseases*. Lancet Publishing Group October 1, 2020, pp e261–e267. https://doi.org/10.1016/S1473-3099(20)30458-8.
(14) Baggerman, J.; M. J. Smulders, M.; Zuilhof, H. Romantic Surfaces: A Systematic Overview of Stable, Biospecific, and Antifouling Zwitterionic Surfaces. *Langmuir* **2019**, *35* (5), 1072–1084. https://doi.org/10.1021/acs.langmuir.8b03360.
(15) Rosso, M.; Nguyen, A. T.; de Jong, E.; Baggerman, J.; Paulusse, J. M. J.; Giesbers, M.; Fokkink, R. G.; Norde, W.; Schroën, K.; Rijn, C. J. M. van; et al. Protein-Repellent Silicon Nitride Surfaces: UV-Induced Formation of Oligoethylene Oxide Monolayers. *ACS Appl. Mater. Interfaces* **2011**, *3* (3), 697–704. https://doi.org/10.1021/am100985c.
(16) Van Andel, E.; De Bus, I.; Tijhaar, E. J.; Smulders, M. M. J.; Savelkoul, H. F. J.; Zuilhof, H. Highly Specific Binding on Antifouling Zwitterionic Polymer-Coated Microbeads as Measured by Flow Cytometry. *ACS Appl. Mater. Interfaces* **2017**, *9* (44), 38211–38221. https://doi.org/10.1021/acsami.7b09725.
(17) Van Andel, E.; Lange, S. C.; Pujari, S. P.; Tijhaar, E. J.; Smulders, M. M. J.; Savelkoul, H. F. J.; Zuilhof, H. Systematic Comparison of Zwitterionic and Non-Zwitterionic Antifouling Polymer Brushes on a Bead-Based Platform. *Langmuir* **2019**, *35* (5), 1181–1191. https://doi.org/10.1021/acs.langmuir.8b01832.
(18) Bruins, J. J.; Westphal, A. H.; Albada, B.; Wagner, K.; Bartels, L.; Spits, H.; Van Berkel, W. J. H.; Van Delft, F. L. Inducible, Site-Specific Protein Labeling by Tyrosine Oxidation-Strain-Promoted (4 + 2) Cycloaddition. *Bioconjug. Chem.* **2017**, *28* (4), 1189–1193. https://doi.org/10.1021/acs.bioconjchem.7b00046.
(19) Bruins, J. J.; Albada, B.; van Delft, F. Ortho-Quinones and Analogues Thereof: Highly Reactive Intermediates for Fast and Selective Biofunctionalization. *Chem. - A Eur. J.* **2018**, *24* (19), 4749–4756. https://doi.org/10.1002/chem.201703919.
(20) Sen, R.; Gahtory, D.; Escorihuela, J.; Firet, J.; Pujari, S. P.; Zuilhof, H. Approach Matters: The Kinetics of Interfacial Inverse-Electron Demand Diels–Alder Reactions. *Chem. - A Eur. J.* **2017**, *23* (53), 13015–13022. https://doi.org/10.1002/chem.201703103.
(21) Roeven, E.; Scheres, L.; Smulders, M. M. J.; Zuilhof, H. Design, Synthesis, and Characterization of Fully Zwitterionic, Functionalized Dendrimers. *ACS Omega* **2019**, *4* (2), 3000–3011. https://doi.org/10.1021/acsomega.8b03521.
(22) Kuzmyn, A. R.; Nguyen, A. T.; Zuilhof, H.; Baggerman, J. Bioactive Antifouling Surfaces by Visible-Light-Triggered Polymerization. *Adv. Mater. Interfaces* **2019**, *6* (12). https://doi.org/10.1002/admi.201900351.
(23) Baggerman, J.; Smulders, M. M. J.; Zuilhof, H. Romantic Surfaces: A Systematic Overview of Stable, Biospecific, and Antifouling Zwitterionic Surfaces. *Langmuir* **2019**, *35* (5), 1072–1084. https://doi.org/10.1021/acs.langmuir.8b03360.
(24) Whitesides, G. The Lab Finally Comes to the Chip! *Lab on a Chip*. Royal Society of Chemistry September 7, 2014, pp 3125–3126. https://doi.org/10.1039/c4lc90072c.
(25) M. Quinn, B.; G. van't Hof, P.; G. Lemay, S. Time-Resolved Electrochemical Detection of Discrete Adsorption Events. *J. Am. Chem. Soc.* **2004**, *126* (27), 8360–8361. https://doi.org/10.1021/ja0478577.
(26) Jung Chung, H.; Lee, J.; Hwang, J.; Hee Seol, K.; Mi Kim, K.; Song, J.; Chang, J. Stochastic Particle Approach Electrochemistry (SPAE): Estimating Size, Drift Velocity, and Electric Force of Insulating Particles. *Anal. Chem.* **2020**, *92* (18), 12226–12234.

https://doi.org/10.1021/acs.analchem.0c01532.
(27) Baker, L. A. Perspective and Prospectus on Single-Entity Electrochemistry. *J. Am. Chem. Soc.* **2018**. https://doi.org/10.1021/jacs.8b09747.
(28) Bai, Y. Y.; Wu, Z.; Xu, C. M.; Zhang, L.; Feng, J.; Pang, D. W.; Zhang, Z. L. One-to-Many Single Entity Electrochemistry Biosensing for Ultrasensitive Detection of Microrna. *Anal. Chem.* **2020**, *92* (1), 853–858. https://doi.org/10.1021/acs.analchem.9b03492.
(29) Yadav, S.; Boriachek, K.; Islam, M. N.; Lobb, R.; Möller, A.; Hill, M. M.; Hossain, M. S. Al; Nguyen, N. T.; Shiddiky, M. J. A. An Electrochemical Method for the Detection of Disease-Specific Exosomes. *ChemElectroChem* **2017**, *4* (4), 967–971. https://doi.org/10.1002/celc.201600391.
(30) Lebègue, E.; Anderson, C. M.; Dick, J. E.; Webb, L. J.; Bard, A. J. Electrochemical Detection of Single Phospholipid Vesicle Collisions at a Pt Ultramicroelectrode. *Langmuir* **2015**, *31* (42), 11734–11739. https://doi.org/10.1021/acs.langmuir.5b03123.
(31) E. Dick, J.; Renault, C.; J. Bard, A. Observation of Single-Protein and DNA Macromolecule Collisions on Ultramicroelectrodes. *J. Am. Chem. Soc.* **2015**, *137* (26), 8376–8379. https://doi.org/10.1021/jacs.5b04545.
(32) Beekman, P.; Enciso-Martinez, A.; Rho, H. S.; Pujari, S. P.; Lenferink, A.; Zuilhof, H.; Terstappen, L. W. M. M.; Otto, C.; Le Gac, S. Immuno-Capture of Extracellular Vesicles for Individual Multi-Modal Characterization Using AFM, SEM and Raman Spectroscopy. *Lab Chip* **2019**, *19* (15), 2526–2536. https://doi.org/10.1039/c9lc00081j.
(33) Bond, A. M.; Luscombe, D.; Oldham, K. B.; Zoski, C. G. A Comparison of the Chronoamperometric Response at Inlaid and Recessed Disc Microelectrodes. *J. Electroanal. Chem.* **1988**, *249* (1–2), 1–14. https://doi.org/10.1016/0022-0728(88)80345-0.
(34) Arrigan, D. W. M. Nanoelectrodes, Nanoelectrode Arrays and Their Applications. In *Analyst*; Royal Society of Chemistry, 2004; Vol. 129, pp 1157–1165. https://doi.org/10.1039/b415395m.
(35) Renault, C.; Lemay, S. G. Electrochemical Collisions of Individual Graphene Oxide Sheets: An Analytical and Fundamental Study. *ChemElectroChem* **2020**, *7* (1), 69–73. https://doi.org/10.1002/celc.201901606.
(36) Bruus, H. *Theoretical Microfluidics*; Oxford University Press, 2008.

Summary

The goal of this project was to develop platforms for the detection and analysis of extracellular vesicles (EVs). Detection, because it was hypothesized that the presence and concentration of various kinds of extracellular vesicles in patient blood samples, as measured in a *liquid biopsy*, would prove to be a valuable parameter to guide therapy of primarily cancer patients.

Analysis, because despite the exponential growth of the field in recent years, there remain many mysteries regarding the biogenesis, composition and physiological behavior of these submicroscopic biological information carriers. In addition, and notwithstanding clear guidelines by expert societies, there is still much confusion in the literature about how to interpret experimental results – *e.g.,* how to properly prepare samples or when to call a detected object an EV. The work described in this thesis aims to support the clinical context by providing technological concepts that could be useful both for fundamental biological studies into the occurrence and behavior of EVs and by giving considerations for sample preparation. It explains why extremely sensitive biosensors are required and describes the development of some *lab-on-a-chip* solutions.

Chapter 1 introduces the concept of liquid biopsy and circulating tumor cells and explains the reasons to explore the feasibility of using EVs instead. It then goes deeper into the composition of EVs and their distribution in the blood. Next, challenges involved in sample preparation are discussed, as well as the barriers to high-throughput reliable detection of EVs.

Chapter 2 gives an overview of the Cancer-ID consortium that provided the framework for this (sub)project. It highlights the findings of colleagues in Amsterdam, Delft, Groningen, Twente and Utrecht, who studied EVs from various perspectives in parallel. It gives a comprehensive comparison of the efficacy and throughput of various methods to study EVs for their corresponding applications.

Chapter 3 explains the necessity for multi-modal analysis and introduces a first platform that allowed studying *individual* tumor-derived extracellular vesicles (tdEVs) with scanning electron microscopy, Raman spectrometry and atomic force microscopy to correlate the respectively morphological, biochemical and mechanical data obtained from these single nanoparticles.

Chapter 4 reports observations made while performing sample preparation of EVs for different purposes. It was found that a class of polymers, *i.e.,* organosilicon compounds, have a stable interaction with phospholipid membranes found in cells, EVs and artificial membrane models. This has implications for the use of these polymers not only in research but even in daily life, as these silicones occur in cosmetics, pharmaceutics and even food.

Chapter 5 presents an integrated system that uses a two-stage identification of tdEVs followed by a two-stage signal amplification. This awarded a highly specific detection method: only tdEVs gave a detectable signal. It also proved to be ultrasensitive; thanks to miniaturization tot the nanoscale of an ELISA-like electrochemical detection mechanism, tdEVs were detectable at concentrations as low as 10 tdEVs/µl.

Chapter 6 explores the qualities of a hypothetically ideal biosensor system and provides those solutions that are technologically available to us now.

The last chapter discusses how the preceding chapters were able to answer questions existing in the field and what is necessary to further explore the remaining mysteries.

7

Discussion

“Everybody has a plan until they get punched in the mouth”
- Mike Tyson

7.1 tdEVs for liquid biopsy

7.1.1 Before Cancer-ID

In 2015, the NWO "Perspectief" programme Cancer-ID started, ultimately involving 22 industrial partners, 11 principal investigators and 9 PhD students, from the universities of Amsterdam (AMC), Delft, Groningen, Utrecht, Twente and Wageningen. There were indications back then that "small tumor cell fragments" were promising predictors of clinical outcome.[1] The field of extracellular vesicle research was still young (the International Society of Extracellular Vesicles was founded in 2011 only, see also Figure 1.2 of this thesis), but it became apparent that these "fragments" were indeed (tumor-derived) EVs. The Cancer-ID programme was designed to investigate the clinical utility of tdEVs. Several research questions had to be answered:

- What is the concentration of tdEVs in patient samples?
- What is the prognostic value of tdEVs?
- What are the physical properties of tdEVs?
- Which biomarkers are present in and on tdEVs?
- How do other components of patient samples interfere with tdEV detection of characterization?
- Which detection method is most suitable for the quantification of tdEV concentration in patient plasma?

7.1.2 Cancer-ID

In the Cancer-ID project, as described in Chapter 2, these questions have been largely addressed. At the AMC, useful insights were gained regarding the isolation of pure fractions of tdEVs[1] and protocols were established for their characterization with transmission electron microscopy.[2] Moreover, impactful lessons were learned about the characterization of tdEVs with flow cytometry.[3–6] Also from the AMC, came the results obtained with SPR which gave meaningful insights regarding the kinetics and stability of tdEV immobilization.[7,8] Altogether, this helped to understand the size and immunological properties of tdEVs, and

importantly also how to visualize tdEVs using fluorescence microscopy.

Raman studies on tdEVs performed in solution (at UT) were very useful in acquiring information about how to recognize tdEVs specifically in a completely label-free manner.[9–11] This knowledge was directly applied in more sophisticated multi-modal analyses along with AFM-related knowledge from RuG[12] (see section 8.2) Most importantly, the tremendous challenge of segregating tdEVs from other plasma components became apparent.[11] Notably, lipoproteins vastly outnumber tdEVs in plasma while being physicochemically strikingly similar.

A paper from the Cancer-ID consortium that is highly relevant to all the work presented in this thesis describes the prognostic value of tdEVs as detected using the CellSearch system.[13] A set of patient samples that had previously been used in clinical studies regarding the validity of CellSearch for cancer diagnosis, was re-analyzed for its tdEV content. The settings were changed such that smaller (<4 μm) objects without a nucleus, which are normally not regarded as cells and therefore ignored, were now counted.

The conclusion from this paper is that these objects have similar prognostic value to CTCs. Moreover, is was shown that within cohorts of patients that received a "favorable" prognosis based on CTC counts, it was possible to further stratify them based on tdEV counts. A limitation of using tdEVs using this system is that no threshold value could be determined to distinguish healthy donors from cancer patients, since there was always a high background of EpCAM-positive particles. As discussed before in Chapters 1 and 2, it should be noted that this system only regards the largest fraction of tdEVs (<1%), so the background may be relatively much lower if the entire population of tdEVs could be considered. Interestingly, already in this small fraction of tdEVs, their prognostic power was proven in the Cancer-ID project.[14]

7.1.3 Remaining challenges (for Cancer-ID 2.0)

Although there are models (based on Cancer-ID results) estimating the tdEV plasma concentration of patient samples (see Chapter 2), the exact range is still unknown, because to this day there is no reliable method to determine this concentration. The system described in Chapter 5 could probably be used to quantify the middle-to-high range of tdEV concentrations in patient plasma, but

there are likely patients with concentrations of tdEVs that fall below this system's limit of detection.

Another goal to pursue is nucleic acid isolation. During multiple meetings of Cancer-ID members and clinicians, it became apparent that there is a need for the reliable specific isolation of tdEVs and subsequent extraction of their genetic material. After amplification (*e.g.*, using PCR) and sequencing, nucleic acid analysis could reveal genetic biomarkers specific to the disease. The platform described in Chapter 3 may prove very useful for this application: it can be easily redesigned to maximize the functionalized surface area of a volume suitable for PCR (as little as 1 µl), and after all other EVs and non-tdEV components are washed away, the specifically bound tdEVs may be lysed in the microchannel to yield an amplifiable sample.

If there will be another nation-wide research consortium focusing on tdEV analysis for cancer diagnostics applications, these two approaches (a fast point-of-care "tdEV counter" and genetic analysis of specific tdEVs) should both be considered. Given the technology readiness of the platforms described in this thesis, it would be interesting to include large-scale validation trials to prove the efficacy of these diagnostic tools.

7.2 Multi-modal analysis

7.2.1 Immunocapture on stainless steel

In Chapter 3, a system was developed for the multi-modal analysis of individual tdEVs. Considering the challenges mentioned throughout this thesis regarding the multitude of non-tdEV particles present in typical samples and the lack of tools to properly discern tdEVs from such contaminants, this platform was designed to provide more certainty regarding the identity of the objects under study. Based on single observations, *e.g.* only regarding size, morphology or presence of antigens, it is a challenge to confidently claim that certain particles are tdEVs. For instance, submicron particles could be one of many different

species (*e.g.* lipoproteins), and particles that interact in some way with anti-EpCAM antibodies could be non-tdEV particles (*e.g.* cells) with EpCAM, or interactions could be non-specific. Moreover, most techniques cannot discern individual particles from particle clusters, whereas measuring only individual particles can be more valuable. While averaging over larger populations may have advantages of speed, reproducibility and overall sensitivity, it can have a detrimental effect on the quality of spectral analysis, because nuances in heterogeneity can go unnoticed, while the distribution of a certain feature can be highly informative but will then necessarily be fully out of scope.

Such uncertainty can be eliminated by combining multiple parameters; a single submicron particle that is EpCAM positive, is very likely a tdEV. To be able to get size and morphological information and to compare it with biological and chemical information, we developed a system that allowed immunocapturing tdEVs and subsequently characterizing these particles using Raman spectroscopy to confirm their identity, *i.e.* to confidently claim these particles are indeed of tumor origin. To allow claiming that such particle is a single vesicle, high-resolution imaging techniques were used like scanning electron microscopy and atomic force microscopy.

To find back individual particles in the sample stages of these various instruments, microscale features were fabricated near the sample immobilization area. The features allowed retracing the exact coordinates of all individual small particles ($<10^{-8}$ cm^2) on the chips (1 cm^2).

The article corresponding to chapter 3 concludes that there is a significant size distribution,[15] that EVs can be isolated in-situ with high purity[14,16,17] and that this platform is a good basis for studying EVs with AFM.[18] In short: individual EVs can be observed and characterized in detail, which would provide the basis for a much larger study of clinically relevant data.

7.2.2 Applications of multi-modal analysis

7.2.2.1 Multi-modal analysis after silicone incubation

As described in Chapter 4, similar multi-modal analysis was employed for an in-depth study regarding the interaction of organo-silicon compounds with biological membranes. In the experiments reported in Chapter 3, it was first observed that HDMS was detectable with Raman spectroscopy in immobilized tdEVs. When HMDS was excluded from the sample preparation, a similar signal was still detected.[1] Based on the hypothesis that the not-fully-cured PDMS contaminated the samples, experiments were repeated after over-curing of the PDMS microchannels and/or extracting any remnant of uncured molecules with ethanol. No signal pertaining to silicon was detected in these samples afterward. On one hand, there was only a scarce explanation of this phenomenon in the literature, and, on the other hand, it is generally known that organosilicon compounds (including HMDS and PDMS) have been approved for a wide spectrum of applications ranging from food to cosmetics and pharmaceuticals (*e.g.,* PDMS is the active ingredient in several over-the-counter pediatric colic drugs). Given this discrepancy, the interactions of organosilicon compounds and lipid membranes were further studied with another multi-modal analysis:

- Using Raman spectroscopy, cells incubated with various silicones were measured to inspect the molecular bonds and examine their spatial distribution inside cells;
- Using scanning Auger electron spectroscopy, it was demonstrated that silicones interact with the membranes of cells;
- Using XPS, it was demonstrated that silicones readily interact with supported lipid bilayers, i.e. that it is a passive physicochemical process rather than an active biological process;
- Using IR, it was observed that the bands of Si-C bonds shifted when the corresponding molecules interact with cell membranes. These last results suggest a strong interaction, not limited to adsorption, occurring

[1] Because these tdEV results were not reproducible, they were left out of the Chapter.

between the apolar regions of the membranes and the methyl groups of the PDMS.

Altogether, these results call for caution when regarding silicones as safe on the assumption that they are not systemically adsorbed, as they evidently are adsorbed.

7.3 Towards a point-of-care test

7.3.1 The Holy Grail

To put the results reported in this thesis into context, based on the background information given in Chapters 1 and 2, it may be helpful to refer to a description of an **ideal** sensor device, perfectly capable of giving the information required to guide therapies based on biomarker concentrations in bodily fluids. Some of the characteristics such a system should present are as follows:

- It is perfectly **selective**. Only analyte particles are observed, and none of the 10^{15} non-analyte particles per ml of sample (see Chapter 2) contribute to the signal.

- It is perfectly **sensitive**. It detects all of the analyte particles in the sample and gives a perfect indication of the concentration. The heterogeneity of tdEVs entails that the device must be able to detect the analyte at the single-particle level to avoid obscuration of the signal of smaller particles by that of bigger particles.

- It is **not prohibitively expensive**.

- It provide **high throughput analysis**. Clinical samples need to be automatable processable on a timescale of maximally (a fraction of) an hour.

- Analytes are available for off-line analysis. After a quick detection of the mere presence of the biomarker, it is interesting for many applications to be able to perform a more in-depth (*e.g.* genetic) analysis of the immobilized particles.

7.3.1.1 Selectivity - Affinity

Selectivity is determined by the affinity of the recognition element (*e.g.* the antibody in the present case) to the biomarker, as well as by the repulsion of other components of the samples.

Ultimately, the most that can be expected is that all particles presenting a certain recognition target (*e.g.* an antigen) are detected. This by itself is only meaningful if that is a good biomarker. Finding a biomarker is a challenge that falls beyond the scope of the development of this technology.[2]

Because of its availability and proven performance on cells, EpCAM was chosen throughout this thesis as a biomarker for tdEVs. It was shown on multiple occasions that it adequately binds EpCAM-positive tdEVs and in Chapter 5 it was shown that platelet-derived EVs did not contribute to the signal.

However, EpCAM is not exclusive to cancer-related particles; because it is present in cells from any epithelial tissue, it can be regarded as "smoking gun" in the bloodstream only, because it does not belong there. Urine and pharyngeal samples contain EpCAM-positive healthy epithelial cells, as does skin. That is, even when blood samples are regarded, it is possible that EpCAM-positive but non-clinically relevant skin particles are part of the sample due to the process of venipuncture. In Chapter 2, it was briefly shown that the presence of EpCAM-positive particles of between 1-4 μm has a certain prognostic value; a high concentration is correlated with a poor prognosis.[19] However, in patients that survived and healthy donors, there was consistently a non-zero concentration of these particles. As such, it was difficult to determine a cut-off value below which a good prognosis could be given.

Specifically regarding EpCAM, it would be interesting to investigate what the background (*i.e.,* the concentration in healthy donors) of *all* EpCAM-positive particles is, including the particles that are smaller than 1 μm, because these are much more abundant. If venipuncture is the source of all EpCAM-positive *micro*particles in blood by forces acting at the microscale, it is possible that the

[2] Although applications in high-throughput screening seem feasible with the technology that was invented in this project

same mechanism yields fewer *nano*particles. In that case, most EpCAM-positive particles would be of tumor origin and a cut-off should be easily determined.

7.3.1.2 Selectivity - Repulsion

In a *perfect* system, there is no non-specific interaction at all, *i.e.* no depletion of the analyte by stable adsorption in areas away from the sensor, and no interaction of non-analytes with the sensor. There are sophisticated options for coating samples with protein-repelling materials, like zwitterionic polymer brushes.[20] Thereby the amount of fouling, in terms of mass per unit area relative to untreated surfaces, is only a few percent. In other words, current state-of-the-art anti-fouling coatings are not perfect. Fortunately, real systems can still perform *acceptably* if fouling is taken into account in the signal interpretation.

In Chapters 5 and 6, a reactive poly(ethylene glycol) derivative was chosen as the surface-bound antifouling species mainly because of its convenient reaction conditions and reduction of non-specific binding of proteins. The exact degree of fouling was not quantified since the sensors functioned as expected, e.g., binding of the analyte was not blocked by other more abundant species and no unspecific signal was recorded. Most importantly, the detection mechanism was designed in such a way that even if there was absorption by non-analyte species, this would not contribute to the signal since there would be no interaction with the reporter antibodies. However, only relatively dilute samples with a limited number of components were studied. It thus remains to be explored how this system would respond to actual patient samples. The much higher abundance of non-analyte components in plasma as compared to cell culture medium may lead to more noise or reduced reproducibility in a system as described in Chapter 5. In Chapter 6, it is shown to reduce the baseline signal, but because of the signal analysis, this did not affect the detection of individual EVs.

7.3.2 Sensitivity

A *perfect* sensor system would detect *all* analytes in the sample, no matter how dilute they are. *Ideally* performing biosensors are sensitive enough to detect species at concentrations that are clinically relevant, *i.e.* the range of concentrations that can be expected in a typical set of patient samples. For some analytes, like tdEVs, most *real* sensors are only able to detect the high end of this

concentration range. There are a few applications where the need for sensitivity is not met by state-of-the-art technology. For instance, in tap water, *E. Coli.* bacteria pose a threat to the water quality if they occur at concentrations > 1 bacterium per 100 ml. In nasopharyngeal swabs for corona tests, using the current gold standard measurement technique, reverse transcription polymerase chain reaction (RT-PCR), viral RNA is only detectable if there are more than ∽100 copies per ml patient sample. But if there is as little as 1 copy in the sample (*e.g.* only shortly after the patient was infected), the patient may still become contagious in the near future.

Most state-of-the art biosensing concepts (see Chapter 5 for a small overview) employ signal amplification. In general, this entails the continuous generation of species that contribute to the signal by probes bound to the analyte specifically. This method has been applied for decades in the form of ELISA (enzyme-linked immunosorbent assay), whereby an enzyme covalently attached to a recognition agent targeting the analyte of interest continually converts a substrate into a colored product. A similar amplification is also part of the detection scheme presented in Chapter 5. In that chapter, a second level of amplification was provided by redox cycling over nanometer distances. This double amplification process yielded a technology that was sensitive enough to detect tdEVs in a range of concentrations largely overlapping with the expected clinically relevant range.[3] However, to span the entire clinically relevant concentration range, the limit of detection should ideally be one or two orders of magnitude lower.

Moreover, a common drawback of biosensing techniques that use amplification is the inherent need for calibration. The signal is generated by a series of reactions (binding of a reporter to analyte – binding of enzyme to reporter – conversion into detectable species) that are all dependent on environmental conditions. That makes it challenging to infer quantitative information from a single measurement. In general, calibration-based quantification is only accurate if all the reactions occur reproducibly. However, in this particular case the

[3] Please note that the lack of a real ideal sensor platform for tdEVs means that the actual concentration range is as yet unknown.

quantification was also based on the assumption that all tdEVs have a fixed size distribution, since the surface area of a tdEV determines the number of target proteins it carries and thereby influences the signal attributable to a single particle. In cell culture media, this was confirmed using AFM (see Chapter3). However, it remains an important aspect to take into account for patient samples.

7.4 Impact on health care

7.4.1 Hurdles to be overcome

7.4.1.1 Clinical approval

After the technological hurdles discussed in the previous section are overcome and before any technology discussed here can be commercialized, it has to be approved for clinical use. In this process, it will be assessed whether a device is safe to use and effective, and whether all suppliers conform with regulatory standards. Since the device uses patient material externally (unlike *e.g.* an implanted device), the challenge is less in establishing whether it is safe to use and more in establishing whether it is effective. This is straightforward to prove for a virus test, simply by comparing the device output with results obtained with the gold standard RT-PCR. For cancer, it would entail following larger patient cohorts for several years until the outcome of the treatment is known, which is therefore much more costly.

7.4.1.2 Societal embedding

Besides regulatory approval, before a device can be commercialized, it must also have a user base. That not only means that it needs to be established that the device performs better than alternative and existing standard solutions, but also that clinicians believe in it and that they are willing to change their protocols to embrace this new technology into their routine. To convince these different groups, the technology must be designed in concordance with the vision of key opinion leaders. Thus, in the early phases of product development, there needs

to be consensus among various stakeholders, *i.a.* clinicians, governmental health departments, insurance companies and patients such that the product (and the supporting clinical trials) can be designed with the proper application and user in mind.

7.4.2. Clinical applications

There are several modes in which health care could benefit from the technologies described in this chapter. In chronological order throughout the treatment process, these are diagnosis → response prediction → patient monitoring. We will briefly describe each of them here.

7.4.2.1 (Early) diagnosis

In this context, diagnosis would simply entail the detection of biomarkers in bodily fluids above a certain threshold, but further irrespective of their concentration. For instance, in today's corona virus testing, diagnosis is the end goal as there are currently relatively few treatment options. If there existed a quick and reliable point-of-care test to diagnose an active (and contagious) SARS-CoV-2 infection even at low concentrations (*i.e.* in an early infection), the impact on health care and all of society would be tremendous. In cancer, early-stage diagnosis could be possible by regularly screening high-risk populations, *e.g.* men above a certain age for colorectal cancer. If the cost and invasiveness of such diagnostic procedures were more agreeable than they currently are, the testing frequency could increase, and it would logically follow that colorectal cancer could on average be identified earlier and therefore treated much more successfully.

7.4.2.2 Response prediction

Therapeutics typically target either a marker on the disease-causing particle (*e.g.* a pathogen or tdEV) or a process in the pathogenesis. In some cases, such therapies fail because these markers are absent in the patient, whereby some other pathogenesis has led to the disease. For example, in some cases of lung cancer, immune therapy is given to patients. The drug (*e.g.* pembrolizumab) blocks a certain function of tumor cells that otherwise allows them to escape the immune system. Immune therapy has advantages over cytotoxic chemotherapy, since the latter yields much more side effects, and the 5-year survival rate in

patients that respond to the therapy is often higher for immune therapy. However, the drug can only work if the marker on which it acts (PD-L1 in this case) is present on tumor cells. In practice, the drug is effective in ∽20% of patients, which makes the cost of up to €100.000 prohibitively expensive. Therefore, it would make sense to include a relatively inexpensive diagnostic test in the treatment procedure for all patients of cancer that is potentially susceptible to such a treatment. However, to date, it is not common practice.

7.4.2.3 Patient monitoring

As discussed before in this thesis, *e.g.* in Chapter 2, the concentration of tdEVs in patients at any time is indicative of their clinical outcome. This type of biomarker has shown to have superior prognostic power compared to MRI. Conversely, the technology described in this thesis could be commercialized in a way that would cost a fraction (∽10%) of the cost of an MRI scan per test. By incorporating such a technology in a treatment procedure, it would be possible to test patients more frequently, giving the opportunity to intervene faster if needed, *e.g.* by changing the drug or the dosage.

7.5 Successive projects

The development of the techniques described in this thesis, has led to the NIPA technique described in chapter 6. This technique is currently being tested in a wide array of different settings, as it provides the combination of easy adaptation to a different biological question, ease of use, and a sufficiently high through-put to analyze a meaningful set of (clinical) samples at low cost. The list below provides a spectrum of this potential.

7.5.1 Cancer

In collaboration with the Oncology department at Deventer Ziekenhuis, a clinical proof-of-concept study will be completed, demonstrating the potential of our nano-electrochemical sensing method (chapter 6). The goal is patient monitoring, *i.e.* to demonstrate (prospectively) that a decrease in tdEV

concentration, as detected by our system, correlates with successful treatment. It was found before that the correlation of EpCAM-positive particles correlate more strongly to clincal outcome than MRI.[19] Anti-EpCAM-coated nanoelectrodes will be used to detect tdEVs in plasma of 40 prostate cancer patients. This project has been funded by the *Pioneers in Health Care* fund.

7.5.2 COPD

In collaboration with the Pulmonology department at Medisch Spectrum Twente and Laboratory for Microbiological research Twente Achterhoek (LabMicTA), a device will be developed for the rapid detection of bacteria in sputum of COPD patients. Currently, when patients with exacerbations are treated, antibiotics are administered in 80% of cases. In contrast, the cause of the exacerbation is of bacterial origin in only 20% of cases, i.e. 75% of the patients that receive antibiotics receive these unnecessarily. Growing a bacterial culture takes several days, which is too long for emergency situations. Using the techniques described in this thesis (Chapter 6), the goal is to develop an electrochemical immunoassay capable of detecting individual bacteria specifically, with minimal processing time (<30 minutes). Because an assay is used, bacteria are not only detected but also identified. The information about which strain of bacteria causes the exacerbation will also help to determine which antibiotic drug could be the most effective. This project is also supported by the *Pioneers in Health Care* fund.

7.5.3 Corona

In another collaboration with the Pulmonology department at the Medisch Spectrum Twente and LabMicTA, a point-of-care device will be developed for the rapid and reliable detection of SARS-CoV-2 (the virus responsible for COVID-19). This project, dubbed "QoroNano", entails the further development of nano-electrochemical sensing technology and a subsequent clinical proof-of-concept study with samples from GGD test facilities, stored at LabMicTA. The collaboration project is co-funded by the PPP Allowance made available by Health~Holland, Top Sector Life Sciences & Health, to stimulate public-private partnerships.

7.6 Concluding remarks

This world is an imperfect place. The current COVID-19 pandemic shows the impact that readily available appropriate testing might have had. It is thus of the greatest importance that further strides in this field are made rapidly, and it is promising that several options towards such progress seem to be within reach. Clinicians are currently oftentimes mostly focused on treating existing conditions; in other words, "*sick* care". The *health* care system of the future may be a system in which there is a strong focus on prevention. Novel technologies, similar to those described in this thesis, enable this through smart diagnostics. This makes care not only more efficient and cost effective, but will also contribute to the well-being of mankind.

7.7 References

(1) Rikkert, L. G.; van der Pol, E.; van Leeuwen, T. G.; Nieuwland, R.; Coumans, F. A. W. Centrifugation Affects the Purity of Liquid Biopsy-Based Tumor Biomarkers. *Cytom. Part A* **2018**, *93* (12), 1207–1212. https://doi.org/10.1002/cyto.a.23641.

(2) Rikkert, L. G.; Nieuwland, R.; Terstappen, L. W. M. M.; Coumans, F. A. W. Quality of Extracellular Vesicle Images by Transmission Electron Microscopy Is Operator and Protocol Dependent. *J. Extracell. Vesicles* **2019**, *8* (1). https://doi.org/10.1080/20013078.2018.1555419.

(3) Bloemen, P. R.; De Rond, L.; Van Der Pol, E.; Van Leeuwen, T. G.; Coumans, F. A. W. Improved Forward Scatter Detection of a Flow Cytometer for Detection of Extracellular Vesicles. In *Progress in Biomedical Optics and Imaging - Proceedings of SPIE*; 2019; Vol. 11073. https://doi.org/10.1117/12.2527919.

(4) de Rond, L.; Libregts, S. F. W. M.; Rikkert, L. G.; Hau, C. M.; van der Pol, E.; Nieuwland, R.; van Leeuwen, T. G.; Coumans, F. A. W. Refractive Index to Evaluate Staining Specificity of Extracellular Vesicles by Flow Cytometry. *J. Extracell. Vesicles* **2019**, *8* (1). https://doi.org/10.1080/20013078.2019.1643671.

(5) de Rond, L.; Coumans, F. A. W.; Nieuwland, R.; van Leeuwen, T. G.; van der Pol, E. Deriving Extracellular Vesicle Size From Scatter Intensities Measured by Flow Cytometry. *Curr. Protoc. Cytom.* **2018**, *86* (1). https://doi.org/10.1002/cpcy.43.

(6) van der Pol, E.; de Rond, L.; Coumans, F. A. W.; Gool, E. L.; Böing, A. N.; Sturk, A.; Nieuwland, R.; van Leeuwen, T. G. Absolute Sizing and Label-Free Identification of Extracellular Vesicles by Flow Cytometry. *Nanomedicine Nanotechnology, Biol. Med.* **2018**, *14* (3), 801–810. https://doi.org/10.1016/j.nano.2017.12.012.

(7) Gool, E. L.; Stojanovic, I.; Schasfoort, R. B. M.; Sturk, A.; van Leeuwen, T. G.; Nieuwland, R.; Terstappen, L. W. M. M.; Coumans, F. A. W. Surface Plasmon Resonance Is an Analytically Sensitive Method for Antigen Profiling of Extracellular Vesicles. *Clin. Chem.* **2017**, *63* (10), 1633–1641. https://doi.org/10.1373/clinchem.2016.271049.

(8) van der Pol, E.; Böing, A. N.; Gool, E. L.; Nieuwland, R. Recent Developments in the Nomenclature, Presence, Isolation, Detection and Clinical Impact of Extracellular Vesicles. *J. Thromb. Haemost.* **2016**, *14* (1), 48–56. https://doi.org/10.1111/jth.13190.

(9) Lee, W.; Nanou, A.; Rikkert, L.; Coumans, F. A. W.; Otto, C.; Terstappen, L. W. M. M.; Offerhaus, H. L. Label-Free Prostate Cancer Detection by Characterization of Extracellular Vesicles Using Raman Spectroscopy. *Anal. Chem.* **2018**, *90* (19), 11290–11296. https://doi.org/10.1021/acs.analchem.8b01831.

(10) Enciso-Martinez, A.; van der Pol, E.; Lenferink, A. T. M.; Terstappen, L. W. M. M.; van Leeuwen, T. G.; Otto, C. Synchronized Rayleigh and Raman Scattering for the Characterization of Single Optically Trapped Extracellular Vesicles. *Nanomedicine Nanotechnology, Biol. Med.* **2020**, *24*. https://doi.org/10.1016/j.nano.2019.102109.

(11) Enciso-Martinez, A.; Van Der Pol, E.; Hau, C. M.; Nieuwland, R.; Van Leeuwen, T. G.; Terstappen, L. W. M. M.; Otto, C. Label-Free Identification and Chemical Characterisation of Single Extracellular Vesicles and Lipoproteins by Synchronous Rayleigh and Raman

Scattering. *J. Extracell. Vesicles* **2020**, *9* (1). https://doi.org/10.1080/20013078.2020.1730134.

(12) Vorselen, D.; van Dommelen, S. M.; Sorkin, R.; Piontek, M. C.; Schiller, J.; Döpp, S. T.; Kooijmans, S. A. A.; van Oirschot, B. A.; Versluijs, B. A.; Bierings, M. B.; et al. The Fluid Membrane Determines Mechanics of Erythrocyte Extracellular Vesicles and Is Softened in Hereditary Spherocytosis. *Nat. Commun.* **2018**, *9* (1). https://doi.org/10.1038/s41467-018-07445-x.

(13) Rikkert, L. G.; Beekman, P.; Caro, J.; Coumans, F. A. W.; Enciso-Martinez, A.; Jenster, G.; Le Gac, S.; Lee, W.; van Leeuwen, T. G.; Loozen, G. B.; et al. Cancer-ID: Toward Identification of Cancer by Tumor-Derived Extracellular Vesicles in Blood. *Front. Oncol.* **2020**, *10*, 608. https://doi.org/10.3389/fonc.2020.00608.

(14) Nanou, A.; Miller, M. C.; Zeune, L. L.; de Wit, S.; Punt, C. J. A.; Groen, H. J. M.; Hayes, D. F.; de Bono, J. S.; Terstappen, L. W. M. M. Tumour-Derived Extracellular Vesicles in Blood of Metastatic Cancer Patients Associate with Overall Survival. *Br. J. Cancer* **2020**, *122* (6), 801–811. https://doi.org/10.1038/s41416-019-0726-9.

(15) Gaillard, M.; Thuaire, A.; Nonglaton, G.; Agache, V.; Roupioz, Y.; Raillon, C. Biosensing Extracellular Vesicles: Contribution of Biomolecules in Affinity-Based Methods for Detection and Isolation. *Analyst*. Royal Society of Chemistry March 21, 2020, pp 1997–2013. https://doi.org/10.1039/c9an01949a.

(16) Wu, J.; Hu, S.; Zhang, L.; Xin, J.; Sun, C.; Wang, L.; Ding, K.; Wang, B. Tumor Circulome in the Liquid Biopsies for Cancer Diagnosis and Prognosis. *Theranostics*. Ivyspring International Publisher 2020, pp 4544–4556. https://doi.org/10.7150/thno.40532.

(17) Mathew, D. G.; Beekman, P.; Lemay, S. G.; Zuilhof, H.; Le Gac, S.; Van Der Wiel, W. G. Electrochemical Detection of Tumor-Derived Extracellular Vesicles on Nanointerdigitated Electrodes. *Nano Lett.* **2020**, *20* (2), 820–828. https://doi.org/10.1021/acs.nanolett.9b02741.

(18) Piontek, M. C.; Lira, R. B.; Roos, W. H. Active Probing of the Mechanical Properties of Biological and Synthetic Vesicles. *Biochim. Biophys. Acta - Gen. Subj.* **2019**. https://doi.org/10.1016/j.bbagen.2019.129486.

(19) Nanou, A.; Miller, M. C.; Zeune, L. L.; de Wit, S.; Punt, C. J. A.; Groen, H. J. M.; Hayes, D. F.; de Bono, J. S.; Terstappen, L. W. M. M. Tumour-Derived Extracellular Vesicles in Blood of Metastatic Cancer Patients Associate with Overall Survival. *Br. J. Cancer* **2020**. https://doi.org/10.1038/s41416-019-0726-9.

(20) Baggerman, J.; M. J. Smulders, M.; Zuilhof, H. Romantic Surfaces: A Systematic Overview of Stable, Biospecific, and Antifouling Zwitterionic Surfaces. *Langmuir* **2019**, *35* (5), 1072–1084. https://doi.org/10.1021/acs.langmuir.8b03360.

Appendix

A

Supplementary information accompanying the publication:

Pepijn Beekman, Agustin Enciso-Martinez, Hoon Suk Rho, Sidharam Pundlik Pujari, Aufried Lenferink, Han Zuilhof, Leon W.M.M. Terstappen, Cees Otto, Séverine Le Gac, *Immuno-capture of extracellular vesicles on stainless steel substrates for individual multi-modal characterization using AFM, SEM and Raman spectroscopy,* Lab on a Chip, 2019,**19**, 2526-2536.

A.1 Raman Spectroscopy of Stainless steel

In order to assess the suitability of functionalized stainless steel as a substrate for Raman spectroscopy, an area of 40 µm x 40 µm was scanned with a laser power of 35mW and an illumination time of 250 ms with a step size of 1 µm. The spectrum of clean stainless steel is comparable to standard CaF_2 and commercial stainless steel (µRIM™, BioTools) used as substrate for Raman spectroscopy. A quartz spectrum is also shown for comparison.

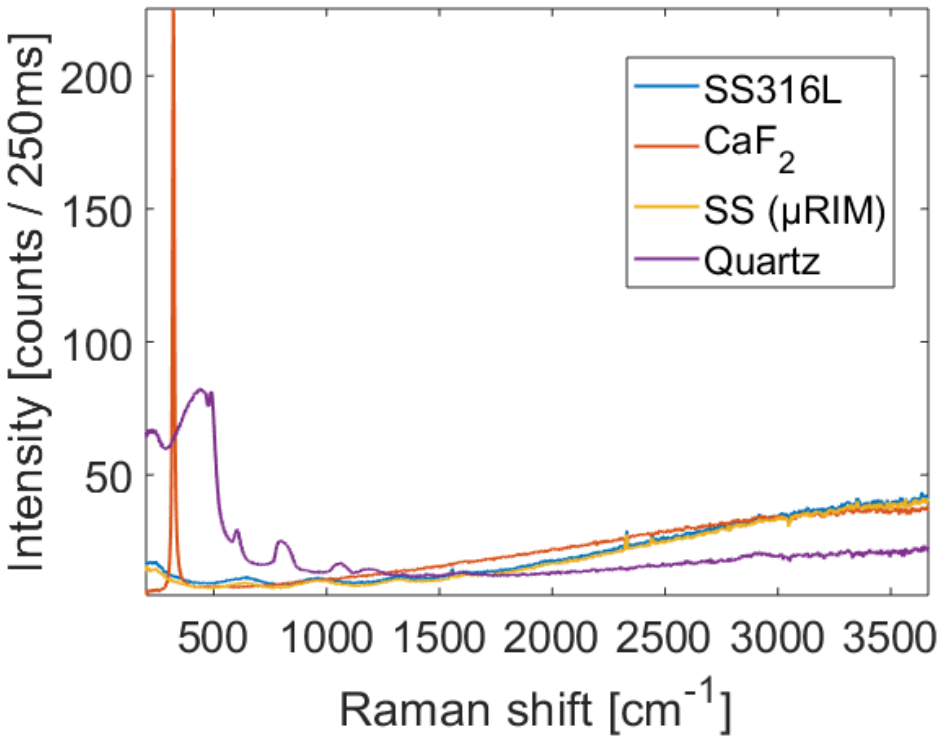

Figure A.1: Mean Raman spectra of Stainless steel (SS316L), CaF2, Stainless steel (µRIMTM) and Quartz.

A.2 Navigation markers

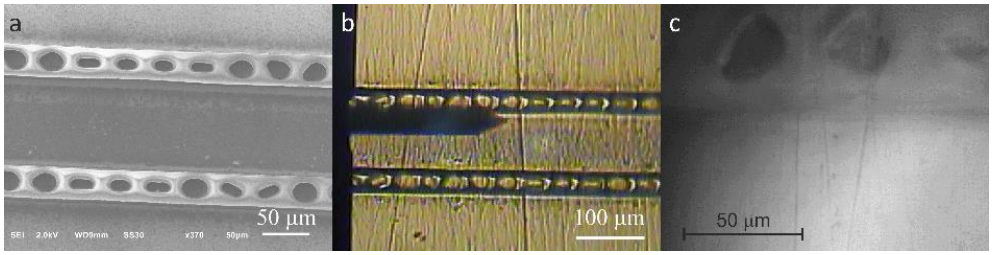

Figure A.2: Navigation markers patterned on the stainless steel substrates next to the sample region, using cyanoacrylate glue. *a) SEM image of the sample region flanked by the navigation markers; navigation markers as seen through the sample stage optics of the AFM (b) and the Raman spectroscopy imaging setup (c). Knowing the position of a particular object of interest relative to a (unique) combination of navigation features allows easily retracing it in all instruments.*

A.3 EV isolation protocol from prostate cancer cell lines (LNCaP)

The LNCaP Prostate cancer cell line purchased at the American Type Culture Collection (ATCC) was used to produce prostate tumor-derived EVs. LNCaP cells were cultured at 37 °C and 5% CO_2 in RPMI-1640 with L-glutamine medium (Lonza, cat.# BE12-702F) supplemented with 10% v/v fetal bovine serum, 10 units/mL penicillin, and 10 µg/mL streptomycin. The initial cell density was 10,000 cells/cm^2 as recommended by the ATCC. Medium was refreshed every second day. When cells reached 80–90% confluence, they were washed three times with PBS and FBS-free RPMI medium supplemented with 1 unit/mL penicillin and 1 µg/mL streptomycin was added to the cells. After 48 h of cell culture, the cell supernatant was collected and centrifuged at 1000g for 30 min. The pellet containing dead or apoptotic cells and the largest EVs was discarded. The supernatant was pooled, and aliquots of 50 µL were frozen in liquid nitrogen and stored at −80 °C. The size distribution of the harvested EVs was assessed with nanoparticle tracking analysis (NTA) (See Appendix A.4).

A.4 NTA measurements of LNCaP EVs

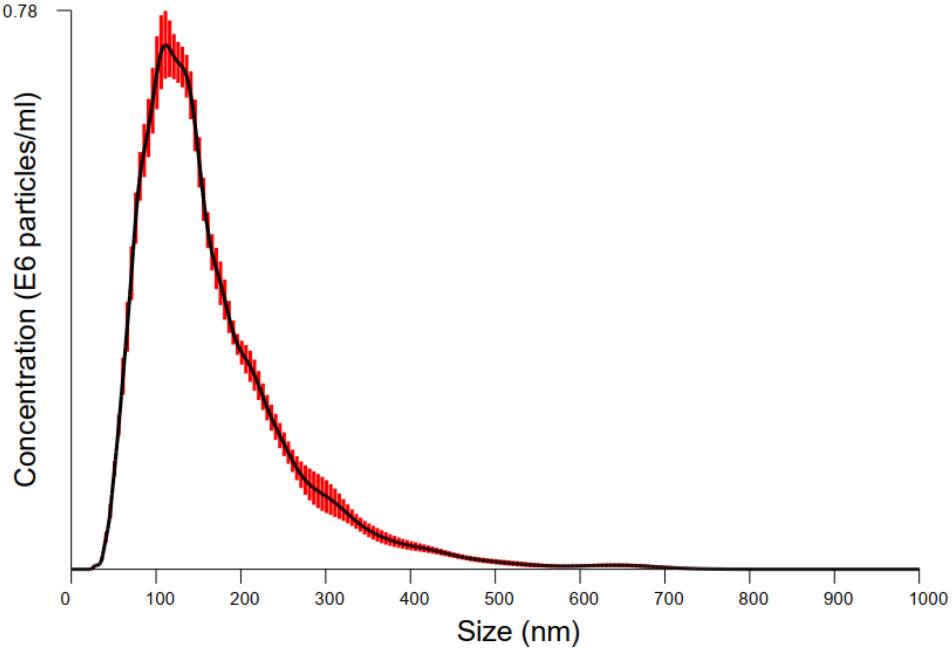

Figure A.4: NTA average concentration over 10 samples. *Measured using a NanoSight 500 dark field microscope (Nanosight, Amesbury, UK). 5607 particles were measured with an average diameter of 167 ± 91 nm (diameter ± s.d.), corresponding to a total concentration (before 10x dilution) of 1.06x109ml-1. The raw data from this measurement was used to obtain a histogram compatible with the AFM data from Figure 8.*

A.5 Control experiments

Table A.5: Overview of the experiments included in this study – EV capture on the antibody-conjugated substrates and negative control experiments.

	EDC/NHS activation	**Antibody**	**EVs**
Sample *EVs to be analyzed*	+	+	+
Control i	-	+	+
Control ii	+	-	+
Control iii	+	+	-

A.6 IRRAS measurements of CDPA as monolayer on stainless steel substrates, and as a powder

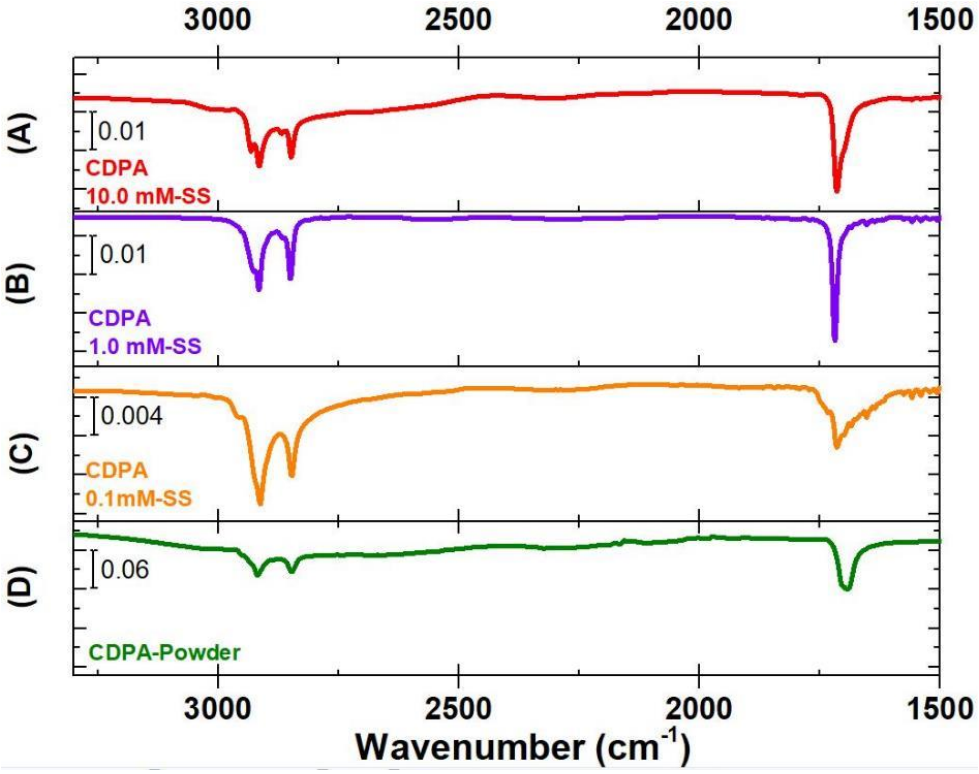

Figure A.6: IRRAS reflection spectra for CDPA monolayers prepared using a CDPA concentration of (A) 0.1 mM, (B) 1 mM, and (C) 10 mM, and using CDPA powder.

A.7 Influence of flow dynamics on capturing efficiency

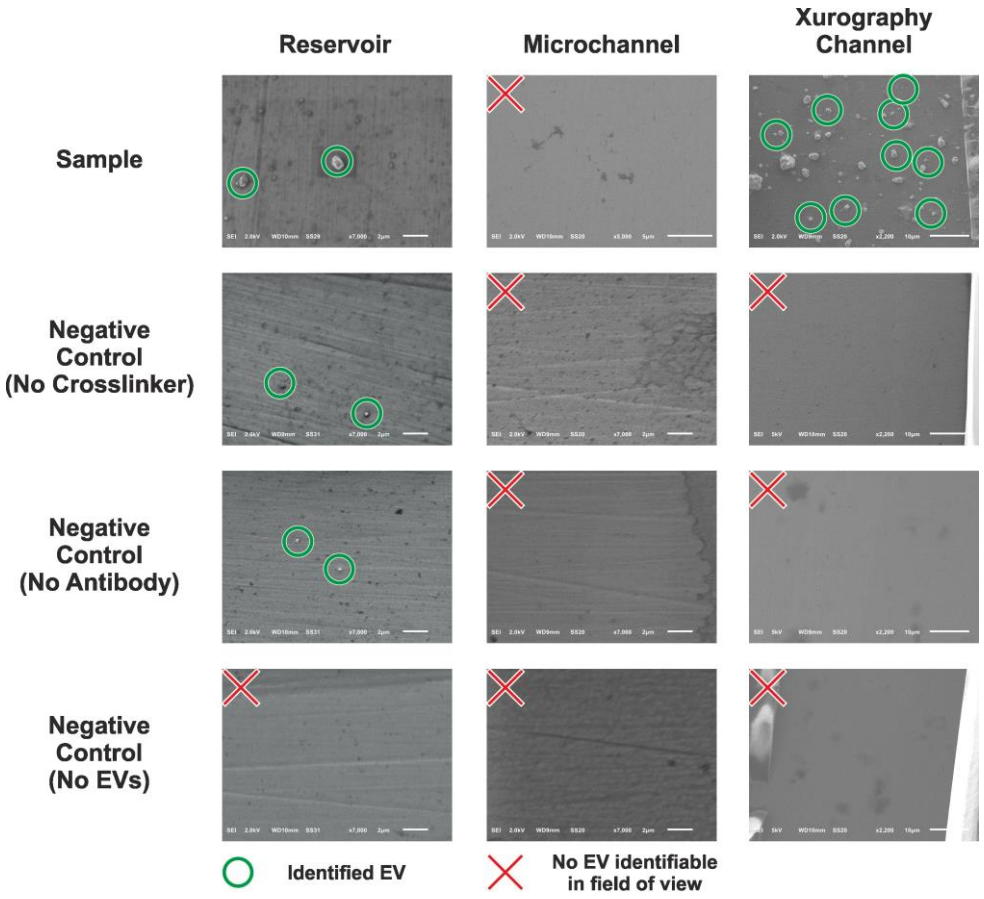

Figure A.7: SEM images; comparison of contrast between specific and non-specifically bound species in various fluidic systems. *In a reservoir (left column, scale bar: 2 µm), where EVs are incubated and dehydration agents are exchanged under semi-static conditions, there is an apparent lack of a force to remove physisorbed EVs as can be seen from the negative controls. Using a microchannel of 20-µm height (middle column, scale bars: 5 µm (top) and 2 µm) entails imposing shear forces so high that specifically bound species are also removed when introducing dehydration agents. An intermediate option, use of exceptionally high (~200µm) microchannels produced by xurography (right column, scale bars: 10 µm) yielded expected results, where EVs were only identified in the positive control.*

Appendix

B

Supplementary information accompanying the publication:

Pepijn Beekman, Agustin Enciso-Martinez, Sidharam P. Pujari, Leon W.M.M. Terstappen, Han Zuilhof, Séverine Le Gac, Cees Otto, *Organosilicon uptake by biological membranes,* Nature Communications Biology (in press)

B.1 Structures

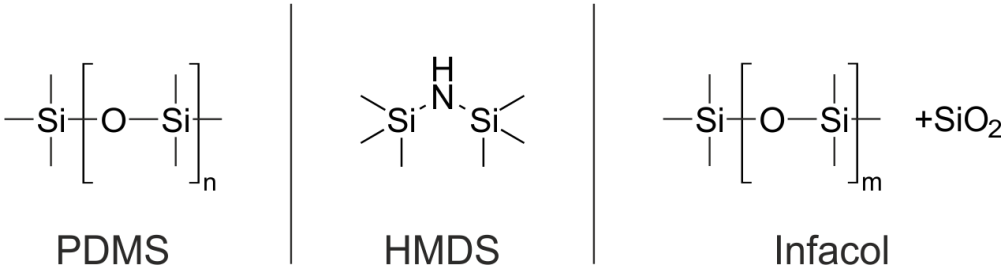

Figure B.1: structures of the molecules used here. *For uncrosslinked PDMS oligomers, n = 20-90. m = 190-280.*

B.2 AES

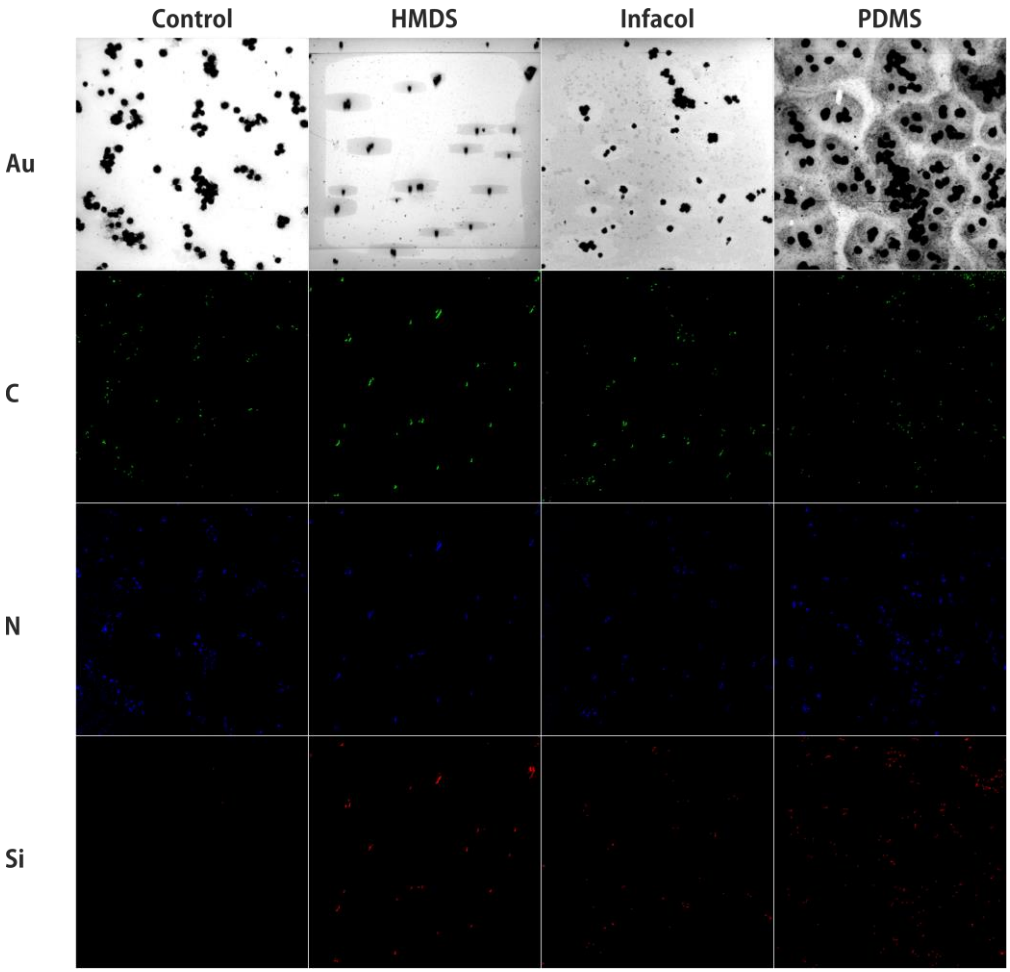

Figure B.2: Further AES data *(C and Si data also shown in main article after image dilution) showing nitrogen species in all cells and the intense gold signal coming from the substrate, for comparison.*

B.3 IR

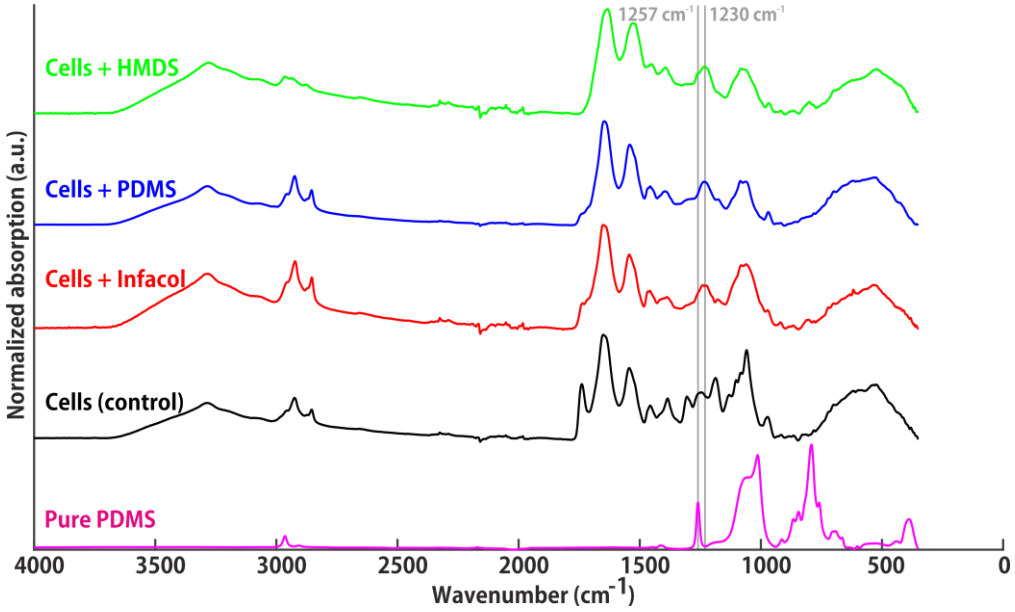

Figure B.3: full IR spectra. *The region of interest, 1180 – 1300 cm^{-1}, is shown in the main text.*

B.4 Raman Spectroscopy

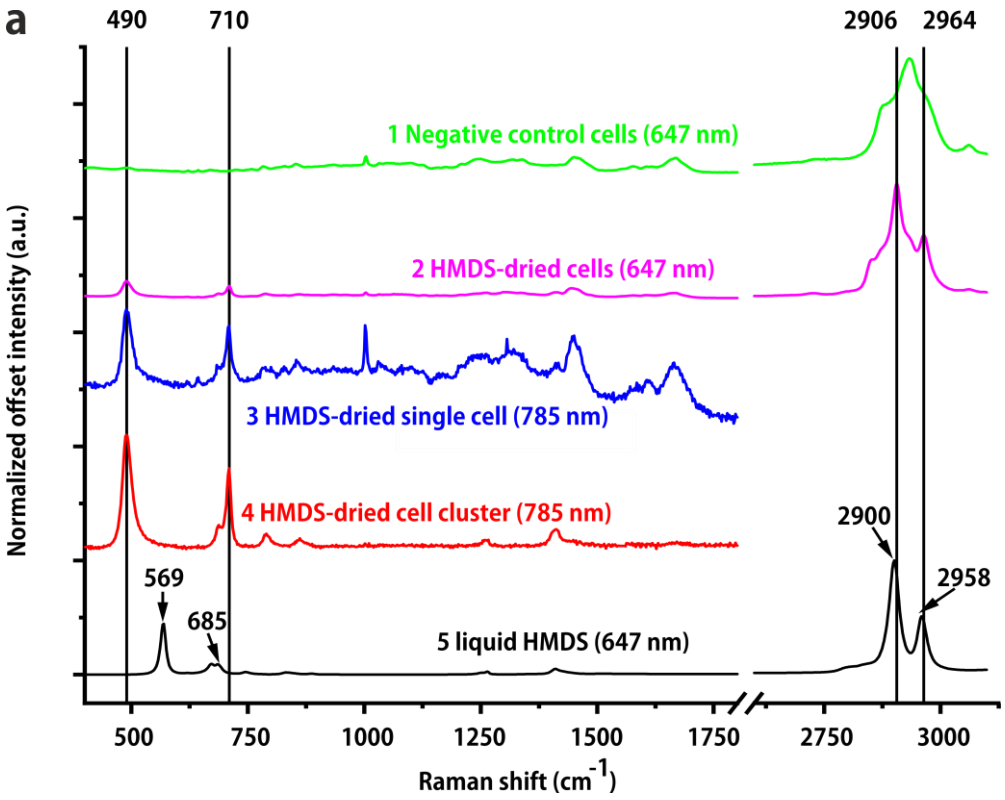

Figure B.4: Additional Raman spectra obtained from other samples. *Spectra (3) and (4) correspond to a cell dried with HMDS (3) and to a cluster of dried cells with excess HMDS (4). Both, (3) and (4) display peaks at 490 and 710 cm^{-1}. The cell contribution to the Raman spectrum in (4) is not significant compared to the peaks at 490 and 710 cm^{-1}, indicating that the reaction with HMDS and biological matter is very efficient and can dominate the outcome of chemical probing.*

Appendix

C

Supplementary information accompanying the publication:

Dilu G. Mathew, Pepijn Beekman, Serge G. Lemay, Han Zuilhof, Séverine Le Gac, Wilfred G. van der Wiel, Electrochemical detection of tumor-derived extracellular vesicles on nano-interdigitated electrodes, *Nano Letters. 2020, 20, 2, 820–828*

C.1 PDMS DEVICE

To enable removal of non-specifically bound species under controlled flow conditions and to allow for proper sequential introduction of buffers and agents in small sample volumes, a PDMS microchannel ($3 \times 6 \times 0.2$ mm^3) was placed on the substrate. The mold was fabricated using a xurography technique described elsewhere.[1-2] Briefly, a foil (nominally 200 µm thickness) was patterned by a desktop plotter and 3x6 mm^2 sheets were laminated on a disposable petri dish. PDMS (Sylgard 184, base : curing agent = 10 : 1) was mixed thoroughly and degassed by centrifugation at $1000 \times g$ for 1 minute. After pouring the PDMS on the xurography mold, it was degassed under vacuum for 15 min. After curing the devices at 80 °C for ∽4 h, inlet and outlet access holes were drilled using a 1 mm biopsy punch. After cleaning the nIDE chip (see next section), the PDMS microchannel was manually aligned over the electrode array. Reagents were introduced manually using an Eppendorf pipette through 200 µl pipette tips inserted directly in the inlet (see Figure SI-1). For electrochemistry measurements, the reference electrode was inserted in this pipette tip.

Figure C.1: PDMS device placed on top of nIDE chip including loading pipettes tips. *After placing the PDMS device on the nIDE chips, it was held in place by applying uncured PDMS on the side walls of the devices and curing the assembly for another 15 min at 80 °C. Any PDMS covering the contact leads was later removed using a surgical blade.*

References

1. Speller, N. C.; Morbioli, G. G.; Cato, M. E.; Cantrell, T. P.; Leydon, E. M.; Schmidt, B. E.; Stockton, A. M., Cutting edge microfluidics: Xurography and a microwave. *Sensors and Actuators B: Chemical* **2019,** *291*, 250-256.

2. Beekman, P. E.-M., A; Rho, H.S.; Pujari, S.P.; Lenferink, A.T.M; Zuilhof, J.T.; Terstappen, L.W.M.M; Otto, C.; Le Gac, S., Immuno-capture of extracellular vesicles for individual multi-modal characterization using AFM, SEM and Raman spectroscopy. *Lab on a Chip* **2019**.

C.2 AFM RESULTS

To demonstrate the performance of the surface modification, bare platinum surfaces were functionalized following the same procedures as the electrode devices. After incubation with tdEVs, the capture efficiency of the positive control (*i.e.*, actual experiment) (top row in Figure SI-2) was compared to 3 negative control samples (rows 2-4), as detailed below: row 2) Fully functionalized substrate after incubation with platelet-derived vesicles, not presenting the EpCAM antigen. The absence of tdEVs on the surface illustrates the selectivity of the surface functionalization.

row 3) Non-functionalized platinum substrates, *i.e.*, no AUT and no PEGDGE, incubated with anti-EpCAM and EpCAM-positive EVs. The absence of tdEVs on the surface proves the necessity of the covalent attachment of the antibodies to the surface.

row 4) Platinum modified with both AUT and PEGDGE but without introduction of antibodies before incubation with EpCAM-positive EVs. The absence of tdEVs on the surface demonstrates that the EV capture in the positive control is indeed due to the presence of antibodies on the surface.

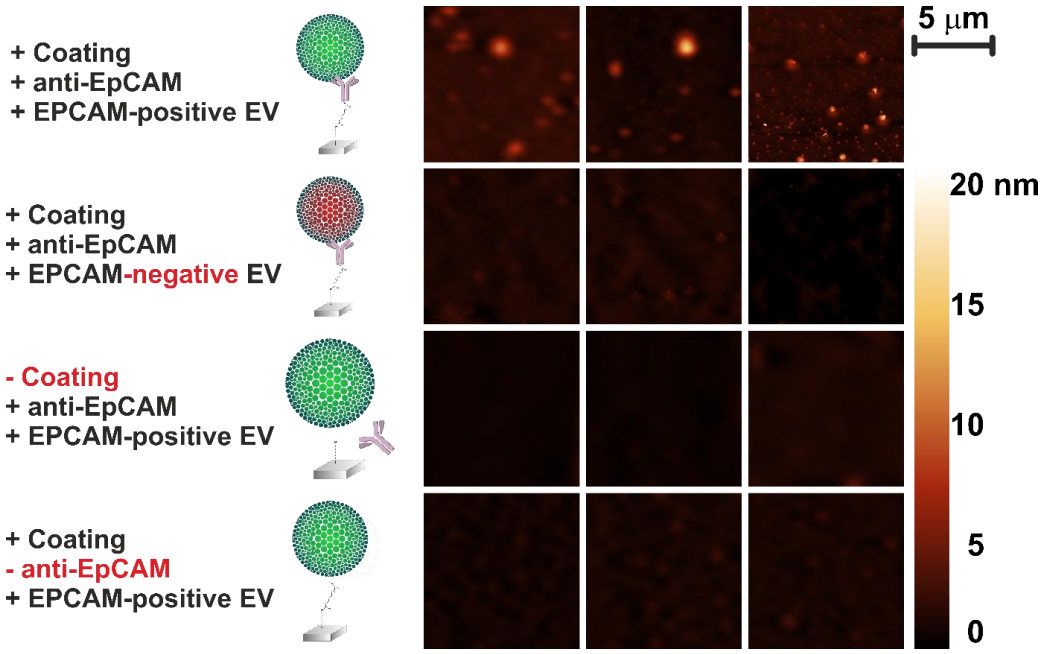

Figure C.2. Atomic force micrographs showing tdEV capture in an actual experiment and the absence of tdEVs in the negative control experiments. *The same scale bar and colormap apply to all images.*

C.3 XPS RESULTS

XPS data obtained from modified unpatterned devices are shown in Fig. SI-3. They showed strong S 2p and N 1s signals (at 164 eV and 400 eV, respectively) after formation of the AUT layer, indicating the presence of the thiol and amine moieties, respectively. After attachment of the anti-fouling PEGDGE layer, these signals were strongly attenuated and additional C 1s (285 eV) and O 1s (532 eV) signals were detected.

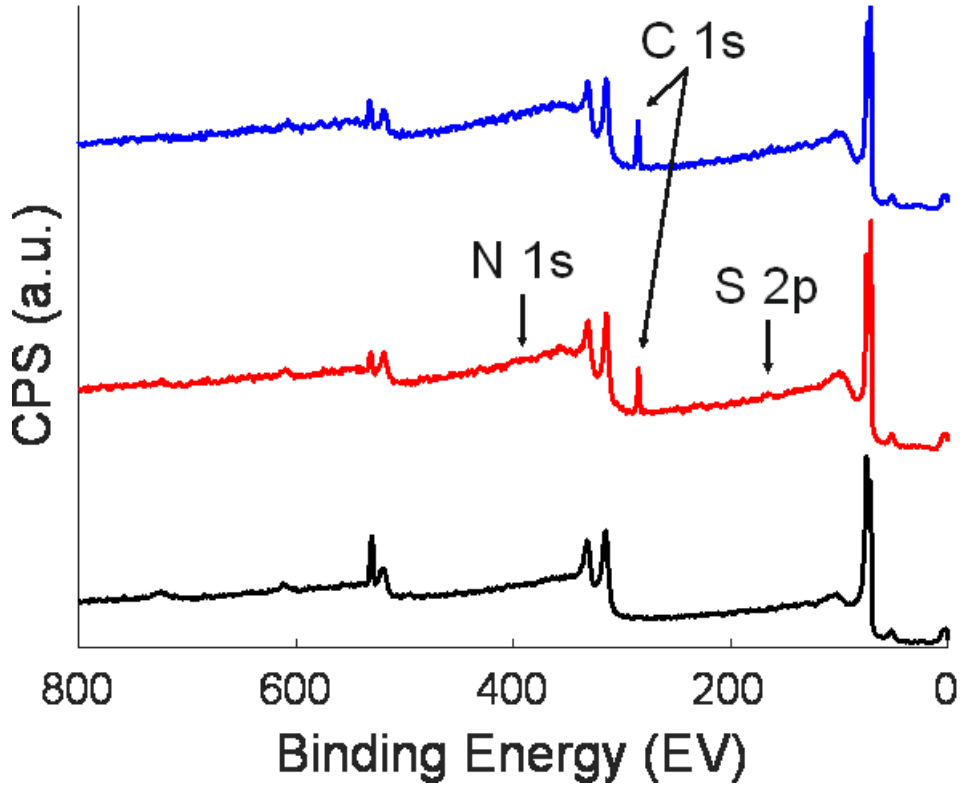

Figure C.3. XPS wide-scans *of bare Pt (black), after AUT modification (red) giving a clear C 1s contribution and S 2p and N 1s peaks each contributing to ~3 atomic percent of the surface, and after subsequent PEGDGE attachment (blue) where these signals are completely attenuated. A C 1s narrow scan (not shown) showed emergence of a carbonyl peak (288 eV) after reacting with PEGDGE.*

Appendix

D

NIPA Chip Design

D.1 Microfabrication (photolithography) mask

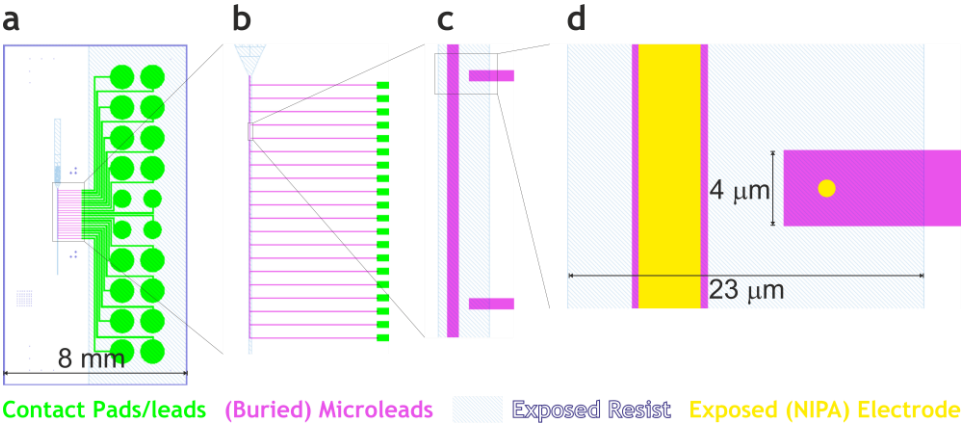

Figure D1: **Photolithography mask (designed in CleWin 5.4, WieWeb, Hengelo, Netherlands) of a chip (a) and zoomed-in highlights of the electrode array (b) and the microchannel (c). In panel (d), the reference (left) and NIPA electrode (right) electrodes are illustrated, but these are not part of the photolithography mask as they are patterned by e-beam lithography.**

Acknowledgements

I've had the time of my life in the past >5 (oops!) years and I'm really grateful to so many people for making it wonderful. The list of entities that deserve my gratitude is probably longer than average, but please keep in mind that I was effectively part of at least 4 research groups. Imagine all the birthday cake I had to eat!

For me, looking back, it is very easy to recognize my personal growth, if not only physically (in which case there should be a minus sign somewhere). I think I became braver, smarter and nicer than I was in 2016 – which is not to say there is no room for improvement of course. If you're reading this, thank you for your patience, for dealing with my stubbornness, my quirkiness, for investing energy into our relationship in whichever way. You're beautiful and I love you!

All EU and especially Dutch tax payers, it was a great gift (and a dubious decision – if you only knew, haha!) to bestow on me a small part of the responsibility to figure out how to improve healthcare. Through *NWO, Horizon 2020, Health Holland, Ministerie van Economische Zaken, University of Twente* and *Wageningen University*, you have clearly voiced your wish and if nothing else, we're doing our best to get it done.

Niels, you put me in contact with Cees which finally got me this job. I always enjoyed working with you and it's too bad we did not get to finish our initial plan. Let's pick it up again when I'm financially independent?

Cees van Rijn, I responded to a job opening on your website for "R&D Scientist". In your response, you told me that you also had a PhD position available. Since I had entirely different ambitions (see before), I respectfully declined and asked

again about the job at Aquamarijn. You then invited me for a Skype meeting to discuss how and when to start my PhD. And here I am, not at Aquamarijn. Thank you for that good call!

Leon, your lab has always felt like home to me, thank you so much for your hospitality and for allowing me to learn from you, in many ways. I hope for a fruitful result soon!

Séverine, I was really happy when you adopted me and I'll always feel indebted to you for it. I enjoy your candor and your thoroughness, even though you sometimes think I don't. I'm not in the Zuidhorst that often but think we make a really good team!

Han, you also inherited me as a rather odd duck at ORC. Thank you for your open-mindedness, the freedom I got, and for the spot-on support at times. I learned a lot and I really appreciate our relationship!

Cees Otto, thank you for the collaborations. The Cancer-ID meetings were my favorite kind of meeting, it was a very pleasant and educative experience!

Serge, of all techniques, NIPA is most similar to SPIE. Thank you for your letting us roll with it – we will do our best to make it worthwhile for everyone. Thank you for the interesting discussions!

Wilfred, one of the first things you taught me is that science is like top-class sports, I think I can fairly say I took that to heart. It has always been a lot of fun working with you and a lot of the success we have had is attributable to the responsibility that you gave us and the ambition that you inspired in us! Thank you!

Dilu, no one paragraph would do justice to my appreciation for you, you should get your own chapter in my thesis. But then, you already have several :) It's been an honor to call you my friend for many years and now we transcended that – and how! The adventure so far has been wild, and the adventure ahead is undoubtedly even beyond what I can currently imagine. I treasure the balance in our relationship and our mode of communication, I try not to be too Dutch most of the time and I appreciate your efforts to pass your Inburgeringsexamen – on top of everything else. I could not wish for a better business partner!

My project partners *Marjolein, Job, Rob, Rob, Alex en Marijn,* thank you for your commitment to making our efforts a success and thank you for your trust in us! "Pioneers in Health Care" is truly an exceptionally valuable instrument in bringing clinicians and high-tech together and I'm gratefully benefiting from it. *Paul,* I think that without your support, my career would have already looked very different. Thank you for that and for your pleasant presence in meetings! I'm learning a lot.

To *Holland Innovative, ITET, RVO, Rabobank, Sportinnovator, Hestia, Close, Micronit, Gemeente Enschede:* thank you for making things possible, for believing in us, and for helping us grow!

To *all journalists* that have shared news (both factual and science fiction) about our efforts: thank you very much, we owe a lot of success to your collective support. I can't list you all here; enough trees have been sacrificed already :)

Our supporters from Novel-T, *Semme, Roy, Martin, Marike, Frank, Peter, Mike, Niels,* thank you all for your help in getting us on our feet! It's thrilling to think what the future holds for us.

A special thanks for my students *Jordi, Tom, Thijs, Hamza, Sambor, Nishant, Aernout, Thijmen, Fjodor, Tanja, Chris* and *Leron. Naoual,* I really admired your attitude, especially for a BSc student. Imagine you as a PhD! *Simon,* your creativity and motivation made it really fun to work with you and I know you'll do great things in your PhD. *Annie,* thanks for being a super motivated intern and our first employee!

Hans, Frank and especially *Barend,* thank you for your support!

Elly, Aleida, Esther, Henny, Karen, Hermine, Judith, Ingrid, Karin, Róża, you're the best! Thank you for making things run so smoothly!

Sidhu, sir, I really learned a lot from you and it's always been a lot of fun to work with you as well as relax after work! You're one of the kindest people and know and I cherish our friendship.

Ai, Jacob, Hien, Anke, thank you for all the support I got from Aquamarijn! *Albert*, I'm proud I got to share a lab with you and I learned a lot!

Thank you, ORC PhD's *Kaustub, Ian, Medea, Gina, Annemieke, Milou, Andriy, Tjerk, Yuri, Ariadni, Jordi, Lucas, EvA, Sybren, Rick, Sweccha, Jorin, Rafaël, Andrada, Stephanie, Jorge, Simon, and Dongdong* for tolerating my presence in your chemical labs – luckily life-threatening situations were avoided 98% of the time. It's been a blast to travel to Scandinavia and Israël with you guys.[1] Esther R, thanks for the many useful consultations – I hope we'll run into one another again. *Rui,* it was fun sharing an old, cold office with you in the Dreijen!

[1] Where is Michel?!?

DJ, thanks for the collaborations and the conversations – who knows if more will follow in the future. *Sjoerd,* I always enjoyed your honesty and your sense of humor. No… "enjoyed" is not the right word for your humor. But I'm not sure what verb in the English language could be assigned to that feeling when your stomach turns in vicarious embarrassment. (Please don't win the ORC fantasy football league again?) Special thanks to the karaoke crew *Alyssa, Ellen, Jay* (always at the right place at the right time), *Adem, Alexandre* and *Satesh*. *Jorick,* I had a magical night with you in Jerusalem. *Sevil,* your lovely and charming presence provided a nice balance with some of our other officemates. *Fred,* lelijkerd, jazeetie, we had a great time! I hope we will someday get to finish what we started in Copenhagen. *Alice,* you're the best. If things don't work out with Jorick, give me a call ;)

Teris, Maurice, Maarten, Floris, Michiel, Gert, Louis, it was a privilege to work with you. *Bauke,* thanks for the laughs in Israël!

Hendra, Anne-Marie, Judith, it was great fun to give practicals with you. I'm glad that they all survived! *Carel,* I'm glad we got stuck with each other in the practicals. I learned a lot from you and you made the time fly by! Next round of coffee is on me.

Martin, Johnny, Ab, Christian, Aufried, Anouk, Yvonne, you have no idea how nice it is to work with people that are skilled as you are. You make a lot of great things possible!

NanoElectronics guys, *Floris, Michel, Peter, Hans-Christian, Johnny, Martin, Unai, Antonio, Pavel, Guus, Tao, Bram, Zhen, Robbert, Michal, Yigitzan, Fab,* thank you for all the fun activities (your PhD parties are the best!). I'm proud to see the

ECsens logo on our incredibly crappy futsal team – can't wait to start that again!

AMBER crew *Bastien, Jean-Baptiste, Agnieszka, Carlo, Renée, Luuk, Maud, Alexya, Lucas, Thomas, Naere, Nanoor, Shanliang, Shuhan, Marleen,* I learned a lot from you, looking forward to colonizing Starbucks again!

Armagan, I´m really enthusiastic about working with you later. Your science is fantastic and you´re one of my favorite next door neighbours – together with Cees, of course.

Joska, let's say you're a remarkable character. I'm glad you're mostly on my side because I'm actually a little afraid of you. But seriously, I really enjoy our mode of conversation. It's an honor to know you and I hope that we can join forces in the future.

Richard, it was a distinct privilege to share an office with a man of your caliber and I was lucky to meet such good fortune. Moreover, it was a lot of fun! If things go our way, we'll accomplish great things together, I'm sure.

Ruchi, nice that you could join us on the 4th floor, I'm looking forward to possibly working together in the future. It's great to have *Richell, Eline, Marit and Lena* with us!

Arjan, Frank, Joost, Sanne, Yoon, Xichen, Ivan, Fikri, Leonie, Joost, Guus, Dodo, Narges, Michiel, Peng and *Joris* thank you for making me feel at home at MCBP. We had great times working late in the lab, but also partying afterward or going on lab trips. I hope for many more to come! *Lisa,* I'm a big fan. You're an amazing creature, don't ever change. *Kiki, Niels,* you're a great couple and the world will be better off with a little copy of you in it. I guess it'll be a while before we go to Erve Asito again! *Edwin,* sinceyoujoinedmeintheofficemyliver hastakenquiteabeatingandyoumaybeFrisianbutallinallitsgreatfuntohaveyouwit hus.

San Agustin, you are the patron saint of arranging salsa and tequila parties. *Pien, Fiona, Leanne, Pien, Lucinda, Martine, Daniek, Sara, Steven, Carlos, Ana, Staś, Jarno, Ilkay, Yoëll, Charline,* I am blessed to have shared such hilarious and meaningful moments with you – I duely feel like a rock star because of it.

Tinus, Linda, oh sorry I mean Leonie, Hoon, Melissa, Jelmer, Gyllion, thank you for the awesome time I had as part of Cancer-ID. I really enjoyed the dynamics of our team which I think had a great impact on the results. *Rikkie* and *Woody*, thank you sexy people for the amazing trip to Japan! I'll never ever forget it. *Agustin san*, I still praise your sense of timing and I don't ever want to share a hotel room with you again. Love you!

Frodo (it's my booklet and I'll call you what I like hehe), not only do you publish the best papers, you must be one of the most charming and delightful people I have the pleasure to know.

Rienk, Frank, Ton, Wouter, Guido, Michiel, Marca, Herman, Jaap, thank you all for making Cancer-ID a success, I hope we can soon start exploring further! *Edwin, Aleksandra*, I had a wonderful time with you in Kyoto, maybe next time we can take it easy with the sushi.

Pani, I love how our friendship evolved the way it did and I can only look back at it in disbelief. You are arguably my biggest inspiration and you enrich my life with your amazing brain. I love you!

Haye, you're my guardian angel and you've saved me probably more times than I know. Few people know me better than you do and it's a mystery to me how despite this, you're still my friend. You're the most honest man I know and you're whom I resort to if I need a moral compass. You are truly one in a million. I love you!

Billy, you're a gem. Don't ever change. The world could learn a lot from you; if we ever start cloning people, I vote you get to go first because the universe would be much better off with many copies of your genome in it. I love you!

Henk-Willem, you boss, if there's one person that could still teach me on how to enjoy life, it's got to be you. You are a true rock star and a great example in that respect. Thank you for INaSCon. Thank you for leading the resistance in CR1528, you're my favorite partner in crime. Thank you for countless more priceless moments, past and future. I love you!

Peter and *Janneke*, you sure are a quirky couple but very cute. Thank you for the diversity!

CR1528 crew, *Jarno, Fernanda, Ani, Kiwi, Floris, Tom, DJ,* thank you for the pointless discussions! Friday afternoon is always something to look out for.

My BSc buddies, *Bart, Chris, Daniel, Le Duc, PJ, Rik, Rupert, Pieter, Frank,* I'm glad we still hang out! I'm curious to see how the group will expand in the coming years…

Sharon, Linda, Sanne, Ellen, Leoni, Sebastiaan, Niels, Frank, Robert, Niek, Gait, thank you for tolerating us in your community, I wish I could say that the neighborhood is better off now… Thank you for your support and your enthusiasm!

Jeroen, Linda, Twan, I'm really proud of you! I love to consider myself part of your family. *Lenie, Bennie,* I think it's pretty rare for someone (with my character!) to consider his parents-in-law to be among his closest friends, so I can count myself lucky! After 17 years I'm blessed to have two sets of parents and I couldn't wish for a better other family. I couldn't begin to thank you enough for all that you've done for us.

Joost, Julian, Nathan, Sophie, I love how our families merged and how the timing for everything has just been perfect! *Jorien,* thanks for giving Tom (and thereby, me) this wonderful family. *Tom,* we've enjoyed some of the most hilarious moments of my life together (I'm thinking about Bad Bentheim for instance) and I could always call on you in the direst situations – I hope you can say the same. You're Monieks cousin, but you're my brother.

Kevin, Sanne, Daan, Tessa, Jojanneke, Mark, Meyke, Barend, we're not a stereotypical family but quirky as we may be individually, we're still remarkably tight as a unit, despite all the time zones that may be between us. Thank you all for your constant support and enthusiasm! *Marjolein,* you have always been a great example for me – although that may not always have been immediately apparent from our personalities. *Tim, Sanne, Daan, Tessa,* I'm really proud of you and I'm looking forward to marvel on all the greatness you will accomplish - if you feel like it. When I think of new scientific hardware to abuse in an attempt to entertain you, I will let you know :)

Paps en *Mams,* I haven't always made thing easy but I've been really lucky to have you as parents. I'm happy your both still healthy and youthful and that I can rely on you to help raise my kids. I couldn't wish for better grandparents! I'm proud of the man I am today and the bits I like most are those parts of you that I recognize in myself. I love you!

Iza, thank you for coming at exactly the right time, *i.e.* <u>after</u> I finished my thesis. I'm hoping for a smooth transition of one type of sleepless night into the other. I can't wait to see if you'll be as cute and pretty as your Mommy! Please choose wisely those traits of me that you want to inherit… either way I'm sure the world will never be the same with you in it.

Lennon, little boss, I'm proud of you like a monkey with 7 tails. Sometimes people tell me you look like me, and that's the greatest compliment I can get because you're the most beautiful man I've ever seen. I hope I can continue to give my best attempt at a good example for you for as long as you need it, but that you will soon outgrow me and save the world with whatever beautiful talents you may develop.

Moniek, I could fill a book with things I should thank you for, and it would still not be enough. We met decades ago so I'm spoiled in the sense that I never had to pursue happiness and could focus on other more trivial things like a professional career. Thank you for our fairytale family. I will never be able to repay you for the magic that you brought into my life. I can hardly consider myself an adult because you take on all responsibility for the grown-up stuff. Thank you for your support, thank you for organizing our whole life while I'm out claiming to save the world but secretly selfishly doing what I really love and can't help doing. Thank you for this freedom that only you could give me. I love you and I'm sure we will live happily ever after.

Overview of completed training activities

Discipline specific activities

INASCON	Baarlo, The Netherlands	2016
ISEV meeting	Rotterdam, The Netherlands	2016
MIRA Day	Enschede, The Netherlands	2016
INASCON	Bristol, United Kingdom	2017
Dutch BioPhysics (NWO)	Veldhoven, The Netherlands	2017
MESA+ Meeting	Enschede, The Netherlands	2018
Dutch BioPhysics (NWO)	Veldhoven, The Netherlands	2018
MicroTAS (CBMS)	Kiaohsiung, Taiwan	2018
ISEV meeting	Kyoto, Japan	2019
MicroTAS (CBMS)	Basel, Switzerland	2019
MicroTAS (CBMS)	online	2020

General courses

Entrepreneurship In and Outside Science (WGS)	Wageningen, The Netherlands	2016
VLAG PhD week (VLAG)	Baarlo, The Netherlands	2016
Brain training (VLAG)	Wageningen, The Netherlands	2017
Project and Time Management (VLAG)	Wageningen, The Netherlands	2017
Data Management Planning (VLAG)	Wageningen, The Netherlands	2017
PhD Workshop Carousel 2017 (WGS)	Wageningen, The Netherlands	2017
Physics with Industry (NWO)	Leiden, The Netherlands	2018
UT Entrepreneurial Challenge workshops (Novel-T)	Enschede, The Netherlands	2019

Optional courses

Preparation of research proposal	2016
Organizing Committee INASCON	2014-2016
PhD study tour to Denmark and Sweden	2016
PhD study tour to Israel	2019
MicroTAS 2020 Social Media Committee (CBMS)	2020

The research described in this thesis was financially supported by NWO, Perspectief Project 14196, “Cancer-ID”.

Financial support from Wageningen University for printing this thesis is gratefully acknowledged.

Thesis printed by GVO Drukkers en Vormgevers.

[Grab your reader's attention with a great quote from the document or use this space to emphasize a key point. To place this text box anywhere on the page, just drag it.]